Analysis of Organic Artefacts from the *Mary Rose*

Lianne Maria Jordan

A thesis submitted in partial fulfilment of the requirements for the degree of
Doctor of Philosophy

The University of Sheffield
Department of Chemical and Biological Engineering

October 2020

Abstract

The *Mary Rose* is a Tudor warship, commissioned by Henry VIII in 1510, which sank in 1545 off the south coast of England. It was raised in 1982 with over 19,000 artefacts. Research into conservation of marine archaeological artefacts has expanded since then but research into organic-based marine archaeological materials is relatively sparse. There is an increased likelihood of these materials surviving in a near anoxic, marine environment but degradation can still occur through mechanical, chemical, and biological processes. This can create complicated pathways of degradation, which need to be explored further. In marine archaeological wood, one of the major degradation pathways is through sulfur species, where reduced sulfur compounds oxidise upon raising the ship to form sulfate salts and sulfuric acid. This hydrolyses cellulose, leading to its breakdown. Iron from ship fixtures and other artefacts catalyse this process.[1]

A conservation treatment that neutralises sulfuric acid and removes iron sulfate is essential to prevent further degradation of organic-based artefacts from the ship. In this thesis, $SrCO_3$-cellulose patches were applied to iron sulfate soaked model wood. After removal, the patches and the wood were analysed by S and Fe K-edge X-ray Absorption Near Edge Structure (XANES) spectroscopy, FTIR, Raman, and portable XRF spectroscopy. The results indicate that sulfur and iron species can be removed by the patch, demonstrating its potential as a useful spot treatment for marine archaeological wood.

Other organic artefacts of sail cloth, anchor rope, wool, and leather from the *Mary Rose* were characterised using optical microscopy, SEM, and FTIR spectroscopy leading to a greater understanding of the organic artefacts from the ship through investigating fibre identification, and extent of degradation. This will influence the development of specific conservation treatments and has further reaching implications for the conservation of marine archaeological organic materials in general.

1   K. M. Wetherall, R. M. Moss, A. M. Jones, A. D. Smith, T. Skinner, D. M. Pickup, S. W. Goatham, A. V. Chadwick and R. J. Newport, J. Archaeol. Sci., 2008, 35, 1317–1328.

Acknowledgements

Contents

List of Abbreviations and Acronyms

ATR	Attenuated total reflectance
a.u	Arbitrary units
$Ca(OH)_2$	Calcium hydroxide
CIF	Crystallographic information file
EDX	Energy dispersive X-ray spectroscopy
EXAFS	Extended X-ray absorption fine structure
$FeCO_3$	Iron carbonate
$FeSO_4$	Iron (II) sulfate
$Fe_2(SO_4)_3$	Iron (III) sulfate
FTIR	Fourier transform infrared
HPLC	High performance liquid chromatography
ICSD	Inorganic crystal structure database
LCF	Linear combination fitting
LC-MS	Liquid chromatography mass spectrometry
LCST	Lower critical solution temperature
MALDI-TOF	Matrix-assisted laser desorption time-of-flight
$Mg(OH)_2$	Magnesium hydroxide
PCA	Principal components analysis
PDF	Pair distribution function
PEG	Polyethylene glycol
PXRD	Powder X-ray diffraction
SAXS	Small angle X-ray scattering
SDD	Silicon drift detector
SEM	Scanning electron microscopy
$SrCO_3$	Strontium carbonate
$Sr(NO_3)_2$	Strontium nitrate
$SrSO_4$	Strontium sulfate
TEM	Transmission electron microscopy
UCST	Upper critical solution temperature
XANES	X-ray absorption near-edge structure

XAS	X-ray absorption spectroscopy
XRD	X-ray diffraction
ZooMS	Zooarchaeology mass spectrometry

List of Tables

List of Figures

Chapter 1: Introduction

1.1 Conservation science

Conservation is based on the principle of minimal intervention and, where possible, reversibility of treatment. Preservation aims to minimise physical, biological, and chemical degradation of cultural heritage. This can be achieved by storage conditions or, when necessary, active treatments. Restoration aims to improve the interpretation of the piece of cultural heritage by maintaining (or restoring) the artefact to its original appearance or state. Original state here is subjective, providing a reason for the extreme care taken in making decisions to restore cultural heritage. For example, bullet hole damage or dirt on clothing or a flag could be part of the artefact's history so to restore the flag to its 'original' condition without any damage would be removing its story and interesting features, even though it may be better to repair the holes for the overall stability of the artefact. Yellowing under arms of a dress, for example, signifies a deterioration problem and will eventually lead to damage at key areas but there could be other avenues to explore besides artefact treatment, such as consideration of storage and display solutions. There are ethical codes of practice to which those working in cultural heritage must abide. Artefacts are not only appreciated from a material perspective but also due to their historical importance or from an aesthetic perspective. The main objectives of this thesis are concerned primarily with the physical state of artefacts but ethical considerations when working with cultural heritage artefacts are also vitally important.

Research into cultural heritage can include: investigation into the story of the artefact (its origins, what it is made from, how it was made, how it was used, its burial environment, previous conservation work and storage conditions); study of how and why it is degrading; kinetics and extent of degradation. This research can all lead into an overall picture of the history of the artefact as well as its material properties and unique concerns for the future. Conservation scientists work with conservators to develop solutions whether they be passive storage solutions and better storage conditions or consideration of active treatments. These decisions are carefully considered with respect to the best course of action for the object in question, usually on a case-by-case basis. Other considerations taken into account include the urgency of treatment, economic concerns and space demands for long-term storage or

display. These concerns are particularly important with regards to the difficulties involved with conserving shipwrecks due to their scale.

Conservation science is similar in some ways to forensic science in that the sample is usually limited (in size or quantity) and irreplaceable, making non-destructive and minimally-invasive techniques essential. Both fields aim to provide background information on a small sample. For example: what the sample is (human hair, dog hair), where it came from, who used it and so on. Conservation science additionally investigates how the artefact is degrading, potential causes of degradation, how the atmosphere and environment affect this, and possible routes for preventative or active treatment.

1.2 History of the *Mary Rose*

The *Mary Rose* is a ship that was commissioned by King Henry VIII in 1509 and built in Portsmouth between 1510 and 1511. It was Henry VIII's favourite and one of the most expensive warships in his fleet. Contrary to popular opinion, it did not sink on its maiden voyage, having spent 34 years active, engaging in naval battles. It did sink in battle off the coast of Portsmouth on 19th July 1545 while facing the French navy (Figure 1).[1] One of the most reliable accounts of how the ship sank is from one of the few survivors. They reported that as the ship turned about to fire with guns on the other side of the ship, a gust of wind caught the sails, tipping the boat, and water flooded through the open gun-ports.[1] The ship had been refitted to include heavier cannons, another contributing factor to its unfortunate end.

Figure 1 The Cowdray engraving which captured the events during the Battle of the Solent on 19th July 1545, when the *Mary Rose* sank.

The variety of artefacts from the *Mary Rose* provide a unique insight into Tudor life generally with personal items such as food bowls, hats, leather jerkins, games, musical instruments, longbows, and shoes recovered from the wreck. It is an important source of a wealth of evidence of what life was like on board a Tudor ship, providing touching details of the lifestyles of the crew including diet, illnesses, and roles of the crew members. It should be remembered that the sinking of the ship led to a massive loss of life as the ship sank quickly and netting on the top deck made it difficult for sailors to escape as it sank, resulting in the deaths of approximately 400 crew members.

Shortly after the ship sank, attempts were made to raise the *Mary Rose,* but were ultimately unsuccessful. Divers John and Charles Deane were able to locate the ship in 1836 and raised a few cannons and the main mast which were of interest more for financial purposes. After these initial failed attempts at raising the ship, the *Mary Rose* was eventually rediscovered in 1971 by Alexander McKee's team and raised from the seafloor in 1982.

The *Mary Rose* is now housed in a purpose-built museum to keep it in a stable condition and for easy and engaging viewing by the public (Figure 2). A massive conservation effort to preserve the hull and its 19,000 artefacts has been in progress since the raising of the ship and is still ongoing. The type of material, depth of burial, and the accessibility of decay agents to the ship led to a wide variety of preservation states in the vast range of artefacts uncovered.[2] Conservation approaches for wood from the *Mary Rose* are considered here as they comprise the main hull of the ship and much research has been carried out with regards to the conservation of marine archaeological wood. This remains an active area of research due to the cultural importance of the artefacts and their increasingly fragile nature since being raised from the seabed.

Figure 2 The wooden hull of the Mary Rose (left) as housed in the *Mary Rose* museum (right) today.

The *Mary Rose* and its many artefacts are in a reasonable state of preservation considering its age, as half of the ship was buried in silt helping to preserve the hull and artefacts due to the near anoxic environment of the sea floor. However, while it was on the seabed, marine organisms, tidal movements, oxygen levels, temperature, and pH all had an impact on the mechanical, physical and chemical degradation of the *Mary Rose.*[2] Many of the timbers were weakened over time on the seabed due to abrasive, silt-laden currents and microorganisms increasing the permeability of the wood structure.[2] This bacterial, fungal and water erosion helped H_2S (produced by sulfur reducing bacteria in polluted seas) diffuse into the timbers and react to form reduced sulfur compounds.[3, 4, 5] Whilst these compounds do not cause a major problem in the near anoxic conditions of the seabed, upon raising the wood, oxidation lead to the formation of sulfuric acid and sulfate salts.[6] Sulfuric acid is problematic because it reduces the mechanical strength of the timber by hydrolysing the cellulose and hemicellulose content.[5] The precipitation of sulfate salts on the surface of the timbers lead to discolouration and splitting of wood fibres, and were observed particularly in areas where iron fittings had been in contact with the wood.[7] Iron (from fittings and other artefacts in the ship) augments the problem by catalysing the formation of sulfuric acid.[5] This self-perpetuating process is commonly known as the 'sulfur problem' and was first exposed in the early 2000s in the *Vasa*; a Swedish ship which sank in Stockholm harbour in 1628.[5,7]

To combat these degradation issues, the *Mary Rose* hull has been sprayed with polyethylene glycol (PEG) for 30 years and is currently air drying in a controlled environment.[2] While recent

reports have suggested that the PEG itself may degrade over time,[6,7] its chief function is to replace lost water to provide structural stability as the wood dries.

The cellulose inside the timbers of the *Vasa* is more degraded than the cellulose at the surface of the wood.[8] This is in direct contrast with the timbers of the *Mary Rose*, which have an outer layer of damaged cells and generally well-preserved wood cells inside.[2] It is thought that the timbers from the *Vasa* are less degraded at the surface due to iron neutralizing the oxalic acid in the wood to prevent cellulose hydrolysis at the surface.[8] This challenges previous findings that suggest iron catalyses the oxidative degradation of cellulose[9, 6, 7, 10, 11] and has not been observed in the wood from the *Mary Rose* so far, showing the importance of considering and treating each artefact individually. Conservation treatments must continue to be thoroughly explored in order to effectively reduce the impact of the 'sulfur problem' along with the problem of instability upon drying and biological deterioration of waterlogged archaeological wood.[12] Polymers for consolidation of the wood, chelating ligands for iron removal, and nanoparticles for deacidification and stabilization of iron and sulfur compounds have all been considered as treatments for the conservation of marine archaeological wood.

1.3 Wood structure and degradation
1.3.1 Structure

The hull of the *Mary Rose* is comprised of oak timbers making understanding wood structure and degradation vitally important for its conservation.[13] Wood has a complex heterogeneous structure; there are differences among species, variability within the same species due to location and the history of the local environment, and even variability between different areas of the same plant. Wood is an anisotropic material; its properties differ in different directions. In broad terms, wood can be separated into two types: softwoods (e.g. pines) and hardwoods (e.g. oak). From outside to the inside of the trunk, wood consists of bark, the secondary meristem, and pith. The secondary meristem produces lignified elements.

At a fundamental level, wood is comprised of cellulose, hemicellulose, lignin, pectin, and extractives. Cellulose is one of the most abundant biopolymers, its structure of glucose units joined by a glycosidic linkage is displayed in Figure 3(a). Its repeating unit is termed cellobiose. Lignin gives the plant structure and is a complex phenolic structure with many useful hydroxyl groups, shown in Figure 3(d). Hemicellulose consists of 5 and 6 carbon sugars in a variety of

arrangements, a basic structure of which is presented in Figure 3(c). They are branched polymers consisting mostly of xylose and mannose.[14] Pectins are covalently linked polysaccharides consisting primarily of pectic acid (Figure 3(b)).[15] Extractives are non-structural molecules not found in the wood cell wall that can be removed by solvents. They are compounds which protect the tree against fungal growth, insects, and bacterial attack and include phenolic compounds (for example tannins).[16]
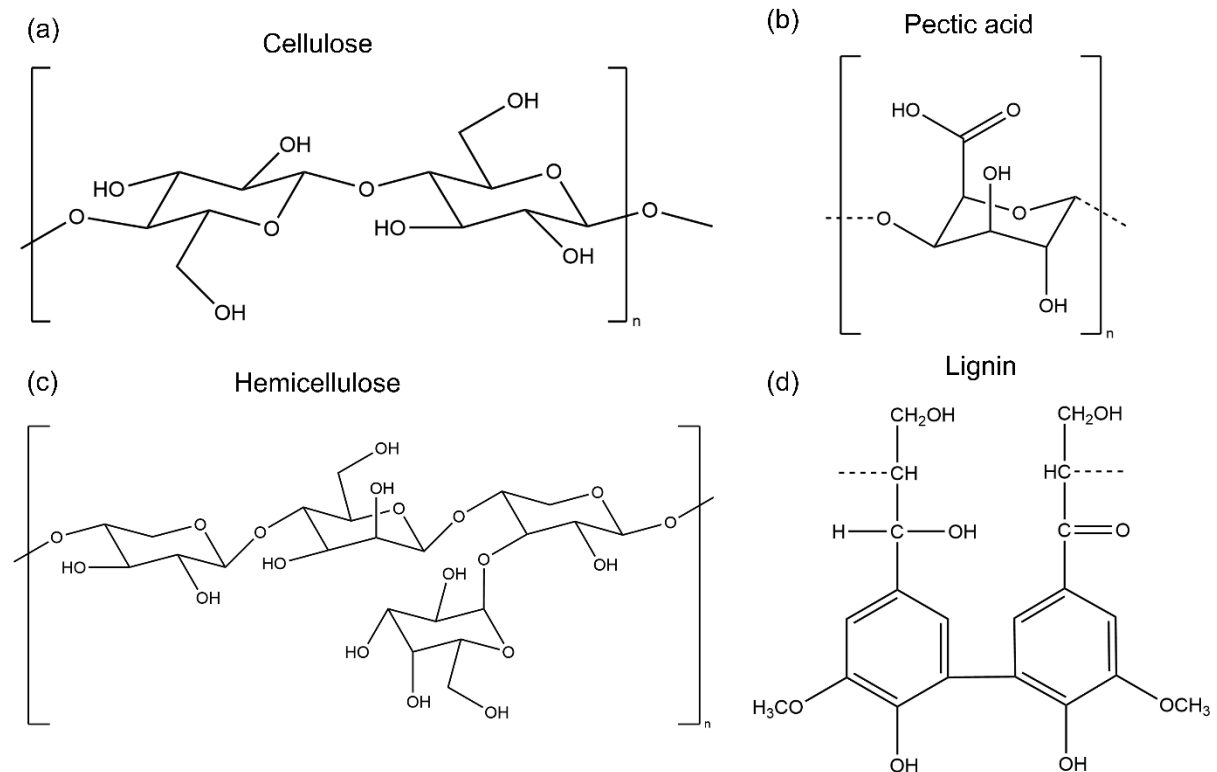
Figure 3 Basic chemical structures of **(a)** cellulose **(b)** pectic acid **(c)** hemicellulose and **(d)** lignin (adapted from V. Daniels in *Conservation Science: Heritage Materials*, 2006 and S. L. Mathews, *Appl. Microbiol. Biotechnol.,* 2015).[17,18]

Cellulose chains are arranged in crystalline bundles which then form elementary fibrils. These aggregate to form microfibrils. Bundles of microfibrils are termed macrofibrils which are found in the cell walls of plant fibres.[14] Amorphous materials (such as amorphous cellulose, hemicellulose, lignin, and pectin) are found in the spaces between the elementary fibrils, microfibrils, macrofibrils, and in the intercellular space (also known as the middle lamella, which is the matrix cementing individual cells together).[14] Cellulose exists in a variety of forms: cellulose I$_\alpha$, cellulose I$_\beta$ (their hydrogen bonding patterns, conformations, and glycosidic linkages differ), cellulose II, III, IV, and amorphous cellulose.[19] In most plants, the

crystal structure of cellulose is I_β which has a monoclinic unit cell of space group $P2_1$ with cellulose chains aligned along the c-axis.[20–22] Cellulose II can be formed from cellulose I *via* the addition of NaOH or solubilisation and recrystallisation, and cellulose III through reaction of cellulose I or II with liquid ammonia.[22] Cellulose IV can be formed by heating cellulose III.[19]

Wood (and fibre) cells consist of a primary and secondary cell wall surrounding a hollow lumen (a simple diagram of which is provided in Figure 4). The secondary cell wall differs significantly from the primary cell wall, usually containing more cellulose.[23] Also, the cellulose microfibrils are oriented differently in the primary and secondary cell walls.[24] Secondary cell walls have a high content of uniformly ordered cellulose enriched with lignin.[25] The secondary cell wall is composed of three layers: S1, S2, and S3 layers. In the S2 layer, cellulose aligns roughly parallel to the length of the cell. The S3 layer is closest to the lumen, which is the hollow space inside plant cells primarily used for water transport.
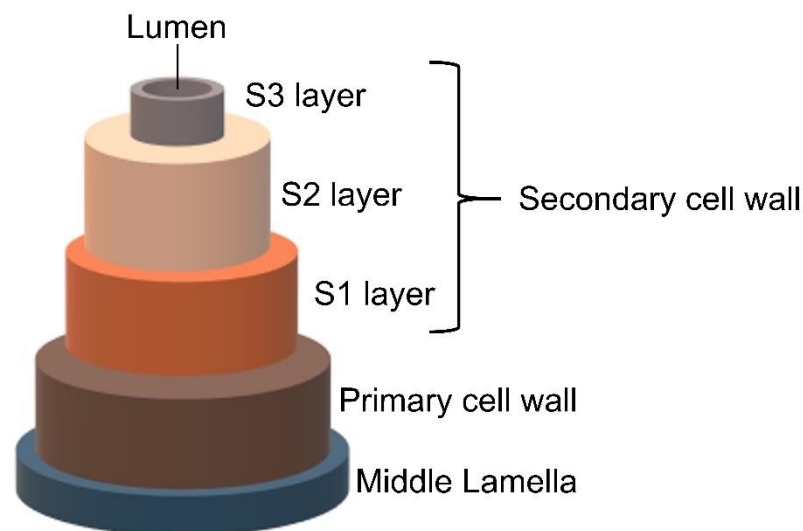
Figure 4 Simplified diagram of the cell wall structure of plants (adapted from S. L. Mathews, *Appl. Microbiol. Biotechnol.*, 2015).[18]

Water is an integral element of wood, being hygroscopic, the moisture content of wood affects nearly all its properties. Cellulose and hemicellulose have great affinity for water, which is very useful for water transport within the plant. Water is found both free in the cell lumen and bound within cell walls. Water can potentially cause damage to the wood as, at a certain saturation point, the moisture content will start to affect cell dimensions.

Wood is biodegradable; it can be degraded by bacteria, fungi, insects, and marine borers. Extractives protect the hollow cells of wood from insects and fungi and give colour to the wood. Once degraded, the wood is prone to letting in more water which can cause swelling and damage to the cells. Sulfur is often a product of bacterial activity which can further harm wood.

Resins are viscous liquids which are not water soluble and their purpose is to protect the plant from decay (tannins also act as preservatives).[26] Tannins are water-soluble and, in the presence of iron, form iron tannate complexes which impart the typical dark brown-black colour of archaeological wood.

1.3.2 Degradation

Marine archaeological wood can be degraded by biological, chemical, and physical means. The cellulose and hemicellulose are often degraded first, leaving the lignin component as this is not as easily degraded. This is the reason some waterlogged wood appears to be in good condition, as its structural components may still be intact, but the cells may have detrimentally changed. Water also plays a role in providing structure to the wood, and once excavated from a waterlogged environment, loss of water can lead to cell collapse.

Agents that decay wood include soft-rot fungi, erosion, tunnelling, and cavitation bacteria. Soft-rot fungi attack the cellulose in the S2 layer, making small holes along the microfibril angle of cellulose.

Water is crucial to maintaining the structure of the deteriorated wood and often, if the archaeological wood is not treated and dried uncontrollably, shrinkage and collapse of the wood structure is often observed. Shrinkage is usually reversible, but collapse is irreversible. Polyethylene glycol (PEG) is a common treatment for marine archaeological wood as it can replace the water in the wood pores and maintain their structure. This and other treatments for marine archaeological wood are examined in the next section.

Oak wood presents a problem when used in a display case for other artefacts as it can off gas volatile organic compounds like tannic acid and acetic acid which can degrade other artefacts.[27]

1.4 Conservation treatments for archaeological wood

The Swedish warship, the *Vasa*, provides a good comparison to the *Mary Rose* ship to help develop a better understanding of marine archaeological wood, especially since they are of a similar era. They spent different lengths of time on the seabed and the *Vasa* sank in harbour whereas the *Mary Rose* sailed for around 34 years.

A crucial treatment for waterlogged wood is polyethylene glycol (PEG), also known as polyethylene oxide (PEO). This has been widely applied to treat marine archaeological wood and has many advantages over other treatments. For example, PEG can be used at varying molecular weights depending on the end goal of the treatment. Lower molecular weight PEG can be used to easily penetrate through the wood pores and higher molecular weight PEG can consolidate the wood structure by replacing water in the pores and consequently supporting the structure from collapse. There has, unfortunately, been a few drawbacks to the use of PEG on waterlogged wood. For example, it has been noted that PEG contributes to oxidation of Fe^{2+} in an acidic environment.[28] Fe^{3+} is problematic as it oxidises reduced sulfur compounds.

An important example of a treatment applied to waterlogged archaeological wood which was later found to be compromising the wood and masking the underlying degradation is alum treatment which was applied to artefacts of the Oseberg ship (in Oslo).[29] The treatment was not well understood at the time it was applied and has caused more problems in conservation.

1.4.1 Polymer treatments

To combat the problems in marine archaeological wood caused by iron and sulfur compounds, polyethylene glycol (PEG) has been widely used in conservation efforts. It is thought that PEG can enter the voids in the wood, replace water and provide structural stability for when the wood is dried in a controlled manner.[10] In the case of the *Mary Rose,* the hull has been sprayed with PEG-200 from 1994 to 2006 and PEG-2000 from 2006-2013 and since then, it has been air drying under controlled conditions.[28] The lower average molecular weight PEG was used for ease of penetration through the wood whilst PEG-2000 was used to provide structural support by filling cell lumens of the wood fibres.[28] To prevent

further biological deterioration, a broad spectrum biocide (PhaseChem305) was also used to treat the wood.[12]

The use of PEG was shown to have a positive effect when comparing untreated, more recently recovered wood samples from the *Mary Rose* with PEG treated wood samples.[9,30] This was concluded from linear combination fitting of X-ray absorption near-edge structure (XANES) spectra of wooden artefacts recovered in 2005, which had not been treated with PEG. These untreated wood core samples showed a large proportion of highly oxidised sulfur and iron on the surface.[9] This was compared to results from Sandström *et al.* for PEG treated wood which showed the highest contribution of sulfate (sulfur in +6 oxidation state) to be 6%, whereas in the untreated samples, the average contribution of sulfate to the spectra was 18% showing the PEG treatment does seem to reduce the contribution of oxidised sulfur in the wood.[9,30] However, there have been several studies reporting disadvantages of PEG treatment on marine archaeological wood. Preston *et al.* have shown that PEG can promote the oxidation of Fe^{2+} under acidic conditions by promoting the growth of iron-oxidising acidophilic bacteria.[28] PEG was also shown to enable iron sulfide corrosion and to catalyse sulfuric acid production. Therefore biocidal treatment and removal or inactivation of reduced iron and sulfur compounds before PEG is considered for future conservation treatments was recommended.[28] As well as leading to further deterioration, PEG treatment has also been criticised for being too time-consuming and for some incidences of "bleeding" from the wood.[31] Other disadvantages of using PEG include its plasticising effect on the wood and its ability to act as a solid-state ion transporter.[12]

With the aim of developing a more effective treatment for conservation of marine archaeological wood than PEG, an aqueous polymer dispersion comprised of butyl methacrylate, methyl methacrylate and trimethoxypropylsilyl methacrylate was tested.[31] Benefits of this system include its low viscosity leading to improved penetration into the wood and its ability to control polymer particle size and surface charge.[31] It was concluded that penetration occurred but unfortunately did not prevent shrinking and deformation of the wood samples upon drying.[31]

More recently, self-assembling supramolecular polymer networks have been shown to effectively chelate iron ions, providing a more reversible and greener solution for the

conservation of timbers from the *Mary Rose* compared with the use of PEG.[32] A cheaper and more renewable treatment of natural polymers like chitosan or guar has also been investigated with promising results. These natural polymers can provide similar mechanical and structural support to PEG but are less prone to degradation into acidic by-products and do not irreversibly affect the wood structure.[12] Chitosan was concluded to be a particularly effective consolidant and has further advantages including natural anti-bacterial properties and the ability to chelate iron ions through its amine backbone.[12]

1.4.2 Chelating treatments

A variety of chelating ligands have been tested for their applicability in conservation treatments. Skinner and Jones investigated the effect of calcium phytate (myo-inositol hexaphosphate) on the oxidation rate of wood samples from the *Mary Rose*.[33] Calcium (or magnesium) phytate is a chelating agent for divalent metal ions, which has been previously used in paper conservation treatments.[34–36] Its structure is presented in Figure 5. It was found that the oxidation rate for wood samples treated with calcium phytate was less than that of PEG-treated and untreated samples, showing the success of this treatment method.[33]
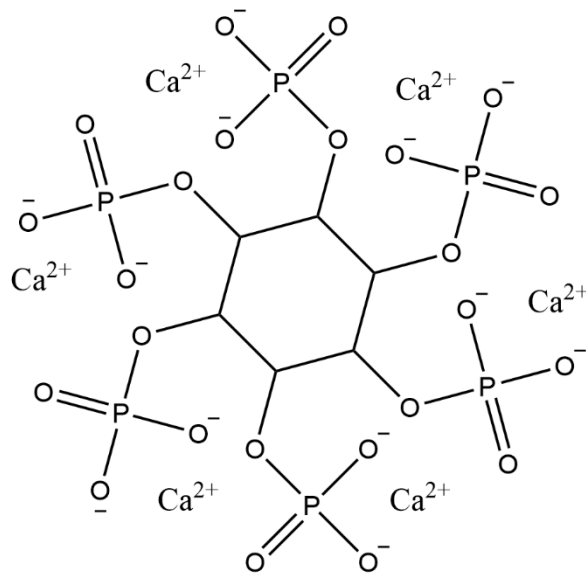
Figure 5 Chemical structure of calcium phytate (adapted from the National Center for Biotechnology Information, PubChem Compound Summary for CID 24495, Calcium phytate).[37]

Although phytate inhibits transition metal catalysed oxidation, it does not inhibit the natural oxidation of cellulose.[38] This treatment also needs to be followed by a deacidification

treatment to prevent hydrolysis of cellulose and the phosphorylated groups of phytate.[38] Another issue with this treatment is that calcium and magnesium phytates are not very soluble in organic solvents but they can be functionalized to improve solubility or lithium aluminium phosphate could be used.[38] The main advantages of phytate treatments are that the iron(III)-phytate complexes formed upon chelation are unreactive, white and do not alter the aesthetics of the treated object.[38]

Further chelating ligands have been proposed for the extraction of iron ions to reduce the rate of oxidation in the wood samples. For example, ethylenediimino-bis(2-hydroxy-4-methyl)acetic acid (EDDHMA) or diethylenetriamine pentaacetatic acid (DTPA) in aqueous solution at high pH was found effective for removal of iron ions and neutralization of acid.[6] However, the extraction process was limited by diffusion through the wood fibres and effective treatment could take months or years; the long-term effect of the treatment is also unknown.[6] Nanoparticles solve this problem of rate of diffusion into artefacts to some extent due to their small size and as such will be investigated further in Section 1.10.

1.5 Characterisation techniques for conservation

There is an abundance of scientific techniques that have been applied to the study of cultural heritage materials. Indeed, there is a wealth of cultural heritage materials themselves, from fossils, tools, clothing, human remains, jewellery, and ceramics to ships, buildings, and environments. Research in these areas is rich and interdisciplinary, traversing the fields of chemistry, biology, archaeology, physics, and history. The scope of this thesis restricts a summary of the breadth of research carried out in this area to either techniques that are used in this thesis, or materials related to those discussed in this thesis, namely, wood and textiles including rope, wool, and leather. The next chapter discusses the theory and practicalities of the techniques used in this thesis, but this section provides a brief overview of the use of these techniques applied to cultural heritage materials in the literature.

Firstly, why are characterisation techniques required? There are many reasons, but mainly: to try to fully understand problems artefacts face; to explore their degradation; to develop conservation treatments; to identify pigments and other important features of the artefacts. A range of analytical methods are applied to a variety of heritage materials, for example:

micro-Raman, Fourier Transform infrared (FTIR), and X-ray fluorescence (XRF) spectroscopy for pigment identification and scanning electron microscopy (SEM) and atomic force microscopy (AFM) for study of ceramic and glass surfaces.[27] Isotopic analysis is not thoroughly considered in this thesis although it forms a large part of characterising artefacts and provides a wealth of information on the provenance of many artefacts.

Synchrotron techniques provide powerful probes for detailed investigation of artefacts, due to the amount and quality of data that can be extracted often non-destructively from artefacts. These are considered in the following section.

1.5.1 X-ray absorption spectroscopy (XAS) for conservation

X-ray absorption spectroscopy (XAS) using synchrotron light sources has been used for a vast range of applications from geology to physics. The power of this technique is in its ability to measure many elements, compounds, and materials as, unlike XRD, it does not rely on symmetry or crystallinity. In the same vein, it does not require long-range ordering to be effective.[39] XAS can be used to give information on the electronic and atomic structure of the material including its oxidation state, type and number of surrounding atoms, distance of the surrounding atoms and their distribution. The extended x-ray absorption fine structure (EXAFS) can provide information on the types of atoms surrounding the absorber, the number of neighbouring atoms and their distance from the absorbing atom. XAS is well suited to analysis of heterogeneous and complex materials, especially heritage materials. The beam size is small, and measurement can be arranged to be as minimally invasive as possible. As it is element-specific, it is useful for identifying species which may only be present in small concentrations in the sample.[40]

For the *Mary Rose* wood samples, X-ray absorption near-edge structure (XANES) spectroscopy has been largely used for identifying sulfur and iron species of different oxidation states to determine the effectiveness of conservation treatments. It has the advantage over other techniques as it is sensitive to very small amounts of the compounds present in the wood and is non-destructive. In this thesis, spectra of known standards have been compared to the spectra of measured samples to ascertain the composition of the sample. Linear combination fitting (LCF) was used on normalised absorption spectra to determine the likely composition

of the measured samples. Linear combination fitting assumes the sample spectrum is a mixture of phases or states that can be seen as a linear combination of the spectra of standard compounds. The problem with applying this method to wood samples lies in the difficulty of predicting which standards would give the best representation of the atomic coordination environment of the atom under examination.

Synchrotron techniques were further utilised in a long-term study of the effects of the PEG spraying and drying processes on sulfur speciation in the *Mary Rose* hull.[41] XANES and XRF imaging showed that oxidised sulfur remains at the wood surface after PEG treatment and drying and FTIR spectroscopy was used to correlate areas of wood degradation with oxidised sulfur species.[41] XANES studies on sulfur and iron speciation in the *Vasa*, the *Mary Rose*, and other ships have been important for exposing how problematic and widespread sulfur and iron compounds can be in historical wooden shipwrecks.[9,42–44] XANES has also been used to distinguish Fe(II) and Fe(III) compounds in ink to try to prevent manuscript degradation.[27]

1.6 Textile conservation

The term textile usually applies to any woven fabric or cloth but is used in this thesis as a way of describing the organic archaeological artefacts that are not composed of wood. The sail cloth was woven and so can be classed as a textile. The rope and wool are described as textiles as they are fibres that have been twisted or spun together. Leather is not strictly a textile as it is not a woven fabric. However, they can all be classed as organic materials or artefacts which are not wood and are often thought of as fabrics. It is often possible to identify the fibre (providing it is not badly degraded) through optical microscopy, SEM, and FTIR spectroscopy. Studying the way the fibres have been woven together and the direction of spin can give details on the manufacture of textile artefacts.[45] Textile studies are important as they can provide information on trade, economic, and technological patterns of the past.[46] They are a unique insight into how people lived, what they wore, and how they worked.

Textile evidence can either be direct (the textile artefact itself remains) or indirect. Indirect textile evidence includes pseudomorphs, where the fabric artefact may be partially or completely replaced with mineral compounds which retain the artefact's original shape. This usually occurs in waterlogged environments in the presence of metals.[47] Metals can catalyse

cellulose degradation. Partially mineralised fibres occur if metal ions bond to cellulose and prevent further degradation. A true pseudomorph is where the organic materials completely decompose and metallic minerals form in their place. Mineralised textiles can preserve fibre materials or retain the physical shape of the original fibre. Mineralisation depends on many factors such as: the concentration of the metal ions, soil or silt composition, temperature, pH, moisture levels, and duration of burial.[48]

In the marine environment fibres are constantly swollen which accelerates degradation and mineralisation. Bacterial activity can also increase fibre degradation, enabling penetration of metal ions. Although bioactivity is inhibited at high concentrations of metal ions.[48] Metal ions are attracted to the negative surface charge of fibres and can aggregate forming insoluble precipitates on the surface. Some areas of the fibre surfaces are more interactive with ions than others, so while in some places the metal ions aggregate, in some areas metal ions can diffuse into the fibre through the pore network.[48]

An example of both direct and indirect textile evidence discussed above can be found in the work of Angiorama *et al.*[49] Metal bracelets discovered in Argentina with textile evidence on their exterior were analysed; some evidence of organic material form the textiles remained while in other areas the organic material had been replaced almost completely, creating a cast or an impression of the textile artefact.[49] The advanced state of mineralisation of the textile evidence on the metal bracelets enabled the researchers to conclude that the metal bracelets were likely from a funerary context, suggesting the provenance of the artefacts.[49]

Conservation of cultural heritage presents a challenge, not only due to its highly interdisciplinary nature, but also due to the need to balance the physical preservation of the artefacts for the future and the preservation of the history of the object.[50] With this in mind, it is important to carefully consider all the ways in which a chemical treatment could affect an artefact. Cleaning of the object, for example, although perhaps necessary to its long-term stability, could remove valuable evidence of its original use or environment, hindering deeper understanding of the artefact.[50] For example, removing the tar from rope recovered from the *Mary Rose* without proper cataloguing or respect for the original use of the artefact could have masked the knowledge that tar was used to preserve the rope during use.

Conserving archaeological material from marine sites is essential, especially for organic material like wood, textiles, rope, and leather. If raised from the sea and allowed to dry without any conservation treatment, these artefacts may crumble into dust within hours.[51] Laboratory conservation usually consists of six stages: storage prior to treatment, evaluation of the conservation process, mechanical cleaning, stabilisation treatment, optional restoration, and long-term storage or exhibition.[51]

Oxygen and gases in the environment can affect the rate of decay of textiles in addition to mould, bacteria, heat, and light exposure.[51] Degradation of paper and canvas has been widely researched and is linked to that of wood and textile samples as they are all composed of cellulose to some extent, the degradation of which is the main concern for many artefacts. It has been found that acidic environments catalyse the hydrolysis of β-(1,4)-glycosidic bonds in cellulose.[52] This is a self-accelerating reaction where oxidation is promoted by acidity, leading to a more acidic environment and to further hydrolysis.[52] The hydrolysis reaction is affected by pH, moisture content and temperature and leads to depolymerisation and loss of the mechanical properties of cellulose, overall weakening the structure of the artefact.[52]

Historic textiles, like wood, are mainly composed of cellulose. To develop effective conservation treatments, the physical state of the artefact must first be assessed. Garside and Wyeth have developed a means of using polarized Attenuated Total Reflectance Fourier Transform Infrared Spectroscopy (ATR-FTIR) spectroscopy to analyse the degradation of materials including linen and silk.[53] Upon ageing, the physical properties of the textile change. Among other changes, the fibres may become brittle and stiff, the dyes may fade and the fibre may decrease in tensile strength.[53] On a microscale, the physical properties of the fibres are linked to the degree of polymerization of cellulose, the fractional crystallinity and orientation of the microfibrils.[53] All of which, if modified, affect the load-bearing capacity of the material.[53] It was shown in silk that a decrease in breaking strength correlated with a decrease in the oriented crystallite parameter.[53]

1.6.1 Polymer treatments

Polymers are commonly used in consolidation conservation treatments, including epoxy resins and polymethylmethacyrlates (PMMAs). Polyvinyl alcohol (PVAl) has been shown to be

useful in textile conservation as it is clearer, shrinks less and is more flexible than polyvinyl acrylate (PVA). However, these polymers have disadvantages when used as conservation treatments; for example PVAl is only soluble in water so requires a fungicide to prevent mould growth and epoxy resins discolour with age.[51] This contradicts conservation ethics that mean treatments should not significantly alter the appearance of the artefact.[51] Ideal polymer treatments should be flexible, transparent, durable, easy to apply, have no colour, have adhesive and cohesive properties, and be as reversible as possible.[54]

Chemical gels of semi-interpenetrating polymers that can be shaped into thin, transparent and removable foils and loaded with cleaning fluids (oil in water micro-emulsions or polar solvents) have been found to be useful for the treatment of water sensitive objects such as parchment, easel paintings and dyed textiles.[55] The nano/microporosity of the covalently bonded polymer network and the hydrophilicity of the gel can be tuned to allow the controlled release of water-based cleaning fluids in a similar vein as targeted drug delivery systems.[55] A polymer film of P(MMA-co-EtA) (poly(methyl methacrylate-co-ethyl acrylate)) deposited by a low pressure non-equilibrium plasma polymerization process onto aged paper has been found to remain unchanged for up to 100 hours of UV treatment.[56]

Polymer treatments are sometimes problematic due to their size making it difficult to penetrate the artefacts. Polymerising the monomers *in situ* is a solution to this issue proposed by Princi *et. al.* who investigated the effects of grafting polymerisation on cellulose for paper and textile conservation. This treatment was shown to be effective in improving the mechanical resistance of the materials studied.[57]

1.7 Cellulosic fibres

Textiles are an invaluable source of information on past technologies, anthropological costumes, cultural transfers, palaeoeconomic, gender studies, and aesthetic traditions.[58] The first evidence of manipulation of fibres comes from the upper Palaeolithic period (starting around 40,000 years ago).[59] There is evidence of cordage and nets from waterlogged environments dating from the Mesolithic period (from 8,000 BCE to 2,700 BCE in Europe).[45] The most widely used fibres in antiquity were cotton and flax; although hemp (*Cannabis sativa*) and nettle (*Urtica dioica*) are commonly found in archaeological samples.[45,60] Hemp

particularly was a vital crop during the Tudor period demonstrated by Henry VIII passing a law in 1533 requiring farmers to grow ¼ acre of flax or hemp for every 60 acres of land they owned.[61] Hemp was an important crop for expanding naval activities as it was more resistant to salt water so useful for cordage, and flax was generally preferred for manufacture of sail cloth.[62]

1.7.1 Fibre structure and identification

Textile fibres can be classified as natural or man-made. Man-made fibres did not appear commercially until 1892, with the commercialisation of viscose rayon.[63] As the *Mary Rose* sank in 1545, man-made fibres will only be considered very briefly (or in terms of a comparison) in this project. Natural fibres include cellulosic (also called vegetable or plant fibres), animal (or proteinaceous), and mineral (e.g. asbestos) fibres. Cellulosic fibres can be separated into three groups: bast, seed, and leaf fibres. Bast fibres are from the outer part of the stem of the plant.[64] Examples of bast fibres include flax, ramie, jute, hemp, and nettle. As flax, hemp, and nettle were commonly utilised in ropes and sail cloth in Europe in the 16th century, these will form the focus of this work. Proteinaceous fibres can be split into categories of hair and silk and tend to have a higher water content than cellulosic fibres.[26] Fibres are usually considered as the individual components that are spun together to extend their length then spun into yarns for strength.[26]

Flax (*Linum usitatissimum*) is an annual plant which is also known as linen once processed into a textile. It is perhaps the oldest fibre used for non-food purposes with evidence of its use since the Neolithic period.[65] Flax fibres overall have an anti-clockwise twist, also referred to as S-twist or left-handed helix. This characteristic twist refers to the orientation of the microfibril bundles, usually in the S2 layer of the cell wall as this is normally much thicker than the other layers.[24] The cross-sections of flax fibres show a polygonal shape with thick cell walls and a small lumen, although as with all natural fibres, features can be very varied. "X-shaped" markings occur perpendicular to the fibre axis.[66] Cross-markings are striations on the fibre surface which do not interfere with its structure; they often occur irregularly and can be due to processing methods or occur during growth of the plant. Dislocations (also known as nodes) usually occur during the growth of the plant and can occur in individual fibres or in bundles of fibres.[67] They occur across the width of the fibre, sometimes altering the fibre structure

and can look like bends or buckles.[68] These are illustrated in micrographs of flax and hemp in Figure 6.

The important fibres for textile manufacturing are found below the outer cortex. The centre of the plant's stem is filled with pith which can break down over time leaving the stems hollow. Flax fibres are usually fine, silky, and white-grey to light-brown but the tow can be quite coarse and contains a lot of stem debris.[64] This may not have been a problem for Tudor rope or sail cloth makers who were probably more concerned with the strength of the fibre for this application. Flax is known to be a strong fibre with a degree of polymerisation of around 20,000. It is stronger when wet and easily absorbs water. Linen or flax is known to be more crystalline than other fibres so is considered slightly more resistant to ageing as most deterioration usually proceeds from amorphous regions. Dislocations occur frequently in flax fibres and cell walls are typically uniform and about six times as wide as the lumen. It is not unusual for plants grown in a botanic garden to have wide lumina, however.[64] This may cause difficulties in comparing the *Mary Rose* fibre samples as the historic comparison fibres used were from a botanic reference collection.
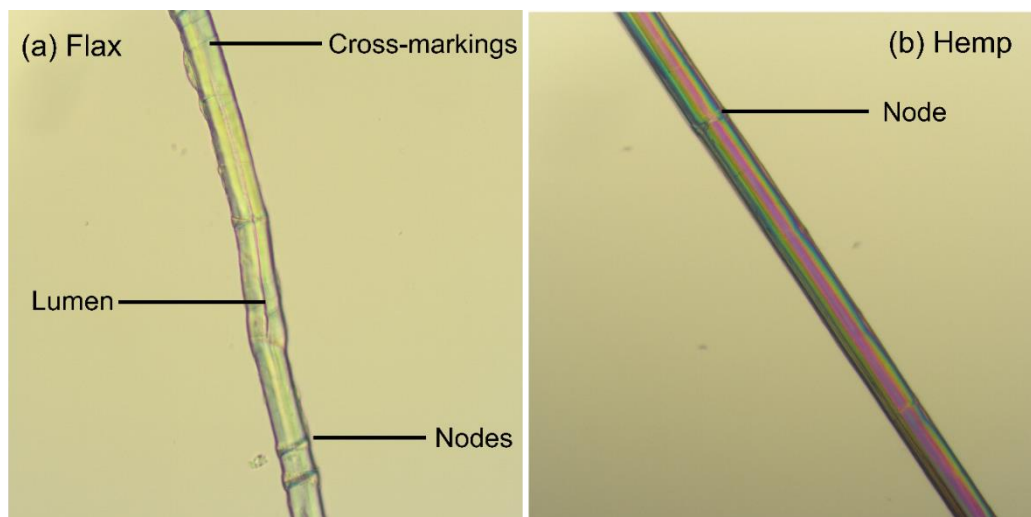
Figure 6 Optical microscope images of **(a)** a flax fibre and **(b)** a hemp fibre with annotations showing features such as the lumen, nodes, and cross-markings.

Hemp (*Cannabis sativa L.*) fibres generally contain fewer nodes or dislocations in comparison with flax and have a clockwise or right-handed (Z-twist) fibrillar orientation overall.[24] Hemp usually has more cross-markings than flax fibres.[64] Hemp is a fast-growing, annual plant that also smothers weeds.[64] It is very resistant to insects and fertilisers and herbicides are not

required. Cluster crystals (calcium oxalate crystals (CaC_2O_4)) are present in the fibre bundles, and frequent in the pith (see Figure 7) and can be used to identify hemp from other bast fibres. Similar to flax, in older hemp plants the pith breaks down, hollowing out the stem. Hemp is very variable but tends to be coarse and grey or yellow-brown in colour. Its cross-section tends to be of a flattened or more rounded shape and includes more bundled ultimates and a wider lumen.[66] Ultimates are individual fibre cells (elementary fibrils) that are usually bundled together, cemented by the middle lamella.[69] The lumen width of flax and hemp fibres can overlap according to natural variations, making it difficult to distinguish these fibres with optical microscopy alone. FTIR can be useful for distinguishing these fibres and addition of a polariser to the IR beam can further aid with characterisation.
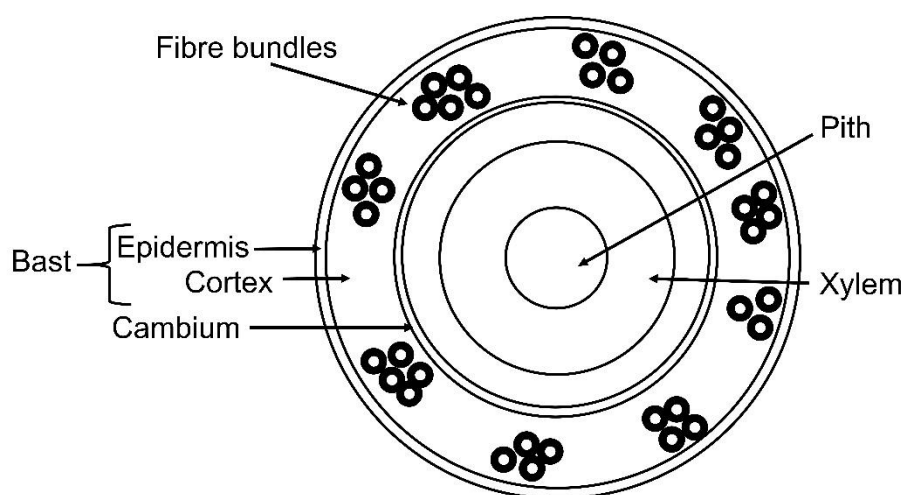
Figure 7 Basic diagrammatic representation of a hemp stem showing the position of the xylem tissue, the pith, fibre bundles of elementary fibres and the outer layer of the epidermis and cortex (adapted from M. Liu, *Industrial Crops and Products*, 108, 2017).[70]

Bast fibres have been in use since the Neolithic period.[65] Nettle (*Urtica dioica*) is another bast fibre that was widespread in northern Europe from prehistory to the industrial revolution and should be considered when looking at possible materials used in some of the *Mary Rose* artefacts.[68] Under the microscope, there would be some evidence of calcium oxalate crystals indicating the fibre was nettle but this is not conclusive as these crystals could be a result of fibre processing.[71]

Sisal is a leaf fibre and is considered here as it could be a component of the *Mary Rose* rope or sail cloth materials. Sisal has a clockwise twist (Z-twist) like hemp but has an irregular lumen

size.[66] The presence of acicular (needle-like) crystals, spiral and annular vessels can help to identify sisal through optical microscopy. Vessels are a type of cell in the xylem tissue of plants, mainly used for water and nutrient transport within plants.[72] Spiral and annular vessels can be found in the stem, roots, and leaves of plants.[72]

A short note on fibre processing is useful here as it can affect the structure of the fibre observed in the final textile product, providing information on past processing methods especially related to materials for ships. Bast fibres are often retted, a process where soft tissues of the plant are broken down by microorganisms. They are often water-retted or dew-retted, consideration of the time spent at this stage is important as retting for too long can damage fibre cells but for too little makes it difficult to separate the fibres. This process is followed by scutching to remove extraneous plant materials.[64] With water-retting, hemp was generally soaked for 7-10 days allowing the pectin binding the plant materials to break down.[73] The fibre can then be separated from the other materials and dried.

Identification of fibres in museum textiles reported in the literature is sparse. Although identification takes place where relevant, it is not published very often. Positive fibre identification is often difficult due to the varied nature of fibres, especially in museum textiles which may be heavily degraded. Textiles are often only a small fraction of the artefacts recovered and displayed in museums due to their susceptibility to degradation. They often only survive in extreme conditions; very wet, anoxic, and dark environments or in very dry environments. Also, there are limited resources available for researching textile history so research in this area is often sporadic.[74]

Identification can be undertaken by a variety of techniques. The most widespread is identification by optical microscopy. The thickness of the fibres and the frequency of dislocations should not be taken solely as evidence of species identification as these features can vary widely.[74] Features of bast, cotton, and wool fibres under an optical microscope are enough to distinguish between these fibres but caution must be taken with identifying fibres further than this through optical microscopy.

FTIR spectroscopy can indicate whether functional groups are present within the fibre which could be characteristic of a particular fibre (for example, amide bands in wool and silk are not

present in cellulosic fibre FTIR spectra). Lignin and cellulose ratios can be extracted from an FTIR spectrum of the fibre to further aid with identification.[75] Polarised ATR-FTIR spectroscopy takes this a step further and has been shown to distinguish between flax and hemp fibres.[76]

Further, scanning electron microscopy (SEM), transmission electron microscopy (TEM), X-ray diffraction (XRD), and nuclear magnetic resonance (NMR) spectroscopy can all be used to investigate fibres.[75] SEM allows for details of the fibre surface to be observed clearly and can help identify certain fibres, to visualise their condition, and can be used in combination with energy dispersive X-ray spectroscopy (EDX) to identify possible dyes or debris on the surface.[77] TEM can study the fine, internal structure within a single fibre or part of a fibre and is usually not used directly for fibre identification, but for studying the crystalline regions of the fibre.[75] The crystallinity of fibre samples can be studied with XRD through investigation of the diffraction peaks of cellulose. Some problems arise with this technique as the small cellulose crystallites lead to peak broadening making it difficult to separate the amorphous and crystalline cellulose components and it being a destructive technique if powder XRD is employed.[21] With NMR spectroscopy, the free and bound water interacting with the fibres can be quantified, which is important for investigating the mechanical properties of fibres and their swelling behaviour.[78] NMR can also be used to investigate the crystallinity and structure of plant fibres, and identify the non-cellulosic aromatic compounds present.[79]

Further techniques for fibre analysis include: chromatography-mass spectrometry (LC-MS and HPLC) to inspect molecular fragments; chemical microanalysis (XRF and MS) for study of trace elements; DNA analysis to confirm genetic origin;[80] and small angle X-ray scattering (SAXS) can be used to identify a single fibre.

Using synchrotron X-ray microbeams, it is possible to quantitatively assess the decay of fibres, which has been used on ancient silk fibres.[81] This method has also been utilised for wool and linen identification from the Qumran caves where the Dead Sea scrolls were found.[82,83] Non-invasive analysis X-ray microdiffraction has been able to distinguish flax, ramie, cotton, and wool fibres using a synchrotron source.[60] The synchrotron microbeam allows for high spatial resolution and high flux density, which is crucial for measuring single fibres, especially cellulosic fibres which are weakly scattering with small crystallites.[82] Diffraction patterns of single fibres can distinguish plant and animal fibres. Diffraction peaks arising from the fibre

itself and from inorganic compounds on the fibres are able to be discerned. The diffraction diagrams of the archaeological textiles from the Qumran caves showed patterns typical of flax or wool, which shows how comparing the diffraction pattern of the sample to those of modern fibres can be utilised for fibre identification.[83] The diffraction patterns can show whether the cellulose microfibrils are highly ordered, and their orientation, which can be further used to assess degradation of the fibres.[84] Fluorescence spectra were collected at the same time to detect contaminants and mordants for dyes.[83] The incomplete powder rings in the diffraction pattern can also provide further evidence of inorganic materials on the fibres, usually due to sediment from the burial context.[83]

Raman spectroscopy has also been used to identify fibres, as well as treatments, and studying the degradation of fibres.[85] At low laser powers, it has the ability to be non-invasive and non-destructive. Raman spectroscopy was used to identify linen as the component of the HMS Victory sail cloth from the late 18th century and to detect that its degradation was largely due to oxidative and hydrolytic processes.[85]

1.7.2 Microscopy in fibre identification

Optical microscopy is considered the primary method for fibre identification. Unlike SEM, it allows study of the interior of the fibre. SEM, however, can provide a detailed view of the surface of the fibres at magnifications greater than can be achieved in conventional optical microscopy. This makes it a useful technique for identifying heavily degraded area of fibres.

When identifying fibres, the following should all be considered: cell wall and lumen thickness, dislocations, cross-markings, presence or absence of crystals, fibre cell dimensions, and cells from tissues other than the sclerenchyma.[64] Sclerenchyma is a type of supportive, structural plant tissue composed of various types of cells, the main type of which are fibres. Sclerenchyma cells typically have a thickened secondary cell wall containing lignin.[69] Other tissues in plants include the phloem and xylem. Xylem tissue includes vessels so the presence of this extraneous material when studying fibres through microscopy can help with fibre identification.

Growing conditions can affect the cell wall causing variations within fibres. As can whether the cells have fully differentiated, for example, the lumen in a mature linen fibre cell is narrow,

but wide if the cell has not finished building its cell wall.[64] Cluster crystals have not been reported in flax samples so their distribution and presence or absence is useful for fibre identification, but other evidence is required to make a positive identification because these crystals could be absent due to fibre processing methods.[71]

The Herzog and the modified Herzog test are methods of distinguishing fibres with optical microscopy.[24,71] The modified Herzog test or red-plate test can determine the fibrillar orientation (Z- or S-twist) in bast fibres using polarised light and a red-plate. For the Herzog test to work, one of the three layers of the secondary fibre cell wall (S1, S2, S3) must be significantly thicker than the others, which is usually the case.[24] It works due to the birefringent properties of the bast fibres.[74] The fibre sample is rotated until extinction, where its optical axis is perpendicular or parallel to the transmission axis of the polariser, which is observed when the fibre turns black.[24,71] When the sample is rotated away from extinction, a blue or yellow shift is observed. Cellulose microfibrils in flax and nettle have an overall S-twist orientation and will turn yellow when rotated 90° under cross polarisers with a red-plate inserted.[24] A hemp fibre, on the other hand, with an overall Z-twist configuration, will turn blue under the same circumstances.[86]The modified Herzog test cannot distinguish between flax and nettle because they have the same microfibrillar orientation (S-twist), for which further analysis would be required, for example, analysis of the cross-section of the fibres and determining the presence or absence of calcium oxalate crystals.[74]

1.7.3 Fibre degradation

As the previous section described, fibres can be separated into three categories: those derived from plants, animals, and man-made sources. Degradation of all fibres can occur through the following processes: acid hydrolysis, alkali hydrolysis, dehydration, photodegradation, oxidation, biological, and thermal degradation.

Acid hydrolysis involves the breakage of glycosidic bonds in the polymer backbone of cellulose, leading to depolymerisation. Acid hydrolysis affects amorphous regions of cellulose more readily and can occur randomly throughout the polymer chains.[14] The mechanism is outlined in Figure 8 and shows the hydrocellulose fragments resulting from breakage of the glycosidic ether bonds.[14] After chain scission, these shorter polymer chains can aggregate,

with extensive hydrogen bonding. This leads to increased crystallinity of the fibres although they may also be brittle and weak due to less flexibility.[87] Alkaline hydrolysis is more controlled, attacking at chain ends, and so not as immediately damaging as acid hydrolysis. In cellulosic fibres, one glucose unit at a time is eliminated from the chain ends, resulting in coloured degradation products. Alkaline hydrolysis requires high temperatures and strong alkalis so is important only when oxidised groups are present. However, if they are, depolymerisation can continue in dilute alkali and can become a large problem to be considered when employing deacidification treatments.[45]
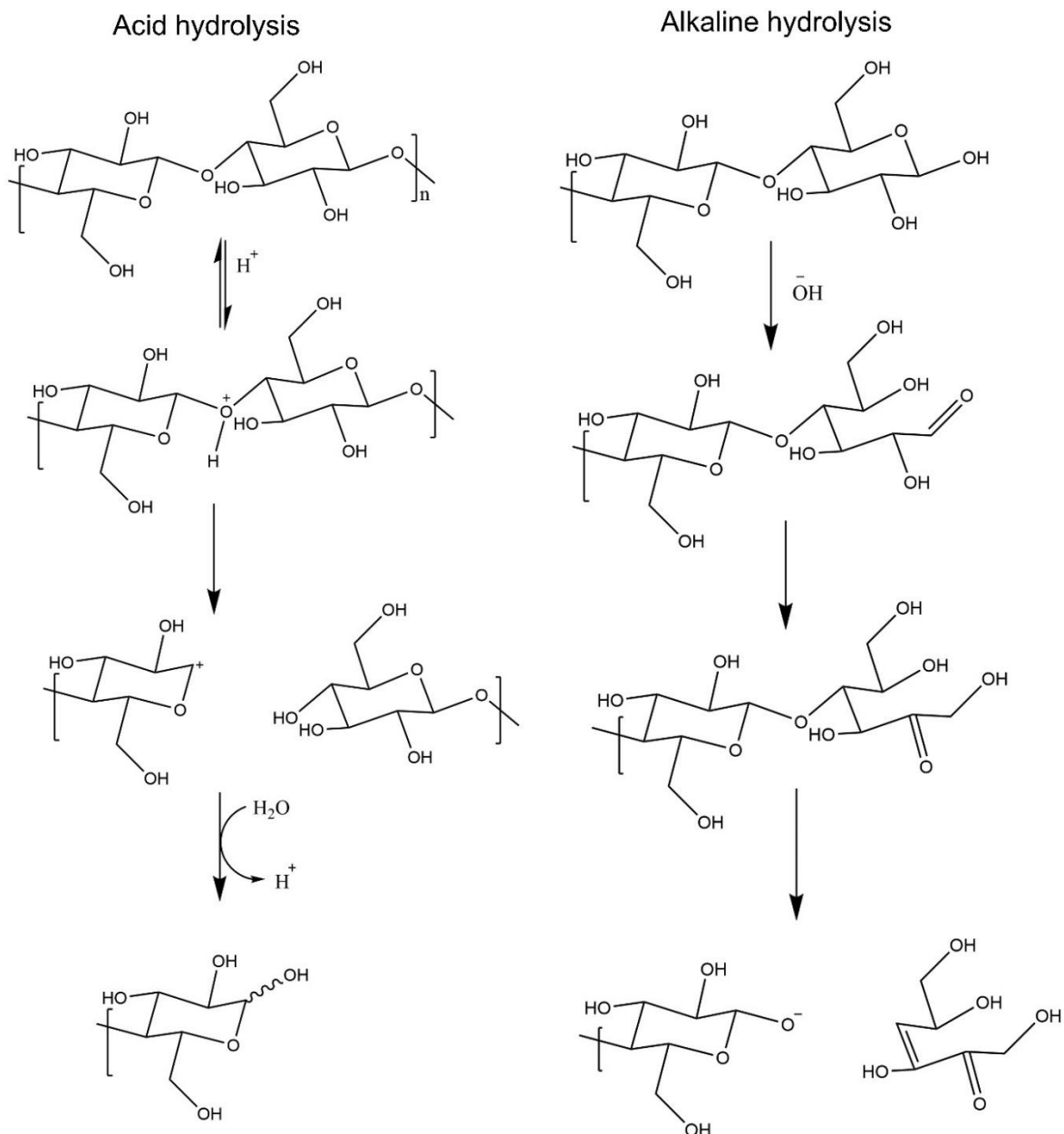
Figure 8 Diagrams of acid (left) and alkaline (right) hydrolysis of cellulose (adapted from Conservation Science: Heritage Materials ed. May and Jones).[14]

Oxidation can take place in both acidic and alkaline environments.[45] In cellulosic fibres, the hydroxyl group can oxidise to an aldehyde, ketone, then a carboxylic acid, affecting the polymer backbone. Oxidation does not need to take place with hydrolysis of the glycosidic bond but it can be affected by slow hydrolysis and the presence of iron (a particular concern for shipwrecks).[26] Iron can also cause staining of fabric artefacts through iron tannates, sulfides, and oxides.[26] Yellow-brown discoloration and a susceptibility to degradation may be

observed when oxidation occurs in amorphous regions of cellulose; fibre strength is implicated when it extends to crystalline areas.[87]

Excessive dehydration results in brittle and rigid fibres. Dehydration of the cellulose polymer chain causes shrinkage as it promotes intermolecular (COC) bonds between the polymer chains, which can cause creases in the fabric. Photodegradation encompasses direct photolysis, photochemical reactions, and radical oxidation. In cellulosic fabrics, photodegradation breaks the polymer chain into shorter, coloured molecules. This results in yellow-brown discolouration observed in some fibres. Fibres can also be degraded through biological means, microorganisms feed on cellulose and excrete the cellulase enzyme, which induces hydrolysis, leading to polymer break down. Biological degradation is more likely in amorphous (disordered) regions of cellulose.

Cellulose is particularly sensitive to thermal degradation after photolysis. Heat can lead to condensation reactions, lowering the degree of polymerisation due to chain scission. Chain scission of cellulose by cleavage of glycosidic bonds leads to an array of problems. A decrease in the degree of polymerization decreases the tenacity of the material. Gradual cross-linking can cause embrittlement of the fibres. Moreover, an increase in crystallinity and reducing end groups leads to an increase in the elastic modulus.[53] Oxidation of cellulose further degrades the material resulting in weaker matrix-filler interactions.[53]

Fibres are often reasonably well preserved in marine and waterlogged environments, but the above routes of degradation may have occurred and can still be occurring during storage and display. Care needs to be taken when these artefacts are removed from their burial environment. Textile artefacts are often carefully washed with water to remove salts and sediment. Sediment is often a problem even after initial treatment as it acts as an abrasive and mud on the artefact can shrink and pull away fibres as it dries, weakening the material.[26] Linen in particular has been show to survive well in a waterlogged environment if conditions are not too acidic.

Water is a crucial component in the preservation of fibres. It is strongly associated with the fibre, either in voids and capillaries or adsorbed to the organic molecules in the plant itself.[26] Water maintains the flexibility and structure of the fibres so their conservation must consider

the balance of water in the material and its environment.[26] Loss of the bound water will lead to an increase in brittleness of the fibre. Fibres can swell due to the uptake of water which can lead to structural changes.[88] Water and ions can disrupt inter- and intramolecular bonds, causing rearrangement of cellulose.[88]

1.7.4 Marine and waterlogged textiles

Biodeterioration is a particular problem for textile artefacts recovered from a marine environment. In 1990, textiles were recovered from a trunk from the *SS Central America* (a deep ocean historic shipwreck) which sank in 1857 off the east coast of North America. The recovery and drying stages of the textiles were published by Jakes and Mitchell.[89] Light microscopy was able to identify linen fibres in the trunk lining and the fibres showed extensive microbiological damage. SEM-EDS was used to confirm and further identified a variety of elements associated with metal corrosion, biological degradation products and sea water permeation. For example, Fe, Cu, and S were observed in significant amounts with Ca, P, Si, Al, and Mg in smaller amounts.[89] An FTIR spectroscopic study of the textiles showed no increase in degradation products due to oxidation and hydrolysis, indicating that different degradation pathways are probably occurring in marine samples compared to dry archaeological textiles.

1.8 Wool fibres
1.8.1 Structure of wool

Wool is categorised as hair and is a proteinaceous fibre. It has been found among the *Mary Rose* artefacts as many clothes were made from this readily available and thermally insulating material. Figure 3 shows a diagram of the structure of a wool fibre. Wool fibres consist of a cuticle surrounding a cortex which in turn usually surrounds a hollow medulla. The cuticle is comprised of amorphous keratin in layers of the exocuticle and endocuticle.[14] The endocuticle is more susceptible to degradation than the sulfur-rich exocuticle layer as it has less stabilising disulfide bonds.[14] The paracortical cells contain more amorphous materials while the orthocortex contains more crystalline fibrils. Wool is generally more amorphous than cellulosic fibres because of the increased bulkiness of its side groups making it difficult for the polymers to orientate. This means it is more flexible, pliable, and absorbent than cellulosic

fibres. Being an easily extensible fibre, wool stretches, which can lead to uncoiling of alpha-helices and beta-sheet formation.[87]

Wool is comprised of the keratin polymer which has a high content of cystine, a sulfur-containing amino acid.[90] However, keratin is a complex polymer of 19 different amino acids including glycine and alanine.[91] The structure and conformation of keratin leads to wool being extendable.[87] There are large variations in the structure of wool depending on the breed of sheep, its diet, and environmental conditions.
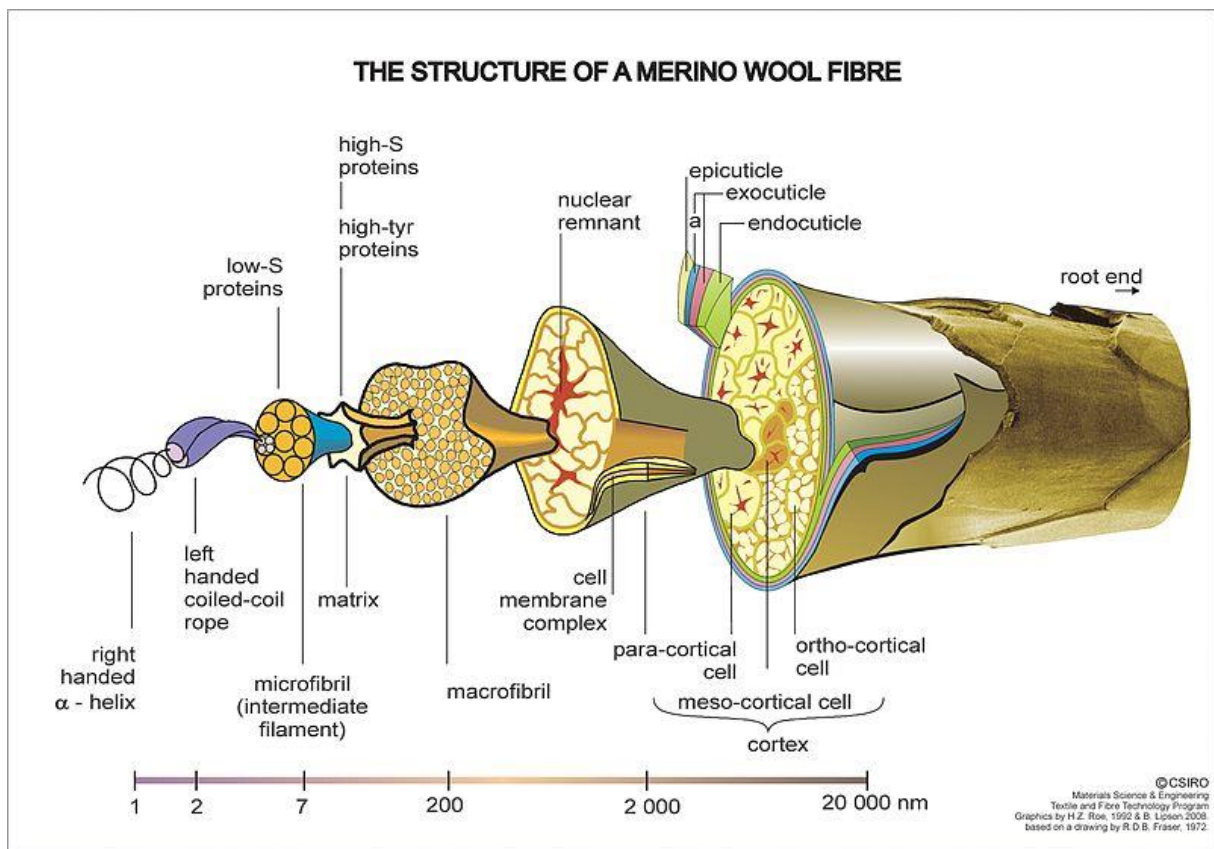
Figure 9 Schematic depicting the structure of a merino wool fibre (from *Color. Technol.,* **2006**, 122, 169).

Mass spectrometry can be used to study the structure and degradation of wool by focusing on the peptides of the keratin protein. Keratin has a secondary structure of left-handed helical segments separated by flexible linker regions and non-helical end regions. The polymer chains are then arranged in heterodimers of a type I (acidic) and type II (basic-neutral) protein, which in turn are assembled into tetramers.[92] Keratin tends to prefer random coil and alpha helix

formations. Wool also contains the melanin pigment, which can produce black or brown wool.[26]

1.8.2 Degradation of wool

Wool artefacts from a waterlogged environment may seem well-preserved, but may have been subject to a process of slow hydrolysis which can weaken the fibres.[26] Wool can be degraded by hydrolytic processes or preserved by protein cross-linking depending on the surrounding environmental conditions, with direct hydrolysis favoured in low pH conditions. Cross-linking can also damage woollen materials as new disulfide bonds are formed between keratin polymers through condensation reactions. This can lead to harmful creases and brittleness of the material. While high levels of cross linking increase the rigidity of wool fibres, lower levels are responsible for the characteristic elasticity of wool, due to its relative bulkiness of its side groups preventing strong cross-links. Keratin also forms cross-links due to condensation during thermal degradation.

Wool tends to be better preserved in a slightly acidic environment (pH 5-6) and in dry environments where metals are present to inhibit bacterial growth. Bacteria affect wool; particularly by attacking the disulfide bond in cystine.[87] Wool is prone to bacteria and fungi that can produce keratinophilic enzymes, which can induce hydrolysis. Acid hydrolysis causes the breakage of peptide bonds in wool. Alkali hydrolysis affects salt bridges in the keratin polymer, which promotes cross-linking of fibres. Photodegradation can occur where UV radiation cleaves the disulfide bonds, producing acidic thiols (-SH) and oxidised thiols.

Keratin contains a large amount of cystine, so its oxidation is important when considering the degradation of wool. Through FTIR studies, the products of cystine oxidation (mainly cystine monoxide, cystine dioxide, and cysteic acid) were proven to relate to the embrittlement and loss of fibres in historic tapestries.[93] MALDI-TOF-MS has also been used to study the degradation of wool by focusing on deamidation, particularly of glutamine and asparagine which are converted to glutamic and aspartic acid respectively. The local environment surrounding the woollen artefact seems to be a more influential on levels of deamidation than the age of the sample.[92] This means that levels of deamidation are not the best way to

determine the age of archaeological wool, even though deamidation levels correlate well with age in a controlled environment.[92]

1.8.3 Conservation of wool

Wool artefacts from the *Mary Rose* were conserved in a similar way to the other textile finds; they were unfolded carefully underwater with a supporting synthetic net frame and brushed to remove sediments.[2] They were soaked and rinsed in deionised water then slowly air dried between paper towels before storage or display in low light conditions and relative humidity of 50-55%.[2]

1.9 Leather samples
1.9.1 Structure of leather

Leather is very different to the other materials studied in this project as it is proteinaceous. It is made from animal skin rather than animal hairs. It is a very important material historically, used ubiquitously from prehistory to the modern day. In fact, the use of tools by early hominids could have been sparked by a need to cut through animal skin and there is evidence of a crude form of leather-making over a million years ago.[94]

Animal skin is composed mainly of the collagen protein. Glycine, proline, and hydroxyproline are among the most common amino acids in collagen (Figure 10).[94] The order of their repeating structures mean the collagen molecule twists in a left-handed helical chain. Three of these chains combine to form a right-handed triple helix structure, stabilised by electrostatic hydrogen bonding. There are three main types of collagen: type I, II, and III. These differ in the strands used to form the helical structures, the three strands of amino acids could be all have the same composition (a homotrimer), or they could differ (a heterotrimer). They can all be different strands, all be the same, or have two genetically similar strands and one distinct strand. Type I collagen is a heterotrimer of two strands of α1(I) and one strand of α2(I) composition.[95] Type II collagen is a homotrimer with three polypeptide chains of α1(II) composition.[96] Type III collagen is also a homotrimer but of three α1(III) chains.[97]

a) Glycine

b) Proline
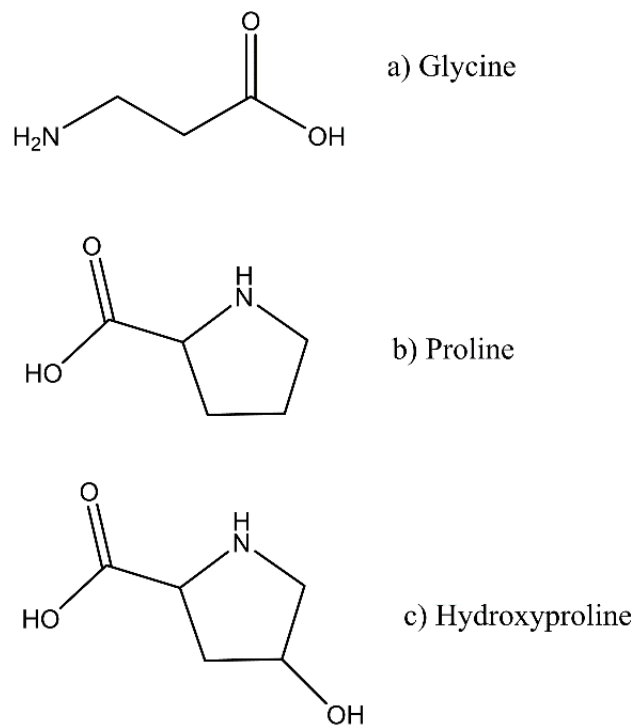
c) Hydroxyproline

Figure 10 Chemical structures of the three common amino acids present in collagen, responsible for its helical structure **(a)** glycine **(b)** proline and **(c)** hydroxyproline.

Leather is commonly obtained from mammals: cattle, goats, sheep, and sometimes pigs and deer.[98] It can be made from any vertebrate as their skins include collagen, the 3D network of which gives leather its useful properties. These properties include good thermal insulation, flexibility, high tensile strength, resistance to abrasion and tearing, and low bulk density.[99] A basic diagram of the structure of mammalian skin commonly used to produce leather is displayed in Figure 11. The epidermis is an outer, keratinous layer that is often removed along with the hair of the animal during leather processing.[99] After processing, the grain is the exposed surface layer of the leather and the corium is the bottom layer of the leather.[100] In the corium layer, interwoven collagen bundles are larger than in the grain layer and are thinner and arranged horizontally near the inside of the skin near the flesh layer (which is also removed during leather processing).[101]
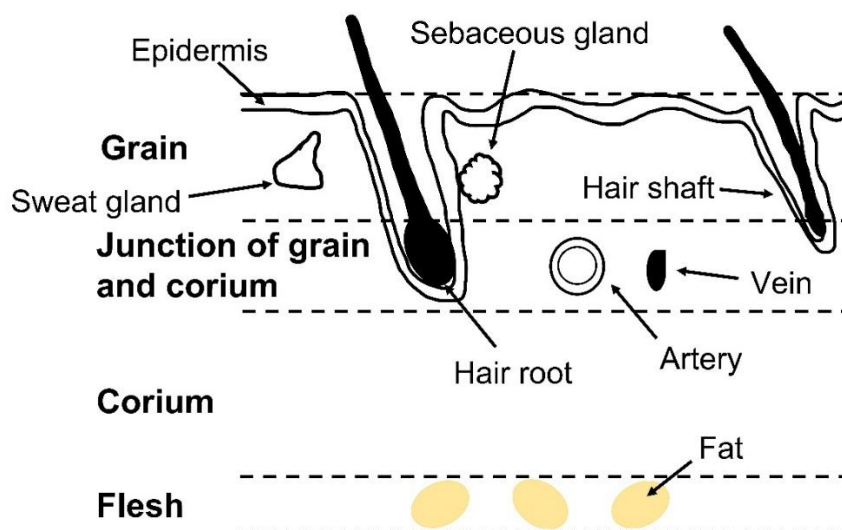
Figure 11 Basic diagram of typical mammalian skin (adapted from M. Kite, *Conservation of Leather and Related Materials*, 2005).[101]

Tanning agents are important when considering leather manufacturing. They cross-link with the collagen molecules mainly through hydrogen bonds between the amino acid side groups of the collagen and the hydroxyl groups of the tannins.[102] These interactions stabilise the structure, lubricate the material improving its flexibility, and provide resistance to microorganisms.[94] Tanning also gives leather its dark brown-black colour.[73] Untanned leather can still be stable, as in the case of parchment, but upon wetting and drying, the leather can become hard and unusable.[94]

Tanning agents, before the 19th century introduction of metal tannins, were derived from plant origins.[73] Here, leather production crosses over back into the realm of plants which relates to the discussion of wood structure in section 1.3. Vegetable tannins are miscible in water and insoluble in organic solvents.[103] They are very complex structures, often containing an array of molecules which vary depending on the source of the tannin. For example, tannins derived from oak bark have distinct, chemical differences from those of sumac leaves. Vegetable tannins share similar structures and can be simplified as deriving from the structure of gallic and ellagic acid, the structures of which are shown in Figure 12.
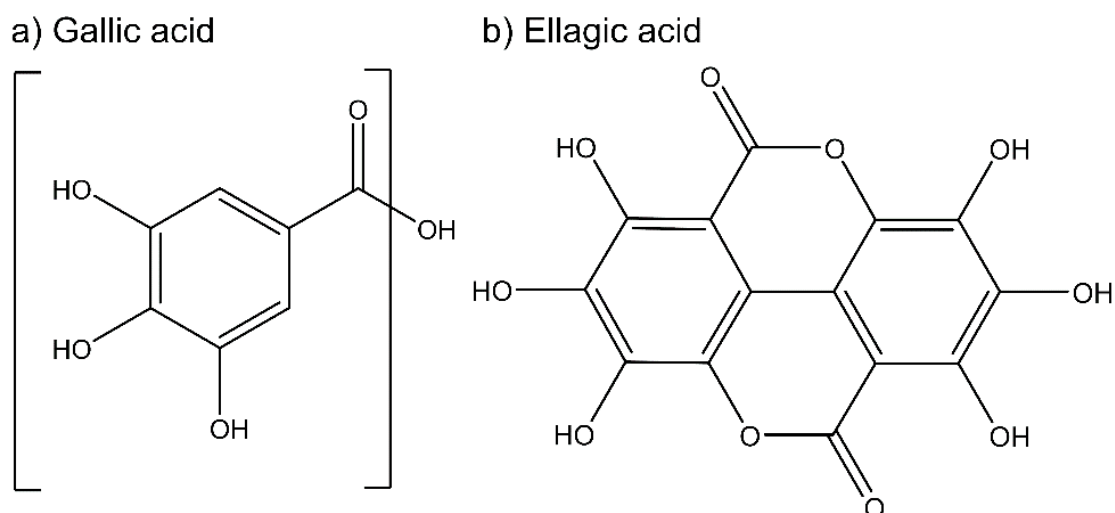
Figure 12 Chemical structures of the main constituents of vegetable tannins **(a)** gallic acid and **(b)** ellagic acid (adapted from L. Falcão, *Vibrational Spectroscopy*, 2014).[104]

Vegetable tannins can be separated into two categories: condensed and hydrolysable tanins.[104] Hydrolysable tannins include gallotannins (mainly from sumac leaves) and ellagitannins (found in oak and chestnut bark).[104] They can be hydrolysed by heat, acids or microbiological action.[99] Condensed tannins are based on flavonoid groups with hydroxyl groups linking to form polymers. They are mainly found in quebracho wood, mimosa bark, and gambier leaves and twigs.[99] They can polymerise further to form high molecular weight, insoluble complexes.[99] The tannins form hydrogen bonds with the electronegative centres on the protein chains of collagen.[99]

1.9.2 Degradation of leather

Leather is often well-preserved in a waterlogged context, for example in bogs or a marine environment. Many leather shoes and clothes were uncovered with the *Mary Rose* shipwreck. Leather is usually still supple in a waterlogged environment but can quickly deteriorate and become brittle if left to dry in an uncontrolled way.[51] Due to the prevalent nature of leather archaeological finds in a waterlogged environment and their historical importance, consideration of conservation and preservation of these artefacts is essential.

Leather, rather like cellulosic fibres, is subject to deterioration by physical, biological, and chemical means. Physical degradation results from wear and tear during original use as well

as from the environment in which the leather has been stored. Most of the issues encountered with leather arise from the ability of leather to absorb and desorb large quantities of water (due to hydrogen bonding and the structure of collagen).[99] Changes in relative humidity can cause differential shrinkage which can result in cracking, splitting, and stiffening, especially as the tannins are removed over time.[99] Water absorption and heat can also bring about the denaturation of collagen, forming gelatin over time. Gelatin is an aqueous colloidal suspension of polypeptide chains.[105] The ratio of collagen to gelatin derived from FTIR spectra can act as an indicator for leather deterioration.[106]

Tanned leathers are resistant to bacterial attack but not to fungi (vegetable-tanned leathers being more prone to attack by mould than chrome-tanned leather and with hydrolysable-tanned leathers more susceptible than condensed). The mechanism of fungal attack is that fungal enzymes digest fats and carbohydrates in leather, which results in the production of organic acids that can go on to react with vegetable tannins to break down the tannin-collagen complex.[99] Mould does not usually grow on leather in an environment where the relative humidity is less than 65% so dehumidification is the best option for preventing fungal attack.[99] Where this is not possible a fungicide is usually used. Controlling the relative humidity is also a useful way for mitigating the effects of physical deterioration.

Leather is generally quite chemically stable; the main causes for concern, however, are hydrolysis and oxidation. In sulfur-polluted environments, direct hydrolysis of the bonds between the amino acids in collagen is the main problem.[99] This can affect condensed-tanned leathers more than hydrolysable-tanned leathers.[99] Hydrolysis is pH and humidity dependent and cleaves peptide linkages resulting in a decrease in the degree of polymerisation of the collagen polymer.[106]

Oxidation tends to predominate in less-polluted areas and can be initiated by heat, light, or free radicals from the breakdown of tannin polyphenols or autoxidation of lipids.[99] With oxidation, the main effect is that basic side groups are changed to acidic side groups, along with significant cross-linking or cleavage depending on the position of attack.[99, 106] Leather with a pH under 2.8 will likely be affected by acid-induced degradation, but the use of strong alkalis in treatments can cause detanning of the leather and cause it to become brittle. Salts like citrates and phthalates are preferred as they buffer between 4 and 5, but the problem

with these is that the water in the aqueous treatment reacts detrimentally before the acid can be neutralised by the salt treatment.[99] Aluminium alkoxide has been used as a treatment to "re-tan" leather as it was soluble in a non-polar solvent. There was an increase in the shrinkage temperature indicating the greater stability of the leather after treatment but there was no improvement in the physical characteristics of the leather.[99]

1.9.3 Determining leather degradation

An indication of the state of deterioration of collagen (as well as the likely tanning process and animal species of the leather) can be given by shrinkage temperatures of leathers. These are measured using differential scanning calorimetry (DSC). The shrinkage temperature is an irreversible change that occurs at the temperature where a wetted skin will shrink dramatically.[99] Ageing due to hydrolytic or oxidative degradation of collagen causes changes in the chemical composition of side chains and breakages in the molecule's backbone which lead to a decrease in the shrinkage temperature.[94] Tanning agents can cause an increase in the shrinkage temperature. A true leather (as opposed to raw hides or pseudo-leathers) is an animal skin that has been through a tanning process. Tanned leathers will have higher shrinkage temperatures than raw skins or oil-tanned leather.[99]

A now common technique for discovering the provenance of leather is matrix-assisted laser desorption/ionisation time-of-flight mass spectrometry (MALDI-TOF-MS). Liquid chromatography tandem mass spectrometry (LC-MS/MS) can provide further, detailed information on decay patterns and post-translational modifications (PTM) of the collagen protein in samples. Together, when applied to archaeological samples, these techniques are known as ZooMS (zooarchaeology by mass spectrometry).

ZooMS was originally carried out on parchment samples and a triboelectric extraction method was devised to make the extraction of collagen as non-invasive as possible. This sampling method uses a plastic eraser to drag electrons from the collagen strands, pulling out any already loose collagen fibres and leaving the rest to return as they were. The eraser residue is collected, and the trypsin enzyme is used to digest the collagen fibres into peptides. After mixing and incubation at 37°C for four hours, the peptide-rich solution is acidified and separated from eraser particles. The peptide solution is spotted onto a metal sample plate

and mixed with a coloured compound (or matrix). As it dries, the matrix crystallises around the peptides. A laser is fired at the sample, vaporising the matrix, releasing peptides. Protons from the vaporised matrix collide and stick to some peptides, giving them a positive charge. The electric field generated from the MALDI-TOF accelerated the charged peptides down a vacuum tube. The peptides smaller in mass accelerated faster than those of larger mass. The peptides are reflected to a detector by an ion mirror which increases the distance the peptides travel, increasing the separation between them so that the larger peptides arrive at the detector later. This means that the time of flight to reach the detector depends on the mass of the peptide, giving a unique fingerprint in the mass spectrum, which can be compared to a database to determine the origin or provenance of the collagen fibres.[100]

1.9.4 Leather conservation

Leather forms part of many different artefacts uncovered with the *Mary Rose*, mainly shoes but also leather jerkins, belts, and accessories. These personal items are important in providing an insight into the lifestyles of the crew members. Active treatments that were regularly employed for the conservation of the *Mary Rose* leather artefacts include freeze drying after immersion in a 10% PEG 400 solution or a 10% solution of Bavon 520 S.[2] Bavon 520 S is an emulsified alkylated succinic acid derivative used as a leather lubricant.[2] A coat of Pliantine (lanolin, oil and beeswax in hexane) was applied for leather artefacts which were to be put on display at a temperature of 18-20°C and relative humidity of 55%.[2]

1.10 Nanoparticles as conservation treatments

Nanoparticles are usually defined as having a dimension under 100 nm and, due to size effects, their surface chemistry, magnetic and electronic properties may differ significantly from bulk material of the same composition.[107] Synthesis of nanoparticles is often a challenge due to their tendency to agglomerate but there are a number of widely used synthetic techniques available.[108]

1.10.1 Synthesis of nanoparticles

Nanoparticles can be synthesised by a variety of methods each with its own advantages and disadvantages. Coprecipitation, hydrothermal, solvothermal, sonochemical, and microwave-

assisted methods are all used to synthesise nanoparticles and to control the shape and size of the final product.

The coprecipitation method is perhaps the most straightforward, fast, and economical method of nanoparticle synthesis. Usually in this method, two different aqueous solutions are mixed leading to formation of the required precipitate.[109] Steps in the coprecipitation method include nucleation, formation, and growth. Reaction times are generally fairly short, but one of the main advantages of the coprecipitation method is that the nanoparticles can be prepared in aqueous solution which is useful for a wide range of applications, including biological applications and conservation treatments. This method has the most potential for easy scale-up due to it generally being quite safe and not requiring high temperatures or pressures. A disadvantage is that this method leads to more polydisperse nanoparticles, leading to some loss of crystallinity.[110]

Hydrothermal methods involve synthesis in water and placing the closed reaction vessel in an oven. With this method and that of thermal decomposition, high temperatures and long reaction times are required but both methods allow for control of the shape and size of the nanoparticles and often quite monodisperse and highly crystalline. Solvothermal methods are similar but rather than water, organic solvents are used.[111] When organic solvents are employed additional work-up is needed to transfer nanoparticles to aqueous environment for biological and conservation applications.[110] Organic solvents sometimes cause problems when used for conservation treatments as they can dissolve dyes, cause further damage through dehydration.

Not requiring high temperatures and pressures for reactions are notable advantages of using sonochemical synthesis methods and these methods can also reduce reaction durations.[112] In ultrasonic methods, formation, growth, and subsequent collapse of bubbles (known as acoustic cavitation) drive reactions. These small pockets of extremely high temperatures and pressures are created where reactions can take place, or can generate radicals that are transferred to solution, which then go on to react.[112]

Microwave-assisted synthesis takes advantage of the heat produced by friction and dielectric loss at particular frequencies from dipoles and ions continually rotating and aligning with an

oscillating field brought about by incoming microwave radiation. Dielectric heating is the name of the mechanism by which the components of the reaction absorb microwave radiation.[113] The advantages of the microwave-assisted method include a decreased reaction time and greater control over product formation, alongside improvements in reproducibility, crystallinity, and monodispersity.[110]

1.10.2 Nanoparticle conservation treatments

Nanoparticles are particularly useful for the conservation treatment of waterlogged archaeological wood as their small size means they can easily penetrate through the degraded wood with the minimal amount of damage, yet have increased reactivity due to their large surface area to volume ratio.[4] When developing a treatment method for heritage objects, particularly archaeological wood, it is necessary to consider that the treatment does not damage or alter the structure and appearance of the object, that the dispersion is stable, and that the pH is suitable at the end of treatment to prevent β-alkoxy elimination in cellulose.[114] This can occur if the pH remains high with alkaline depolymerisation of cellulose a possible problem in the long-term.

A range of conservation treatments have been considered in this introduction already including the use of polymers for both wood and textile conservation (here, not only woven materials, but also leather and wool has been included in the description of 'textile'). Nanoparticles have advantages over polymer treatments in terms of penetration depth due to their size and they tend to be easier to disperse in solvents useful in conservation of artefacts - mainly aqueous environments.[115]

One novel treatment proposed for conservation of marine archaeological wood is the use of magnetic nanocomposites. A magnetic nanocomposite is a surface-functionalised magnetic nanoparticle. In the instance of this novel treatment a magnetic nanoparticle is attached to a polymer and an iron-sequestering agent e.g. EDDHMA) and embedded in a thermoresponsive polymer gel.[110] The polymer could easily be applied to a problematic area in need of conservation. Polymers have a upper critical solution temperature (UCST) and a lower critical solution temperature (LCST) allowing them to be manipulated by changes in temperature, useful for a variety of applications.[116] Polymers undergo changes in solubility due to changes

in temperature of the solution, depending on their concentration, the solvent, and the pH.[117] UCST is the upper temperature where a polymer will dissolve, whereas the LCST is the lower temperture where the polymer will precipitate out of solution.[117] By altering the temperature a few degrees, the polymer will become less gel-like, and the magnetic nanocomposites can be enticed in and out of the wood by an external magnetic field. This is explored in the doctoral thesis of E. Sánchez-Pérez where it was found that a sequestering agent (such as EDDHMA or EDTA) attached to the magnetic nanoparticle can sequester harmful iron compounds present in marine archaeological wood and that the temperature can be altered slightly again to return the polymer to a gel for removal of the nanoparticles and harmful iron containing compounds.[118]

1.10.2.1 Alkaline earth-based nanoparticle treatments

Alkaline earth metal hydroxide nanoparticles can be problematic to synthesise, mainly due to the difficulty of achieving high supersaturation for nucleation, the important effect of co-ions, and the tendency of nanoparticles to agglomerate.[108] However, calcium and magnesium hydroxide nanoparticles have been proven to be good acid neutralising agents, predominantly in the conservation of paper.[108] Under atmospheric conditions, these nanoparticles can react with atmospheric carbon dioxide, converting from the hydroxide to the carbonate. Calcium or magnesium carbonate can act as an alkaline reserve, reacting with any acids which may be produced in the future to prevent possible pH increases.[108,114] In aqueous solutions, however, they have been shown to lead to alkaline depolymerisation of cellulose, decreasing paper strength.[108] Many techniques have been developed to combat this problem using non-aqueous solvents and still forming magnesium hydroxide, but some methods displayed problems such as decreased paper strength, discolouration or white deposits on the surface.[108] The method with the fewer disadvantages appears to be the Bookkeeper process whereby a suspension of magnesium oxide particles in perfluoroheptane reacts to form magnesium hydroxide upon contact with moisture.[108] This was reported to lead to a decrease in the rate of paper degradation but white deposits were sometimes formed on the surface of the paper.[108]

A stable, concentrated solution of $Ca(OH)_2$ nanoparticles in both ethanol and n-propanol was obtained by Poggi *et. al.* using a solvothermal method, allowing for future upscaling at low

cost.[114,52] In this method, calcium metal was oxidised by either ethanol or n-propanol at high temperature and pressure, leading to the corresponding alkoxide which was then hydrolysed at 70°C.[52] The nanoparticle solution was successfully tested on artificially aged, acidified canvas and paper samples and it was suggested that the increase in cellulose resistance to thermal degradation observed could be due to the bivalent calcium ion interacting with the carboxylate groups of the cellulose, creating a strong, interacting network.[52] Another solvothermal method used a similar approach whereby calcium metal was oxidized by ethanol or propan-1-ol to form the alkoxide, then water was added to precipitate colloidal calcium hydroxide. The product was shown to have good dispersibility in apolar solvents and in cyclohexane the application of the nanoparticles was fast and did not damage cellulose fibres.[119]

1.10.3 Strontium carbonate nanoparticles

The *Mary Rose* timbers show significant quantities of calcium and magnesium salts which would conceal the effect of calcium or magnesium hydroxide nanoparticle treatments when analysing with X-ray absorption spectroscopy (XAS). $SrCO_3$ nanoparticles were originally proposed and investigated by Schofield *et. al*. for deacidifying the timbers from the *Mary Rose*.[10] The nanoparticles were found to react with reduced sulfur compounds to form $SrSO_4$, which is insoluble in water and inert.[3] $SrCO_3$ was used as it is a weak base that can neutralise the sulfuric acid to stop immediate degradation of the wood. Sr^{2+} ions have a high affinity for sulfate ions so could form insoluble and inert $SrSO_4$.[119] it has advantages in that it could act as an alkaline reservoir helping to prevent long-term cellulose degradation due to increases in acidity.[119] When the $SrCO_3$ treatment was brushed onto an artefact displaying iron and sulfur problems, penetration throughout the wood structure was noted but concentration of the nanoparticles was highest at the surface.[3] Although $SrCO_3$ was mainly chosen for analytical purposes, $MgCO_3$ or $CaCO_3$ nanoparticles could be considered a more economical alternative treatment in the future as they would be expected to react in much the same way as $SrCO_3$ as the neutralisation of acid in the wood is a major priority to prevent further cellulose degradation.[120] The effect of a $CaCO_3$ treatment could perhaps be studied with in-depth analysis of the extended X-ray absorption fine structure (EXAFS) region in the future, but the calcium salts already in the *Mary Rose* wood may still complicate the analysis.

1.11 Aims and scope

Development of conservation treatments and analysis of archaeological or historical artefacts of cultural importance requires careful consideration of multiple factors. For marine archaeological artefacts (which are the main focus of this thesis), these include biodeterioration (bacterial, fungal, and by marine organisms); the presence of metals and metallic salts; acidity of the surrounding environment and further causes of acid production (including metals catalysing acid production); temperature and salinity; how the artefacts were recovered from the marine environment and subsequently stored; and finally, the effect of any prior conservation treatment.

In light of these considerations, this project aims to investigate the degradation of marine archaeological fibres from the Tudor shipwreck, the *Mary Rose*, with a view to expanding the work to develop viable conservation treatments for a variety of organic archaeological artefacts in the future. One of the primary difficulties in developing a conservation treatment for these materials is the need to understand each artefact on an individual basis. Both its current state of degradation and the causes of the degradation must be understood before a possible treatment is conceived.

Determination of the effect of a promising nanocomposite conservation treatment is a second aspect to this project. The goal was to analyse whether the proposed treatment was effective on model wood before applying it to marine archaeological wood. Nanoparticles of $SrCO_3$ have been investigated to see how commercial samples can be incorporated into a cellulose 'patch' or poultice for spot conservation treatments on areas of wood with problems caused by iron and sulfur compounds. X-ray absorption spectroscopic methods, in particular XANES, has been used to study the effectiveness of this treatment on model wood samples as well as assessing the applicability of the $SrCO_3$-cellulose patch treatment for *Mary Rose* wood samples. The ease-of-use and affordability of the treatment mean that this has the potential to be a viable treatment for a wide range of marine archaeological wooden artefacts. The examination of different routes to $SrCO_3$ nanoparticle synthesis with controlled size and shape is also considered as future wood treatments.

Cellulosic fibres are also investigated with an aim of fibre identification through microscopy and spectroscopic techniques. This is not only interesting from a materials characterisation perspective, but this information can feed into further detailed information on the history of the artefacts. Moreover, the state of degradation or preservation of these fibres is considered by visual assessment and spectroscopic methods. This information is of theoretical interest but also has very practical implications, especially when developing future treatments for these textiles. Finally, reference wool samples and wool and leather from the *Mary Rose* are studied by microscopy and FTIR spectroscopy. In particular, the FTIR spectra of leather fragments and leather shoe sole are analysed and discussed in comparison with findings in the literature.

Investigating how different techniques provide insight into these historically important materials is crucial for discovering more about the artefacts, but also provides a foundation for expanding this research into how conservation treatments might interact with the artefacts and how to characterise materials before and after treatment to determine whether treatments were successful.

References

1   L. S. Bell, J. A. Lee Thorp and A. Elkerton, The sinking of the Mary Rose warship: a medieval mystery solved?, *J. Archaeol. Sci.*, 2009, **36**, 166–173.

2   M. Jones, *For Future Generations: Conservation of a Tudor Maritime Collection*, The Mary Rose Trust, 2003.

3   E. J. Schofield, R. Sarangi, A. Mehta, A. M. Jones, A. Smith, J. F. W. Mosselmans and A. V. Chadwick, Strontium carbonate nanoparticles for the surface treatment of problematic sulfur and iron in waterlogged archaeological wood, *J. Cult. Herit.*, 2016, **18**, 306–312.

4   E. J. Schofield, R. Sarangi, A. Mehta, A. M. Jones, F. J. W. Mosselmans and A. V. Chadwick, Nanoparticle de-acidification of the mary rose, *Mater. Today*, 2011, **14**, 354–358.

5   A. V. Chadwick, E. J. Schofield, A. M. Jones, G. Cibin and J. F. W. Mosselmans, Ionic nanoparticles in heritage conservation; Treatments for the Mary Rose timbers, *Solid State Ionics*, 2012, **225**, 742–746.

6   G. Almkvist and I. Persson, Extraction of iron compounds from wood from the Vasa, *Holzforschung*, 2006, **60**, 678–684.

7   A. V. Chadwick, K. Howland, M. J. Went, E. J. Schofield and A. M. Jones, The application of ionic nanoparticles in the conservation of archaelogical wood, *Macromol. Symp.*, 2014, **337**, 74–79.

8   D. Dedic, T. Iversen and M. Ek, Cellulose degradation in the *Vasa* : The role of acids and rust, *Stud. Conserv.*, 2013, **58**, 308–313.

9   K. M. Wetherall, R. M. Moss, A. M. Jones, A. D. Smith, T. Skinner, D. M. Pickup, S. W. Goatham, A. V. Chadwick and R. J. Newport, Sulfur and iron speciation in recently recovered timbers of the Mary Rose revealed via X-ray absorption spectroscopy, *J. Archaeol. Sci.*, 2008, **35**, 1317–1328.

10   A. V Chadwick, E. J. Schofield and M. Jones, The Use of Nanoparticles in Securing Cultural Heritage, *IOP Conf. Ser. Mater. Sci. Eng.*, 2010, **15**, 012009.

11   A. Berko, A. D. Smith, A. M. Jones, E. J. Schofield, J. F. W. Mosselmans and A. V

Chadwick, XAS studies of the effectiveness of iron chelating treatments of Mary Rose timbers, *J. Phys. Conf. Ser.*, 2009, **190**, 012147.

12   Z. Walsh, E.-R. Janeček, M. Jones and O. A. Scherman, Natural polymers as alternative consolidants for the preservation of waterlogged archaeological wood, *Stud. Conserv.*, 2016, **3630**, 1–11.

13   J. Hill, S. Willis and R. Pacheco-Ruiz, *People and the Sea: A Maritime Archaeological Research Agenda for England*, 2013.

14   P. Garside and P. Wyeth, in *Conservation Science: Heritage Materials*, eds. E. May and M. Jones, RSC Publishing, Cambridge, UK, 2006, pp. 56–91.

15   D. Mohnen, Pectin structure and biosynthesis, *Curr. Opin. Plant Biol.*, 2008, **11**, 266–277.

16   N. Valette, T. Perrot, R. Sormani, E. Gelhaye and M. Morel-Rouhier, Antifungal activities of wood extractives, *Fungal Biol. Rev.*, 2017, **31**, 113–123.

17   V. Daniels, in *Conservation Science: Heritage Materials*, eds. E. May and M. Jones, Royal Society of Chemistry, 2006, pp. 32–55.

18   S. L. Mathews, J. Pawlak and A. M. Grunden, Bacterial biodegradation and bioconversion of industrial lignocellulosic streams, *Appl. Microbiol. Biotechnol.*, 2015, **99**, 2939–2954.

19   R. N. Goldberg, J. Schliesser, A. Mittal, S. R. Decker, A. F. L. O. . Santos, V. L. S. Freitas, A. Urbas, B. E. Lang, C. Heiss, M. D. M. . R. da Silva, B. F. Woodfield, R. Katahira, W. Wang and D. K. Johnson, A thermodynamic investigation of the cellulose allomorphs: cellulose(am), cellulose Iβ(cr), cellulose II(cr), and cellulose III(cr), *J. Chem. Thermodyn.*, 2015, **81(C)**, 184–226.

20   S. Rongpipi, D. Ye, E. D. Gomez and E. W. Gomez, Progress and opportunities in the characterization of cellulose – an important regulator of cell wall growth and mechanics, *Front. Plant Sci.*, 2019, **9**, 1–28.

21   A. Thygesen, J. Oddershede, H. Lilholt, A. B. Thomsen and K. Ståhl, On the determination of crystallinity and cellulose content in plant fibres, *Cellulose*, 2005, **12**, 563–576.

22   R. J. Maurer, A. F. Sax and V. Ribitsch, Moleular simulation of surface reorganization and wetting in crystalline cellulose I and II, *Cellulose*, 2013, **20**, 25–42.

23   S. Pattathil, M. G. Hahn, B. E. Dale and S. P. S. Chundawat, Insights into plant cell wall structure, architecture, and integrity using glycome profiling of native and AFEXTM-pretreated biomass, *J. Exp. Bot.*, 2015, **66**, 4279–4294.

24   E. Haugan and B. Holst, Determining the fibrillar orientation of bast fibres with polarized light microscopy: The modified Herzog test (red plate test) explained, *J. Microsc.*, 2013, **252**, 159–168.

25   I. Shtein, B. Bar-On and Z. A. Popper, Plant and algal structure: from cell walls to biomechanical function, *Physiol. Plant.*, 2018, **164**, 56–66.

26   J. M. Cronyn, *The Elements of Archaeological Conservation*, Routeledge, London, 1990.

27   M. Aucouturier and E. Darque-Ceretti, The surface of cultural heritage artefacts: Physicochemical investigations for their knowledge and their conservation, *Chem. Soc. Rev.*, 2007, **36**, 1605–1621.

28   J. Preston, A. D. Smith, E. J. Schofield, A. V. Chadwick, M. A. Jones and J. E. M. Watts, The effects of Mary Rose conservation treatment on iron oxidation processes and microbial communities contributing to acid production in marine archaeological timbers, *PLoS One*, 2014, **9**, 1–8.

29   C. M. A. McQueen, D. Tamburini, J. J. Łucejko, S. Braovac, F. Gambineri, F. Modugno, M. P. Colombini and H. Kutzke, New insights into the degradation processes and influence of the conservation treatment in alum-treated wood from the Oseberg collection, *Microchem. J.*, 2017, **132**, 119–129.

30   M. Sandstrom, F. Jalilehvand, E. Damian, Y. Fors, U. Gelius, M. Jones and M. Salome, Sulfur accumulation in the timbers of King Henry VIII's warship Mary Rose: A pathway in the sulfur cycle of conservation concern, *Proc. Natl. Acad. Sci.*, 2005, **102**, 14165–14170.

31   V. Castelvetro and A. Manariti, Milan, Italy, 2007.

32   Z. Walsh, E.-R. Janeček, J. T. Hodgkinson, J. Sedlmair, A. Koutsioubas, D. R. Spring, M.

Welch, C. J. Hirschmugl, C. Toprakcioglu, J. R. Nitschke, M. Jones and O. A. Scherman, Multifunctional supramolecular polymer networks as next-generation consolidants for archaeological wood conservation, *Proc. Natl. Acad. Sci.*, 2014, **111**, 17743–17748.

33 T. Skinner and M. Jones, Milan, Italy, 2007.

34 U. Henniges, R. Reibke, G. Banik, E. Huhsmann, U. Hähner, T. Prohaska and A. Potthast, Iron gall ink-induced corrosion of cellulose: Aging, degradation and stabilization. Part 2: Application on historic sample material, *Cellulose*, 2008, **15**, 861–870.

35 J. Kolar, A. Mozir, A. Balazic, M. Strlic, G. Ceres, V. Conte, V. Mirruzzo, T. Steemers and G. de Bruin, No Title, *Restaur.-Int. J. Preserv. Libr. Arch. Mater.*, 2008, **29**, 184–198.

36 A. Potthast, U. Henniges and G. Banik, No Title, *Cellulose*, 2008, **15**, 849–859.

37 National Center for Biotechnology Information. PubChem Compound Summary for CID 24495, Calcium phytate., https://pubchem.ncbi.nlm.nih.gov/compound/Calcium-phytate, (accessed 7 October 2021).

38 R. Giorgi, in *Nanoscience for the conservation of works of art*, eds. P. Baglioni and D. Chelazzi, RSC Publishing, Cambridge, 2013, pp. 396–429.

39 Y. Iwasawa, K. Asakura and M. Tada, *XAFS Techniques for Catalysts, Nanomaterials, and Surfaces*, 2016.

40 S. Calvin, *XAFS for Everyone*, CRC Press, Boca Raton, FL, 2013.

41 E. R. Aluri, C. Reynaud, H. Bardas, E. Piva, G. Cibin, J. F. W. Mosselmans, A. V. Chadwick and E. J. Schofield, The Formation of Chemical Degraders during the Conservation of a Wooden Tudor Shipwreck, *Chempluschem*, 2020, **85**, 1–8.

42 F. Jalilehvand, Sulfur: not a "silent" element any more, *Chem. Soc. Rev.*, 2006, **35**, 1256–1268.

43 Y. Fors, F. Jalilehvand, E. Damian Risberg, C. Björdal, E. Phillips and M. Sandström, Sulfur and iron analyses of marine archaeological wood in shipwrecks from the Baltic Sea and Scandinavian waters, *J. Archaeol. Sci.*, 2012, **39**, 2521–2532.

44 Y. Fors and M. Sandström, Sulfur and iron in shipwrecks cause conservation concerns, *Chem. Soc. Rev.*, 2006, **35**, 399.

45   G. Artioli, *Scientific Methods and Cultural Heritage*, Oxford University Press, New York, 2010.

46   M. Ballard and I. Skals, in *Preprints of the contributions to the Copenhagen Congress*, 1996, pp. 6–10.

47   L. R. Sibley and K. A. Jakes, in *Historic Textile and Paper Materials: Conservation and Characterisation*, eds. H. L. Needles and S. H. Zeronian, 1984.

48   H. L. Chen, K. A. Jakes and D. W. Foreman, Preservation of archaeological textiles through fibre mineralization, *J. Archaeol. Sci.*, 1998, **25**, 1015–1021.

49   C. I. Angiorama, S. M. L. López Campeny and C. Taboada, Exceptional cases of textile mineralization in archaeological metallic objects from Santiago del Estero's lowlands (Argentina), *J. Archaeol. Sci. Reports*, 2020, **33**, 102478.

50   P. Ewer, F. Lennard and L. Hillyer, *Textile Conservation*, Butterworth-Heinemann, Oxford, 1st edn., 2010.

51   D. L. Hamilton, Methods of conserving archaeological material from underwater sites, *Conserv. Files ANTH 605, Conserv. Cult. Resour. I. Naut. Archaeol. Program, Texas A&M Univ.*, 1999, 1–110.

52   G. Poggi, N. Toccafondi, L. N. Melita, J. C. Knowles, L. Bozec, R. Giorgi and P. Baglioni, Calcium hydroxide nanoparticles for the conservation of cultural heritage: New formulations for the deacidification of cellulose-based artifacts, *Appl. Phys. A Mater. Sci. Process.*, 2014, **114**, 685–693.

53   P. Garside, University of Southampton, 2002.

54   M. Cocca, L. D'Arienzo, L. D'Orazio, G. Gentile, C. Mancarella, E. Martuscelli and C. Polcaro, Water dispersed polymers for textile conservation: a molecular, thermal, structural, mechanical and optical characterisation, *J. Cult. Herit.*, 2006, **7**, 236–243.

55   P. Baglioni, E. Carretti and D. Chelazzi, Nanomaterials in art conservation, *Nat. Nanotechnol.*, 2015, **10**, 287–290.

56   M. I. Totolin and I. Neamţu, Positive findings for plasma polymer (meth)acrylate thin films in heritage protective applications, *J. Cult. Herit.*, 2011, **12**, 392–398.

57   E. Princi, S. Vicini, E. Pedemonte, V. Arrighi and I. McEwen, New polymeric materials

for paper and textile conservation. I. Synthesis and characterization of acrylic copolymers, *J. Appl. Polym. Sci.*, 2005, **98**, 1157–1164.

58   I. Good, A RCHAEOLOGICAL T EXTILES : A Review of Current Research, *Annu. Rev. Anthropol.*, 2001, **30**, 209–226.

59   J. M. Adovasio, O. Soffer and B. Klíma, Upper Palaeolithic fibre technology: interlaced woven finds from Pavlov I, Czech Republic, *c.* 26,000 years ago, *Antiquity*, 1996, **70**, 526–534.

60   C. Bergfjord and B. Holst, A procedure for identifying textile bast fibres using microscopy: Flax, nettle/ramie, hemp and jute, *Ultramicroscopy*, 2010, **110**, 1192–1197.

61   H. Godwin, The Ancient Cultivation of Hemp, *Antiquity*, 1967, **41**, 42–49.

62   N. Mattingly, Southern Cross University, 2013.

63   A. Quye, Factors influencing the stability of man-made fibers: A retrospective view for historical textiles, *Polym. Degrad. Stab.*, 2014, **107**, 210–218.

64   D. Catling and J. Grayson, *Identification of Vegetable FIbres*, Archetype Publications, 2004.

65   S. Harris, Flax fibre : Innovation and Change in the Early Neolithic A Technological and Material Perspective, *Text. Soc. Am. Symp. Proc.*, 2014, 1–10.

66   R. K. Nayak, R. Padhye and S. Fergusson, *Identification of natural textile fibres*, Woodhead Publishing, 2012.

67   D. E. Akin, Linen Most Useful: Perspectives on Structure, Chemistry, and Enzymes for Retting Flax, *ISRN Biotechnol.*, 2013, **2013**, 1–23.

68   J. A. Suomela, K. Vajanto and R. Räisänen, Seeking Nettle Textiles – Utilizing a Combination of Microscopic Methods for Fibre Identification, *Stud. Conserv.*, 2018, **63**, 412–422.

69   J. F. V. Vincent, Unified nomenclature for plant fibres for industrial use, *Appl. Compos. Mater.*, 2000, **7**, 269–271.

70   L. G. Thygesen, J. B. Bilde-Sørensen and P. Hoffmeyer, Visualisation of dislocations in hemp fibres: A comparison between scanning electron microscopy (SEM) and

polarized light microscopy (PLM), *Ind. Crops Prod.*, 2006, **24**, 181–185.

71   H. Lukešová, A. S. Palau and B. Holst, Identifying plant fibre textiles from Norwegian Merovingian Period and Viking Age graves: The Late Iron Age Collection of the University Museum of Bergen, *J. Archaeol. Sci. Reports*, 2017, **13**, 281–285.

72   W. C. Evans, in *Trease and Evans' Pharmacognosy: Sixteenth Edition*, 2009, pp. 551–562.

73   A. Vichi, G. Eliazyan and S. G. Kazarian, Study of the Degradation and Conservation of Historical Leather Book Covers with Macro Attenuated Total Reflection-Fourier Transform Infrared Spectroscopic Imaging, *ACS Omega*, 2018, **3**, 7150–7157.

74   J. A. Suomela, K. Vajanto and R. Räisänen, Seeking Nettle Textiles – Utilizing a Combination of Microscopic Methods for Fibre Identification, *Stud. Conserv.*, 2018, **63**, 412–422.

75   R. M. Kozłowski, *Handbook of natural fibres: 1. Types, Properties, and Factors Affecting Breeding and Cultivation*, Woodhead Publishing, 2012.

76   P. Garside and P. Wyeth, Identification of Cellulosic Fibres by FTIR Spectroscopy: Differentiation of Flax and Hemp by Polarized ATR FTIR, 2006, **51**, 205–211.

77   I. Joosten, M. R. Van Bommel, R. H. De Keijzer and H. Reschreiter, Micro analysis on hallstatt textiles: Colour and condition, *Microchim. Acta*, 2006, **155**, 169–174.

78   A. Célino, S. Fréour, F. Jacquemin and P. Casari, The hygroscopic behavior of plant fibers: a review, *Front. Chem.*, 2014, **1**, 1–12.

79   B. Duchemin, A. Thuault, A. Vicente, B. Rigaud, C. Fernandez and S. Eve, Ultrastructure of cellulose crystallites in flax textile fibres, *Cellulose*, 2012, **19**, 1837–1854.

80   P. B. Drooker and L. D. Webster, *Beyond Cloth and Cordage : Archaeological Textile Research in the Americas*, University of Utah Press, Salt Lake City, UNITED STATES, 2000.

81   A. C. Hermes, R. J. Davies, S. Greiff, H. Kutzke, S. Lahlil, P. Wyeth and C. Riekel, Characterizing the decay of ancient Chinese silk fabrics by microbeam synchrotron radiation diffraction, *Biomacromolecules*, 2006, **7**, 777–783.

82   M. Muller, B. Murphy, M. Burghammer, C. Riekel, M. Roberts, M. Papiz, D. Clarke, J. Gunneweg and E. Pantos, Identification of ancient textile fibres from Khirbet Qumran caves using synchrotron radiation microbeam diffraction B, , DOI:10.1016/j.sab.2004.07.018.

83   M. Müller, B. Murphy, M. Burghammer, I. Snigireva, C. Riekel, J. Gunneweg and E. Pantos, Identification of single archaeological textile fibres from the cave of letters using synchrotron radiation microbeam diffraction and microfluorescence, *Appl. Phys. A Mater. Sci. Process.*, 2006, **83**, 183–188.

84   M. Müller, B. Murphy, M. Burghammer, C. Riekel, E. Pantos and J. Gunneweg, Ageing of native cellulose fibres under archaeological conditions: Textiles from the Dead Sea region studied using synchrotron X-ray microdiffraction, *Appl. Phys. A Mater. Sci. Process.*, 2007, **89**, 877–881.

85   H. G. M. Edwards, N. F. Nikhassan, D. W. Farwell, P. Garside and P. Wyeth, Raman Spectroscopic Analysis of a Unique Linen Artefact: the HMS Victory Trafalgar Sail, *J. Raman Spectrosc.*, 2007, **37**, 1193–1200.

86   G. Skoglund, M. Nockert and B. Holst, Viking and early middle ages northern scandinavian textiles proven to be made with hemp, *Sci. Rep.*, 2013, **3**, 1–6.

87   H. G. M. Edwards and P. Wyeth, in *Raman Spectroscopy in Art and Archaeology*, eds. H. G. M. Edwards and J. M. Chalmers, Royal Society of Chemistry, Cambridge, UK, 2005, pp. 304–324.

88   J. M. Cardamone and M. T. Baker, *Historic Textiles, Papers, and Polymers in Museums*, American Chemical Society, 2000, vol. 779.

89   K. A. Jakes and J. C. Mitchell, The Recovery And Drying Of Textiles From A Deep Ocean Historic Shipwreck, http://www.conservation-us.org/resources/disaster-response-recovery/jaic/textiles-from-whipwreck#.WyzKolVKiUk, (accessed 22 June 2018).

90   R. R. Mather and R. H. Wardman, *The Chemistry of Textile Fibres*, Royal Society of Chemistry, Cambridge, UK, 2011.

91   B. A. Mcgregor, X. Liu and X. G. Wang, Comparisons of the Fourier Transform Infrared Spectra of cashmere, guard hair, wool and other animal fibres, *J. Text. Inst.*, 2018, **109**, 813–822.

92   C. Solazzo, J. Wilson, J. M. Dyer, S. Clerens, J. E. Plowman, I. Von Holstein, P. Walton Rogers, E. E. Peacock and M. J. Collins, Modeling deamidation in sheep α-keratin peptides and application to archeological wool textiles, *Anal. Chem.*, 2014, **86**, 567–575.

93   N. Kissi, K. Curran, C. Vlachou-Mogire, T. Fearn and L. Mccullough, Developing a non-invasive tool to assess the impact of oxidation on the structural integrity of historic wool in Tudor tapestries, *Herit Sci*, 2017, **5**, 49.

94   M. Kite and R. Thomson, *Conservation of Leather and Related Materials*, Routledge, 2005.

95   E. Makareeva and S. Leikin, in *Osteogenesis Imperfecta*, eds. J. R. Shapiro, P. H. Byers, F. H. Glorieux and P. D. Sponseller, 2014.

96   H. P. BächingerKazunori MizunoJanice, A. VrankaSergei and P. Boudko, in *Comprehensive Natural Products II*, eds. H. (Ben) Liu and L. Mander, Elsevier Science, 2010.

97   M. J. Nielsen and M. A. Karsdal, in *Biochemistry of Collagens, Laminins and Elastin*, ed. M. A. Karsdal, 1st edn., 2016, pp. 21–30.

98   F. Serchisu, University of York, 2014.

99   R. Thomson, in *Conservation Science: Heritage Materials*, eds. E. May and M. Jones, RSC Publishing, Cambridge, UK, 2006, pp. 92–120.

100   J. A. Ebsen, K. Haase, R. Larsen, D. V. P. Sommer and L. Ø. Brandt, Identifying archaeological leather – discussing the potential of grain pattern analysis and zooarchaeology by mass spectrometry (ZooMS) through a case study involving medieval shoe parts from Denmark, *J. Cult. Herit.*, 2019, **39**, 21–31.

101   M. Kite and R. Thomson, *Conservation of Leather and Related Materials*, Routledge, 2005.

102   M. Baglioni, A. Bartoletti, L. Bozec, D. Chelazzi, R. Giorgi, M. Odlyha, D. Pianorsi, G. Poggi and P. Baglioni, Nanomaterials for the cleaning and pH adjustment of vegetable-tanned leather, *Appl. Phys. A Mater. Sci. Process.*, 2016, **122**, 1–11.

103   N. M. Puică, A. Pui and M. Florescu, FTIR Spectroscopy for the analysis of vegetable

tanned ancient leather, *Eur. J. Sci. Theol.*, 2006, **2**, 49–53.

104   L. Falcão and M. E. M. Araújo, Application of ATR-FTIR spectroscopy to the analysis of tannins in historic leathers: The case study of the upholstery from the 19th century Portuguese Royal Train, *Vib. Spectrosc.*, 2014, **74**, 98–103.

105   M. R. Derrick, D. Stulik and J. M. Landry, *Scientific Tools for Conservation: Infrared Spectroscopy in Conservation Science*, 1999.

106   M. R. Derrick and J. M. Landry, *Scientific Tools for Conservation I nfrared S p ectrosco p y in Conservation Science*, .

107   E. R. Aluri, University of Saskatchewan, 2015.

108   P. Baglioni and R. Giorgi, Soft and hard nanomaterials for restoration and conservation of cultural heritage, *Soft Matter*, 2006, **2**, 293.

109   I. F. Cruz, C. Freire, J. P. Araújo, C. Pereira and A. M. Pereira, in *Magnetic Nanostructured Materials: From Lab to Fab*, Elsevier, 2018, pp. 59–116.

110   M. J. Williams, E. Sánchez, E. R. Aluri, F. J. Douglas, D. A. MacLaren, O. M. Collins, E. J. Cussen, J. D. Budge, L. C. Sanders, M. Michaelis, C. M. Smales, J. Cinatl, S. Lorrio, D. Krueger, R. T. M. de Rosales and S. A. Corr, Microwave-assisted synthesis of highly crystalline, multifunctional iron oxide nanocomposites for imaging applications, *RSC Adv.*, 2016, **6**, 83520–83528.

111   M. K. Devaraju, I. Honma, M. Kempaiah Devaraju and I. Honma, Hydrothermal and Solvothermal Process Towards Development of LiMPO 4 (M = Fe, Mn) Nanomaterials for Lithium-Ion Batteries, 2012, **2**, 284–297.

112   X. Hangxun, B. W. Zeiger and K. S. Suslick, Sonochemical synthesis of nanomaterials, *Chem. Soc. Rev.*, 2013, **42**, 2555–2567.

113   M. Nüchter, B. Ondruschka, W. Bonrath and A. Gum, Microwave assisted synthesis – a critical technology overview, *Green Chem.*, 2004, **6**, 128–141.

114   G. Poggi, N. Toccafondi, D. Chelazzi, P. Canton, R. Giorgi and P. Baglioni, Calcium hydroxide nanoparticles from solvothermal reaction for the deacidification of degraded waterlogged wood, *J. Colloid Interface Sci.*, 2016, **473**, 1–8.

115   L. Dei, in *Nanoscience for the conservation of works of art*, eds. P. Baglioni and D.

Chelazzi, RSC Publishing, Cambridge, UK, 2013.

116   M. I. Gibson and R. K. O'reilly, To aggregate, or not to aggregate? considerations in the design and application of polymeric thermally-responsive nanoparticles, *Chem. Soc. Rev. Chem. Soc. Rev. Chem. Soc. Rev*, 2013, **42**, 7204–7213.

117   J. Niskanen and H. Tenhu, How to manipulate the upper critical solution temperature (UCST)?, *Polym. Chem.*, 2017, **8**, 220–232.

118   E. Sanchez Perez, University of Sheffield, 2019.

119   P. Baglioni, D. Chelazzi, R. Giorgi, H. Xing and G. Poggi, *Nanoscience and Cultural Heritage*, Atlantis Press, 2016.

120   E. J. Schofield, C. Delaveris and R. Sarangi, Alkaline earth carbonates for the treatment of problematic sulfur associated with marine archeological wood, *J. Archaeol. Sci. Reports*, 2015, **4**, 427–433.

Chapter 2: Experimental

In this chapter the basics of the characterisation techniques employed throughout this thesis are explained. It then moves on to provide details of the materials, procedures, and equipment used.

2.1 Infrared (IR) spectroscopy

When exposed to infrared radiation, chemical bonds undergo vibrations at certain characteristic frequencies. Fourier transform infrared (FTIR) spectroscopy can be used to identify and distinguish functional groups present in a sample based upon the frequency at which these vibrations take place. The most common vibrations are stretching, bending, and torsional modes, all of which can be symmetrical or asymmetrical. Whether a vibration is active in the IR spectrum will depend on selection rules, the main rule being that to be active, the vibrational mode must include a change in the dipole moment of the molecule. A non-symmetrical vibration of a heteronuclear molecule will therefore be observed in the spectrum. Reasons some bands will not be observed are due to degeneracy, overlapping, and weak absorptions.[1] Combination bands and overtones may also occur in the spectrum.

Attenuated total reflectance (ATR) in FTIR spectroscopy is where IR radiation is totally reflected by a crystal, producing an evanescent electric field beyond the surface of the crystal. The field is not uniform and having components in all directions means that the resulting spectra are sensitive to anisotropy in the sample. Anisotropy is the directionally dependent properties of the sample, which cause band intensities to change depending on the direction of the sample in the measurement. The incident radiation has components of its electric field both parallel and perpendicular to the plane of incidence. For a zinc selenide or diamond crystal, the effective pathlength is higher for the component polarised parallel to the plane of incidence which enhances absorbance of vibrations with a dipole change in the plane relative to those with a perpendicular dipole change.

Transmittance is routinely used to display an IR spectrum. Transmittance is defined as the ratio between the radiation transmitted by the sample and the amount of incoming radiation; however, absorbance is more commonly used during quantitative analysis of IR spectra so

most of the spectra in this thesis are measured in absorbance. The differences between absorbance and transmittance are displayed in the equations below.

$$T(\%) = \frac{I}{I_0} \times 100$$

$$A = log_{10}\left(\frac{I_0}{I}\right) = \varepsilon cl$$

Regarding the analysis of IR spectra, detailed information on the sample under study can be derived. The position of the peaks in the spectrum, their shape, and their intensity all help in providing information on unique materials.[1] The peak position gives information on functional groups in the material and slight shifts in the positions can indicate differences in the surrounding bonding environment. The shape of the bands provides information on the purity of the material. If there are deviations away from a symmetrical band, this also indicates the peak is formed of overlapping bands. The intensity of the peak correlates with the amount of the particular functional group in the molecule.

Some useful applications of FTIR spectroscopy are that it can be used to differentiate between fibre types to identify fibres based on relative lignin and holocellulose content.[2] Further, FTIR can be employed to investigate other parameters, such as the degree of crystallinity in fibres and to determine the extent of oxidative degradation.

Some peak ratios used in the literature for investigating cellulose-based FTIR spectra include the total crystallinity index (TCI), lateral order index (LOI), R_1 and R_2 ratios. The TCI probes both cellulose I and II.[3] The intensity of the C-H vibration at 2900 cm^{-1} was chosen to represent the overall organic content as it is less affected by crystallinity changes than other bands and is usually constant.[4] The LOI probes cellulose I and the intensity at 1430 cm^{-1} represents the crystalline cellulose content.[3] If slight shifts from this wavenumber are observed, this is an indication of degradation. The intensity of the peak at 897 cm^{-1} represents the amorphous cellulose content. If broadening is observed in this band, greater disorder is present in the structure.[5] The formulae for TCI and LOI are given by:

$$TCI = \frac{I_{1372}}{I_{2900}}$$

$$LOI = \frac{I_{1430}}{I_{897}}$$

In R_1 and R_2, the peak at 1595 cm^{-1} represents the lignin content and the peak at 1105 cm^{-1} represents the cellulose content:[2,6]

$$R_1 = \frac{I_{1595}}{I_{1105}}$$

$$R_2 = \frac{I_{1595}}{I_{2900}}$$

Standard IR spectroscopy can be used to monitor some characteristics of cellulose degradation but not crystallite orientation, for this, polarised ATR-FTIR is required.[4]

2.1.1 Polarised Fourier transform infrared spectroscopy (Pol-FTIR)

A method for using polarised ATR-FTIR spectroscopy to study the degradation of cellulose in archaeological textiles based on crystalline orientation has been established by Garside and Wyeth.[7–9] It was developed as a way of differentiating between fibres based on their level of degradation rather than relying on microscopic methods, which can be fairly subjective. The degradation of silk, flax, and hemp fibres have all been assessed using this polarised ATR-FTIR method. Polymer orientation is important in this context as it also relates to mechanical properties of the fibre such as tensile strength.[10] The ATR technique can be used to measure the degree of orientation of polymer chains. With a polariser in the ATR-FTIR set-up the orientation effects are more distinct. With the polariser perpendicular to the plane of incidence, the evanescent field is parallel to the crystal, without a perpendicular component. If the sample has some degree of orientation relative to the surface, intensity changes will be seen if the polariser or the sample orientation is changed. When the polariser is set perpendicular to the plane of incidence, a reduction in IR band intensity signifies a dipole moment change perpendicular (normal) to the surface. The dichroic ratio is often measured for specific absorbance bands in the spectrum to give information on the structure of the sample.

With the ATR set-up, an evanescent IR wave probes the surface of the sample to a certain depth (d_p) based on the refractive index of the sample and the crystal, the angle of incidence at the interface, and the wavelength of the radiation. The sampling depth usually increases at

lower wavenumbers. A polariser can be introduced to the beam path so that the polarised radiation will only interact with bonds aligned with the electric vector. Some vibrations have dipole moment changes aligned in the plane of the crystals, some perpendicular. These IR bands can be assigned based on their dichroism by measuring two spectra, one where the fibre is aligned parallel and one where it is perpendicular to the electric vector of the incident radiation. If a band is dichroic, it means the intensity of the band is dependent on the orientation of the fibre with respect to the electric vector of the IR radiation. Dichroism can be either perpendicular or parallel to the orientation of the polymer meaning IR bands will be more intense when polymer chains are in either alignment with respect to the electric vector of the incident radiation. Information on the microstructural order of the fibre can be derived from the relative intensity of a dichroic band at a particular orientation of the fibre. The dichroic ratio is the ratio between the absorbance measured using parallel polarised radiation and the absorbance measured using perpendicular polarised radiation. Orientation index (the ratio between the intensities of strongly dichroic and non-dichroic bands) can be plotted against the angle of alignment of the fibre to determine the crystallinity index.

Figure 13 displays an example of how intenisites of specific bands can change based on the alignment of the fibre and how the intensity of a strongly dichroic band (for example at 1160 cm^{-1}) can be compared with what of a non-dichroic band (for example at 1050 cm^{-1}) to determine an orientation index. It is necessary to normalise against a non-dichroic band as this reduces the effect of differing sample contact with the ATR crystal (although a constant force was applied on all samples to help keep contact as consistent as possible).[10]
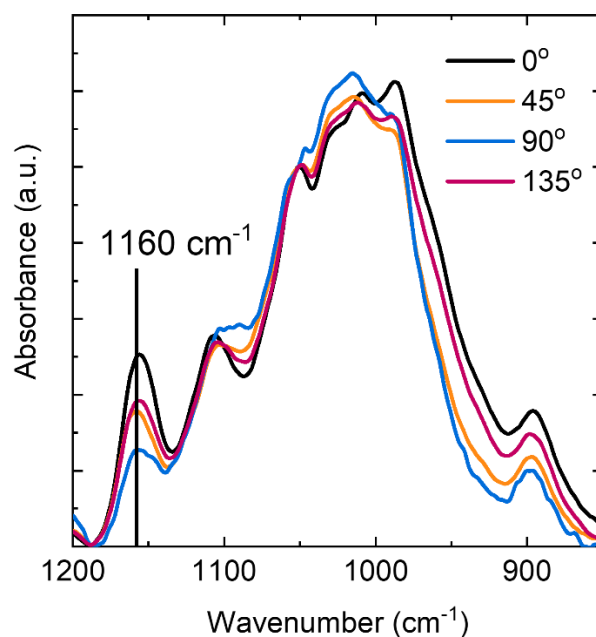
Figure 13 FTIR spectra of a flax fibre at different orientation angles (0, 45, 90 and 135°) to show how certain band intensities can differ with fibre orientation. The 1160 cm^{-1} band (asymmetric C-C ring breathing stretch) is highlighted as it is a strongly dichroic band.

With fibres and other solid samples, pressure is required to provide good contact between the solid and the ATR crystal. The pressure applied should be consistent between measurements as less degraded fibres will have a higher crystallinity index as more polymer chains will be parallel to the fibre twist, so $\chi_{\parallel}$ will be higher. The crystallinity index is defined by the following equation:

$$X = \frac{\chi_{\parallel} - \chi_{\perp}}{\chi_{\parallel}}$$

For example, if $\chi_{\parallel} = 1$ and $\chi_{\perp} = 0$, the crystallinity index will be 1 but if $\chi_{\perp}$ was larger, the crystallinity index would be smaller, meaning the polymer (therefore the fibre as a whole) would be more degraded. More crystallinity observed parallel to the twist of the fibre indicates the fibre is more intact.
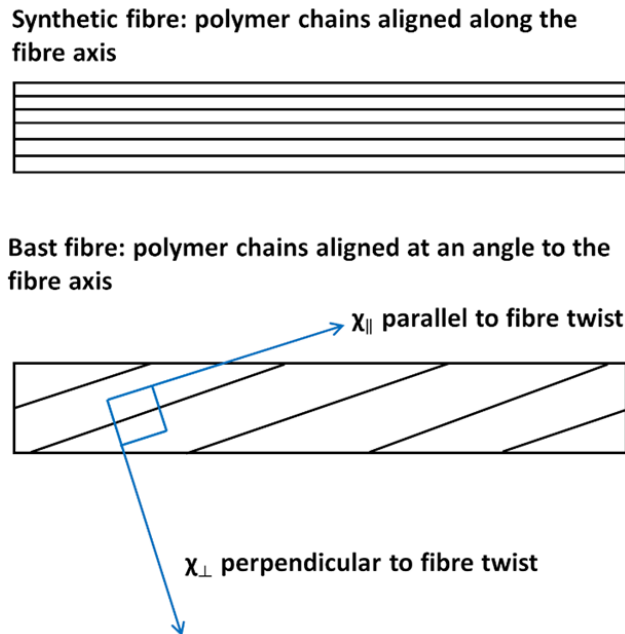
Figure 14 A diagram of the orientation of polymer chains in synthetic fibres (top) and bast fibres (bottom) (adapted from P. Garside, *Applied Spectroscopy*, 2007).[11]

An increase in crystallinity is often observed first in textiles, even if it is degrading, before a drastic decrease in crystallinity as the amorphous regions holding together the crystalline fragments break. An increase in crystallinity is probably observed at first as amorphous regions are more vulnerable to attack so there seems to be more order, more alignment with the fibre axis as disordered regions are removed. However, when the degradation reaches a point where the amorphous regions are no longer holding the crystalline regions together, more disorder is observed, and degradation of crystalline regions is more likely to occur.

2.2 Raman spectroscopy

Raman and IR spectroscopy are complementary techniques. In Raman spectroscopy, a monochromatic (of a narrow range of frequencies) radiation source is directed on the sample. In this thesis a 532 nm visible laser is used as the excitation source. The incoming photons are scattered by the sample. There is a resultant increase in frequency if the incident radiation collects energy from the molecule (anti-Stokes lines) or a decreased frequency if it loses

energy to the molecule (Stokes lines).[12] Rayleigh scattering (elastic scattering) arises if no change in energy occurs. The difference between the frequencies of the scattered and incident radiation is determined by the transitions that occur within the molecule.[12] Raman spectroscopy studies molecular vibrations and rotations. As these occur at characteristic frequencies, detailed molecular structure information can be obtained from Raman spectroscopy. The laser is commonly introduced to the sample through a microscope (a typical set-up is displayed in Figure 15) so that the laser can be focused on a small area of the sample, which makes sample preparation straight-forward and makes this technique potentially non-destructive.[13]
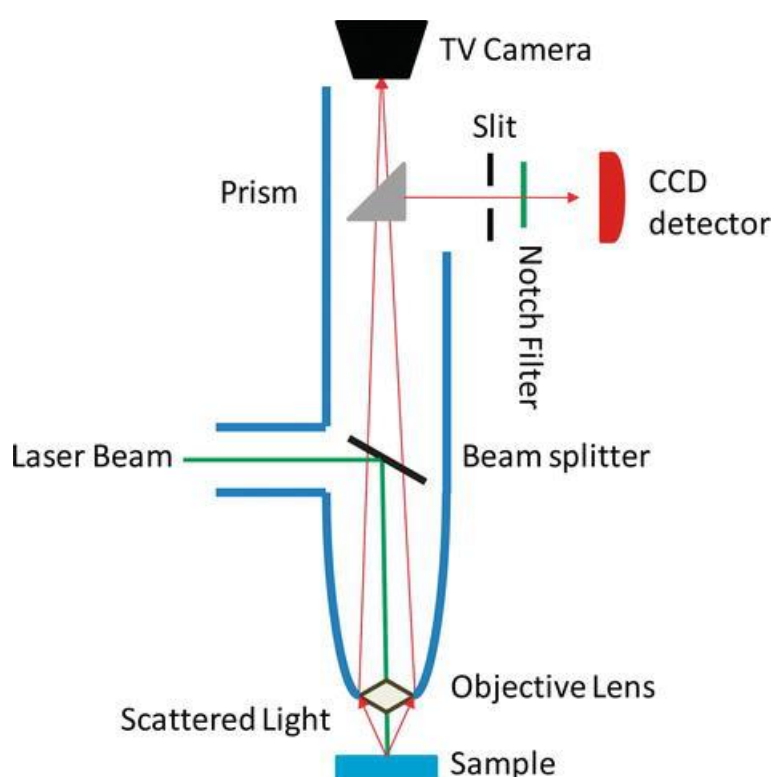
Figure 15 A diagram of a conventional Raman microscope (from G. M. do Nascimento, Introductory Chapter: The Multiple Applications of Raman Spectroscopy, Raman Spectroscopy, 2018).[13]

For a vibration to be Raman active, the vibration must result in a change in polarisability of the molecule. An induced dipole moment is brought about by molecular distortion when it is exposed to an electric field (the laser beam in this case) and the nuclei are attracted to the negative pole and the electrons are attracted to the positive.[14] If a molecule has a centre of symmetry, no modes can be both IR and Raman active – this is the exclusion rule. A mode can

be inactive in both IR and Raman though. A Raman spectrum is displayed as intensity against Raman shift, which is the difference in frequency between the incident and scattered radiation expressed in wavenumbers.

Raman spectroscopy is key in the fields of conservation science and archaeology as it can give information on a micrometre scale and is non-destructive. It is particularly useful for characterising fibres and identifying pigments.[15–19] Raman spectra of fibres under glass are able to be measured but cannot measure FTIR spectra through glass due to glass absorption in IR.[20] Water is a weak Raman scatterer but displays strong absorption in IR spectra so Raman spectroscopy is advantageous for biological samples.[14] With characterisation of cellulosic fibres, fluorescence is often a problem especially when using a visible excitation source. This fluorescence is usually decreased by using infrared excitation. Another problem that can occur with Raman spectroscopy is damage to the sample due to photodegradation or localised heating from the laser beam.

2.3 Powder X-ray diffraction (PXRD)

X-ray diffraction (XRD) is used to examine the crystalline structure of a material. X-ray radiation is useful for studying crystalline samples as its wavelength is of the same magnitude as the interatomic spacings in the materials. Powder XRD (PXRD) observes the scattering of X-rays from randomly ordered, small crystallites rather than from a single crystal. In polycrystalline materials, some of these crystallites will be orientated to give rise to diffraction. Incident X-rays will be scattered by atoms in the lattice structure of the crystallites. If the diffracted waves are out-of-phase they will destructively interfere. The incident and diffracted waves in Figure 16 will be in-phase (constructively interfere) if the additional distance travelled by the second scattered wave is an integer of the wavelength ($n\lambda$). Crystalline solids can be considered as lattice planes with the spacing between them given by

d, so the additional distance the second wave travels is given by the Bragg equation, $n\lambda = 2d\sin\theta$, where θ is half of the diffraction angle.
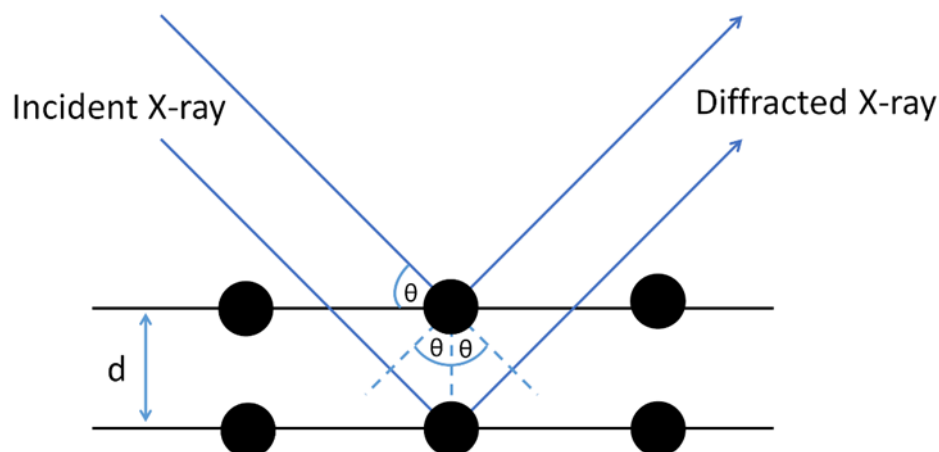
Figure 16 A diagram explaining the Bragg equation by showing the relationship between incoming X-ray radiation and the diffracted X-rays. Diagram adapted from M. Kaliva, Polymer Science and Nanotechnology, 2020.[21]

There are different methods of collecting PXRD data, the most common of which is with a Bragg-Brentano configuration. In this set-up, monochromatic X-ray radiation from a fixed source (in some instruments the source rotates) is directed to a flat sample holder containing the polycrystalline material and the sample stage and detector are rotated. The output data consists of scattered intensities as a function of the diffraction angle (2θ). PXRD is useful for phase identification as the position and intensity of the diffraction lines can be compared to standard diffraction patterns stored on a database for the compound of interest.

Crystallite sizes can be determined from PXRD data using the Scherrer equation. The Scherrer equation is displayed below where τ is the average particle size, λ is the wavelength of the X-ray (1.5418 Å for Cu Kα), k is the shape factor (0.9 for spherical particles), θ is the Bragg angle, and β is the full width at half maximum (FWHM) in radians which is inversely proportional to the crystallite size (broader peaks with smaller crystallite sizes).

$$\tau = \frac{k\lambda}{\beta \cos\theta}$$

The Scherrer equation uses the broadening of the peaks in the XRD pattern to determine crystallite size. It should be noted that this does not consider amorphous regions in the material so cannot be relied upon to give accurate crystallite sizes.

A common structure refinement is a Rietveld refinement which uses least squares method to adjust the theoretical pattern to match the observed pattern by minimising the weighted squared difference between the patterns against the parameter vector. The goodness of fit in a Rietveld refinement is evaluated by the weighted R-factor (R_{wp}) and the expected R-factor (R_{exp}). χ^2 is defined as $(R_{wp}/R_{exp})^2$. Lower R-factors indicate a better fit. A lower reduced chi-square (χ^2) value means the sample pattern and the theoretical pattern are more closely aligned. The Rietveld refinements in this thesis were performed with Fullprof software. Rietveld analysis can be used to determine parameters of crystal structures such as lattice constants, FWHMs, unit cell lengths, and the volume of the unit cell.

2.4 X-ray fluorescence (XRF) spectroscopy

XRF is useful as it is generally a non-destructive technique and is capable of detecting multiple elements.[22] Portable XRF (PXRF) is crucial for a variety of applications including in an archaeological and museum setting.[22] It has the advantage of being able to be used *in situ* and results are able to be analysed and processed very quickly. PXRF can be hand-held and taken to the site of interest.

An X-ray tube or a sealed radioactive source emit X-ray photons which excite the sample resulting in an X-ray spectrum recorded by the detector. The radiation emitted is characteristic of elements present in the sample. Theoretically, PXRF can measure almost all elements, but in practise, carrying out the experiments in air means low-energy fluorescence X-rays are attenuated so elements below silicon in the periodic table are unable to be detected. Elements can be detected from Si to approximately Mo depending on the excitation source. Lower atomic number elements emit low energy fluorescence lines and have critical penetration depths in the micrometre range whereas higher atomic number elements have penetration depths in the 1-10 mm range. The critical penetration depth is the depth below

the surface of sample beyond which over 99% of X-ray line emission of an element is absorbed within the sample and so is not available for detection.[22] Due to these penetration depth ranges, best estimates of analysed mass for elements obtained by PXRF is with sample weights from approximately 10 μg to 100 mg.

A PXRF instrument consists of an excitation source (miniature X-ray tubes or sealed radiation sources), sample positioning facility, detector, and pulse processing and analysis facility. A basic diagram of these components is displayed in Figure 17. An ideal sample surface is perfectly flat and aligned with the analytical plane of the instrument. Attenuation in air (particularly for elements below Ca) is a problem for PXRF but not in laboratory XRF as the sample is usually placed under vacuum. Silicon drift detectors (SDDs) allow higher count rates than with a conventional detector (Si(Li) and Si(PIN)). SDDs work by applying an electric field parallel to the surface of the detector where concentric ring electrodes are etched. Ionised electrons drift towards the anode at the centre of the detector.[22]
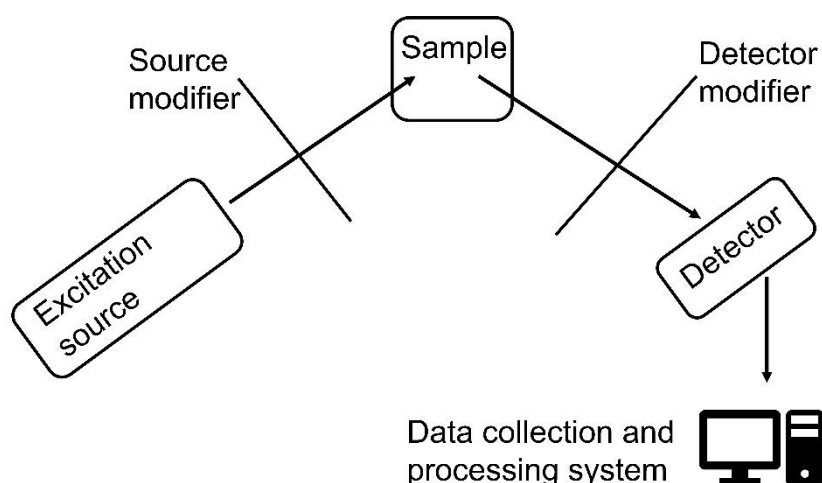
Figure 17 Basic diagram of the components in an X-ray fluorescence spectrometer (adapted from E. Margui, X-ray Fluorescence Spectrometry and Related Techniques: An Introduction, 2013).[23]

2.5 Synchrotron-based techniques

Electrons are injected into a storage ring and travel around the circular path at around the speed of light, guided by vertical magnetic fields. Whenever their trajectory changes, the electrons accelerate, emitting electromagnetic radiation. Relativistic effects due to the electrons travelling near the speed of light mean that X-rays can be produced of greater

energy and power and are more directional, making monochromators easier to use.[24] Magnetic insertion devices including wigglers and undulators are inserted in the storage ring to manipulate the electrons in an oscillatory way so their direction is unaffected, but enhanced synchrotron radiation is produced.[25] These insertion devices define third generation synchrotron sources. A beamline is used to bring the synchrotron radiation from the storage ring to the experimental hutch through a series of apertures and optics tailored to the specific end application. A basic diagram of a synchrotron is provided in Figure 18 showing the electron gun where electrons are produced, the linear accelerator (LINAC) and booster synchrotron where the electrons are accelerated, the main storage ring where their energy is maintained and the beamlines which lead to the experimental hutches. In this thesis, X-ray absorption spectroscopy will be the focus and experiments were undertaken on B18 of Diamond Light Source.
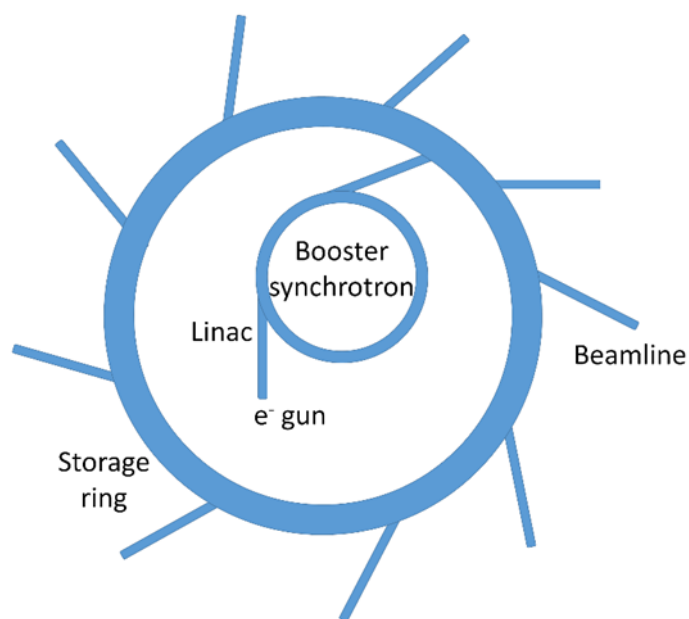
Figure 18 Basic diagram of a synchrotron where electrons are accelerated by the LINAC, booster synchrotron, and their energy maintained by the storage ring. (Adapted from https://www.diamond.ac.uk/Science/Machine/Components.html)

X-rays are electromagnetic radiation which can be described quantum mechanically as a stream of photons of energy. Hard X-rays are in the range of a few keV to 100 keV and soft X-rays occupy the region of a few hundred eV to a few keV.[24] X-rays can interact with matter in

the following ways: inelastic (Compton) scattering, elastic (Thomson) scattering, and absorption leading to fluorescence and Auger or photoelectron ejection. Inelastic scattering involves change in the kinetic energy of the incident radiation. Elastic scattering conserves the kinetic energy of the incoming radiation but involves a change in its direction.

2.5.1 X-ray absorption spectroscopy (XAS)

X-ray absorption spectroscopy (XAS) using synchrotron light sources has been used for a vast range of applications from geology to physics. The power of this technique is due to its ability to measure many elements, compounds, and materials as, unlike XRD, it does not rely on symmetry or crystallinity.

This technique makes use of the photoelectric effect whereby an incoming X-ray is absorbed if it has an energy greater than or equal to the binding energy of a tightly-bound core energy level. If the X-ray has enough energy, a photoelectron (with an energy equal to the incident X-ray energy minus the binding energy of a core electron) will be ejected to unoccupied energy levels or the continuum (illustrated in Figure 19). In this process, a core hole will be left and decay from the excited state of the atom will take place through one of two mechanisms: X-ray fluorescence or the Auger effect. In the X-ray fluorescence mechanism, a higher energy electron drops in energy to fill the core hole, leading to the emission of an X-ray of a well-defined energy. Similarly, in the Auger mechanism, a higher energy electron drops in energy to fill the core hole, but the difference here is that a second electron is ejected to continuum. Either mechanism can be used to measure the absorption coefficient (μ), but fluorescence is more common.
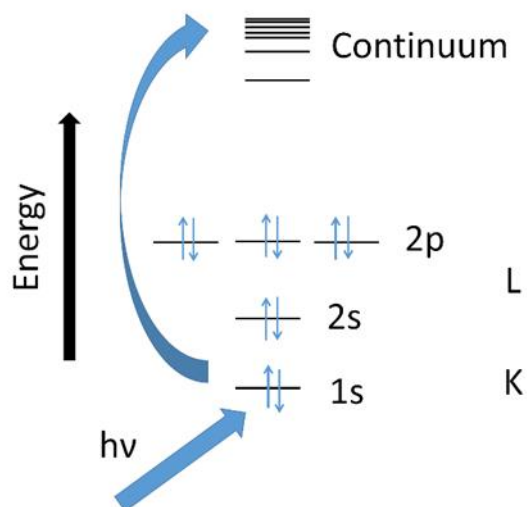
Figure 19 Diagram showing X-ray absorption by the electron in the 1s or K orbital, prompting ejection to the continuum or unoccupied energy levels (adapted from K. Kvashnina, 2007).[26]

The absorption coefficient is related to the incident X-ray intensity and the thickness of the sample through Beer's law: $I_t = I_0 e^{-\mu t}$ where I_t is the transmitted intensity, I_0 is the incoming X-ray intensity, μ is the absorption coefficient, and t is the thickness of the sample.

Data can be collected in transmission, total electron yield, or fluorescence mode. In transmission mode, $\mu(E)$ is calculated using $\mu(E) = \ln(I_0/I_t)$ where I_0 is the intensity of the incident X-ray, and I_t is the intensity of the transmitted X-ray. Diagrams of the experimental set-up when measuring in transmission mode and fluorescence mode are displayed in Figure 20, where I_f is the intensity of the fluorescence associated with the absorption process and I_{ref} is the intensity of the radiation from the reference foil. Fluorescence mode is especially utilised for measurement of thick samples. Total electron yield measurements are specifically surface sensitive.
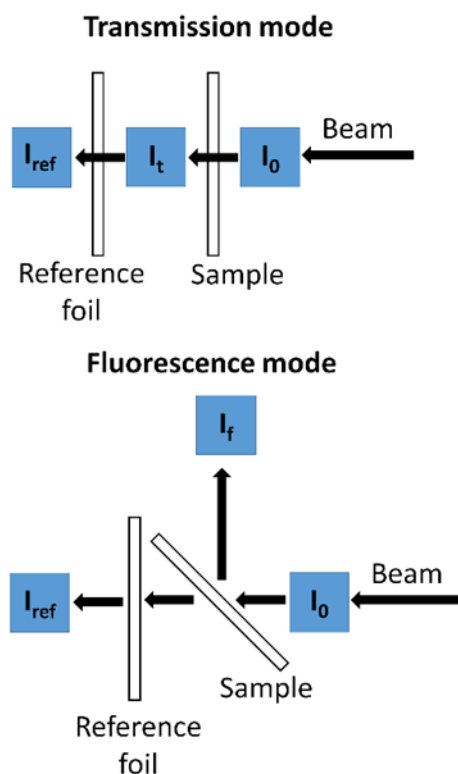
Figure 20 A diagram showing the experimental set-up in transmission mode (top) and fluorescence mode (bottom).

XAS can provide information on the electronic and atomic structure of an element of interest (for example, sulfur) including its oxidation state, type and number of surrounding atoms, distance of the surrounding atoms, and their distribution. Figure 21 presents an X-ray absorption near edge structure (XANES) spectrum of the sulfur K-edge to explain the key features and the terminology used to describe an X-ray absorption spectrum. Before the absorption edge, the X-ray photons do not have enough energy to excite an electron. The extended X-ray absorption fine structure (EXAFS) region can provide information on the bond distances and coordination number of the scattering atoms from the absorbing atoms. Before the absorption edge, the pre-edge region gives information on the local symmetry of the element under study. It occurs before the main edge as it is due to the core electron being ejected into another energy level, not into the continuum. Hybridisation of the d-orbitals of the measured element and the p-orbitals of its ligands can also lead to pre-edge features. Pre-edge features can also arise due to transitions between s- and d-orbitals. These transitions are usually forbidden by the dipole selection rule for centrosymmetric coordination environments, but, in a non-centrosymmetric environment, these transitions can take place.

An isolated atom would show a sharp absorption at the binding energy of the core energy level, then would decay slightly and smoothly after the edge. This is not usually seen in X-ray absorption spectra because the photoelectron can be scattered from neighbouring atoms in a real sample. This interference will change with energy at the absorbing atom, so oscillations are observed after the edge. These oscillations provide information on the environment of the element of interest.
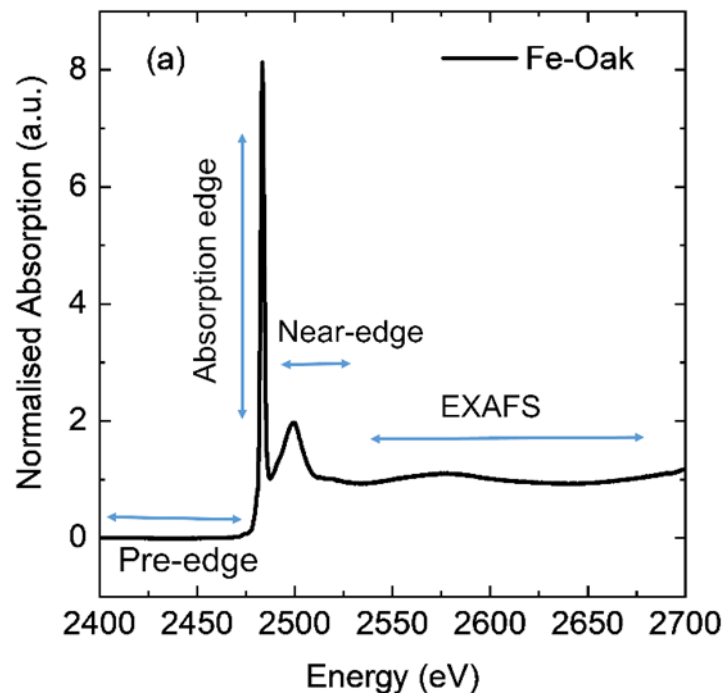
Figure 21 Diagram showing the features of a normalised X-ray absorption spectrum. The spectrum is the sulfur K-edge of a wood sample soaked in iron (II) sulfate solution.

The data in Figure 21 has been normalised to remove other effects present when measuring the sample, for example the thickness of the sample. Prior to normalisation, the data should be calibrated and aligned correctly. During normalisation in the Athena program, a line is regressed to the pre-edge range and extrapolated along the data. Then, a quadratic is regressed to the post-edge range and extrapolated to the edge. At the edge energy, the difference between the post-edge and pre-edge lines is evaluated to obtain the edge step. The pre-edge line is subtracted from the original data and divided by the calculated edge step. When all data sets are normalised in the same range in this way, the data will be on the same scale and can be further analysed using linear combination fitting, for example.

It is important to correctly align, calibrate, and normalise the data before subsequent analysis of X-ray absorption spectra. Alignment with reference scans is critical as monochromators may not retain energy calibration over time. Calibration involves finding the first peak of the first derivative of the sample spectra and assigning it a value for the material under study (for example, elemental sulfur K-edge assigned the calibration value of 2472.0 eV)[27] so that spectra can be compared consistently with others.[28] Further analysis methods are discussed in the next sections. Before analysing the data, the sample data is often merged (averaged), at this stage it is important to study the data to ensure no significant glitches or diversions are merged with the other repeat scans. Once the data is merged, the position of E_0 in the spectrum is chosen. E_0 is the energy corresponding to the transition of the core electron to unoccupied energy levels or continuum. The analyst must choose the E_0 and be consistent with applying this choice. Throughout this thesis the E_0 has been defined experimentally from the first inflection point of the first derivative of the spectrum.

2.5.1.1 XANES

XANES is usually defined as being within 50 eV of the absorption edge but there is some overlap between the different regions.[29] It is often more important to draw the distinction between XANES and EXAFS by how they are analysed. XANES is often qualitatively or quantitatively examined, whereas EXAFS is statistically analysed based on multiple scattering theory.[29] The XANES region can be helpful in identifying species of a particular element in differing oxidation states. For example, focusing measurements on the S K-edge provides information on the sulfur species present in the sample and XANES is particularly good at observing the different species based upon their oxidation state as this will alter the absorption edge energy. K-edge is used to refer to the energy level the core electron was emitted from, where the core hole is left and where the higher energy electron falls back to, this being the 1s orbital in the case of the K-edge. XAS is a useful technique as it is sensitive to incredibly small amounts of compounds present in the sample. This is mainly because it is an element specific technique. From a conservation perspective, XAS is a very useful technique as it is non-destructive.

A popular method of interpreting the XANES region is fingerprinting, where a known standard spectrum is compared to the sample spectrum of interest to give an idea of what is in your

sample or to confirm the presence of a particular compound. Moving on to quantitative analysis methods, linear combination fitting (LCF) assumes the sample spectrum is a mixture of phases and states that can be interpreted as a linear combination of spectra from standard compounds. In this way, a database of standard spectra can be collected and fitted to the collected sample data to ascertain an idea of the compounds that make up the sample spectrum and their proportions in the sample. Other analysis methods include principle component analysis (PCA), modelling, and curve fitting.

2.5.1.2 EXAFS

EXAFS can provide information on the types of atoms surrounding the absorber, the number of neighbouring atoms and their distance from the absorbing atom. When the X-ray ejects an electron, the photoelectron can scatter off nearby atoms before returning to the absorbing atom, this gives rise to the EXAFS region in the spectrum. When analysing the EXAFS region of the X-ray absorption spectra, the contribution from each part of the following equation needs to be evaluated.

$$\chi(k) = \frac{NS_o^2 F(k)}{2kR} \sin\left(2kR + \delta(k)\right)e^{-2\sigma^2 k^2}$$

Where N is the coordination number and R is the distance between the absorber and the scattering atom for a single scattering path (the distance the photoelectron travels). S_o^2 is the passive electron amplitude reduction factor that takes into consideration the effect of all the other electrons relaxing around the core hole due to the change in screening once the photoelectron is ejected. $F(k)$ is the scattering amplitude which can be obtained from the Feff calculation. $\sin\left(2kR + \delta(k)\right)$ is the oscillatory part of the equation. $\delta(k)$ is the phase shift due to scattering off a nearby atom and is also calculated from Feff. As the photoelectron is ejected, it propagates, and phase shifts when it scatters off the neighbouring atoms. The phase shift depends on the type of scattering atom.[28] $e^{-2\sigma^2 k^2}$ is the part of the equation describing disorder in the system, it dampens the signal, decreasing peak size.[30]

In the Artemis program, the Fourier transform of $\chi(k)$ is plotted and analysed to extract information about the radial distribution of atoms around the absorbing atom. Magnitude and oscillatory functions all add up in the fit of the data spectrum. First, crystallographic data

is inputted as a list of atomic coordinates, then a Feff calculation is undertaken. For every scattering path, an R_0 value is calculated, which is the distance of each scattering path. $\delta(k)$ and $F(k)$ are also calculated in this process. The fit then evaluates the change in the path distance (ΔR) from the crystallographic data to the measured data, the S_o^2, σ^2, N and ΔE_0 (the energy shift of the data to where k=0, which is assigned during XANES analysis). Using chemical knowledge of the system and critically evaluating the data from the fit allows information of the environment surrounding the absorbing atom to be determined.

2.6 Light microscopy

Light or optical microscopy uses visible light and objective lenses to create a magnified image of a sample, either directly to the eye or to a camera. This technique has been employed since the 1600s. The light can be transmitted through the sample or reflected from the surface of the sample before detection. In transmitted light microscopy, light is passed through a field diaphragm and the sample and is collected by the objective where it can be directed to the eyepiece or a camera. The objective collects the diffracted light from the sample and forms a magnified image, which is either directly projected to a camera or further magnified by the cornea and lens producing an image on the retina.[31] The field diaphragm determines the size and portion of the sample illuminated. The condenser aperture diaphragm is above the condenser and below the sample. The condenser focuses light onto a small area of the sample. Köhler illumination is a method of illuminating the sample that positions the image and diffraction planes in their optimal locations.[31]

A couple of disadvantages of optical microscopy are the resolution limit and poor contrast with very thin or very reflective samples. Poor contrast can be aided by using polarised light microscopy, darkfield microscopy, and stereomicroscopy among other techniques. Polarised light microscopy not only increases the contrast of the images, it can be used to determine birefringent properties of the sample. Resolution and field depth can be improved by reducing the angle of convergence by adjusting the aperture diaphragm and increasing the refractive index of the mounting medium. An advantage of optical microscopy for the study of fibres is the ability to observe colour differences in the samples. Also, the ability to observe internal structures in the fibres is valuable.

2.7 Scanning electron microscopy (SEM)

Scanning electron microscopy (SEM) works on the basis of a focused electron beam interacting with the sample. Electrons are produced and accelerated down the column and focused on the sample. The sample chamber and the column must be under vacuum so that the electrons do not interfere with atmospheric gas. However, there are environmental SEMs where the sample chamber is under a lower vacuum which is useful for a wider range of samples. Also, in environmental SEM, gold and palladium sputter coating is not necessary to make the sample conductive.

The electron beam interacts with the sample, emitting primary backscattered electrons, secondary electrons, and X-rays. Primary backscattered electrons are used to distinguish different chemical areas and regions of crystallinity. Darker regions are indicative of heavier atoms. Backscattered electrons arise from an electron from the beam interacting with an atomic nucleus and being elastically scattered (energy is conserved but direction is changed). Secondary electrons are mainly used to produce the common SEM images showing the surface of the sample. They arise from interaction of the electron beam with the outer shell of a sample atom resulting in the ejection a secondary electron.

Energy dispersive X-ray spectroscopy (EDS) can be used in conjunction with SEM, where the electron beam displaces an electron from a low energy level allowing a higher energy electron to drop down to fill the hole. In doing so, this electron loses energy in the form of an X-ray. The energy of the emitted X-rays is characteristic of specific elements so the presence of elements can be confirmed in the sample under analysis.

2.8 Synthesis and characterisation procedures
2.8.1 Synthesis of $SrCO_3$ nanoparticles

There is a wide variety of methods for synthesis of strontium carbonate. These include hydrothermal, solvothermal, and sonochemical methods. Microwave-assisted synthesis has a number of advantages over other methods such as producing products of increased purity, improved yields and shorter reaction times. The microwave-assisted method has previously been employed for synthesis of $SrCO_3$ to produce $SrCO_3$ nanoparticles with a size distribution of around 20-50 nm. Microwave time can be tuned for desired morphology.[32] An investigation

of the effect of microwave heating time and power concluded that both have a significant effect on the size and morphology of the SrCO$_3$. Additionally, sonochemical synthesis has been investigated in this report as ultrasonic sound waves have been shown to be a facile way of synthesising nanoparticles due to the localised high pressures and temperatures it can produce to drive reactions. Microwave radiation affects the spin-state of molecules with unpaired electrons and can change the rotational energy of molecules.[1]

SrCO$_3$ was purchased from Alfa Aesar (97.5%, 147.63 g mol^{-1}, mp. 1100 °C, density 3.70 g mL^{-1}), Sr(NO$_3$)$_2$ was purchased from Alfa Aesar (99.0 %, ACS) and Na$_2$CO$_3$ was purchased from Fisher Scientific (99.96 %, analytical grade).

2.8.1.1 Mechanochemical synthesis of SrCO$_3$

SrCO$_3$ (1.40 g, 9.4 mmol) white powder was placed in a stainless-steel ball mill capsule (with a stainless-steel ball) and ball milled at a frequency of 20/s for 6 hours with approximately 2 mins rest time every 60 mins. A fine white-grey powder (1.33 g, 9.0 mmol) was obtained. The same method was followed again but with ball milling for 8 hours rather than 6 and this time the capsule was sealed under argon in a glovebox before ball milling commenced. The powder obtained was whiter and "fluffier" than the previous sample.

2.8.1.2 Microwave synthesis of SrCO$_3$

Sr(NO$_3$)$_2$ (2.50 mmol) and anhydrous Na$_2$CO$_3$ (2.50 mmol) were dissolved separately in half of the ethylene glycol (EG) (25 mL) with vigorous stirring for 1.5 hours (due to the difficulty in dissolving the sodium carbonate in EG). The Na$_2$CO$_3$ solution was added to the Sr(NO$_3$)$_2$ solution and stirred for 15 mins. The resulting cloudy, white solution was poured into a microwave cavity and stirred for 2 mins before microwaving at 80°C for 20 mins (max power 200 W, max pressure 300). The product was centrifuged for 10 mins at 4000 rpm and the supernatant was poured off. It was then washed three times with distilled water and two times with ethanol, centrifuging each time for 5 mins at 4000 rpm. The product was rotary evaporated at 35°C for 20 mins. The microwaved product yielded 0.21 g (57% yield).

This exact synthesis procedure was followed to examine the effect of solvent on the resulting materials, with two solvent systems studied: 1:1 ratio of EG:distilled water and pure distilled water, respectively.

2.8.1.3 Controlled precipitation synthesis of SrCO$_3$

Sr(NO$_3$)$_2$ (0.534 g, 2.52 mmol) and anhydrous Na$_2$CO$_3$ (0.267 g, 2.52 mmol) were dissolved separately, each in half of the EG (25 mL) with vigorous stirring for 3 hours. The Na$_2$CO$_3$ solution was added to the Sr(NO$_3$)$_2$ solution and stirred for 24 hours (only after around 3 hours did the solution turn white and cloudy, possibly due to the difficulty in dissolving starting materials in EG). The product was centrifuged for 10 mins at 4000 rpm and the supernatant was poured off. It was then washed three times with distilled water and two times with ethanol, centrifuging each time for 2 mins at 4000 rpm. The product was rotary evaporated at 35°C for 30 mins. The product yielded 0.20 g (54% yield).

This exact synthesis procedure was followed with pure distilled water (0.30 g, 81% yield). With a 1:1 ratio of EG:distilled water solvent system (0.13 g yield) after 15 minutes of stirring once the Na$_2$CO$_3$ solution was added, half of the solution was removed and centrifuged for 5 mins at 4000 rpm, the supernatant poured off and then washed three times with distilled water and two times with ethanol. During rotary evaporation for 20 mins at 30°C, the product turned brownish (possibly due to contamination from the flask) and yielded 0.10 g of brown-yellow powder (LJ014a) The rest of the solution was stirred for 24 hours, centrifuged for 10 mins at 4000 rpm, and the supernatant poured off. The product was washed three times with distilled water and two times with ethanol, centrifuging each time for 2 mins at 4000 rpm, then rotary evaporated at 35°C for 20 mins. The product (LJ014b) yielded 0.13 g. Characterisation was only carried out on the LJ014b sample.

2.8.1.4 Sonochemical synthesis of SrCO$_3$

Sr(NO$_3$)$_2$ (0.530 g, 2.50 mmol) and anhydrous Na$_2$CO$_3$ (0.269 g, 2.54 mmol) were dissolved separately, each in half of the EG (25 mL) with vigorous stirring for 3 hours. The Na$_2$CO$_3$ solution was added to the Sr(NO$_3$)$_2$ solution and stirred for 5 mins. The solution was poured into a round bottomed flask and sonicated for 1 hour. The flask was warm after this time (this occurred with the microwaved solutions also). The product was centrifuged for 10 mins at

4000 rpm and the supernatant was poured off. It was washed three times with distilled water and two times with ethanol, centrifuging each time for 2 mins at 4000 rpm. The product was rotary evaporated at 35°C for 30 mins. The yield of the product was 0.22 g (60% yield).

This exact synthesis procedure was followed to examine the effect of solvent on the resulting materials, with two solvent systems studied: 1:1 ratio of EG:distilled water (0.26 g, 70% yield) and pure distilled water (0.30 g, 81% yield), respectively.

2.8.2 SrCO$_3$ characterisation

Powder XRD data were collected on the samples using a PANalytical X'pert PRO diffractometer with Cu-Kα radiation of wavelength 1.5418 Å. The samples were loaded onto a glass sample holder and flattened with a glass slide before being placed in the bracket sample stage in Bragg-Brentano geometry with 2θ range between 10-90°, a scan step of 0.016711° and time per step of 81.915 s. The centrifuge used was a Hettich Rotofix 32A. The rotary evaporator employed was a Büchi Rotavapor <R> with Heidolph WB2000 water bath. An ultrasonic bath, Camlab Camsonix C425, and a ball mill, Retsch MM200, were also utilised in this work. A Carl Zeiss Sigma variable pressure SEM was used to collect the high-resolution scanning electron microscope (HR-SEM) images with a 5 kV accelerating voltage, 30 μm aperture, and an approximate working distance of 5 mm. Images were obtained from the scattered secondary electrons. Gold and palladium sputter coating with a thickness of 15 nm was used to prevent charging of SrCO$_3$ for the HR-SEM images. The FTIR spectra were collected on a Shimadzu IRAffinity-1S with an ATR accessory used over the range 400-4000 cm^{-1}. 32 scans were taken for each sample with a resolution of 4 cm^{-1}. The Raman spectrometer used was a Horiba LabRAM HR. The spectra were measured using the 532 nm (visible) laser with an aperture of 200 μm over a range of 50 – 3000 cm^{-1}. 100% of the laser power (approximately 100 mW) was used and 5 scans were taken, each measured for 6 seconds due to saturation if a longer timescale was used.

2.8.3 Patch treatment

SrCO$_3$-cellulose patches were prepared by manually mixing 1 g of α-cellulose (Sigma-Aldrich) with 5 mL distilled water to form a paste to which 0.5g of SrCO$_3$ (Alfa Aesar, 97.5%, 147.63 g mol^{-1}, mp. 1100°C, density 3.70 g mL^{-1}) was added to reach the desired consistency (so the

patch would adhere to the wood). Oak blocks were soaked in 100 mM iron (II) sulfate ($FeSO_4.7H_2O$) solution for 1 month then removed and left to dry. This was in order to approximately model wood from the *Mary Rose*. Two of the cubes were left unsoaked for comparison purposes (BM-Oak samples). One of these was treated by applying the $SrCO_3$-cellulose patch (BM-Oak after treatment) and one was left untreated (BM-Oak). The $SrCO_3$-cellulose paste was applied with a spatula to the sides of the dried iron sulfate-soaked oak samples (Fe-Oak treated) or the iron sulfate soaked oak sample was left untreated as a control (Fe-Oak). The patches were removed with a spatula after 24 hours. This time was chosen as it was by this time that the patches were dry and hard so could be easily removed. The patch from the iron-soaked sample had become noticeably brown in areas. The time it takes for the patches to dry could be increased to allow for longer diffusion times into the wood by keeping the wood in a damp environment such as in a plastic bag, but previous experiments by Sandström showed this often led to mould growth so was not carried out here.[33] Both the patches and wood were analysed using S and Fe K-edge XANES, FTIR, Raman and portable XRF spectroscopy.

S and Fe K-edge XANES spectra were collected of the patches and wood in fluorescence mode using the B18 beamline at Diamond Light Source, Didcot, UK. The spectra were averaged, calibrated, and normalised before the linear combination analysis was carried out in the in the Athena program. The S K-edge XANES of the standards were measured at the Stanford Synchrotron Radiation Laboratory, California, USA. The Fe K-edge XANES standards were obtained from the Canadian Light Source, Saskatchewan, Canada.

The $SrCO_3$-cellulose patches (after having been used to treat the oak samples) were ground with a pestle and mortar until homogeneous and then pressed into pellets (7 mm in diameter) of known weights between 50-70 mg for XRF analysis. The XRF spectrum was measured to obtain quantities of each element detected in mg/g before converting to percentage. XRF data were collected using an X-MET8000 by Oxford Instruments with an X-ray tube of 50 kV and a large area SDD. The FTIR spectra were collected on a Shimadzu IRAffinity-1S with an ATR accessory used over the range 400-4000 cm^{-1}. 32 scans were taken for each sample with a resolution of 4 cm^{-1}. The Raman spectrometer used was a Horiba LabRAM HR. The spectra were measured using the 532 nm (visible) laser with an aperture of 200 µm over a range of

50 – 3000 cm^{-1}. For the Raman spectra of SrCO$_3$, 100% of the laser power was used and 5 scans were taken, each measured for 6 seconds due to saturation if a longer timescale was used. The cellulose and SrCO$_3$-cellulose patches were each measured using 1% laser power with a total of 3 scans, each 300 s in duration.

2.8.4 Fibre characterisation

Reference samples include viscose (to test pol-ATR-FTIR method), modern linen and soiled linen 1800s all from the Centre of Textile Conservation at the University of Glasgow. The Flax 1851 (*Linum utitatissimum L*.) sample is from Royal Botanic Gardens, Kew, reference collection from the International Exhibition, Portugal. The Hemp 1910 (*Cannabis sativa L*.) sample is also from the Royal Botanic Gardens, Kew reference collection but from the Japan Exhibition in 1910.

The *Mary Rose* samples include anchor rope, sail cloth, leather shoe, leather fragments, and wool. The anchor cable sample was from fragments and as such has no artefact number. Initial XRF results identified mainly Cl, Fe, S, Si and Ca with greater count of Fe from more frayed areas. The sail cloth sample is part of the MR81 A2603/9 artefact. Cl, Ca, S, Si, Fe and Al were mainly identified in preliminary XRF experiments. The leather fragment, like the anchor cable fragments, have no artefact number. S, Fe, Ca, Si, Pb, Cu, As and Cl were mainly identified by XRF in the sample. The leather shoe sample from artefact MR83 A486 is specified as leather (bovine) on the artefact card. It is identified as a leather shoe with iron concretion. Fe, S, Ca, Si, Zn, and Cu were mainly identified by XRF. The wool analysed here is from the MR81 A4124 artefact. This wool was attached to what looked like encrusted sail cloth. Fe, S, Ca, Si, and Al were mainly identified by XRF. The elements identified by XRF in the *Mary Rose* samples are consistent with expected contaminants from a marine environment.

Fibre samples were all photographed with a colour match card and scale. They were then studied using the portable Dino-Lite digital microscope, useful in the conservation field as it can be taken to a site of interest. They can connect to a laptop via USB and thus are very portable. Small samples were taken from the main body of the sample from easily accessible areas so as not to cause too much damage. Samples were taken for optical microscopy, FTIR spectroscopy, and SEM.

The FTIR spectrometer used was a Perkin Elmer Spectrum One with a Universal ATR stage. 32 scans were taken for each spectrum with a resolution of 4 cm^{-1}. For polarised ATR-FTIR experiments, the polarisation filter was set to 0 and the filter was fully inserted into the beam path to the left of the ATR stage. A bespoke degree overlay was placed on top of the stage to make it easier to orient the fibre to a precise angle. A single fibre (if possible) was laid in the metal holder over the ATR crystal, inside the degree overlay. Using the tapered tip, a consistent pressure of approximately 50 was applied to every sample to maintain good contact between the sample and the ATR crystal. Spectra were measured at angles from 0 to 180˚ in 7.5˚ intervals (this is because the sense of wind in bast fibres relative to the fibre axis is usually 7.5˚). The spectra were measured in a random order to avoid systematic effects due to the degradation of the fibre from the ATR tip (due to the pressure applied). Spectra were collected at random angles until a complete set was collected. This was repeated twice more on different fibres from the same sample (this should improve reliability and reduce systematic errors). To test whether the method is effective, high-tenacity viscose fibres were measured, as all the polymer chains should be aligned with the fibre axis due to the extrusion process. Once this method was proven effective for the viscose and modern linen fibres, and crystallinity index was calculated, historic fibre samples were tested to compare with the *Mary Rose* samples.

SEM of the fibres was conducted using the Inspect F50 microscope. Fibres were gold coated with a Quorum Q150T ES coater with a thickness of approximately 7 nm. The images were taken with an accelerating voltage of 5 kV and a spot size of 3.5 with a working distance of approximately 10 mm.

References

1   M. R. Derrick, D. Stulik and J. M. Landry, *Scientific Tools for Conservation: Infrared Spectroscopy in Conservation Science*, 1999.

2   P. Garside and P. Wyeth, Identification of Cellulosic Fibres by FTIR Spectroscopy, *Stud. Conserv.*, 2003, **48**, 269–275.

3   K. Kavkler, N. Gunde-Cimerman, P. Zalar and A. Demšar, FTIR spectroscopy of biodegraded historical textiles, *Polym. Degrad. Stab.*, 2011, **96**, 574–580.

4   P. Garside, University of Southampton, 2002.

5   K. Kavkler, Z. Smit, D. Jezersek, D. Eichert and A. Demsar, Investigation of biodeteriorated historical textiles by conventional and synchrotron radiation FTIR spectroscopy, *Polym. Degrad. Stab.*, 2011, **96**, 1081–1086.

6   V. Raditoiu, I. E. Chican, A. Raditoiu, I. Fierascu, R. C. Fierascu and P. Fotea, in *VR Technologies in Cultural Heritage*, eds. D. M., C. M., G. M. and T. I., Springer, Cham, 2019, pp. 3–9.

7   P. Garside and P. Wyeth, Identification of Cellulosic Fibres by FTIR Spectroscopy: Differentiation of Flax and Hemp by Polarized ATR FTIR, 2006, **51**, 205–211.

8   P. Garside and P. Wyeth, Polarised ATR-FTIR characterisation of cellulosic fibres in relation to historic artefacts, *Restaurator*, 2004, **25**, 249–259.

9   P. Garside, S. Lahlil and P. Wyeth, Characterization of historic silk by polarized attenuated total reflectance fourier transform infrared spectroscopy for informed conservation, *Appl. Spectrosc.*, 2005, **59**, 1242–1247.

10   Investigating Polymer Orientation with FTIR-ATR - ProQuest, https://search-proquest-com.sheffield.idm.oclc.org/docview/1505018918?rfr_id=info%3Axri%2Fsid%3Aprimo, (accessed 9 March 2020).

11   P. Garside and P. Wyeth, Use of polarized spectroscopy as a tool for examining the microstructure of cellulosic textile fibers, *Appl. Spectrosc.*, 2007, **61**, 523–529.

12   P. Atkins and J. De Paula, *Physical Chemistry*, Oxford University Press, Oxford, 9th edn., 2010.

13   G. M. do Nascimento, *Introductory Chapter: The Multiple Applications of Raman*

Spectroscopy, Raman Spectroscopy, InTechOpen, 2018.

14   J. R. Ferraro, K. Nakamoto and C. W. Brown, *Introductory Raman Spectroscopy*, Elsevier Science and Technology, 2nd edn., 2003.

15   H. G. M. Edwards, M. G. Sibley, B. Derham and C. P. Heron, Raman spectroscopy of archaeological samples from the Barber-Surgeon's medicine chest on theMary Rose, *J. Raman Spectrosc.*, 2004, **35**, 746–753.

16   P. Vandenabeele, H. G. M. Edwards and L. Moens, A decade of Raman spectroscopy in art and archeology, *Chem. Rev.*, 2007, **107**, 675–686.

17   K. Kavkler and A. Demšar, Examination of cellulose textile fibres in historical objects by micro-Raman spectroscopy, *Spectrochim. Acta - Part A Mol. Biomol. Spectrosc.*, 2011, **78**, 740–746.

18   F. Bianchi, N. Riboni, V. Trolla, G. Furlan, G. Avantaggiato, G. Iacobellis and M. Careri, Differentiation of aged fibers by Raman spectroscopy and multivariate data analysis, *Talanta*, 2016, **154**, 467–473.

19   P. Buzzini and G. Massonnet, The Discrimination of Colored Acrylic, Cotton, and Wool Textile Fibers Using Micro-Raman Spectroscopy. Part 1: In situ Detection and Characterization of Dyes, *J. Forensic Sci.*, 2013, **58**, 1593–1600.

20   R. K. Nayak, R. Padhye and S. Fergusson, Identification of natural textile fibres, *Handb. Nat. Fibres*, 2012, 314–344.

21   M. Kaliva and M. Vamvakaki, in *Polymer science and nanotechnology*, ed. R. Narain, Elsevier, 2020, pp. 401–433.

22   P. J. Potts and M. West, Eds., *Portable X-ray Fluorescence Spectrometry: Capabilities for In Situ Analysis*, RSC Publishing, Cambridge, UK, 2008.

23   E. Margui and R. Van Grieken, *X-ray Fluorescence Spectrometry and Related Techniques: An Introduction*, Momentum Press, 1st edn., 2013.

24   G. Bunker, *Introduction to XAFS*, Cambridge University Press, Cambridge, 2010.

25   P. Willmott, *An Introduction to Synchrotron Radiation : Techniques and Applications*, John Wiley & Sons, 2011.

26   K. Kvashnina, *Resonant Inelastic X-ray Scattering of Rare-Earth and Copper Systems*,

2007.

27   J. A. Bearden and A. F. Burr, Reevaluation of X-Ray Atomic Energy Levels, *Rev. Mod. Phys.*

28   S. Calvin, *XAFS for Everyone*, CRC Press, Boca Raton, FL, 2013.

29   B. Ravel, A practical introduction to multiple scattering theory, *J. Alloys Compd.*, 2005, **401**, 118–126.

30   B. Ravel, X-ray Absorption Spectroscopy, http://bruceravel.github.io/demeter/#docs.

31   D. B. Murphy and M. W. Davidson, *Fundamentals of Light Microscopy and Electronic Imaging*, John Wiley & Sons, 2nd edn., 2012.

32   H. Jahangiri, M. Ranjbar, M. A. Taher and H. kazerooni, Using microwave heating for synthesis of SrCO3 nanostructures with different morphologies, *J. Ind. Eng. Chem.*, 2015, **21**, 1132–1136.

33   J. Sandström and E. J. Schofield, in *Proceedings of the 13th ICOM-CC group on wet organic archaeological materials conference*, eds. E. Williams and E. Hocker, Florence, 2016, pp. 249–255.

Chapter 3: SrCO₃ Nanoparticle Treatments for *Mary Rose* Timbers

3.1 General Introduction

This chapter presents the analysis of the effectiveness of a $SrCO_3$ cellulose-based nanoparticle treatment applied to test oak, chosen to mimic *Mary Rose* wood. $SrCO_3$ was incorporated into a cellulose patch and after treatment both the wood before and after treatment and the patch after treatment were analysed with XANES, FTIR, and Raman spectroscopy. The results of which are presented in section 3.1. Section 3.2 discusses the characterisation of $SrCO_3$ samples synthesised by various methods with a view to incorporating these into a cellulose-based conservation treatment for waterlogged wood.

Alkaline earth-based nanoparticles have shown particular promise for the deacidification of cellulose-based heritage materials.[1,2] Calcium and magnesium hydroxide nanoparticles are good acid neutralising agents, used predominantly in the conservation of paper.[3] Once the alkaline earth hydroxide nanoparticles have absorbed to the fibres in wood, they release hydroxyls as the non-aqueous solvent evaporates to neutralise any acidity.[4] Calcium and magnesium hydroxide nanoparticles can react with sulfuric acid to produce the more stable alkaline earth sulfate and water. Oxidation of cellulose is catalysed by free iron ions and increasing the pH reduces the catalytic activity of the metal ions, breaking the cycle of cellulose degradation.[5,6] Upon reaction with atmospheric carbon dioxide, the hydroxide nanoparticles can convert to the carbonate to act as an alkaline reserve, preventing future pH increases.[2,3] Quantifying this behaviour, however, is challenging as the *Mary Rose* timbers contain significant quantities of calcium and magnesium salts (for example, possibly gypsum ($CaSO_4.2H_2O$), calcite ($CaSO_4$), $MgSO_4$, calcium and magnesium chlorides) through marine exposure, which makes distinguishing these natural sources from nanoparticle treatments difficult using traditional characterisation methods (e.g. X-ray absorption spectroscopy, XAS).[7] To combat this problem, $SrCO_3$ nanoparticles were first proposed as a deacidification treatment for the *Mary Rose* by Schofield *et al.*[7] Alkaline earth hydroxide nanoparticles were considered but their longer and more expensive preparation meant they were less suitable than $SrCO_3$ nanoparticles in this instance. With an alkaline earth hydroxide nanoparticle treatment, there is also a possibility of alkali-catalysed cellulose degradation if large concentrations are uncontrollably added, they also convert to the carbonate eventually,

making $SrCO_3$ a more practical solution for larger scale use.[8] Being a weak base, $SrCO_3$ can potentially neutralise sulfuric acid to prevent immediate degradation of the wood. Additionally, the high affinity of Sr^{2+} ions for sulfate ions means $SrCO_3$ nanoparticles may react with reduced sulfur compounds in the wood to form $SrSO_4$, which is inert and insoluble in water.[7] Any unreacted $SrCO_3$ left in the wood after treatment could advantageously act as an alkaline reservoir to neutralise acidity and to sequester further sulfates in the future, helping to prevent long-term degradation.[7]

3.2 SrCO₃ Cellulose Patch Treatment

Preserving waterlogged marine archaeological wood presents a series of challenges, one of which is the major degradation pathways caused by sulfur species, where reduced sulfur compounds oxidise upon raising the ship to form sulfate salts and sulfuric acid.[3] Sulfuric acid is a key problem as it hydrolyses cellulose, leading to the eventual breakdown of the wood structure. This process is further catalysed by iron, which is readily available through degradation of ship fixtures and other artefacts.[9]

Given the cultural importance of such artefacts, there is an urgent requirement for selective treatments to resolve this sulfur problem and provide targeted methodologies for preserving the *Mary Rose* artefacts. Achieving this requires detailed information on the effect of specific treatments on the underlying wood. To date, a number of routes have been considered, including polymers for consolidation of the wood;[10] iron ion removal through the activity of chelating ligands;[11,12] biological treatments for potentially harmful ion removal,[13] and the application of nanoparticles for deacidification and stabilisation of iron and sulfur compounds (for example, in the case of alkaline-earth hydroxide nanoparticles on Swedish warship the *Vasa*).[3,4,14–16] The latter nano-based treatments are of particular interest as their small size allows for easy penetration into the waterlogged wood structure and their large surface area-to-volume ratio affords greater interactions for neutralising sulfuric acid and reacting with iron and sulfur compounds.

$SrCO_3$ nanoparticles have previously been suggested as a treatment to de-acidify the wood. The application of $SrCO_3$ in solution by spraying or brushing onto small wooden artefacts recovered from the *Mary Rose* in the literature has demonstrated that the treatment has potential and that the presence of PEG does not affect the reactivity of the $SrCO_3$.[17,18] However, these treatment applications require cycling between wet and dry states, which

may cause stress to the underlying wood.[18] It is vital therefore that development of more appropriate methodologies is continued for the application of nanoparticle-based treatments to degraded waterlogged wood. A suggested improvement upon soaking artefacts in $SrCO_3$ solution is by introducing the alkaline earth treatment in a cellulose patch. The use of a cellulose patch to introduce $SrCO_3$ is advantageous as it reduces unnecessary stresses from cycling the wood samples through wet and dry periods. Another advantage of patches is the ability to treat artefacts *in-situ* with multiple applications where necessary. It can also be used on specific problem areas where treatment is needed quickly and without needing to immerse the artefact or remove it from display.

Previous conservation work in application of alkaline-earth carbonates to wood using a cellulose poultice highlighted the practical use of this treatment and that it was working in a qualitative manner with SEM-EDX. The SEM-EDX of the treated wood showed strontium had accumulated on the surface of the wood and there was some evidence of penetration through the wood up to a depth of 1 mm depending on the wood structure.[19] Moreover, it was observed that strontium often occurred where sulfur was also found in the sample.[19] pH measurements in previous work also showed an increase in pH on the surface of the wood after treatment.[19] Colour changes of the cellulose-$SrCO_3$ patches from white to brown during treatment were noted, which are also observed throughout this work. This colour change could be due to iron compounds being removed from the wood in the patches, which the XANES experiments aimed to clarify.

This prior work is further expanded here by demonstrating quantitatively the treatment of test samples of iron sulfate-soaked oak (representing a model system for *Mary Rose* wood) with $SrCO_3$ nanoparticles embedded in a cellulose patch and has shown that this patch can neutralise acid formation and react with iron- and sulfur-containing compounds that are the main causes of wood degradation. A comprehensive characterisation approach using S and Fe K-edge XANES, FTIR, Raman, and XRF spectroscopic techniques has been used to assess reactivity of iron and sulfur compounds with the $SrCO_3$ treatment. XANES analysis of the nanoparticle-based $SrCO_3$ treatment has allowed the study of both the sulfur and iron K-edges, including quantitative analysis by LCF. Through LCF of the XANES spectra, identification and quantification of the iron and sulfur compounds present in the wood and the $SrCO_3$-cellulose patches is possible.

3.2.1 Patch Treatment of Benchmark-Oak (BM-Oak)

Benchmark-oak blocks were sourced from trees in the Portsmouth area, as roughly 1 cm^3 blocks (referred throughout as "BM-Oak"). As a control experiment, a $SrCO_3$-cellulose patch was applied to this BM-Oak, left for 24 hours, then removed. After treatment with the patch, the oak sample is then referred to as "BM-Oak-Treated". To approximately model oak from the *Mary Rose*, where the main problems are iron and sulfur-based compounds, BM-Oak cubes were soaked in $Fe_2(SO_4)_3$ solution for 1 month then left to dry. The resulting sample is referred to throughout as "Fe-Oak". A $SrCO_3$-cellulose patch was applied to the sides of the Fe-Oak sample and left for 24 hours. The patch was then removed resulting in two samples: "Fe-Oak-Treated" and "Patch-Post-Treatment". A schematic depicting these samples and treatments is displayed in Figure 22. In the following section, the results for wood soaked in Fe(III) sulfate solution are presented. However, complementary experiments were also carried out on oak samples soaked in Fe(II) sulfate solution and the LCF results are presented in the appendix (Figures 61 and 62). The graphs of the fits for the Fe(II) sulfate soaked samples are included in the appendix for clarity but a summary of the results of the fitting is included in Tables 1 and 2 for comparison purposes.

XANES data were collected on the wood samples and the $SrCO_3$-cellulose patches to test the effectiveness of the patches in the removal of iron and sulfur compounds from the test wood samples. The S K-edge and Fe K-edge data collected in this work have been averaged from three scans of the same sample and normalised using the Athena program. LCF was carried out on the data to establish the composition of each spectrum by fitting spectra of known standards to the sample data. The goodness of fit depends on how well the data are calibrated, aligned, normalised, and which standards are selected for each sample.[20]
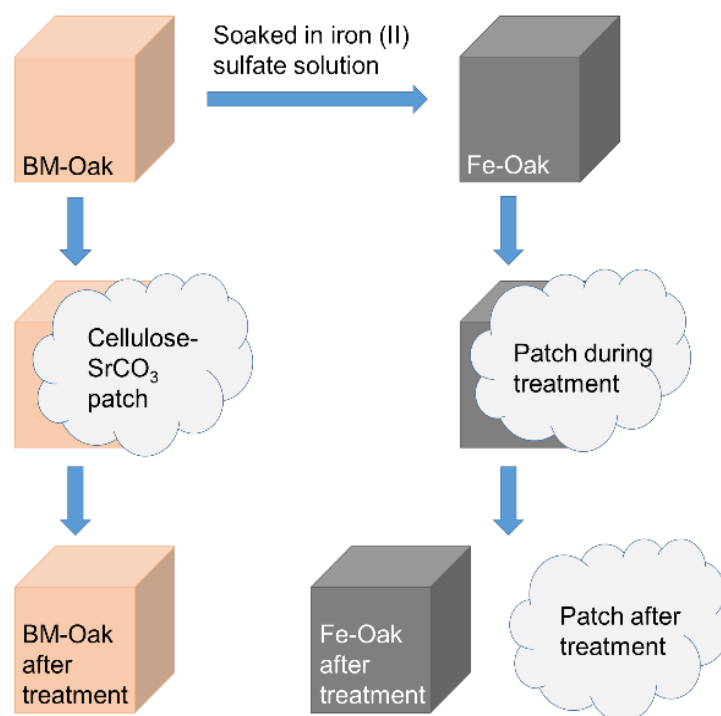
Figure 22 Schematic showing the different samples acquired during the SrCO₃-cellulose patch treatment of test oak samples.

Before assessing iron and sulfur removal from Fe-Oak samples, it is first necessary to investigate any effect the SrCO₃ nanoparticles have on the BM-Oak, *i.e.* before iron sulfate is introduced. To do this, XANES experiments were performed on the BM-Oak to establish the presence of any sulfur species which naturally occur in oak. The S K-edge spectra of BM-Oak before and after treatment with the SrCO₃-cellulose patch are compared in Figure 23 (Fe K-edge spectra are presented in the appendix, Figure 58(b)). By simply observing the S K-edge XANES spectrum of BM-Oak, it is clear a variety of sulfur oxidation states are naturally present in oak which is expected for natural wood. For example, lower sulfur oxidation states are likely due to the presence of naturally occurring amino acids. Sulfur in plants may also be introduced *via* the exposure to sulfur-containing fertiliser and organic sulfur compounds from surrounding decaying organic matter.[21] Although only significant in polluted areas, leaves can absorb sulfur dioxide from the atmosphere.[21] Moreover, roots can absorb sulfur compounds such as sulfites, sulfides, and sulfates which are involved in important biochemical processes within the plant.[21]

The presence of various sulfur oxidation states and their coordination environments are confirmed from LCF. In this analysis, a linear combination of spectra of standard compounds are fitted to the sample spectrum of interest providing a quantitative description of the sample spectra. However, a judgement of which standards to include in the fit is required. This is based on the current chemical knowledge of the sample and so quantities obtained from LCF should be critically evaluated.[20] From work studying sulfur evolution in *Mary Rose* wood by XANES, a database of standards has been collected.[9,20,22,23] For the BM-Oak samples, the following standards have been used in the fit: cysteine ($HO_2CCH(NH_2)CH_2SH$, abbreviated to R-SH), cystine ($(SCH_2CH(NH_2)CO_2H)_2$, abbreviated to R-S-S-R), methionine sulfoxide ($CH_3S(O)CH_2CH_2CH(NH_2)CO_2H$, abbreviated to R-SO-R), sulfonate ($HS(=O)_2(O^-)$, abbreviated to R-SO$_3^-$), and natrojarosite ($NaFe_3(SO_4)_2(OH)_6$ abbreviated to $(SO_4)^{2-}$). These standards represent a range of sulfur oxidation states (from -2 to +6) and were chosen as they are most likely to occur naturally in oak. Given the complexity of the wood structure, it is likely that other compounds are not accounted for in the LCF and for this reason there are some discrepancies between the fit and the residual obtained (orange and blue lines in Figure 23, respectively).
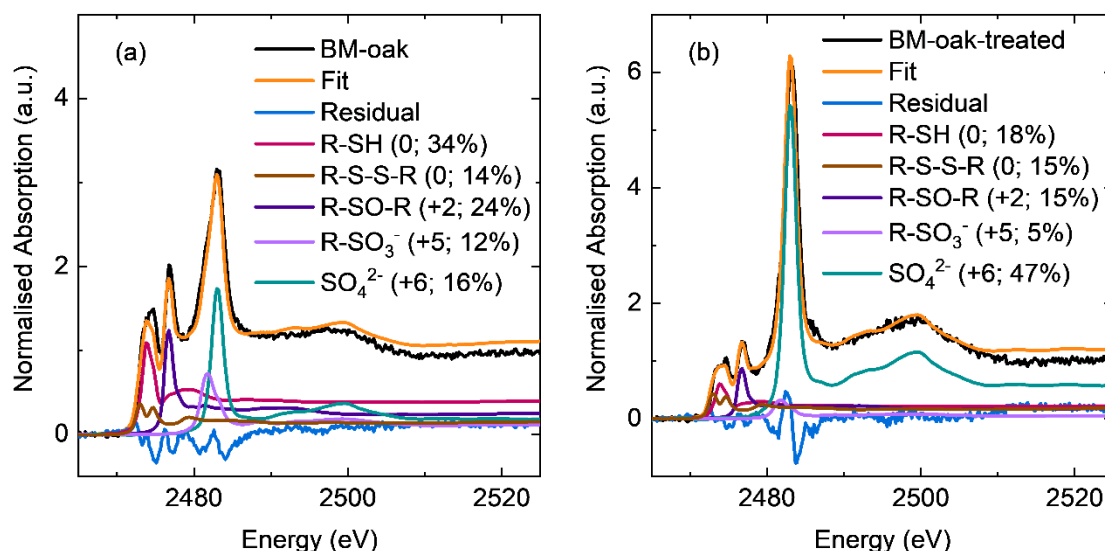
Figure 23 LCF of BM-Oak at the S K-edge XANES spectra **(a)** before and **(b)** after treatment with the SrCO$_3$-cellulose patch. In brackets are the sulfur oxidation states of each standard and the relative amount of each standard present in the normalised sample spectrum.

Table 1 Summary of results from LCF analysis of S K-edge XANES spectra of BM-Oak and BM-Oak-treated samples.

Standard	BM-Oak %	Error	BM-Oak-treated %	Error
R-SH	34.55	2.50	17.74	3.22
R-S-S-R	13.66	2.59	15.02	3.30
R-SO-R	23.66	0.89	15.43	1.16
R-SO$_3^-$	11.88	0.89	4.87	1.07
SO$_4^{2-}$	16.25	0.54	46.95	0.66

After treating the BM-Oak sample with the SrCO$_3$-cellulose patch, the feature representing the oxidised +6 sulfur species at 2483 eV appears to increase in intensity (see appendix, Figure 58(a)). LCF analysis of the BM-Oak and BM-Oak-treated samples is displayed graphically in Figure 23 and the results are summarised with corresponding errors in Table 1. These results show this intensity change corresponds to an increase in the contribution from oxidised sulfur species (from approximately 16% to 47% after treatment). Correspondingly, the contribution of reduced sulfur species is decreased after the patch treatment. This indicates that the SrCO$_3$ nanoparticles are reacting with naturally occurring reduced sulfur species in the wood such as R-SH to produce SrSO$_4$ (i.e. sulfur in a +6 oxidation state). The Fe K-edge XANES spectra for BM-Oak before and after treatment with the SrCO$_3$-cellulose patch also reveal naturally occurring iron species in the wood, such as iron-complexed tannins which are prominent in oak (appendix, Figure 58(b)).[24,25] Figure 58(b) of the appendix further illustrates that the SrCO$_3$-cellulose patch treatment does not appear to affect this natural iron speciation.

3.2.2 Soaking BM-Oak in Iron Sulfate Solution

To mimic *Mary Rose* wood, oak blocks were soaked in iron (III) sulfate solution to model the artefact timber conditions. S K-edge and Fe K-edge XANES were measured on the wood before and after cellulose patch treatment, described as Fe-Oak and Fe-Oak-treated, respectively. Similar measurements were made on the cellulose patch post-treatment, labelled "Patch-Post-Treatment". Inspection of the S K-edge XANES spectrum of Fe-Oak confirms the presence of sulfate species, when compared with FeSO$_4$ and Fe$_2$(SO$_4$)$_3$ standards, i.e. sulfur in

oxidation state +6 (Figure 59(a) in the appendix). This incorporation of iron sulfate into the wood is also visually apparent, with a colour-change of the oak cube from light brown to dark blue-black noted after iron sulfate soaking.

The linear combination fit in Figure 24(a) to the S K-edge reveals that the Fe-Oak sample contains sulfur in a similar environment to both Fe(II) and Fe(III) sulfate, but with a much greater contribution from Fe(II)SO_4 (80% compared with 20% in an environment like $Fe_2(SO_4)_3$). With S K-edge XANES spectra, sulfur is the absorbing atom and has the same oxidation state in both $FeSO_4$ and $Fe_2(SO_4)_3$. The edge energy does not differ significantly between these standards, making it challenging to evaluate the S K-edge XANES data for this sample in detail and to distinguish between these two iron sulfate standards. There are, however, subtle differences between the S K-edge XANES spectra of the $FeSO_4$ and $Fe_2(SO_4)_3$ standards, mainly in the pre-edge region due to the different geometry surrounding the sulfur atom, and in the region after the absorption edge due to long-range multiple scattering effects which are unique to each complex and dependent on the different cation in each standard.[26] There may also be issues due to self-absorption. Self-absorption can be corrected for but only if the composition of the sample is known, which is not possible for these samples. The matter is further complicated when observing S K-edge spectrum of the Fe-Oak sample alongside the $FeSO_4$ and $Fe_2(SO_4)_3$ standard spectra (Appendix Figure 59(a)), because the differences in intensity of the white lines between the standards mean that the $FeSO_4$ standard fits the sample spectrum better than the $Fe_2(SO_4)_3$ standard because the edge intensity matches that of the Fe-Oak sample spectrum better. This would mean the results from the fit would more likely favour the presence of $FeSO_4$ in the oak even though these samples were soaked in $Fe_2(SO_4)_3$. To further understand this sample, Fe K-edge XANES data on the Fe-Oak sample have been analysed in Figure 24(b).
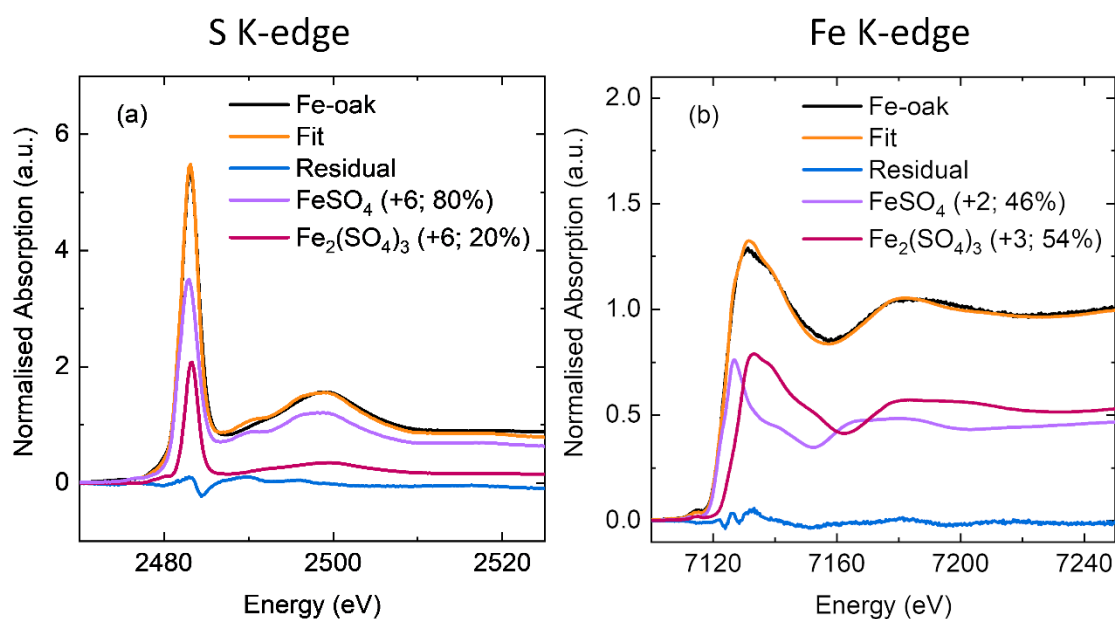
Figure 24 LCF analysis of **(a)** the S K-edge data of the $Fe_2(SO_4)_3$ soaked oak sample (Fe-Oak) before treatment, including spectra for standards used in the fit and their relative percentages obtained from the fit and **(b)** the Fe K-edge of Fe-Oak before treatment.

Fe K-edge XANES results provide information on the iron oxidation state in the wood. Qualitative fingerprinting shows that the iron in the Fe-Oak XANES spectrum is in an environment more similar to that of Fe(III) sulfate than Fe(II) sulfate, although the edge energy of the Fe-Oak sample is closer to that of the $FeCO_3$ standard, indicating that the Fe-Oak sample includes a mixture of iron compounds (Appendix Figure 59(b)). The pre-edge feature in the Fe-Oak sample spectrum is more intense than the pre-edge observed in the $FeSO_4$ and $Fe_2(SO_4)_3$ standard spectra (this is highlighted in the appendix, Figure 59(b)). This is likely a result of the iron complexes in the sample being less centrosymmetric than these standards due to 3d-4p mixing allowed by a distorted octahedral geometry.[27] Also, the pre-edge feature in the Fe-Oak spectrum is shifted to a higher energy than that of $FeSO_4$ standard spectrum and is closer to that of the $Fe_2(SO_4)_3$ spectrum.

LCF analysis (Figure 24(b)), reveals a slightly larger contribution of iron in the +3 oxidation state to the fitted Fe K-edge spectrum. Interestingly, this somewhat contradicts the S K-edge XANES results in Figure 24(a). Nevertheless, the Fe K-edge results are more reliable due to the larger difference in edge energy between the different iron oxidation states, making it easier to distinguish between the standards. Also, the white line intensities of the Fe K-edge spectra

were more similar between the standards and the samples than when studying the S K-edge spectra, making the Fe K-edge LCF results a more reliable indicator of iron speciation in the samples.

There is an appreciable contribution from the FeSO$_4$ standard in the LCF of the Fe-Oak sample spectrum which could indicate that the reality of Fe compounds present in the wood is more complex than being mainly present as Fe$_2$(SO$_4$)$_3$ (although this was expected to be the majority due to soaking the wood in Fe$_2$(SO$_4$)$_3$ solution). Especially since qualitative fingerprinting hints that the Fe-Oak sample spectrum compares well to the FeCO$_3$ standard spectrum (Appendix Figure 59(b)). It is possible that there are iron compounds present in the wood that have not been accounted for in the fits, for example iron hydroxides and iron tannate complexes. This is likely since Fe K-edge XANES data of BM-Oak (Appendix Figure 58(b)) showed there were iron compounds already in the wood before it was soaked in Fe$_2$(SO$_4$)$_3$ solution. Further work would be needed to collect more iron standards for comparison to these sample spectra to establish a clearer idea of iron speciation in the BM-Oak and Fe-Oak samples.

3.2.3 Patch Treatment of Iron Soaked Oak

The S K-edge XANES spectrum for Fe-Oak-treated with the SrCO$_3$-cellulose patch, shown in Figure 25(a), displays distinct features in the post-edge region which compares well with the strontium sulfate standard spectrum. Sulfur has the same oxidation state in FeSO$_4$, Fe$_2$(SO$_4$)$_3$, and SrSO$_4$ standards so the absorption edge occurs at a very similar energy. However, SrSO$_4$ has a very characteristic post-edge region (as can be observed in Appendix Figure 60(a)) due to multiple scattering effects, making the spectra differ significantly in this region from that of the FeSO$_4$ and Fe$_2$(SO$_4$)$_3$ spectra. This qualitatively demonstrates that the SrCO$_3$ treatment has reacted with iron sulfate to produce SrSO$_4$, which has remained in the wood. The SrCO$_3$-cellulose patch-post-treatment (Figure 25(b)) displays the same profile as the Fe-Oak-treated sample, suggesting that some of the SrSO$_4$ is being removed or retained by the SrCO$_3$-cellulose patch after treatment.

The LCF results on the S K-edge for the Fe-Oak-treated with the SrCO$_3$-cellulose patch in Figure 25(a) reveal that SrSO$_4$ (43%) and FeSO$_4$ (57%) are representative of the main sulfur-containing constituents in the XANES spectrum of the wood after treatment. This indicates that unreacted iron sulfate remains in the wood after the patch treatment. LCF analysis on

the S K-edge of the patch post-treatment, Figure 25(b), indicates that the patch is likely to contain sulfur in two different local environments: $SrSO_4$ (65%) and $FeSO_4$ (35%). This provides evidence for the efficacy of the treatment, as it reveals the patch has removed sulfate (as well as iron) ions from the wood.

The Fe K-edge spectra of the Fe-Oak-treated sample and the $SrCO_3$-cellulose patch after removal both have a very similar profile to that of the $FeCO_3$ standard (see appendix, Figure 60(b)). The main discrepancy is that the absorption edge in the patch-post-treatment sample is lower in intensity than that of the Fe-Oak-treated spectrum. Figure 25(c) shows that the Fe-Oak-treated is very similar to the Fe-Oak before treatment in terms of iron speciation, where the largest contribution is from iron in the +3 oxidation state. Figure 25(d) shows the LCF data for the patch after treatment. This analysis demonstrates that the patch is likely comprised of iron in a local environment resembling that of $FeCO_3$ and some unreacted iron remaining as $Fe_2(SO_4)_3$. This indicates that the $SrCO_3$-cellulose patch is not only reacting with the iron sulfate in the soaked wood but is also removing iron in a +2 and +3 oxidation state from the wood, complementing the S K-edge XANES results, which also indicates that iron sulfate is being removed by the patch. These are very promising results for the development of $SrCO_3$-cellulose patches as a conservation treatment for marine archaeological artefacts where iron and sulfur compounds are a major concern.
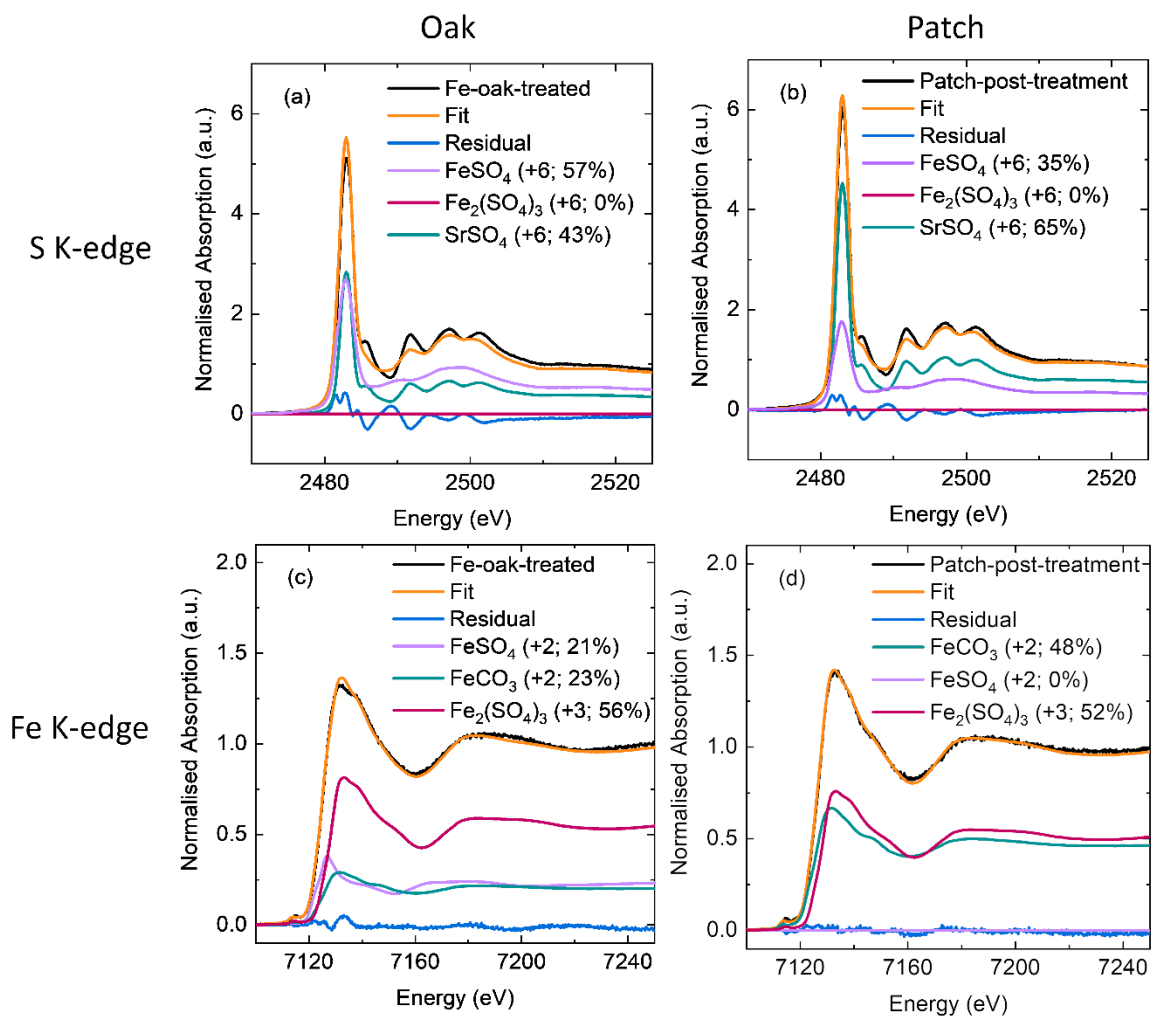
Figure 25 LCF of S K-edge XANES spectra of **(a)** iron sulfate-soaked wood after treatment with the SrCO₃-cellulose patch and **(b)** the SrCO₃-cellulose patch after it has been applied as a treatment to the wood. LCF analysis of Fe K-edge XANES data of **(c)** iron sulfate-soaked wood after SrCO₃-cellulose patch treatment and **(d)** the SrCO₃-cellulose patch after it had been removed from the soaked wood.

Table 2 Summary of results from LCF of the S and Fe K-edge XANES spectra for both Fe(II) and Fe(III) sulfate soaked samples

Samples		Fe(II)		Fe(III)			Fe(II)		Fe(III)	
	S Standards	S K-edge (%)	Error	S K-edge (%)	Error	Fe Standards	Fe K-edge (%)	Error	Fe K-edge (%)	Error
Fe-Oak	$FeSO_4$	71.89	0.69	80.19	0.72	$FeSO_4$	28.70	0.72	46.12	0.40
	$Fe_2(SO_4)_3$	28.11	0.49	19.81	0.36	$Fe_2(SO_4)_3$	71.30	0.72	53.88	0.40
Fe-Oak treated	$FeSO_4$	49.56	1.77	56.69	2.76	$FeSO_4$	0.00	2.29	20.69	1.43
	$Fe_2(SO_4)_3$	0.00	1.42	0.00	1.66	$Fe_2(SO_4)_3$	53.28	3.86	56.07	2.55
	$SrSO_4$	50.44	2.04	43.31	3.98	$FeCO_3$	46.72	5.84	23.14	3.77
Patch	$FeSO_4$	30.56	1.69	34.93	1.77	$FeSO_4$	0.00	2.05	0.00	1.33
	$Fe_2(SO_4)_3$	19.44	1.35	0.00	1.04	$Fe_2(SO_4)_3$	46.47	3.48	52.35	2.14
	$SrSO_4$	50.00	1.91	65.07	2.49	$FeCO_3$	53.53	5.22	47.65	3.27

A summary of the data from the LCF of the S K-edge and Fe K-edge XANES of the Fe(II) sulfate and Fe(III) sulfate soaked samples is presented in Table 2 to easily compare the results. The graphs from the LCF of the Fe(II) sulfate soaked samples are presented in the appendix for clarity (Figures 61 and 62). A summary table of the raw data obtained from the LCF analysis is also included in the appendix Table 12. In Table 2 the S K-edge results can be compared to the Fe K-edge results for each sample.

The contradictions between the Fe and S K-edge results with respect to the contributions of the $FeSO_4$ and $Fe_2(SO_4)_3$ standards in the Fe-Oak-treated and Patch-post-treatment sample spectra is likely due to the discrepancy between the absorption edge intensity of the $Fe_2(SO_4)_3$ standard spectrum and that of the S K-edge spectra of the samples (this can be more clearly observed in the appendix Figure 59(a) and 60(a)). This is likely to affect the fit results, favouring the $FeSO_4$ and $SrSO_4$ standards which better match the intensity of the spectra of the samples. The discrepancy between the Fe and S K-edge LCF results could also be due to there not being a large difference in the edge energy between the $FeSO_4$ and $Fe_2(SO_4)_3$ standards in the S K-edge spectra. This makes it difficult to distinguish between these two standards using the S K-edge, making the Fe K-edge a more useful indicator in this respect.

Figure 25(c) and Table 2 show that the $FeSO_4$ standard spectrum contributes to the fit of the Fe K-edge of the Fe(III)-Oak-treated sample spectrum. It is possible that $Fe_2(SO_4)_3$ could be reduced to iron(II) sulfate, for example if another metal was present. Cellulose degradation compounds, tannic and gallic acids present in oak are also known to reduce iron(III) ions so this mechanism could also be considered for these samples.[28] This could explain why, although the oak cubes were soaked in $Fe_2(SO_4)_3$ solution, $FeSO_4$ is contributing to the Fe K-edge XANES spectra of the Fe-Oak and Fe-Oak-treated samples. Another explanation could be that there are Fe and S compounds present in the samples, contributing to their spectra, that have not been accounted for in the fits, for example, iron hydroxides, Fe_2O_3, Fe_3O_4, and iron tannates.

When analysing the patch LCF results, there is fairly good agreement between the Fe(II) and Fe(III) sulfate soaked samples, except in the case of the S K-edge data where the $Fe_2(SO_4)_3$ contributed 19% in the Fe(II)-sulfate-soaked sample spectrum and 0% in the Fe(III)-sulfate-

soaked sample spectrum. However, from the LCF results and simple, qualitative fingerprinting of the SrSO$_4$ standard spectrum, there is a significant contribution of SrSO$_4$ to the patch sample spectra in both the Fe(II) and Fe(III) sulfate soaked samples.

The FTIR spectrum of the Fe-Oak-treated sample (Figure 26(a)) shows that SrCO$_3$ has reacted to form relatively stable SrSO$_4$ as desired, since sulfate vibrational modes are present and correlate with those of SrSO$_4$. This means, however, that the SrCO$_3$-cellulose patch is not removing all the products from the wood after treatment as strontium sulfate remains in the wood. It is more desirable though to have SrSO$_4$ rather than iron sulfate present in the wood as SrSO$_4$ is more stable, chemically inert, and less soluble in water.[26] Any iron that can be removed from the wood in the patches is useful, as iron can act as a catalyst for sulfuric acid production leading to degradation of cellulose. It is difficult to determine how the iron interacts from FTIR data, but Fe K-edge XANES data show that iron is most likely present as FeCO$_3$ and Fe$_2$(SO$_4$)$_3$. No evidence was found of carbonate stretches in the FTIR spectrum of the Fe-Oak-treated sample, suggesting this has been removed by the patch or converted to SrSO$_4$ in the wood. This contradicts the Fe K-edge XANES results which indicates the likely presence of FeCO$_3$ (see Figure 25(d)) in the wood after treatment. It is more likely that the absence of carbonate peaks is due to the inhomogeneous nature of wood, the fact the spectra were taken from different areas of the wood and averaged but only in specific spots each time, and that the evanescent wave of the IR radiation only penetrates the surface up to a certain depth. Also, the quality of the spectra is heavily influenced by the contact of the sample to the ATR crystal, which was difficult to achieve for the wood samples. A map of FTIR spectra from different points over the wood surface and through the wood would be desirable. Alternatively, the wood samples could be ground until homogeneous but with this method there is a risk of contamination.
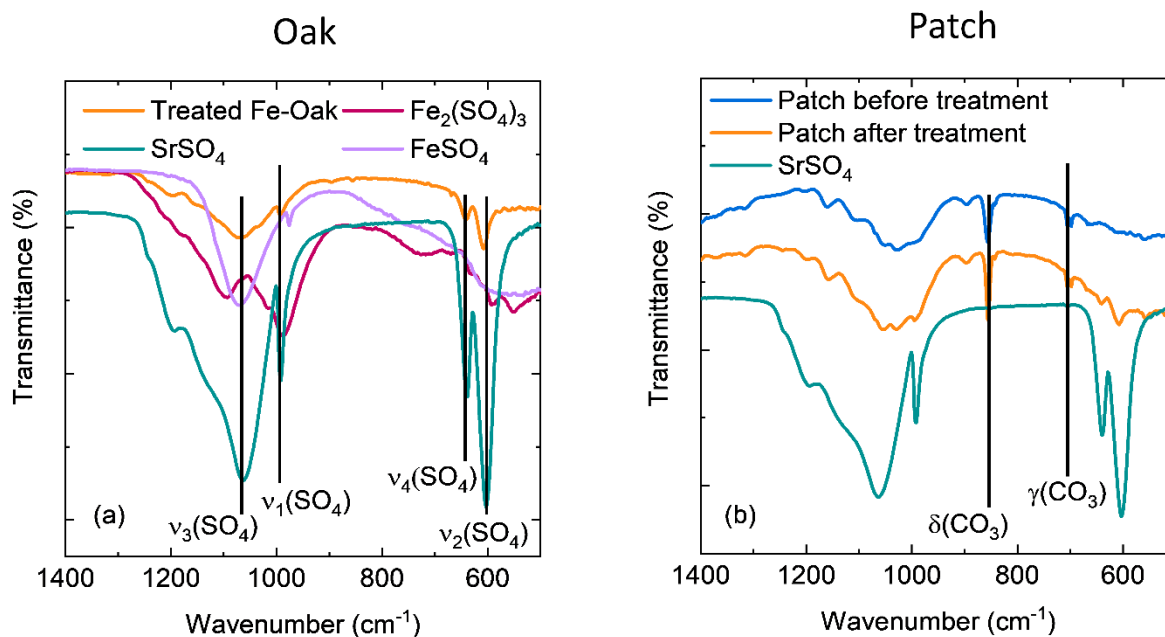
Figure 26 ATR-FTIR spectra of **(a)** Fe-Oak after treatment compared with the spectra of $Fe_2(SO_4)_3$ and $SrSO_4$ standards and **(b)** $SrCO_3$-cellulose patch before and after treatment compared with the $SrSO_4$ standard.

Comparing the FTIR spectra of the $SrCO_3$-cellulose patch before and after application to the Fe-Oak (Figure 26(b)) shows that carbonate bands are still present in the patch after treatment, providing evidence of unreacted $SrCO_3$. There is further evidence of sulfate bands in the patch after treatment, which are not observed before the patch was used for treatment and which correlate with those of $SrSO_4$, showing the patch goes some way in removing sulfates from the wood.

Figure 27(a) shows the Raman spectra of commercial $SrCO_3$ and a cellulose patch without $SrCO_3$. These spectra were measured as standards for comparison with the $SrCO_3$-cellulose patch after it had been used to treat the Fe-Oak (shown in Figure 27(b)). Raman spectroscopy supports both the XANES and FTIR data. It provides further evidence of unreacted $SrCO_3$ in the patch after treatment and sulfate peaks show there is some uptake of sulfate into the patch. There is a challenge with a high fluorescence background when measuring cellulose and lignin-based materials, which means longer timescales are required for each measurement and peaks were still not very well resolved.
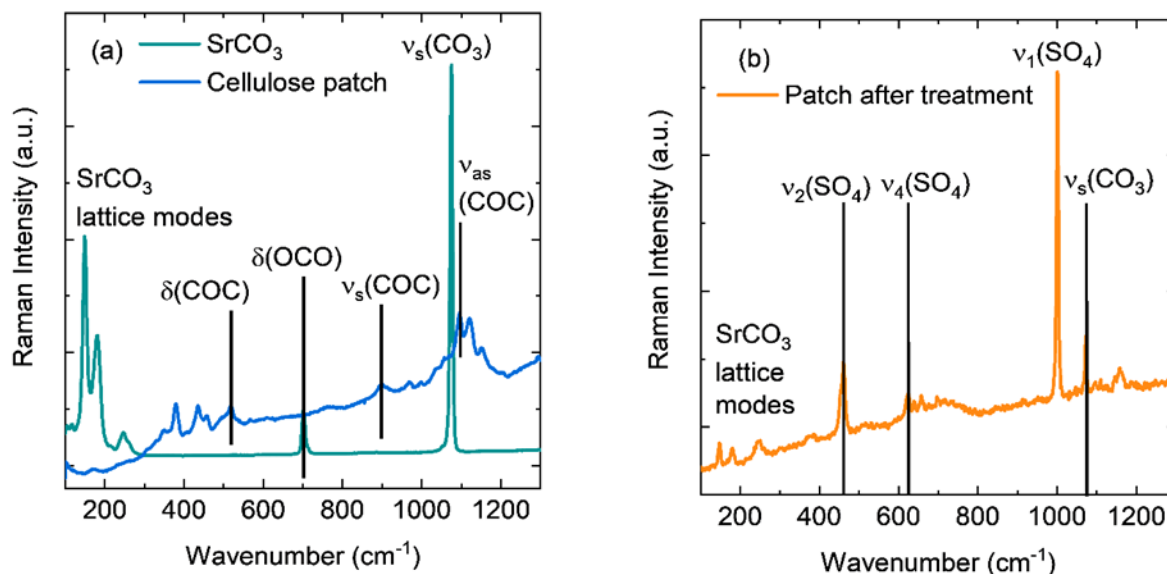
Figure 27 Raman spectra of **(a)** commercial $SrCO_3$ and a patch composed only of α-cellulose and water and **(b)** a $SrCO_3$ cellulose patch after removal from the Fe-Oak sample.

XRF results correlate with the XANES, FTIR, and Raman results to provide evidence for iron and sulfur in the patches after treatment on the Fe-Oak samples. Most of the inorganic components of the patch are comprised of strontium and comparatively small amounts of iron and sulfur were detected as shown in Table 3. Interestingly, more sulfur and iron were detected in the patch used to treat the $Fe_2(SO_4)_3$-soaked wood than the $FeSO_4$ soaked wood. Gold and barium were detected along with other elements in trace amounts, but these could be due to overlap in energy with the elements of interest. The values in Table 3 of the percentage of elements in the patches were converted to percentages from the ppm values from the raw data to mg/g knowing the weight of the pellet, then the mg/g of each element detected out of all elements detected was used to calculate the percentage e.g. 12.35 mg/g of the Fe(III) patch is Sr and all elements detected in that patch came to 13.76 mg/g of patch making Sr approx. 89.70% of all elements detected in the patch.

Table 3 XRF data for the SrCO$_3$-cellulose patches used to treat Fe(II) and Fe(III) sulfate soaked wood samples. Further trace elements were exempt for clarity.

Element	Fe(II) patch (%)	Fe(III) patch (%)
Sr	98.73	89.70
Fe	0.51	2.88
S	0.23	6.83
Au	0.24	0.27
Ba	0.22	0.22

As the XAS data were primarily collected for XANES analysis, study of the EXAFS region is only considered relatively briefly here. The EXAFS region can be used to obtain absorber-scatterer distances and information on the type of coordination environment. The EXAFS region gives an average picture of the absorber (in this case iron) in a heterogeneous material such as wood, making it difficult to model the spectra theoretically as there can be a complex mixture of compounds present.[29] This means that only general conclusions as to the dominance of certain compounds present in the samples can be made. Here, the EXAFS region of the Fe K-edge spectrum of the BM-Oak, BM-Oak-treated, Fe-Oak, Fe-Oak-treated and patch is studied. The fits were undertaken using the first single scattering path. More information and paths can be included in the fit to provide further details, but the analysis was restricted to the first coordination shell due to the reliability of the data and the heterogeneous nature of the samples. In fitting model data to the first coordination shell of the observed data, a more detailed picture of the nearest neighbour structure can be obtained. For example, here, the first scattering path of literature data calculated from Fe$_2$(SO$_4$)$_3$ (reference code from ICSD 4301) is fitted to the Fe K-edge sample spectrum.

Modelling can provide atom-atom distances, although the positions of peaks in the R plots do not correspond to real distances. In Artemis, theoretical EXAFS paths are created from a model, usually starting from the crystallographic information file (CIF). The single and multiple scattering paths are computed using the FEFF program. The model is then refined to fit the sample data. IFEFFIT is a freely available library of XAS algorithms which can be used to evaluate the EXAFS equation.[30] As the crystallographic files are used to calculate the paths for

the fit, there will be some discrepancy if the compounds in the sample are likely to be amorphous, which is another reason for only fitting the first single scattering path. Even if the data is not ideal for this analysis, it is useful to be able to compare the sample data to calculated data from crystallographic files of standards as well as the measured standards used in the XANES fitting.

Figure 28 shows the EXAFS region of the Fe K-edge spectra of the measured samples to qualitatively compare the spectra. Figure 28 shows the data used from the XANES analysis but plotted in R-space, which allows the scattering paths computed from the FEFF program to be compared to the sample data. The differences between the BM-Oak before and after treatment (in Figure 28(a)) are clear to see. This shows that the iron in the wood must be in a different environment after the patch treatment, which contradicts the XANES region (see Appendix Figure 58(b) where the absorption edge and near-edge region seem qualitatively very similar. This further indicates that iron compounds naturally in the wood, perhaps for example, iron tannate complexes, must be undergoing changes during the patch treatment, so the $SrCO_3$ is not just reacting with iron sulfates as originally expected. The data quality for the Fe K-edge of the BM-Oak and BM-Oak-treated samples was not as good as for the other samples, possibly due to the smaller quantities of iron compounds present in these samples.

Figure 28(b) and (c) show similarities between the Fe-Oak before and after treatment in the Fe(II) and Fe(III) sulfate soaked samples. This indicates that the iron is in a very similar environment in the wood before and after treatment with the patch in both cases, contradicting the XANES LCF results, where the iron carbonate standard spectrum contributed to the spectra of the treated oak samples. There does not seem to be much difference between the Fe(II) and Fe(III) samples until the spectra of the corresponding patches are observed (also in Figure 28(b and c)). This was not unexpected because the samples were not prepared in a controlled environment, so the $FeSO_4$ would be expected to oxidise. The data of the patch from the Fe(III) sample is more similar to that of the BM-Oak-treated sample (this comparison is plotted in Figure 28(d)). This was unexpected and interesting because it indicates that a reaction with iron compounds naturally occurring in oak may have more of an influence during the treatment than was originally considered. The difference in the Fe(II) patch (seen in Figure 28(d)) suggests that the influence of the

heterogeneous nature of wood and the distribution of iron compounds is important for the treatment and warrants further investigation.
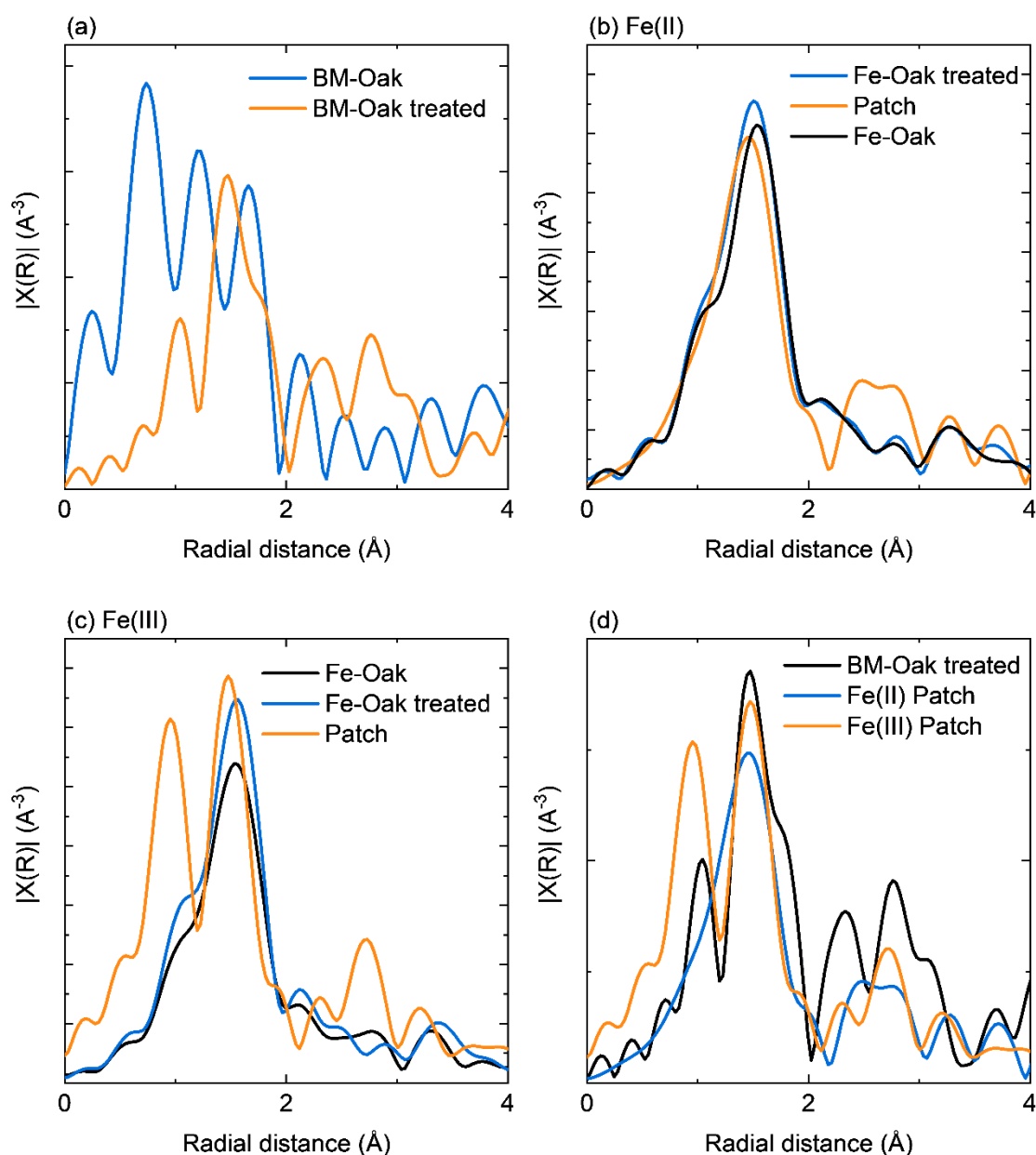
Figure 28 EXAFS region of Fe K-edge data for all samples in magnitude **(a)** BM-Oak before and after treatment **(b)** Fe(II) sulfate samples of Fe-Oak sample before and after treatment and the corresponding removed patch **(c)** Fe(III)-Oak before treatment, after treatment and the patch after treatment and **(d)** comparison between BM-Oak treated, Fe(II) Patch and Fe(III) patch.

The fits displayed in Figure 29 were all fitted in the region of r=1 to r=3.8 Å. The Fe(III)-Oak and Fe(III)-Oak treated data were fitted with data calculated from the $Fe_2(SO_4)_3$ (ICSD reference code 4301) and the Fe(III) Patch was fitted with data calculated from the $FeCO_3$ CIF

(ICSD reference code 169789). The data from all the samples would be difficult to fit further than the first coordination shell because the spectra are a mixture of contributions from many different Fe-containing compounds and likely contain amorphous material. For every path in the fit, the EXAFS equation is evaluated to determine ΔR, σ^2, S_o^2, N, ΔE_0 values. R is the distance the photoelectron travels and is allowed to adjust in the fit to determine the actual distances in the sample. If ΔR from the fit is consistent with 0, then the distance from the crystallographic data used in the fit is consistent with the sample data. The goodness of fit values were considered but can only be used comparatively. In this case they showed the fit in Figure 29(c) to be poorer than the fits in Figure 29(a) and (b). The data are presented in magnitude of $\chi(k)$ and the real part of $\chi(k)$.

The fits in Figure 29(a) and (b) show that the Fe-Oak and Fe-Oak-treated sample spectra are consistent with the 1st scattering path calculated from the $Fe_2(SO_4)_3$ CIF. This is expected as the wood was soaked in $Fe_2(SO_4)_3$ solution. However, it contradicts the LCF analysis of the Fe K-edge XANES region which suggested that $FeSO_4$ contributed to the Fe-Oak and Fe-Oak-treated sample spectra (see Table 2). As the fitting of the EXAFS region uses crystallographic information of the standards, it is likely that $Fe_2(SO_4)_3$ does contribute to the spectra in the Fe-Oak and Fe-Oak-treated samples, but as the data were not collected for EXAFS analysis, the LCF analysis and qualitative fingerprinting of the XANES region should still be considered. It could be that a standard is missing from the LCF of the XANES spectra or that a difference in intensity between the sample and standard spectra is the cause of $FeSO_4$ occurring in the LCF of the Fe(III)-Oak-treated spectrum but not in the Fe(II)-Oak-treated sample spectrum.

The comparatively poor fit of the Fe(III) Patch sample data showed that the data was not consistent with the first scattering path calculated from the $FeCO_3$ CIF. This also contradicts the LCF results (presented in Table 2) which suggested a significant contribution of the $FeCO_3$ standard to the patch sample spectrum. This could be due to the contribution of paths from $Fe_2(SO_4)_3$ and it is quite likely that contributions from $Fe_2(SO_4)_3$ and other unknown contributions, not just $FeCO_3$, are present. This could be investigated further by collecting data on the samples specifically for EXAFS analysis and including other scattering paths in the fit.
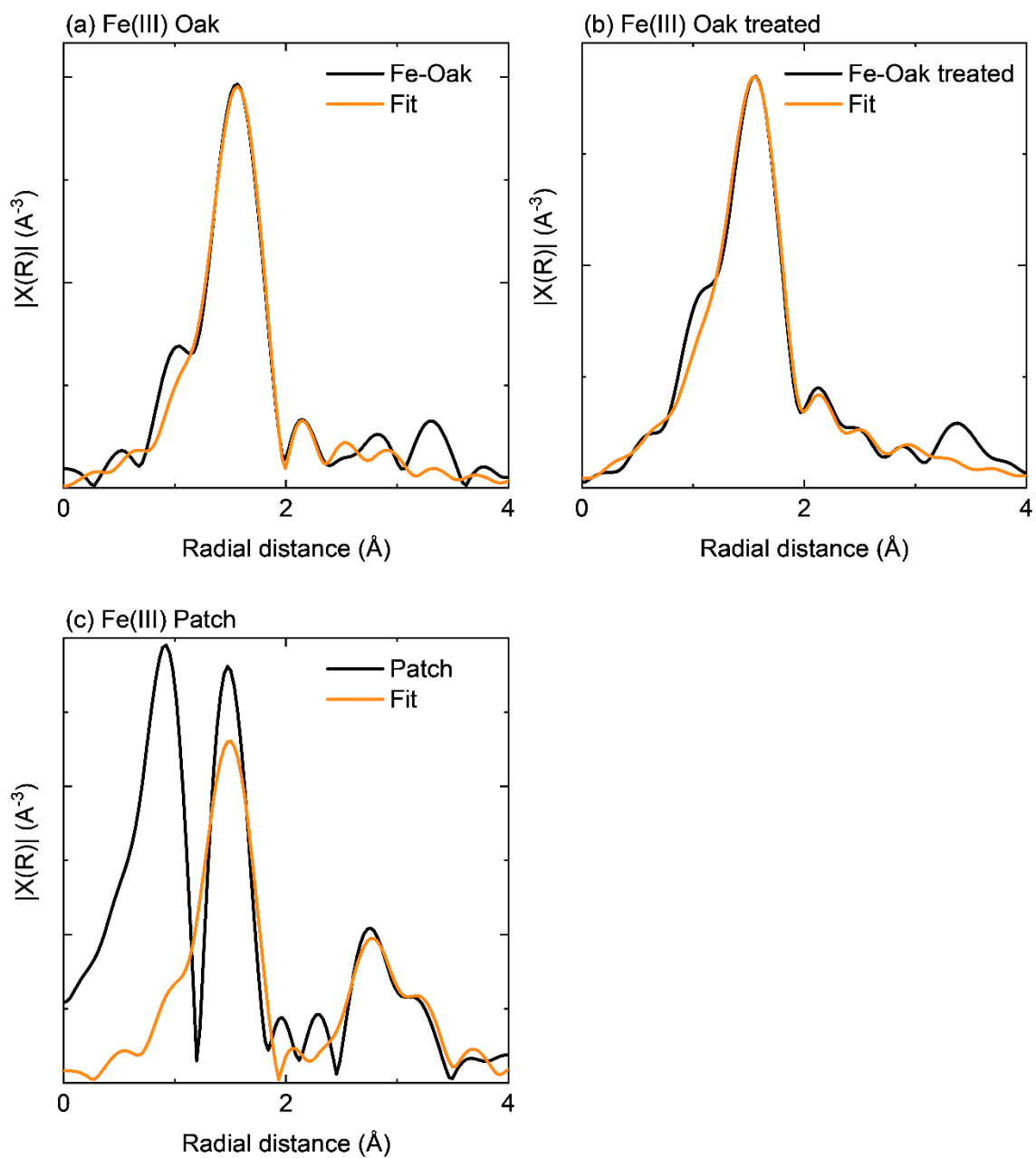
Figure 29 Fits of EXAFS regions of **(a)** the Fe(III) sulfate soaked oak sample fitted with $Fe_2(SO_4)_3$ CIF reference 4301 data **(b)** Fe(III)-Oak treated sample fitted with the same CIF data and **(c)** the patch from the Fe(III) sulfate soaked oak fitted with data from the $FeCO_3$ CIF reference 169789.

3.3 Synthesis of SrCO₃ nanoparticles

Strontium carbonate nanoparticles have found applications in various fields from pigments and paints to pyrotechnics and catalysts.[31] The starting materials and the reaction temperature, among other factors, can influence the final particle size and morphology which in turn can influence the resulting particle properties. For use as a conservation treatment tool, $SrCO_3$ presents a number of advantages over alternative systems. Firstly, $SrCO_3$ nanoparticles are non-toxic.[32] Moreover, they are relatively inexpensive which is often important when considering their use in a conservation environment and the synthesis route is straightforward.

There are several routes which can be employed for the synthesis of strontium carbonate. These include traditional methods such as mechanochemical, precipitation, hydrothermal and solvothermal methods. Sonochemical routes, where ultrasonic sound waves are applied, have also been shown in the past to be a facile way of synthesising nanoparticles due to the localised high pressures and temperatures this can produce to drive reactions. Recently developed microwave-assisted routes present some advantages over other methods such as improved product purity due to lack of side reactions, higher yields and shorter reaction times. The microwave-assisted method has previously been employed for synthesis of $SrCO_3$ to produce nanoparticles with a size distribution of around 20-50 nm.[33] An investigation of the effect of microwave heating time and power concluded that both have a significant effect on the size and morphology of the $SrCO_3$. The effect of primary particle size and morphology is of particular interest as a treatment tool, where a particular size regime may present advantages for use on *Mary Rose* timbers.

In this thesis, four main synthetic routes were investigated: ball-milling, controlled precipitation, microwave-assisted and sonochemical synthesis. Ball-milling experiments on commercial-obtained samples were carried out at two different times (6h and 8h) to check the effect of this ball-milling time on resulting particle size. Solvents such as ethylene glycol (EG) and EG-water mix were employed for liquid-based syntheses. EG has been shown to effectively couple with microwave irradiation by investigating the dielectric properties which have demonstrated its effectiveness as a microwave absorber. Therefore, EG was selected as a solvent for $SrCO_3$ reactions to investigate the effect this had on reaction times and resulting particle morphology. Specific reaction conditions are provided in Chapter 2.

The effect of different methods of synthesis and varying solvents on the morphology and size of the SrCO$_3$ particles were studied using PXRD and SEM. FTIR and Raman spectroscopy were employed to further ensure that SrCO$_3$ was synthesised and to detect whether any impurities were present.

3.3.1 FTIR and Raman spectroscopic analysis of SrCO$_3$ nanoparticles

FTIR spectroscopy has been applied to confirm the presence of the carbonate functional group in the synthesised SrCO$_3$ samples and to probe for impurity products. The FTIR spectra for both ball milled samples are shown in Figure 30 and are compared to the commercial SrCO$_3$ product purchased from Alfa Aesar to ensure impurities were not present. The FTIR spectra of the starting products for the SrCO$_3$ nanoparticle synthesis (anhydrous sodium carbonate and Sr(NO$_3$)$_2$) were also obtained to compare with the final products of the microwave-assisted, controlled-precipitation, and sonochemical methods in three solvents (water, ethylene glycol (EG), and 1:1 EG:water) to investigate if any starting materials persist in the final product. For commercial SrCO$_3$, the peaks at 700 cm^{-1} and 860 cm^{-1} correspond to the in-plane and out-of-plane bending vibrations of carbonate, respectively. The peaks at 1070 and 1430 cm^{-1} are attributed to the symmetric and asymmetric stretching carbonate vibrations. The weak peak at 1770 cm^{-1} most likely corresponds to the carbon-oxygen partial double bond of carbonate. An absence of a water vibrational stretching mode around 3500 cm^{-1} shows all products were dried thoroughly. Figure 30(a) confirms the carbonate vibrational modes are clearly noted for all samples.

Figure 30(b-d) highlight the spectra for sonicated, precipitated and microwave samples, respectively. All display very similar FTIR spectra for all the synthesised SrCO$_3$ samples in varying solvent mixtures. These spectra indicate that the products synthesised by the controlled-precipitation, sonochemical, and microwave methods compare to the commercial SrCO$_3$ product, regardless of the solvent system or synthesis method employed.
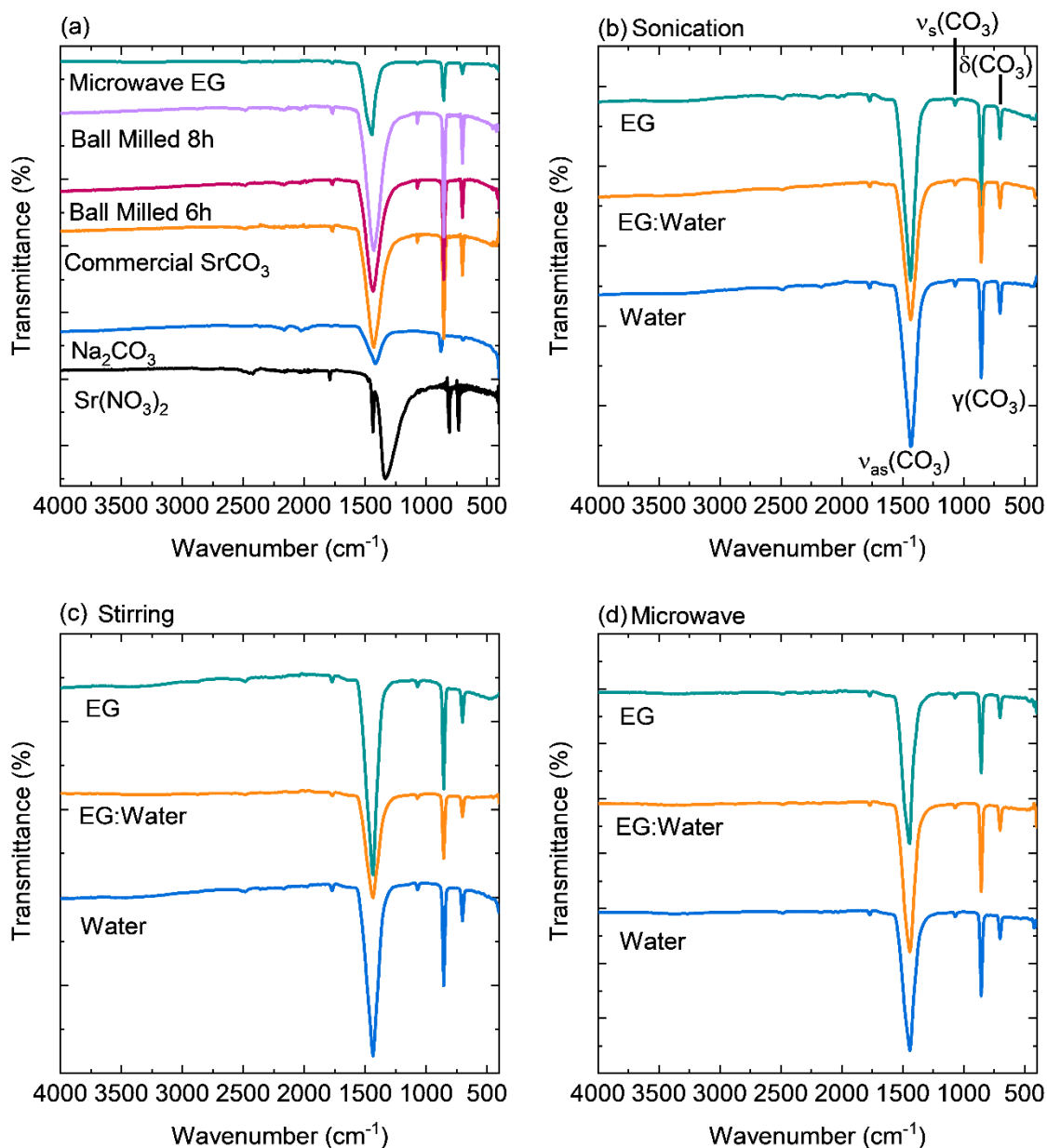
Figure 30 (a) FTIR spectra of sodium carbonate and strontium nitrate starting materials, commercial SrCO₃, and samples obtained by ball milling (6hr, 8hr), and microwave reactions in EG. Annotated FTIR spectra of SrCO₃ synthesised by **(b)** sonication **(c)** controlled precipitation and **(d)** microwave synthesis in EG, water and EG:water solvents.

Raman spectroscopy has been used to further verify the synthesis of a SrCO₃ product by comparison with the commercial product (Figure 31). SrCO₃ lattice modes occur between 50 and 300 cm^{-1} with the in-plane carbonate deformation at 700 cm^{-1} and symmetrical and asymmetrical stretching vibrations for carbonate at 1075 cm^{-1} and 1450 cm^{-1} respectively. Although the asymmetrical stretch is not seen in the microwave synthesised SrCO₃ sample

spectrum, this vibration is weak even in the spectrum of the commercial product. The Raman and FTIR spectra both complement each other and indicate the successful synthesis of $SrCO_3$.
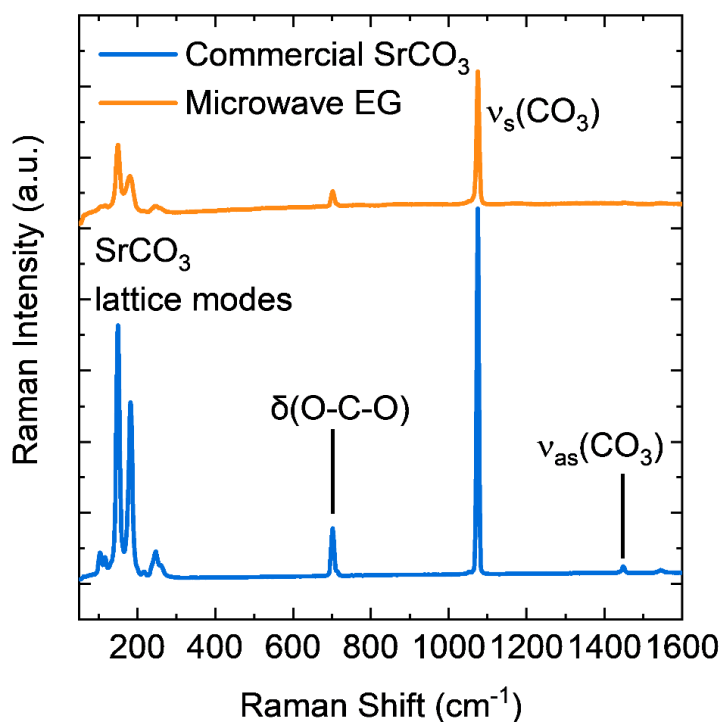
Figure 31 Comparison between Raman spectra of the microwave synthesised $SrCO_3$ product and the commercial $SrCO_3$.

3.3.2 Diffraction analysis of SrCO₃ nanoparticles

PXRD patterns for all samples were collected, analysed, and compared to the commercial $SrCO_3$ sample. $SrCO_3$ crystallises in the *Pmcn* space group and the corresponding diffraction pattern for the commercial sample is displayed in Figure 32(a). Sharper Bragg peaks are noted for the commercial sample and the ball-milled samples, compared to those materials prepared by wet-chemical means. This indicates that samples prepared by wet chemical means have smaller crystallite sizes. By applying the Scherrer equation, the mean crystallite sizes were calculated for the ball milled samples (6h, 8h) and the commercial $SrCO_3$ sample and were found to be 46.6 nm, 31.7 nm, and 43.3 nm respectively, which is considerably larger than the crystallite sizes obtained by the wet chemical methods (see Table 4). It should be noted that the Scherrer equation provides information on the crystallite size (i.e. not any amorphous material) and assumes a spherical shape.

Figure 32(b-d) presents the PXRD patterns of the $SrCO_3$ samples prepared by sonochemical, controlled-precipitation, and microwave-assisted methods in EG, 1:1 EG:water, and distilled water. What is apparent from these plots is that while all peaks can be assigned to $SrCO_3$, there is a clear broadening in the peaks of the samples prepared by wet chemical methods, which can indicate smaller crystallite sizes or defects in the crystal structure. Peak broadening can also be due to the instrument, but the samples prepared by wet chemical means show more broadening than the commercial and ball milled samples indicating this is due to the crystallite size. This broadening is observed particularly in the patterns of the samples prepared in EG where the broadening precludes peak splitting from being observed for some peaks.
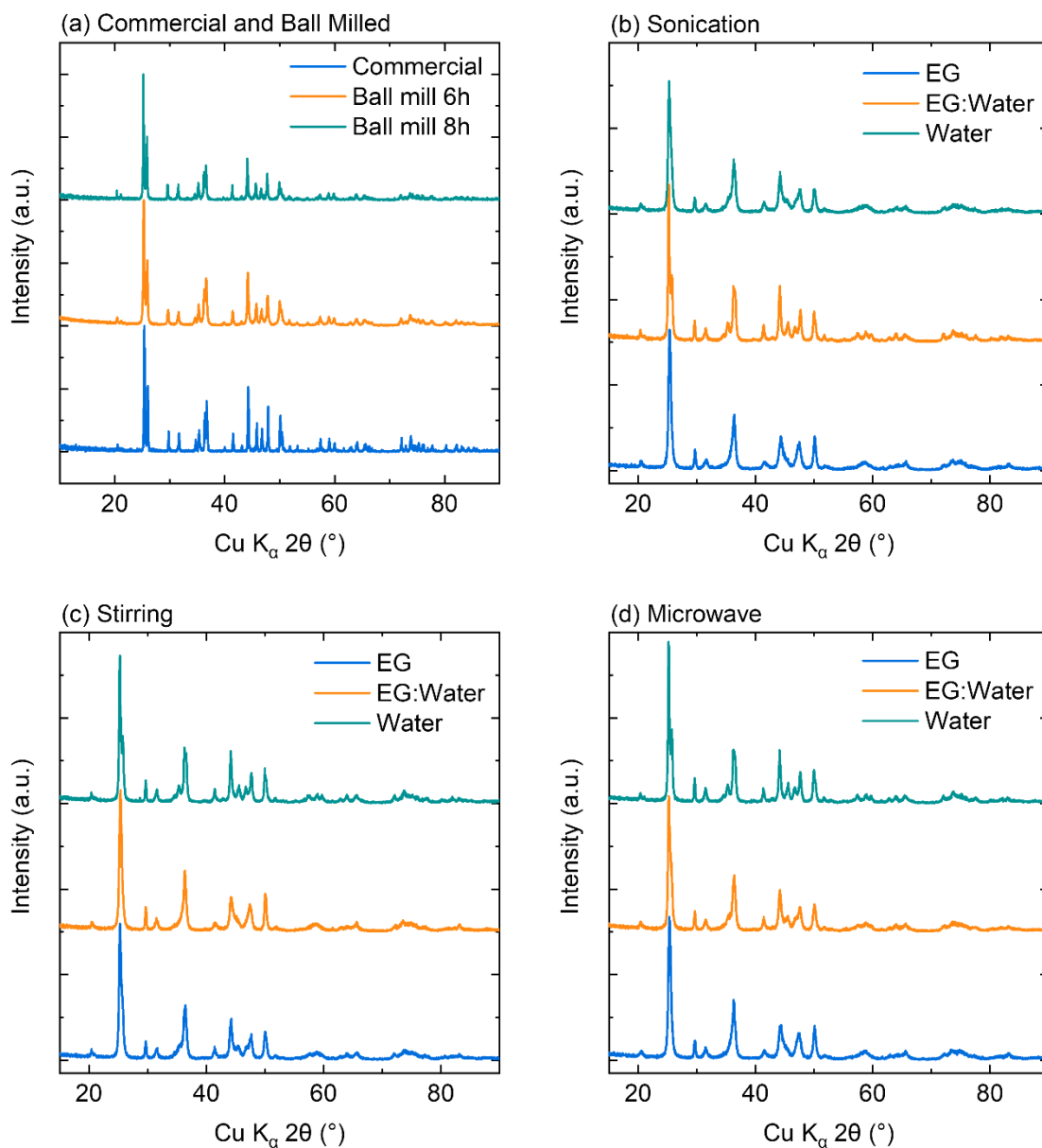
Figure 32 PXRD patterns of **(a)** commercial $SrCO_3$ and ball milled samples (6h and 8h); $SrCO_3$ synthesised by **(b)** sonication, **(c)** controlled precipitation and **(d)** microwave methods in different solvent mixes (EG, EG:Water, and water).

Crystallite sizes were obtained by fitting the (2 2 1) peak (with 2θ of approximately 44.2°), to obtain the FWHM, which were then applied to the Scherrer equation. Table 4 shows the crystallite sizes obtained from the Scherrer equation for all synthesised samples as well as commercial $SrCO_3$ and the ball milled samples. It can be seen from these results that crystallite sizes between the synthesis methods are quite similar. However, when the solvent is changed from EG to water, the crystallite size increases slightly in all cases. This indicates that the

smallest crystallite sizes can be obtained when EG is used as a solvent, with crystallite sizes of 14.7 nm, 16.6 nm, and 12.7 nm for microwave-assisted, controlled precipitation, and sonochemical methods respectively. It was expected that the microwave-assisted method would lead to smaller, more uniform crystallites due to the speed of the reaction, but the sonochemical method seems to yield the smallest crystallite sizes. This could be due to the sonochemical method keeping the precursors dispersed so they could react in a more controlled manner. This method could also prevent the product from aggregating as much as the other methods. Smaller crystallite sizes were obtained when only EG was used as a solvent, than when water was a co-solvent or the only solvent. A similar trend has been observed in research by J. Wojnarowicz *et al.* on the influence of water in ZnO nanoparticle synthesis where the addition of water to EG in the synthesis procedure led to increased crystallite sizes which the authors considered to be due to water increasing the dissociation of the precursor.[34] It could be that the viscosity of EG means the precursors react in a more controlled way, leading to smaller crystallites. The viscosity of EG could be helping to keep the nanoparticles dispersed, perhaps preventing them from aggregating so much as they precipitate. Strontium nitrate is also less soluble in EG than in water so the respective solubilities could lead to different reaction routes.

Table 4 Crystallite sizes determined using the Scherrer equation applied to the (2 2 1) peak (at 44° 2θ) for all the SrCO$_3$ samples.

Sample	Solvent	Crystallite Size (nm)
Commercial	-	46.6
Ball mill 6h	-	31.7
Ball mill 8h	-	43.3
Microwave	EG	14.7
Microwave	1:1 EG:water	20.5
Microwave	Water	25.7
Controlled Precipitation	EG	16.6
Controlled Precipitation	1:1 EG:water	17.7
Controlled Precipitation	Water	23.5
Sonochemical	EG	12.7
Sonochemical	1:1 EG:water	17.4
Sonochemical	Water	22.8

Rietveld refinements were performed on diffraction data to further check for any impurities and to obtain unit cell parameters. Figure 33 shows the Rietveld refinement obtained for the $SrCO_3$ sample synthesised by the microwave-assisted method in EG.
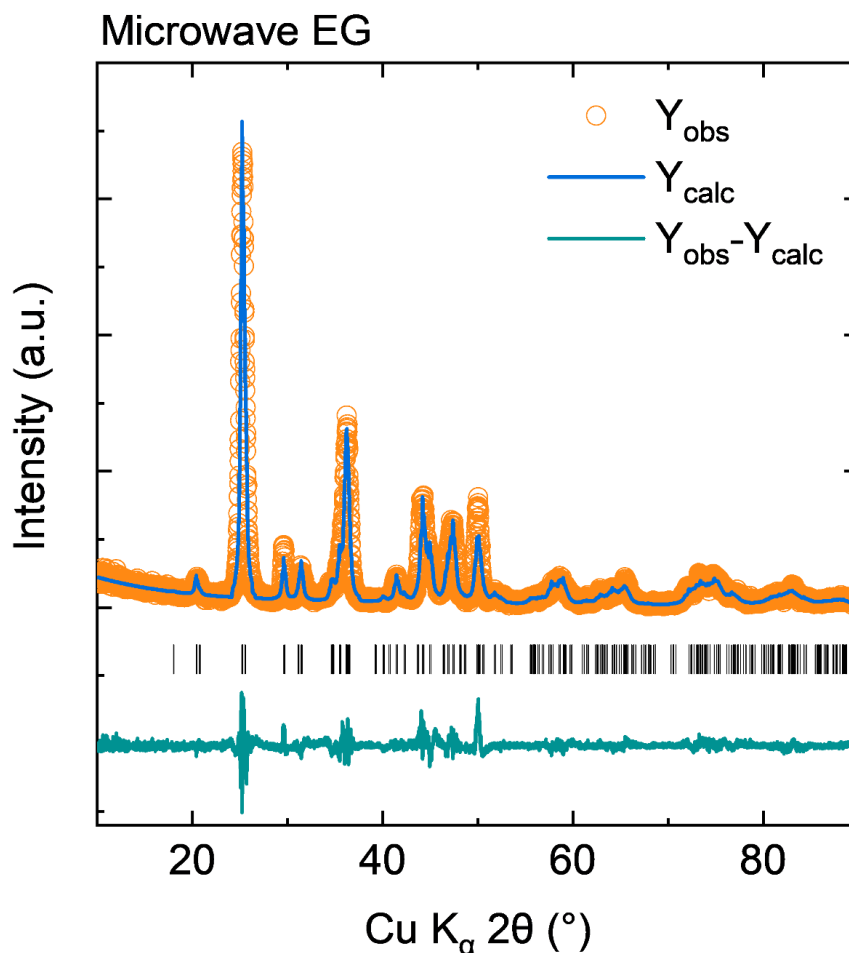
Figure 33 Rietveld refinement of $SrCO_3$ synthesised by the microwave-assisted method in EG, where the orange circles represent the data collected, the blue line is the fit to these data and the green line is the difference between the observed and calculated data (Y_{obs}-Y_{calc}). The black tick marks indicate where reflections from $SrCO_3$ (ICSD code 15195) are expected to appear.

Parameters obtained from the Rietveld fits are given in Table 5, including unit cell parameters and goodness of fit values. The corresponding figures showing the Rietveld fits for these values are given in the appendix (Figures 63-65). The literature values for the unit cell parameters are different to those of the samples probably due to the Rietveld method not fitting the peaks well, possibly due to size effects or structural distortions. To improve the quality of the PXRD pattern, the collection time could be increased. Pawley or LeBail fits could be used to fit this data more reliably due to the nanocrystalline nature of the samples. The

poor fit could also be a result of the large size distribution of crystallites, which would require other methods, such as transmission electron microscopy (TEM) and dynamic light scattering, to determine if this is the case. If the literature XRD pattern is a calculated powder XRD pattern from the single crystal data, the discrepancies in the values from the fit could be due to possible differences between the structure of the crystal of $SrCO_3$ and the crystallites present in the samples.

Table 5 Fitting parameters obtained from Rietveld refinements to all $SrCO_3$ samples prepared, as well as literature values (ICSD code 15195) and a commercial sample. S.D. indicates standard deviation.

Sample	a (Å)	S.D.	b (Å)	S.D.	c (Å)	S.D.	volume (Å^2)	S.D.	R_p	R_{wp}	R_{exp}	χ^2
Literature $SrCO_3$	5.090		8.358		5.997		255.13					
Commercial $SrCO_3$	5.111		8.427		6.037		260.03		36.7	44.3	32.0	1.917
Ball mill 6h	5.108	2.6×10^{-4}	8.427	4.3×10^{-4}	6.038	3.5×10^{-4}	259.91	0.024	14.1	18.1	13.2	1.873
Microwave EG	5.058	6.5×10^{-4}	8.553	1.1×10^{-3}	6.032	8.0×10^{-4}	260.97	0.058	18.3	22.6	14.1	2.572
Microwave EG:Water	5.081	5.7×10^{-4}	8.501	9.1×10^{-4}	6.034	7.1×10^{-4}	260.62	0.051	18.2	22.8	14.3	2.546
Microwave Water	5.095	4.3×10^{-4}	8.461	7.1×10^{-4}	6.038	5.7×10^{-4}	260.31	0.04	18.1	22.5	14.1	2.545
Precipitation EG	5.064	6.9×10^{-4}	8.547	1.1×10^{-3}	6.036	8.8×10^{-4}	261.23	0.063	20.8	25.8	14.5	3.178
Precipitation EG:Water	5.083	8.4×10^{-4}	8.505	1.3×10^{-3}	6.039	1.0×10^{-3}	261.05	0.074	17.5	22.0	14.8	2.204
Precipitation Water	5.093	5.5×10^{-4}	8.468	9.2×10^{-4}	6.038	7.2×10^{-4}	260.37	0.05	19.0	23.1	14.7	2.471
Sonochemical EG	5.060	6.6×10^{-4}	8.558	1.1×10^{-3}	6.036	8.2×10^{-4}	261.37	0.059	19.0	23.7	14.4	2.705
Sonochemical EG:Water	5.070	6.6×10^{-4}	8.512	1.1×10^{-3}	6.034	8.3×10^{-4}	260.37	0.06	18.7	23.7	14.4	2.692
Sonochemical Water	5.093	4.7×10^{-4}	8.459	7.7×10^{-4}	6.036	6.1×10^{-4}	260.04	0.043	19.2	23.9	14.1	2.877

3.3.3 Analysis of SrCO₃ particle morphology from electron microscopy

High resolution SEM images were obtained for $SrCO_3$ samples obtained from wet-chemical preparative methods in EG and 1:1 EG:water and are shown in Figure 34. Comparing the synthesised $SrCO_3$ samples, large changes in morphology are observed depending on both the synthesis method and the choice of solvent. In the case of samples prepared by sonication methods, for example, spherical aggregates are observed when EG alone is used as a solvent; such secondary structures are not observed when water is added as a co-solvent. Samples prepared in EG are smaller in crystallite size. This is in agreement with crystallite sizes obtained from PXRD analysis.
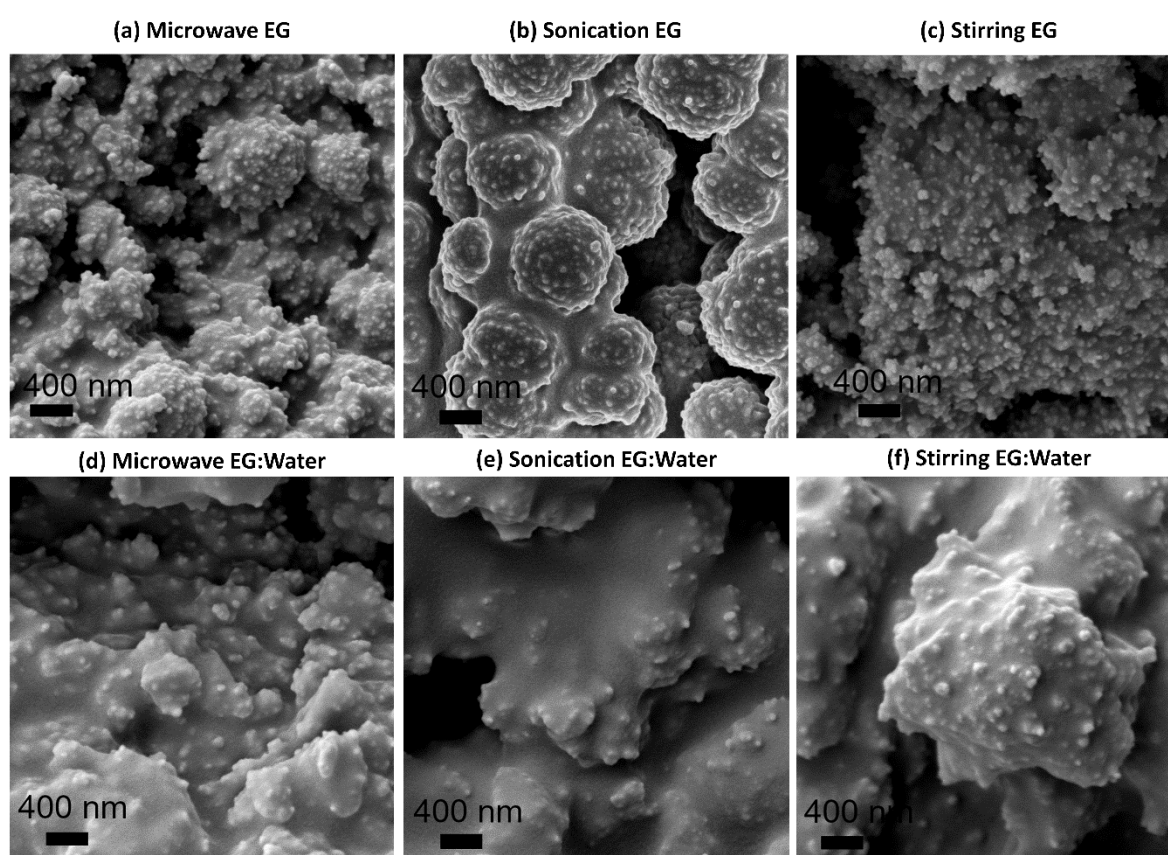
Figure 34 SEM micrographs of the synthesised $SrCO_3$ samples via: microwave methods in **(a)** EG and **(d)** EG:water; sonochemical methods in **(a)** EG and **(e)** EG:water; and controlled precipitation in **(c)** EG and **(f)** EG:water.

3.4 Conclusions

XANES analysis has demonstrated that $SrCO_3$-cellulose patches are a promising treatment method for marine archaeological wood through the reaction of $SrCO_3$ nanoparticles with the iron and sulfur compounds to form stable $SrSO_4$. In combination with FTIR, Raman, and XRF spectroscopy, XANES results show that the $SrCO_3$-cellulose patches partially remove iron and sulfur compounds from test wood samples soaked in an iron sulfate solution. Fingerprinting of the S K-edge XANES spectra of the Fe-Oak-treated and the patch sample showed the sulfur present in these samples was in a very similar environment to the sulfur in the $SrSO_4$ standard (Appendix Figure 60(a)). XANES LCF results of the S K-edge show that the sulfur in the patch after treatment is likely in a similar environment to the sulfur in $SrSO_4$ (65%), with a contribution from iron sulfate (see Table 2). Due to the similarity in the edge energy and difference in edge intensity of the iron sulfate standards in the S K-edge spectra, the Fe K-edge data were considered to be more reliable for distinguishing between the iron sulfate standards.

Fingerprinting of the Fe K-edge XANES spectra of the Fe-Oak-treated and patch after treatment samples show that the iron in the wood is in a similar environment to that of the $FeCO_3$ standard (Appendix 60(b)) but there are certain features that cannot be attributed only to the contribution of the $FeCO_3$ spectrum. LCF analysis of the Fe K-edge favoured the presence of iron(III) sulfate as well as $FeCO_3$ in the Fe-Oak-treated and patch sample spectra as was expected since the oak was soaked in $Fe_2(SO_4)_3$ solution. It was expected that in the Fe(II)-sulfate-soaked samples the iron would oxidise as the samples were not kept in a controlled environment, and the LCF results confirm this (see Table 2) for the Fe-Oak-treated and patch samples. However, the LCF results show the contribution of $FeSO_4$ in the Fe-Oak sample spectra which could indicate that the iron speciation in the oak after soaking is not as simple as only $Fe_2(SO_4)_3$ but contains a mixture of iron compounds that were not originally considered in the fits, such as iron tannate complexes, iron oxides, and iron hydroxides. It is also possible that the iron could be reduced during the treatment by cellulose degradation compounds or gallic acid for example, which could account for the presence of Fe(II) standards in the LCF of the Fe(III)-Oak-treated sample spectrum.

Fitting of the EXAFS region of the Fe K-edge spectra provides complementary information to the XANES analysis. The fits show that Fe(III)-Oak and Fe(III)-Oak-treated samples likely

contain path contributions from $Fe_2(SO_4)_3$ (Figure 29(a) and (b)) and that the spectra of the patch removed from the treated oak does not solely have contributions from $FeCO_3$, but must contain other iron compounds (Figure 29(c)) . These results contradict some of the XANES LCF results (Table 2) which showed a contribution from the $FeSO_4$ standard spectrum to the Fe(III)-Oak and Fe(III)-Oak-treated sample spectra. As noted above this could be due to other iron compounds not accounted for in the fits. Measuring more iron standards for including in the fits would be useful in the future to better determine how the iron compounds in the iron-soaked oak are reacting with the treatment. Study of the EXAFS region further highlighted the importance of understanding how the treatment might affect the iron compounds naturally present in oak, as there were similarities between the patch from the Fe(III)-Oak and the BM-Oak-treated samples but differences from the patch from Fe(II)-Oak (Figure 28(d)). The presence of an Fe K-edge spectrum for both patch samples does provide evidence that iron is being removed from the wood by the patch as desired.

FTIR spectroscopy shows sulfates remain in the wood after treatment but most likely as $SrSO_4$, showing the desired reaction has taken place, which is preferable to iron sulfate remaining in the wood. FTIR and Raman spectroscopy provide further evidence of sulfates in the patch as well as unreacted $SrCO_3$ remaining in the patch after treatment. Additionally, XRF spectroscopy confirms these results by indicating that a small amount of iron and sulfur is being removed from the wood in the patch. The depth of treatment and the effect of treatment duration should be investigated further. The quantity of iron sulfate removed from the wood by the patch and the amount of $SrCO_3$ needed to fully react with iron sulfate and effectively neutralise sulfuric acid was not quantitatively determined. Overall, this shows the potential of the $SrCO_3$-cellulose patches as a surface treatment to target specific areas of artefacts with iron and sulfur problems and remove these species, which is different from traditional approaches where consolidants remain within the wood.

This combination of spectroscopic techniques has shown that iron and sulfur compounds sequestered in the wood can be drawn into the $SrCO_3$-cellulose patch, which can then be removed. These findings extend the possibility of developing more targeted approaches to the iron and sulfur problem through additional functionalisation of the nanocomposite treatment. The patches have potential for use as spot conservation treatments for, not only *Mary Rose* wood, but a variety of artefacts plagued by iron and sulfur problems. An advantage

of the patches is that they could be applied multiple times for problematic areas of artefacts to keep removing iron and sulfur compounds from the wood, however, more research into how this might affect the wooden artefacts in the long-term would need to be considered.

Strontium carbonate nanoparticles have been successfully synthesised by three different methods (microwave, sonication and controlled-precipitation) and in three solvent systems (EG, 1:1 EG:water, and water). Powder XRD patterns and SEM show to some extent that the solvent has a greater effect on the properties of the strontium carbonate than the method of synthesis. Crystallite sizes are similar between methods but show a decrease when changing the solvent from water to EG. SEM images show large agglomerates of smaller nanoparticles. FTIR and Raman spectroscopy have confirmed bending and stretching modes typical for carbonates and Rietveld refinements confirm $SrCO_3$ has been synthesised. Future work on the $SrCO_3$ synthesis and characterisation includes transmission electron microscopy (TEM) to determine actual particle size distribution (this can also be carried out on the collected HR-SEM images, perhaps at higher magnification). Dynamic light scattering or photoelectron correlation spectroscopy could also be employed for the same purpose.

References

1   E. J. Schofield, C. Delaveris and R. Sarangi, Alkaline earth carbonates for the treatment of problematic sulfur associated with marine archeological wood, *J. Archaeol. Sci. Reports*, 2015, **4**, 427–433.

2   G. Poggi, N. Toccafondi, D. Chelazzi, P. Canton, R. Giorgi and P. Baglioni, Calcium hydroxide nanoparticles from solvothermal reaction for the deacidification of degraded waterlogged wood, *J. Colloid Interface Sci.*, 2016, **473**, 1–8.

3   P. Baglioni and R. Giorgi, Soft and hard nanomaterials for restoration and conservation of cultural heritage, *Soft Matter*, 2006, **2**, 293.

4   D. Chelazzi, R. Giorgi and P. Baglioni, Nanotechnology for Vasa wood de-acidification, *Macromol. Symp.*, 2006, **238**, 30–36.

5   G. Poggi, P. Baglioni and R. Giorgi, Alkaline earth hydroxide nanoparticles for the inhibition of metal gall ink corrosion, *Restaurator*, 2011, **32**, 247–273.

6   U. Henniges, R. Reibke, G. Banik, E. Huhsmann, U. Hähner, T. Prohaska and A. Potthast, Iron gall ink-induced corrosion of cellulose: Aging, degradation and stabilization. Part 2: Application on historic sample material, *Cellulose*, 2008, **15**, 861–870.

7   E. J. Schofield, R. Sarangi, A. Mehta, A. M. Jones, F. J. W. Mosselmans and A. V. Chadwick, Nanoparticle de-acidification of the mary rose, *Mater. Today*, 2011, **14**, 354–358.

8   R. Giorgi, D. Chelazzi and P. Baglioni, Nanoparticles of calcium hydroxide for wood conservation. The deacidification of the Vasa warship, *Langmuir*, 2005, **21**, 10743–10748.

9   K. M. Wetherall, R. M. Moss, A. M. Jones, A. D. Smith, T. Skinner, D. M. Pickup, S. W. Goatham, A. V. Chadwick and R. J. Newport, Sulfur and iron speciation in recently recovered timbers of the Mary Rose revealed via X-ray absorption spectroscopy, *J. Archaeol. Sci.*, 2008, **35**, 1317–1328.

10   Z. Walsh, E.-R. Janeček, M. Jones and O. A. Scherman, Natural polymers as alternative consolidants for the preservation of waterlogged archaeological wood, *Stud. Conserv.*, 2016, **3630**, 1–11.

11   A. V. Chadwick, A. Berko, E. J. Schofield, A. D. Smith, J. F. W. Mosselmans, A. M. Jones and G. Cibin, The application of X-ray absorption spectroscopy in archaeological conservation: Example of an artefact from Henry VIII warship, the Mary Rose, *J. Non. Cryst. Solids*, 2016, **451**, 49–55.

12   J. Hill, S. Willis and R. Pacheco-Ruiz, *People and the Sea: A Maritime Archaeological Research Agenda for England*, 2013.

13   M. Albelda Berenguer, M. Monachon, C. Jacquet, P. Junier, C. Rémazeilles, E. J. Schofield and E. Joseph, Biological oxidation of sulfur compounds in artificially degraded wood, *Int. Biodeterior. Biodegrad.*, , DOI:10.1016/j.ibiod.2018.06.009.

14   R. Giorgi, D. Chelazzi and P. Baglioni, Conservation of acid waterlogged shipwrecks: Nanotechnologies for de-acidification, *Appl. Phys. A Mater. Sci. Process.*, 2006, **83**, 567–571.

15   G. Poggi, N. Toccafondi, L. N. Melita, J. C. Knowles, L. Bozec, R. Giorgi and P. Baglioni, Calcium hydroxide nanoparticles for the conservation of cultural heritage: New formulations for the deacidification of cellulose-based artifacts, *Appl. Phys. A Mater. Sci. Process.*, 2014, **114**, 685–693.

16   P. Dillmann, L. Bellot-Gurlet and I. Nenner, *Nanoscience and Cultural Heritage*, Atlantis Press, 2016.

17   A. V. Chadwick, E. J. Schofield, A. M. Jones, G. Cibin and J. F. W. Mosselmans, Ionic nanoparticles in heritage conservation; Treatments for the Mary Rose timbers, *Solid State Ionics*, 2012, **225**, 742–746.

18   E. J. Schofield, R. Sarangi, A. Mehta, A. M. Jones, A. Smith, J. F. W. Mosselmans and A. V. Chadwick, Strontium carbonate nanoparticles for the surface treatment of problematic sulfur and iron in waterlogged archaeological wood, *J. Cult. Herit.*, 2016, **18**, 306–312.

19   J. Sandström and E. J. Schofield, in *Proceedings of the 13th ICOM-CC group on wet organic archaeological materials conference*, eds. E. Williams and E. Hocker, Florence, 2016, pp. 249–55.

20   B. Ravel, X-ray Absorption Spectroscopy, http://bruceravel.github.io/XAS-Education/, (accessed 28 January 2018).

21   J. Kesselmeier, P. Schröder and J. W. Erisman, in *Biosphere-Atmosphere Exchange of Pollutants and Trace Substances*, Springer, 1997.

22   A. Berko, A. D. Smith, A. M. Jones, E. J. Schofield, J. F. W. Mosselmans and A. V Chadwick, XAS studies of the effectiveness of iron chelating treatments of Mary Rose timbers, *J. Phys. Conf. Ser.*, 2009, **190**, 012147.

23   M. Sandstrom, F. Jalilehvand, E. Damian, Y. Fors, U. Gelius, M. Jones and M. Salome, Sulfur accumulation in the timbers of King Henry VIII's warship Mary Rose: A pathway in the sulfur cycle of conservation concern, *Proc. Natl. Acad. Sci.*, 2005, **102**, 14165–14170.

24   A. Ricci, K. J. Olejar, G. P. Parpinello, P. A. Kilmartin and A. Versari, Application of Fourier transform infrared (FTIR) spectroscopy in the characterization of tannins, *Appl. Spectrosc. Rev.*, 2015, **50**, 407–442.

25   D. E. Hathway, Oak-bark tannins, *Biochem. J.*, 1958, **70**, 34–42.

26   E. J. Schofield, R. Sarangi, A. Mehta, A. M. Jones, F. J. W. Mosselmans and A. V. Chadwick, Nanoparticle de-acidification of the mary rose, *Mater. Today*, 2011, **14**, 354–358.

27   T. E. Westre, P. Kennepohl, J. G. DeWitt, B. Hedman, K. O. Hodgson and E. I. Solomon, A multiplet analysis of Fe K-edge 1s → 3d pre-Edge features of iron complexes, *J. Am. Chem. Soc.*, 1997, **119**, 6297–6314.

28   J. Neevel and B. and Reissland, Bathophenanthroline indicator paper: development of a new test for iron ions, *PapierRestaurierung*, 2005, **6**, 28–36.

29   G. Almkvist, Swedish University of Agricultural Sciences, 2008.

30   B. Ravel and M. Newville, ATHENA, ARTEMIS, HEPHAESTUS: Data analysis for X-ray absorption spectroscopy using IFEFFIT, *J. Synchrotron Radiat.*, 2005, **12**, 537–541.

31   S. Ni, X. Yang and T. Li, Hydrothermal synthesis and photoluminescence properties of SrCO 3, , DOI:10.1016/j.matlet.2010.11.056.

32   W. Y. Qian, D. M. Sun, R. R. Zhu, X. L. Du, H. Liu and S. L. Wang, pH-sensitive strontium carbonate nanoparticles as new anticancer vehicles for controlled etoposide release, *Int. J. Nanomedicine*, 2012, **7**, 5781–5792.

33   H. Jahangiri, M. Ranjbar, M. A. Taher and H. kazerooni, Using microwave heating for synthesis of SrCO3 nanostructures with different morphologies, *J. Ind. Eng. Chem.*, 2015, **21**, 1132–1136.

34   J. Wojnarowicz, A. Opalinska, T. Chudoba, S. Gierlotka, R. Mukhovskyi, E. Pietrzykowska, K. Sobczak and W. Lojkowski, Effect of Water Content in Ethylene Glycol Solvent on the Size of ZnO Nanoparticles Prepared Using Microwave Solvothermal Synthesis, *J. Nanomater.*, , DOI:10.1155/2016/2789871.

Chapter 4: Cellulosic Fibre Characterisation

4.1 General Introduction

This chapter investigates methods of characterising cellulosic fibres. A range of reference samples were studied for comparison to fibres from artefacts recovered from the *Mary Rose*. The aim here was to identify the type of fibres present in these samples and to gather information and explore their state of degradation to help inform future conservation decisions. Cellulosic fibre samples studied included anchor rope and sail cloth from the *Mary Rose* collection along with historic flax and hemp samples from the Royal Botanic Gardens, Kew, and modern reference samples.

Focusing on the textiles recovered from the *Mary Rose*, these can be split into two categories of personal belongings and ship equipment.[1] Here, the emphasis is on ship equipment including the sail cloth and rope. Chapter 5 explores proteinaceous fibres, with more personal belongings are considered (for example, leather shoes). Upon initial observation, the sail cloth is in a fragmented state while the samples of rope appear better preserved as it had been impregnated with tar to preserve it during use on the ship (Figure 35).[1] Plant fibres from textiles are primarily composed of cellulose microfibrils in a matrix of hemicellulose, pectin, and lignin.[1] Unfortunately, these components are all susceptible to physical, chemical, and biological degradation processes.[1] After the ship and its artefacts were raised, cleaning, drying and storage processes were carefully undertaken. The majority of the textile artefacts were unfolded under water and brushed whilst supported on a net frame.[1] The textiles were further soaked and rinsed in deionized water.[1] If, after slow air drying, the artefacts showed brittleness, they were treated with carboxymethyl cellulose (CMC) although this is known to be prone to oxidation.[1] While active conservation procedures are developed, the textiles are stored under low or no light conditions with a constant relative humidity of 50-55% and dust and dirt are prevented from reaching them.[1]

Figure 35 Photographs of **(a)** *Mary Rose* anchor cable fragments and **(b)** sail cloth fragments from the *Mary Rose* collection. A colour card is included as a reference.

The main research questions explored here include the following; how to identify and distinguish archaeological fibres; how can degradation be detected in cellulosic fibres; what is the extent of the degradation (particularly in comparison with historic (not waterlogged) and modern fibre samples) and is it possible to quantify any observed degradation or only to investigate it on a comparative basis?

Identification of fibres is not a simple task and is complicated when studying archaeological fibres due to possible contamination and effects of degradation. Fibres are usually identified primarily by optical microscopy, which typically requires a lot of experience for positive identification or a good database for purposes of comparison. It is straightforward to distinguish an animal fibre from a vegetable fibre due to the occurrence of scales which are indicative of animal fibres. Distinguishing *between* animal fibres is a more challenging task (this is discussed in greater detail in Chapter 5), as is distinguishing between vegetable (cellulosic) fibres. Some vegetable fibres are easier to distinguish, such as cotton fibres from bast fibres under a light microscope. Cotton fibres show a characteristic twisting, whereas bast fibres do not twist. Bast fibres can be distinguished based on their overall width, whether there is a narrow or wide lumen, and the presence of dislocation, nodes, and cross-markings. There is a wide variability in natural fibres, adding to the challenge of identification. A key method for distinguishing between bast fibres is the modified Herzog test which uses a waveplate and by rotating the sample viewing stage can distinguish between Z- and S-twist fibres.[2–4] In the modified Herzog test, a polariser and a waveplate are used and as the fibre is rotated, the birefringent properties of the fibre mean that the observed colours change

depending on orientation of the cellulose chains in the fibres. Using this test, Z- and S-twists can be inferred and a reasonable fibre identification can be made.[3] DNA analysis is another way of identifying fibres but is generally not applicable to bast fibres due to the difficulty in extraction.[5] Nevertheless, DNA analysis has been carried out in a forensic science context to distinguish plant materials used in rope samples but difficulties may arise if the rope is contaminated (as is probably the case for archaeological fibres) or composed of a mix of fibres.[6]

FTIR spectroscopy is another method of identifying fibres, but, as with light microscopy, difficulties remain in distinguishing between different bast fibres like hemp, flax, nettle, and jute. This method does provide a distinguishing probe between animal and plant fibres however, due to a typical cellulose spectrum seen with plant fibres and distinct amide bands of the proteins present in animal fibres. This chapter examines an anchor rope and a sail cloth sample from the *Mary Rose* collection and investigates potential methods of identification to shed further light on the nature of these samples. Optical microscopy, scanning electron microscopy (SEM), and FTIR spectroscopy are all used in this chapter as methods of identifying these fibres.

Degradation can be detected and assessed by simply observing the artefact. This often yields important information and there is no replacement for looking carefully. Enhancing our own visualisation of these artefacts through microscopy can highlight a wealth of further detail about the artefact. Methods of trying to quantify what can be observed have been investigated, including the analysis of peak ratios and wavenumber shifts. In this thesis, SEM was employed to visualise surface fibre degradation. Optical microscopy also shows damage and any breakages in the fibres. Analysis of FTIR spectra of fibres provides insight into microstructural changes at the surface.

The question of whether there is degradation or not then becomes how to assess the extent of degradation and whether there is a way to determine if an artefact is in a severely fragile state objectively. By comparing FTIR spectra of fibres using key bands and their intensities, the extent of degradation can be assessed. Polarised-ATR-FTIR has been used in this thesis as a way of trying to distinguish between flax and hemp fibres and to obtain a crystallinity index. This crystallinity index is important for comparing levels of degradation between the samples.

Ideally, these indices could be compared with other work in the area and could be expanded further to produce a database of cellulose-based artefacts and comparative crystallinities. This crystallinity index and other peak ratios give a semi-quantitative idea of degradation in the fibres, but a holistic approach is required when dealing with archaeological samples by taking into account information from historical sources, optical microscope and SEM images, and FTIR data, along with any other information that can be collected to build a picture of the state of the artefact.

In this chapter, initial characterisation by optical microscopy and FTIR spectroscopy was carried out on viscose and modern linen samples before historic flax, and historic hemp fibre samples. This was to firstly experiment with how to carry out ethical sampling of fibres from a woven material and to observe any issues with the set-up of the equipment and procedures which could cause damage to the fibres. Polarised ATR-FTIR experiments were undertaken on viscose to check the method and on modern linen to serve as a useful reference when using this technique on the historic and *Mary Rose* samples. The cellulose-based *Mary Rose* artefacts studied in this chapter are displayed in Figure 35. These included anchor cable fragments and sail cloth fragments. Optical microscopy, SEM, FTIR, and polarised FTIR spectroscopy experiments were performed on these samples.

4.2 Characterisation of fibre samples

4.2.1 Digital microscopy imaging of fibre samples

When characterising fibres, it is initially useful to have a detailed look at them from a macroscopic level, working down to the microscopic. It is useful to study the weave pattern, if the textile is intact, and the wind of the yarn to give details on the manufacture of the textile. Digital microscopy images in Figure 36 were taken with a 200x portable Dino-Lite microscope at 60x magnification. These images give an idea of the colour, scale, and physical state of the fibres. The viscose fibre (Figure 36(a)) was characterised as it serves as a reference fibre for polarised ATR-FTIR investigations since cellulose in individual viscose fibres are all oriented with the fibre axis due to the extrusion process.

Modern linen was used for comparison to the historic and *Mary Rose* samples for the purposes of identification and to develop a comparative scale of deterioration. Figure 36(b) shows one of the samples taken from the modern linen fabric used for reference. This was an

undyed sample and relatively unprocessed. The variation in the fibres is easily seen and darker areas observed look almost like a sheath around the finer fibres which would probably be removed with heavier processing. The fibres are much less uniform and more heterogeneous than the viscose sample.
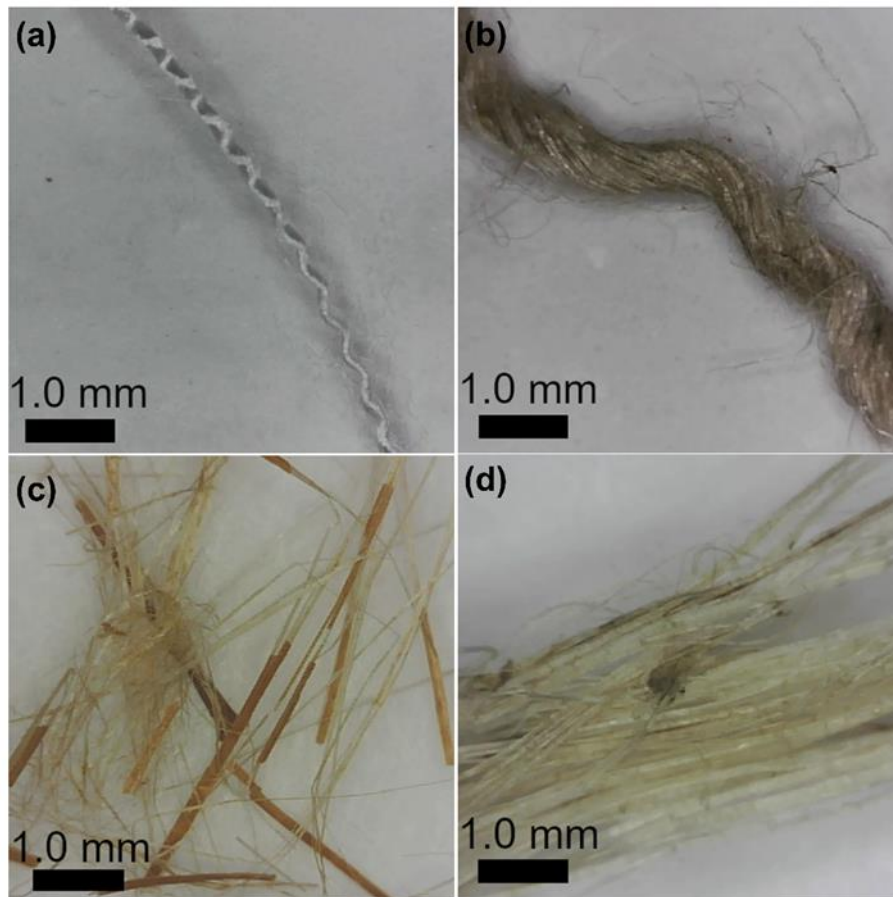
Figure 36 Digital microscope images taken with a handheld Dino-Lite system of **(a)** a viscose fibre **(b)** the modern linen reference sample **(c)** sample from Flax 1851 fibres and **(d)** Hemp 1910 sample

Figure 36(c) shows nearly 200-year-old samples of flax fibres (*Linum utitatissimum* L.) from International Exhibition (Portugal) reference collection at the Royal Botanic Gardens, Kew. There are similarities here to the modern linen sample, in that the fibres have areas where they are enclosed by darker material. This is to be expected as linen is a fabric composed of fibres from the flax plant. Further optical microscopy and IR spectroscopy in the following sections confirm these similarities. *Cannabis sativa* L. is the variety of hemp that was most common throughout Europe in the Tudor period. The 100-year-old sample from the Royal Botanic Gardens, Kew, obtained from the Japan Exhibition in 1910 (Figure 36(d)), serves as a useful reference and aids with the identification of fibres from the rope and sail cloth of the

Mary Rose. Flax and hemp are not easy to distinguish using optical microscopy or even with FTIR spectroscopy. This is the reason polarised-ATR-FTIR spectroscopy is also required for purposes of identification.

Digital microscope images of the *Mary Rose* samples were taken and are presented below. The sail cloth (Figure 37(a) and (b)) is very friable, brittle, and prone to fragmentation. It is coated or encrusted heavily with dirt, with orange areas likely indicating rust (through the oxidation of iron fixtures aboard the *Mary Rose*). It contains concretions along its length possibly of silt and salts from its time in the marine environment. The thread appears to be Z-twisted which would indicate hemp, rather than flax or nettle. These are loose fragments of an interwoven sail cloth (MR81 A2603/9) which was found still attached to rope. Some areas of the spun together fibres (yarn) are thinner than others indicating probable loss of material over time. Simply unwrapping the sample or during small movements, dirt and loss of material occurs. This highlights the importance of minimising handling and the need to test characterisation methods with the reference materials first.
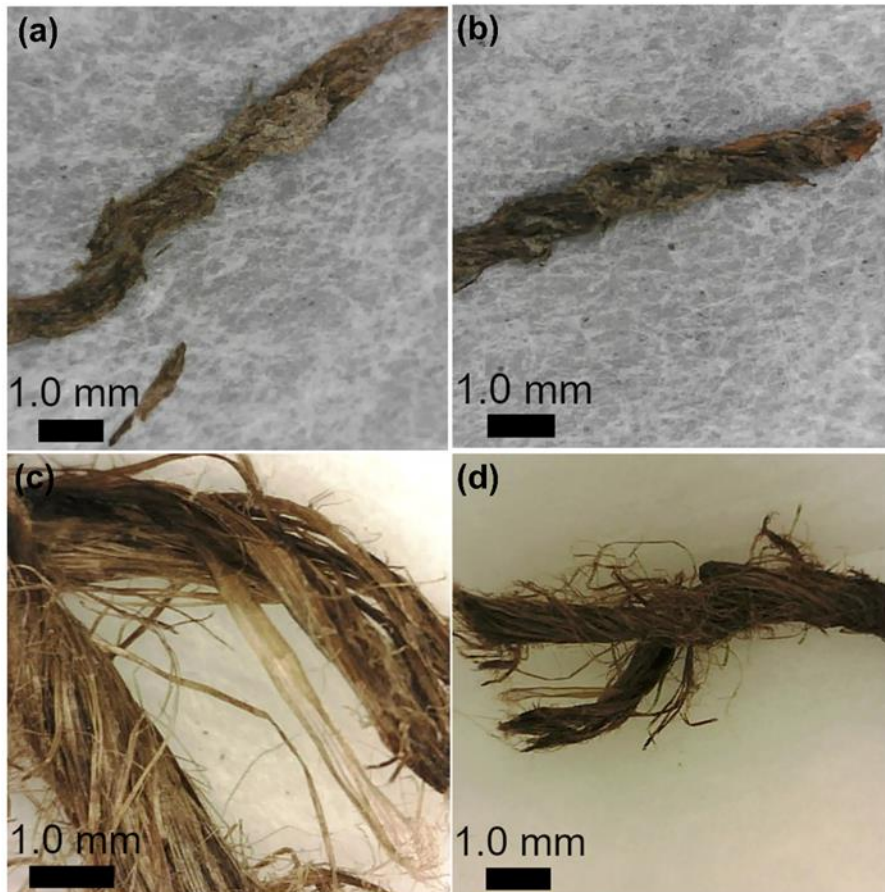
Figure 37 Digital images taken with a handheld Dino-Lite system of *Mary Rose* samples of sail cloth (**(a)** and **(b)**) and anchor cable (**(c)** and **(d)**).

Anchor cable fragments used as samples were unnumbered artefacts, which means not a lot of information on them is known. It is clear from the digital images in Figure 37(c) and (d), that they have been coated in tar as was common practise with anchor rope at the time to weatherproof it for use at sea. The rope is very roughly spun in a Z-twist suggesting hemp. It seems strong but its thin segments and its fragmented state suggests that these sections of the rope have come from deterioration of a larger artefact. The apparent strength of the anchor cable fragments could be due to the rope being stiff with tar and not flexible due to healthy fibres, or the tar could have protected the fibres from more severe degradation.

4.2.2 Optical microscopy imaging of fibre samples

The digital microscope is very useful when considering large or fragile artefacts since it is very mobile and can be easily manoeuvred to the region of interest. A traditional optical microscope uses visible light like the digital microscope but allows for greater magnification and resolution than with a basic digital microscope. This makes it easier to distinguish

between an artificial fibre (like viscose) and natural fibres with optical microscopy. Figure 38(a) shows a single viscose fibre with the characteristic features of no nodes or dislocation and with internal fibres aligned with the fibre axis due to the extrusion process. There is a slight twist observed in this fibre which could be due to the way it was spun together which results in kinked fibres demonstrated in the digital image (Figure 36(a)). Distinguishing fibres with optical microscopy becomes slightly trickier when considering bast fibres. Figure 38(b) shows a single fibre from the modern linen sample with Figure 38(c) and (d) presenting fibres from the Hemp1910 and Flax1851 reference samples. These are microscope images taken when observed with polarised light. Polarised light can be useful for distinguishing between fibres for identification purposes and for highlighting important features such as cross-markings and dislocations.
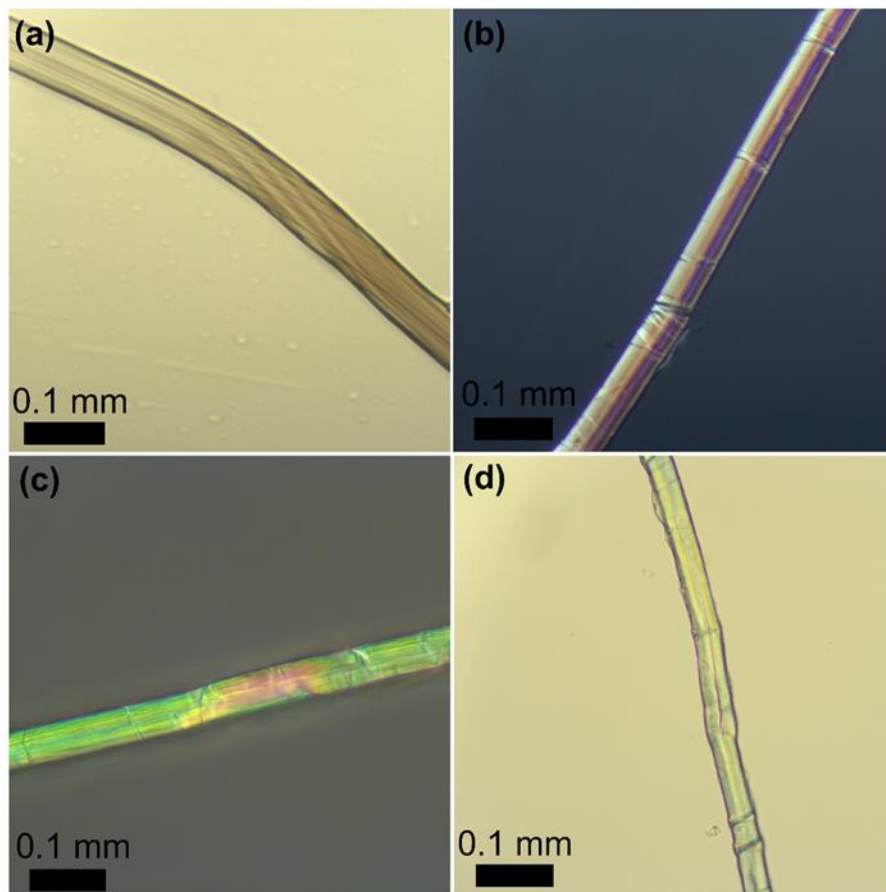
Figure 38 Microscope images with 40x lens of **(a)** viscose **(b)** modern linen reference fibre under polarised light **(c)** Hemp 1910 historic reference under polarised light and **(d)** Flax 1851 reference fibre.

Anchor rope samples from the *Mary Rose* are shown in Figure 39. Deterioration can be observed in these microscope images on the edges and surfaces of the fibres.
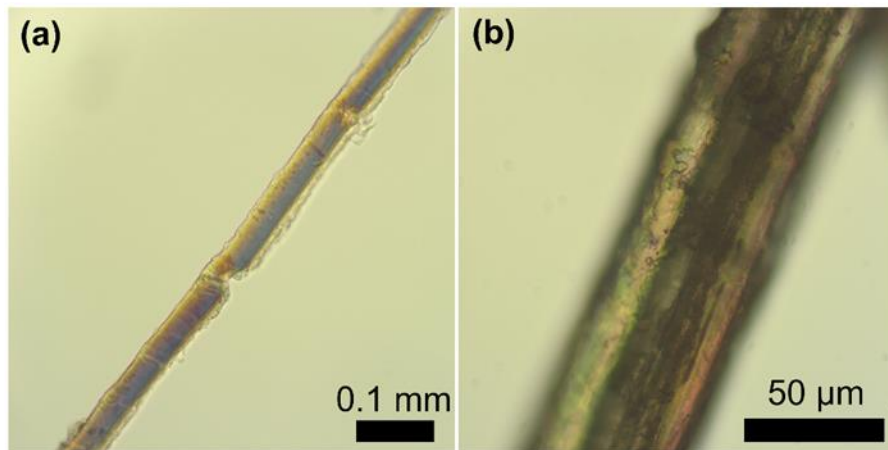
Figure 39 Microscope images of fibres from the *Mary Rose* anchor cable fragments.

Sail cloth from the *Mary Rose* is presented in Figure 40 in which the sample appears to be in a very degraded state, making it difficult to observe individual fibres. Fibres are observed in bundles and dislocations, with broken fibres and twisted fibres also seen. In polarised light, crystal-like material can be seen covering the fibres, particularly at the ends. Fibre bundles can also be observed, obscured by concretion, possibly comprised of a dirt, silt, or salts. This indicates that the organic material of the sail cloth fibres could be heavily mineralised (organic matter replaced largely by inorganic minerals).
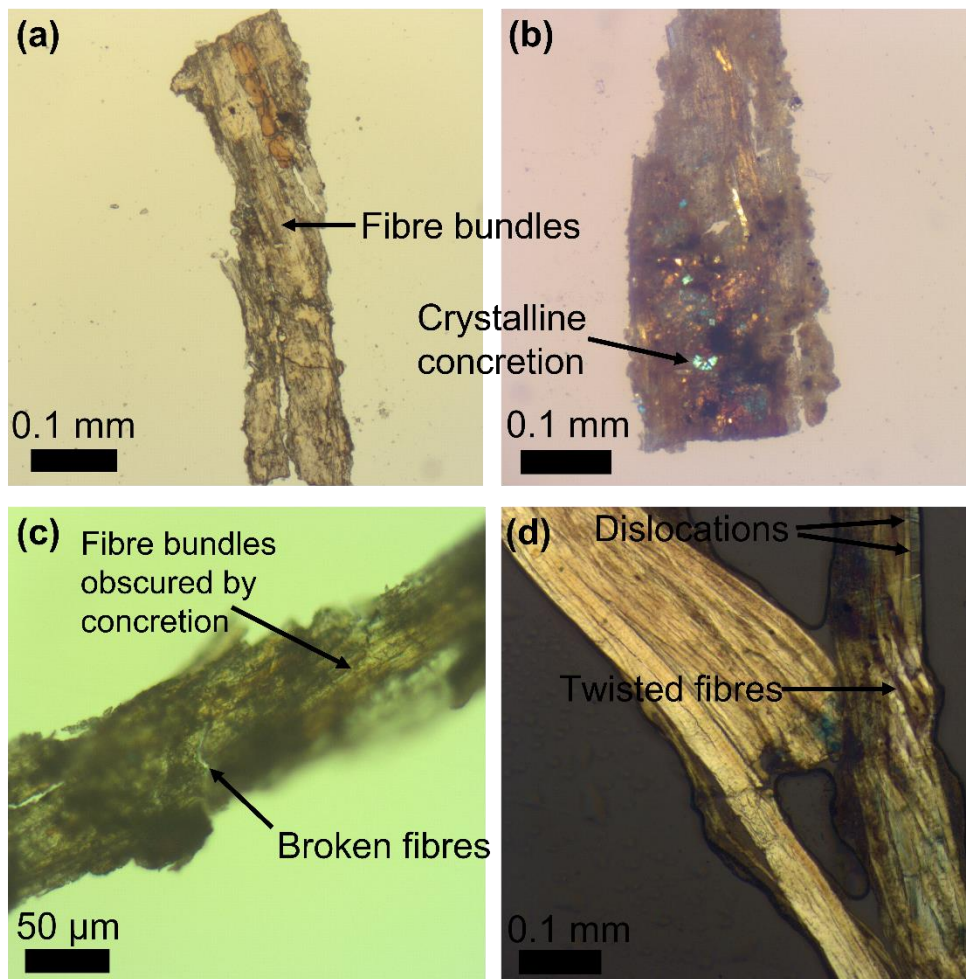
Figure 40 Microscope images of *Mary Rose* sail cloth fragments

4.2.3 Scanning electron microscopy (SEM) imaging of fibre samples

SEM of the fibres was carried out using the Inspect F50. Fibres were gold coated with a Quorum Q150T ES coater with a thickness of approximately 7 nm. Images needed to be taken quickly due to the charging effect observed in the sample. This is most likely due to the gold coating unable to completely coat under the fibres, especially when the fibres are bunched together. Single fibres did not appear to undergo charging effects as much as bunches of fibres. This bundle of fibres was difficult to avoid with the archaeological samples because they were already clumped together in bundles, probably due to partial mineralisation of the fibres from their time on the seabed.

Figure 41 shows the SEM images of the modern linen fibre sample at different magnifications while trying to get a representative idea of the sample. Cross-markings, nodes or dislocations are easily observed at higher magnifications and the way the individual fibres are twisted into a thread is easily observed at lower magnification. From these images, the variable nature of

the fibres can be seen. There are many rough pieces around the fibres most likely remaining from a simple or coarse processing method. The cross-markings are typical of bast fibres and the lines on the surface give an idea of the fibrillar orientation in the individual fibre. In this sample, the orientation seems to be Z or clockwise which would indicate hemp rather than flax or nettle fibres. The approximate width of these fibres is 20 µm though the width of the fibres is not a particularly useful way of identifying the fibre as there is huge variety in width of fibres from the same plant species.
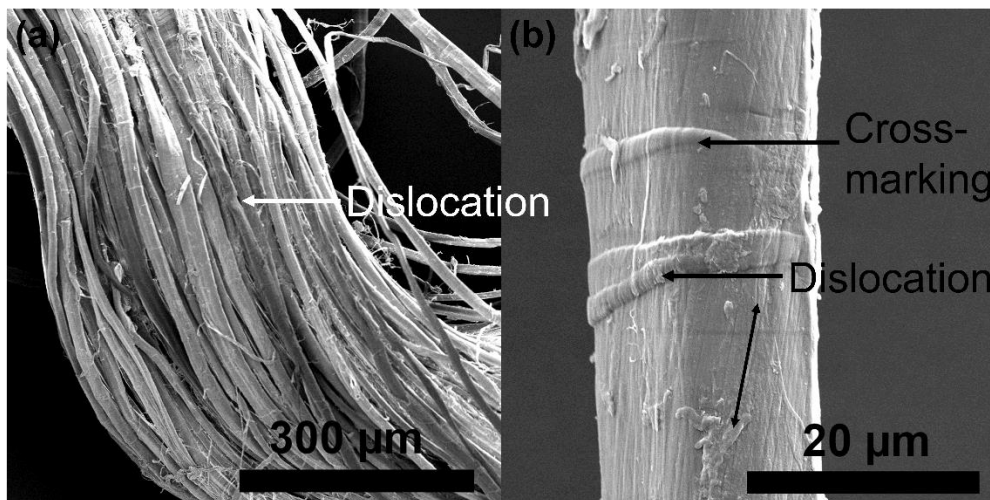
Figure 41 SEM micrographs of the modern linen reference sample at **(a)** 400x and **(b)** 6000x magnification. Both images are annotated to give an example of the cross-markings and dislocations observed in the samples and the diagonal arrow demonstrates the Z-twist fibrillar orientation.

Flax1851 sample micrographs in Figure 42(a) and (b) show dislocations. The surface appears littered with dirt or extraneous material. Sheaths around fibres indicate not heavily or simply processed fibres. Some fibres seem to be joined with this extraneous material, possibly pectin. Hemp 1910 SEM images (Figure 42(c) and (d)) show clear nodes. There is no evidence of the rough sheaths found around some of the flax fibres in this hemp sample. It is difficult to see clear areas of degradation but some material on the surface is noted. The fibres are also bundled together, and some are split and joined together by extraneous material.
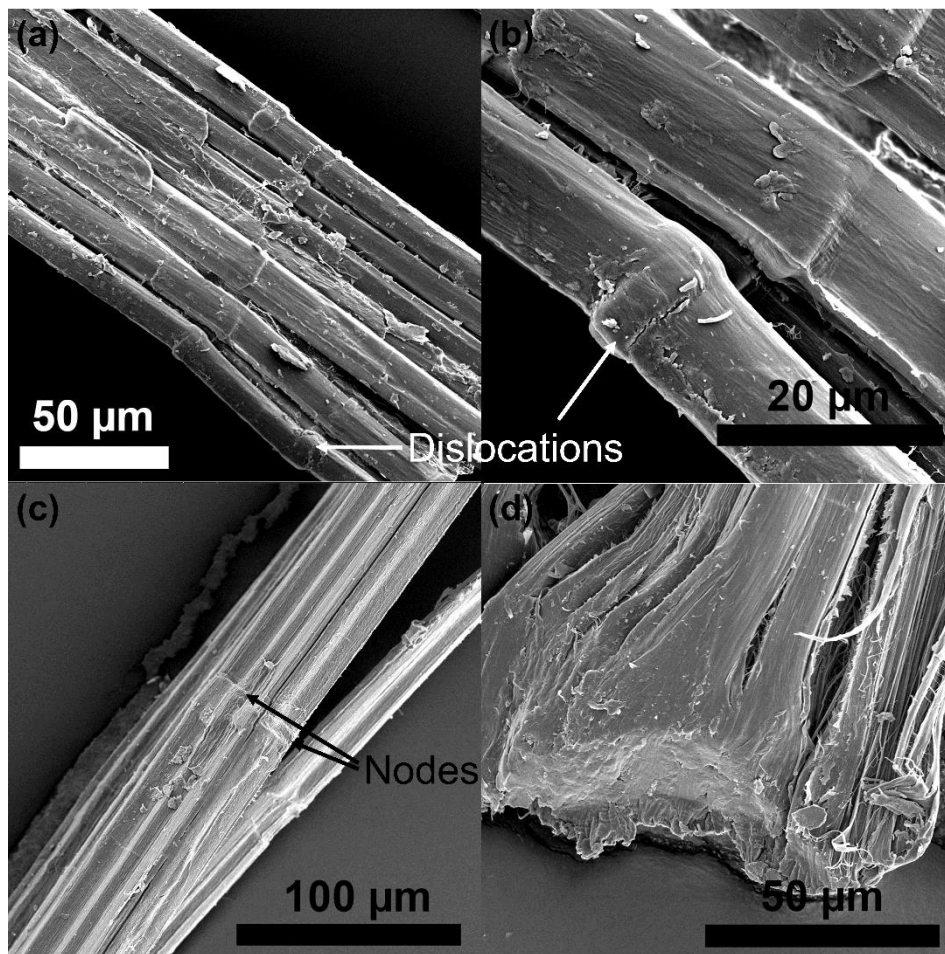
Figure 42 SEM micrographs of historical reference fibres **(a)** Flax 1851 fibres at 1600x **(b)** same fibres at 6000x **(c)** Hemp 1910 fibres at 1200x and **(d)** Hemp1910 fibres from a different area at 2500x.

The *Mary Rose* anchor cable fibres appear to be in a degraded state which is evident in the SEM micrographs in Figure 43. The degradation appears to be heterogeneous, with some fibres appearing more degraded than others. It is interesting to observe that degradation seems to be occurring within the fibres rather than concentrated on the surfaces. Figure 43(a) (with further magnified version of the same fibre in Figure 43(b)) shows this anchor rope fibre is reminiscent of other archaeological fibres which have been mineralised.[7] Figure 43(d) also shows evidence of fibrils in an S-twist orientation which would suggest flax or nettle fibres.
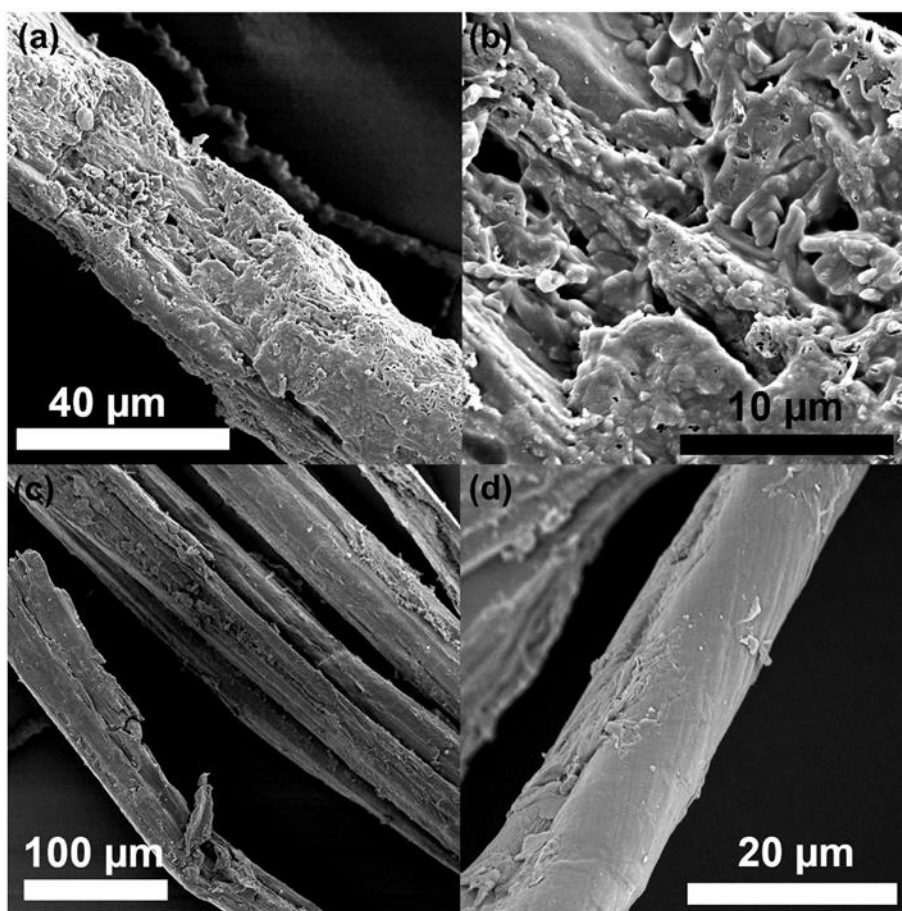
Figure 43 SEM micrographs of *Mary Rose* anchor cable fragments **(a)** at 3000x **(b)** same area at 12000x **(c)** a different area of the anchor cable fragments at 800x and **(d)** another area at 6000x

4.2.4 FTIR spectroscopic investigations of fibre samples

FTIR spectroscopy can unveil a myriad of information about fibre samples. The spectra of fibres give details on their microstructure and differences in wavenumber positions and intensities can indicate fibre degradation. Unpolarised ATR-FTIR spectra of the modern linen, historic flax (Flax1851 and soiled linen 1800s samples), and historic hemp (Hemp1910) fibres are analysed in this section in order to compare with the *Mary Rose* anchor cable and sail cloth samples. All spectra presented have been baseline corrected. As the method of measurement was ATR, only the surface of the fibres was studied (up to a penetration depth of around 1 μm). This means that the differences observed in the spectra between the fibres arises due to differences in the surface structure, rather than the bulk of the fibre.

An annotated FTIR spectrum of modern linen is provided in Figure 44 for reference of positions of common bands in a bast fibre FTIR spectrum and is later compared with the

historic fibres in Figure 46. A table showing the main band assignments for cellulosic fibres and giving more information on these bands is presented in Table 6 for reference.
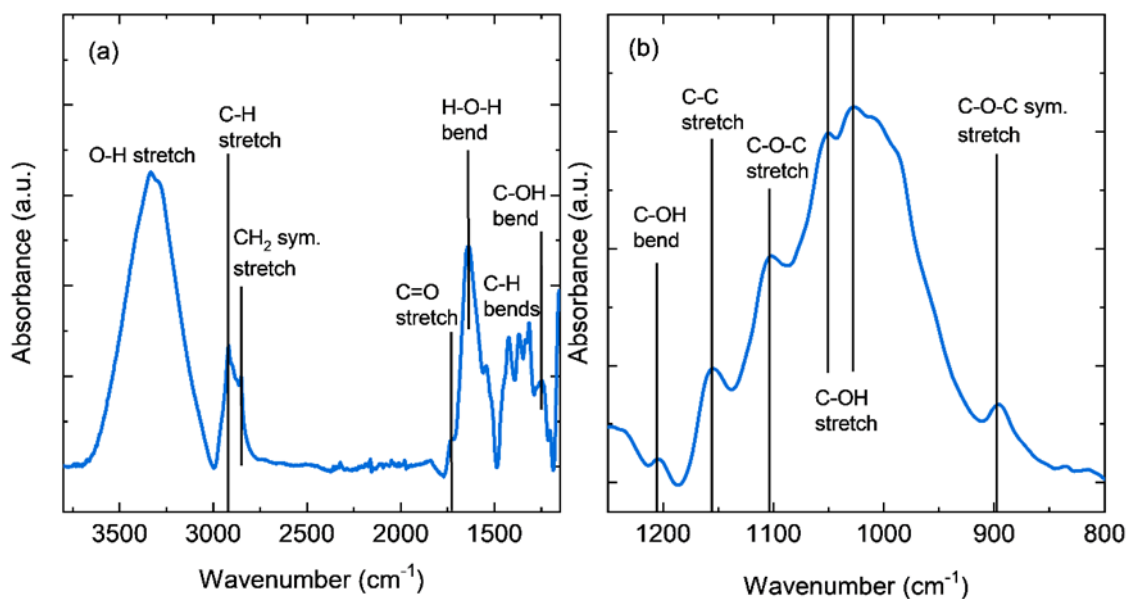
Figure 44 FTIR spectrum of the Modern Linen sample with band assignments split into wavenumber ranges **(a)** 3800 to 1300 cm^{-1} and **(b)** 1300 to 800 cm^{-1}.

Table 6 Band assignments from FTIR spectra for cellulosic fibres (wavenumbers are approximate).[8]

Wavenumber (cm^{-1})	Assignment	Extra information
3336	O-H stretch	
2886	C-H stretch	
2852	CH$_2$ symmetrical stretch	Flax
1734	C=O ester stretch	From flax or methylesterified pectin[9]
1640	H-O-H bend (absorbed water)	1600-1650 peaks could be nonesterified pectin[9]
1616	Benzene ring	lignin
1500	Benzene ring	lignin[10]
1430	CH$_2$ bend[9]	Cellulose, lignin[10]
1416	C-H bend	CH$_2$ and CH$_3$
1368	C-H bend	CH$_2$ or OH bend
1336	C-H bend	OH bend[9]
1320	CH$_2$ wagging	cellulose[9] or lignin[10]
1314	C-H bend	
1262	C-O stretch, C-H and O-H wagging	
1234	C-OH out-of-plane bend	C-O stretch of acetyl lignin
1202	C-OH bend, C-CH bend	
1156	C-C asymmetric ring breathing stretch	
1112	C-O-C stretch	cellulose
1052	C-OH stretch (2^0)	Hemicellulose and cellulose
1016	C-OH stretch (1^0)	lignin, hemicellulose and cellulose
994	-CH- bend	
894	C-O-C symmetric in-plane stretch	Beta glycosidic linkage[10]
700	CH$_2$ rocking[9]	
600	O-H bend	

As can be seen from the spectra in Figure 45, it is not easy to distinguish between the different cellulosic fibres using their FTIR spectra. The C=O band at around 1734 cm^{-1} observed in the Flax1851 sample shows the presence of pectin; however, it could also arise due to fibre degradation as the presence of carbonyl groups of oxycellulose increase.[8] As there is some evidence of this peak in the modern linen sample, it could be that this peak is an indication of historically processed or relatively unprocessed samples. Kavkler *et al.* noted that this peak was absent in flax and hemp samples from more recent objects than the mid-19th century which indicates this peak occurs due to improved processing methods removing impurities.[11]
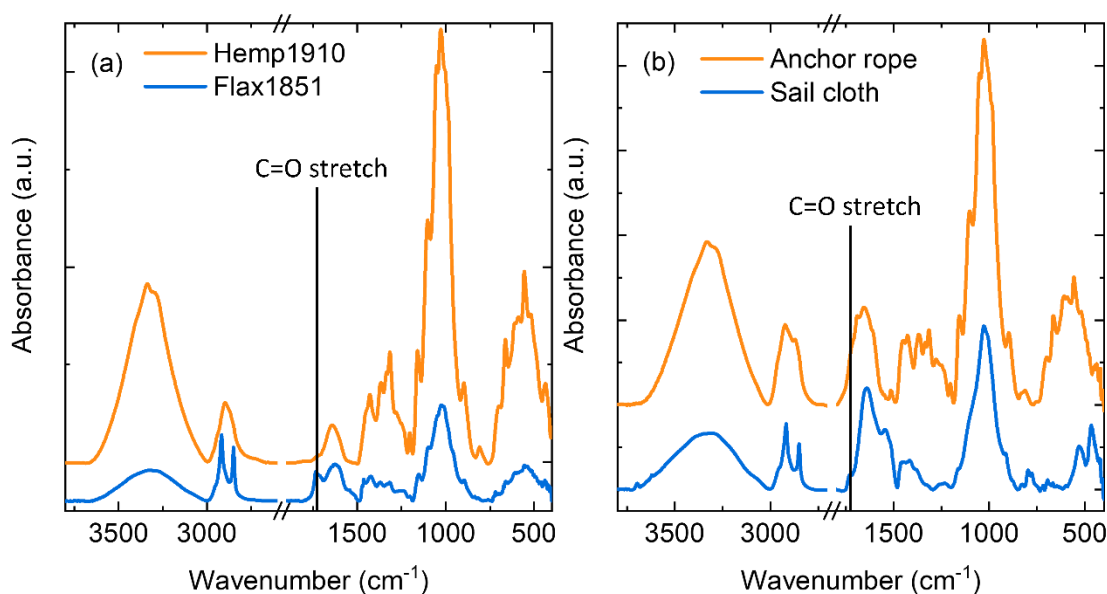
Figure 45 FTIR spectra of **(a)** Hemp 1910 and Flax 1851 historic reference samples and **(b)** the *Mary Rose* anchor rope and sail cloth samples.

In the following graphs, all spectra have been baseline corrected and normalised to 1050 cm^{-1} so that the different spectra can be compared. The 4000 to 3000 cm^{-1} region (as shown in Figure 46(a)) represents higher energy vibrational modes such as O-H and N-H stretching vibrations. Water is important in the fibre for flexibility and influences degradation through factors such as swelling. Water can be further investigated through controlled water sorption measurements (dynamic vapour sorption). The differences in intensity of the OH band may relate to degradation of the fibre as it could relate to the reactivity of the hydroxyl group on the surface of the fibres.[10] Also, hydrogen bonding is important to the structure of the fibre. There does not seem to be a clear trend with age and physical condition of the samples studied with respect to the changing intensity of the O-H band.
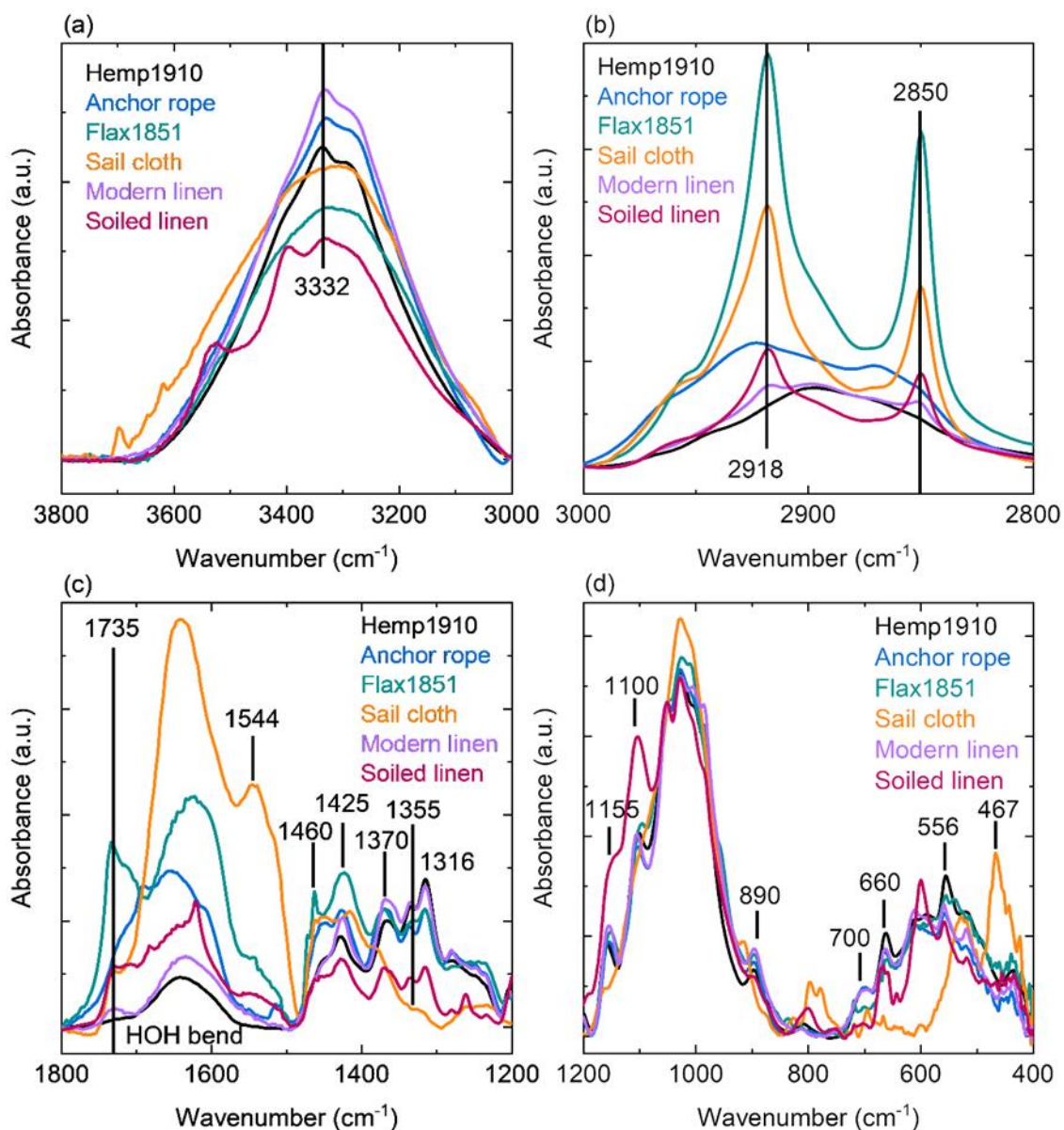
Figure 46 Comparison of the FTIR spectra of the modern linen, Hemp1910, Flax 1851, anchor rope and sail cloth fibres **(a)** O-H stretching region **(b)** CH_2 stretching region **(c)** fingerprint region from 1800 to 1200 cm^{-1} and **(d)** from 1200 to 400 cm^{-1}.

The next region from 3000 to 2800 cm^{-1} presented in Figure 46(b) is important with regards to peak ratios which are discussed in more detail in the next section. The total crystallinity index (TCI) and R_2 index, which describe the overall organic content of the fibre samples, use the peak at 2900 cm^{-1} to analyse for this. This is straightforward for the FTIR spectra of Hemp1910 and modern linen (see Figure 46(b)), but for samples where this peak is split into two distinct peaks (around 2917 and 2851 cm^{-1}) this can pose a challenge as the analysis may underestimate the overall organic content leading to misleading comparisons between the TCI and R_2.

The peak at 2851 cm^{-1} is assigned to the symmetrical CH$_2$ stretch most commonly found in flax fibres. This distinct feature found in Flax1851 and the sail cloth sample may indicate that the sail cloth is comprised of flax. However, definitive identification is difficult as there is no distinct feature at this position in the spectrum of the modern linen sample. This could be due to more modern processing methods or degradation causing a stronger distinction between the peaks. The broader peak around this wavenumber of Hemp1910, anchor rope, and modern linen could be a superimposition of the CH$_2$ peak with the C-H stretching vibration. The splitting of this peak may be due to the lignin content of the fibre as this peak splitting is not seen in a pure cellulose spectrum. It is interesting that this splitting is only present in the older flax samples (with some evidence of it in the modern linen sample but not as distinctly, which could mean this sample is a composite of flax and hemp, which is not unlikely because modern linen is sometimes not well defined as deriving from flax or hemp). The similarities between these peaks in the historic flax and the *Mary Rose* sail cloth spectra, suggest that the sail cloth is likely composed of flax which is common for sail cloth at that time.

Moving to the next region of interest (presented in Figure 46(c)), the 1735 cm^{-1} peak is attributed to the C=O stretch prevalent in spectra taken for flax samples. However, this could also be due to degradation and is associated with lignin. Absence of this peak is more common in more recent fibres (post mid-19th century), which could explain why it is not observed in Hemp1910. It is thought that this is due to the ability of different processing methods at removing impurities but it also increases with ageing cellulose.[11]

The 1544 cm^{-1} peak in the sail cloth spectrum is likely attributed to lignin.[12] If this assignment is correct, this would imply that the increased intensity of this peak in sail cloth compared with the CH and COH bands is an indicator of degradation of the cellulose in the sail cloth as the lignin peak dominates. This would, in turn, suggest that the anchor rope is not as degraded as sail cloth sample. It should be noted that such signatures may differ depending on where the spectra are measured in the sample and therefore may indicate regions of degradation. The shoulder feature which appears in the Flax1851 spectrum at this wavelength could also indicate this is more heavily degraded than all other fibres studied except the sail cloth sample. The band at 1282 cm^{-1} is not observed in either the Flax1851 or the sail cloth samples, but its presence in other fibres may indicate these fibres are more heavily degraded. The 1620 to 1660 cm^{-1} bands are common to all samples and are assigned to the water bending mode.

The bands are slightly shifted from each other which could suggest differences in the way the water interacts with these fibres. The peak in the anchor rope spectrum at 1691 cm^{-1} could also be associated with degradation products.

The C-H peaks are not as distinct or intense in the sail cloth spectrum compared to all other samples measured. This could be due to issues arising during measurement, such as poor contact with the ATR crystal. Alternatively, it could be due to heavy degradation, even mineralisation of the fibre such that there is little organic material left. The anchor rope and Flax 1851 samples have C-H peaks with lower intensities than Hemp1910 and modern linen samples, which is again likely due to degradation.

The 1335 cm^{-1} and 1316 peaks are associated with COH and HCC bending and the intensity of these peaks are known to decrease with increasing amorphous cellulose.[12] The 1335/1316 doublet also only occurs in very crystalline cellulose samples.[12] The 1370 cm^{-1} peak does not change in intensity between the fibres as much as the 1335 and 1316 peaks. This correlates with Kavkler's results where changing intensities of 1335 and 1316 peaks are attributed to the greater influence of adsorbed water on these peaks.[12] These bands are commonly used to investigate crystallinity of cellulose. Decrease in intensity of this band at approximately 1370 cm^{-1} has been correlated with increase in degradation of fibres.[12] This can be noted in Figure 46(c) as the band decreases in intensity from modern linen to Flax1851 and anchor rope, to Hemp1910 and soiled linen 1800s. The band is not distinct in the sail cloth spectrum which gives further evidence of the more severely degraded state of this sample.

The band at 1430 cm^{-1} is associated with the cellulose I form. Absence of this band and the band at 1111 cm^{-1} indicates the absence of the cellulose I form in the sample.[11] If the cellulose II form dominates, then peak shifts can be observed.[11] Due to the deviation from the 1430 cm^{-1} band and the less distinct contribution around 1100 cm^{-1} in the Sail Cloth spectrum, it can be concluded this sample showed signs of significant deterioration. The 1280 cm^{-1} band also represents crystalline cellulose.[11] This peak is less distinct in Flax1851 and the Sail Cloth spectra indicating that these are less crystalline, therefore more degraded. It is also less intense in the soiled linen 1800s spectrum.

In the final wavenumber region of interest displayed in Figure 46(d), the 432 cm^{-1} band is common to the Hemp 1910 and modern linen fibres, but is not observed in the sail cloth, Flax

1851, and anchor rope spectra. Peaks around 780 and 800 cm^{-1} in the spectrum of sail cloth could indicate the presence of sand (silicon dioxide). The band at approximately 900 cm^{-1} can represent amorphous cellulose, where broadening indicates increased amorphous cellulose content.[11] For all fibres studied except for the sail cloth, this band occurs at 890 cm^{-1}; it is shifted to a higher wavenumber in the sail cloth spectrum. This indicates sail cloth may have an increased proportion of amorphous cellulose in comparison with the other fibres. The peak at 1050 cm^{-1} for sand overlaps with bands common to cellulose making positive identification of inclusion of sand in the sample difficult. The band at approximately 1100 cm^{-1} is attributed to the C-O-C stretch. This band is marked at 1105 cm^{-1} in the Hemp1910, Soiled linen 1800s, and modern linen spectra. It is shifted slightly to a lower wavenumber in the Flax1851 spectrum and is not distinct in the sail cloth spectrum. This could indicate degradation in these fibres, particularly in the sail cloth, showing that C-O-C bonds may not be as prevalent. This could arise due to hydrolysis and oxidation processes.

This section has interpreted the FTIR spectra of the fibre samples qualitatively and used the positions of peaks in comparison with details found in the literature to arrive at provisional conclusions about the nature of the fibres. The next section takes a more quantitative approach in interpreting the same spectra, by using the absorbance intensity at particular wavenumbers to provide further information on the deterioration of the samples.

4.2.4.1 Peak Ratios

Peak ratios can provide information on the degradation of fibres and the total crystallinity index (TCI), lateral order index (LOI), R_1 and R_2 ratios for the samples under study are presented in Table 5. These ratios were explained in further detail in section 2.1. R_1 and R_2 ratios represent the lignin and cellulose content over the overall organic content respectively. More lignified fibres tend to be found at higher values for both R_1 and R_2 ratios.[13] These ratios for the Sail cloth sample may indicate that this sample does not have much cellulose remaining, with mainly lignin and/or amorphous cellulose remaining.

The ratio between the 1336 cm^{-1} and 1316 cm^{-1} bands has been shown to give an indication of degradation in fibre samples.[11] This is due to these bands only occurring in highly crystalline cellulose I and the band at 1336 cm^{-1} usually decreases during degradation. For the samples under study, the ratios obtained from the intensities of these peaks are displayed in Table 7.

Further studies, for example a comparative analysis with a modern hemp sample, could be helpful in fully assessing the extent of degradation in these samples. However, it should be noted that while FTIR peak analysis is helpful in assessing degradation, it is not always possible to reach definite conclusions since plants may have been cultivated and processed in different ways and the environment in which the textile has been stored also varies. These factors all influence the structure of the polymer chains in the fibre, thus likely contributing to spectra observations.

Table 7 Table displaying calculated peak ratios from baseline corrected spectra normalised to the intensity of the 1050 cm^{-1} band.

Sample	1336/1316	TCI	LOI	R_1	R_2
Modern linen	0.88	1.50	0.75	0.15	0.57
Hemp1910	0.81	1.29	0.85	0.09	0.35
Soiled linen 1800s	0.88	1.15	0.82	0.11	0.63
Anchor cable	0.85	1.07	0.97	0.30	0.81
Flax1851	0.89	0.61	1.15	0.61	1.01
Sail cloth	1.44	0.57	1.41	1.01	2.35

The TCI is generally decreasing with the age of the sample. A lower TCI has been previously linked to more heavily biodegraded samples.[12] Also, higher TCI values were related to an increase in tensile strength, which is related to higher levels of fibre preservation.[14] Applying this information to the samples under study reveals the *Mary Rose* sail cloth sample to be the most degraded sample, with other features in the spectrum supporting this conclusion. However, the difference in TCI between the anchor rope and sail cloth, which are presumably of a similar age, shows that differences between individual artefacts and how they were treated at the time and in the burial and conservation processes may be more influential.

The LOI represents the ratio of crystalline to amorphous cellulose content of the fibre. Flax1851 and sail cloth samples display a higher proportion of crystalline cellulose to amorphous cellulose. This is surprising when peak identification and the TCI indicates these fibres are more degraded than the others. However, it has been suggested that degradation of cellulosic fibres proceeds with amorphous regions as they are more readily accessible for chemical attack. This would cause a higher ratio of crystalline to amorphous cellulose in the fibres if the amorphous regions were heavily degraded. This can still mean the fibres are not structurally sound as there could be discrete regions of crystalline cellulose.

4.2.4.2 Polarised ATR-FTIR Spectroscopy

Polarised ATR-FTIR spectra were measured between 0 and 180° in 7.5° intervals for all fibres. All spectra were baseline corrected to allow comparison of peak intensities. With a polariser in the beam, the intensity of certain bands change as the fibre is rotated. This phenomenon is known as dichroism and can be defined as being parallel or perpendicular to the beam. Table 8 shows important bands from a cellulosic fibre IR spectrum and highlights the dichroic properties of each band. Polymer orientation is not only of theoretical interest, it is important as it can be related to mechanical properties such as tensile strength.[15]

Table 8 Band assignments from bast fibre FTIR spectra with orientation information of each band.

Band	Assignment	Dichroism
3300	ν(OH) free	Parallel
3260	ν(OH) free	Parallel
2900	ν(CH)	Perpendicular
2850	ν(CH$_2$) symmetrical stretching	Non
1425	δ(CH)	Parallel
1370	δ(CH)	Parallel
1355	δ(CH$_2$) wagging	Parallel
1280	δ(CH$_2$) twisting	Parallel
1160	ν(C-C) ring, breathing, asymmetric	Parallel
1060	ν(C-OH) secondary alcohol	non

Figure 47 shows the polarised spectra of the Flax1851 sample at angles between 0° and at 180°. This demonstrates how the orientation of the fibre while using a polariser in the ATR-FTIR set-up leads to differences in band intensities. These differences in intensity can then be used to derive the crystallinity index to ultimately determine how degraded the fibre is in comparison with others and to help identify the fibre. For example, flax and hemp have very similar FTIR spectra so the polarised-ATR-FTIR method can be used to distinguish these fibres.[16]

The absorbance at 1050 cm^{-1} and 1160 cm^{-1} was recorded for each spectrum at each angle. The orientational index, X, was given for each angle by dividing the intensity at 1160 cm^{-1} by the intensity at 1050 cm^{-1}.

$$X = \frac{I_{1160}}{I_{1050}}$$
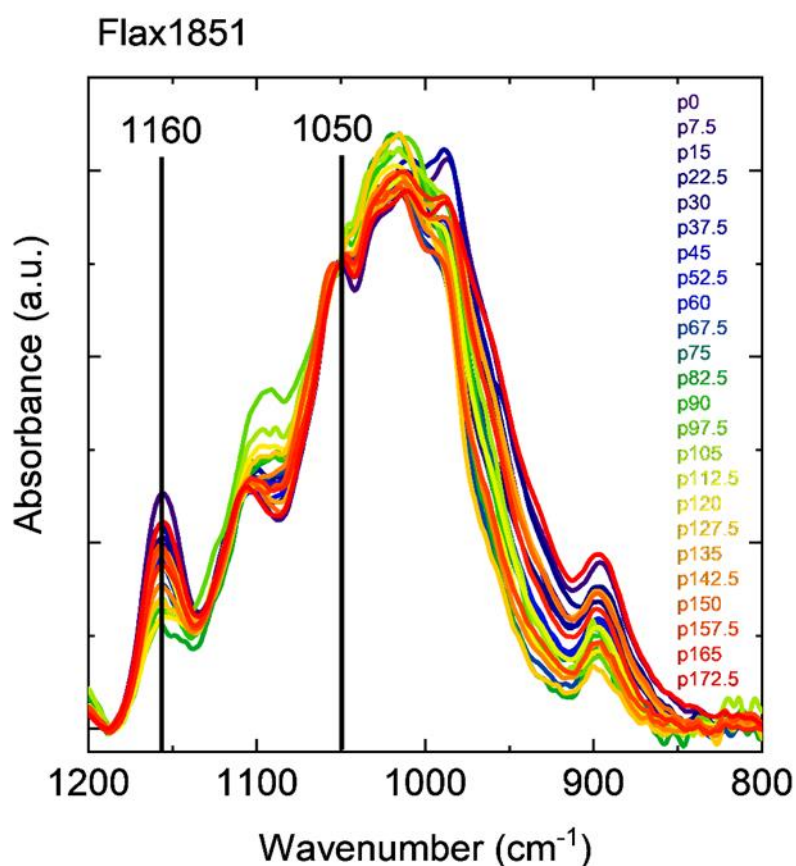
Figure 47 Polarised ATR-FTIR spectra of the Flax1851 sample measured at 7.5° intervals from 0° to 180°. Lines at 1050 cm^{-1} and 1160 cm^{-1} show where the intensity of the band was recorded for input into the crystallinity index calculation.

The whole experiment was completed three times on each sample type. Fibres were replaced every few measurements at random angles in the run to prevent systematic errors due to pressure of the ATR tip. The whole run (0° to 180°) was repeated three times for the sample in question. Once an orientational index had been obtained for each angle and replicated on different fibres, the values were averaged and the maximum and minimum highlighted. The maximum orientational index corresponds with the parallel fibre component and the minimum with the perpendicular.

Table 9 Average orientational index, X, of the Flax1851 fibre sample at angles from 0-180°. Highlighted areas show the angle of the highest orientational index and the lowest, which correspond to the parallel and perpendicular fibre components, respectively.

Angle (º)	Average X	
0.0	0.502	
7.5	0.493	
15.0	0.463	
22.5	0.507	Maximum parallel
30.0	0.443	
37.5	0.419	
45.0	0.399	
52.5	0.368	
60.0	0.327	
67.5	0.259	
75.0	0.194	
82.5	0.184	
90.0	0.155	
97.5	0.145	
105.0	0.138	Minimum perpendicular
112.5	0.208	
120.0	0.204	
127.5	0.219	
135.0	0.280	
142.5	0.310	
150.0	0.365	
157.5	0.438	
165.0	0.420	
172.5	0.448	
180.0	0.469	

The crystallinity parameter, X, was calculated using these maximum and minimum values of the orientational index according to:

$$\chi = \frac{X_{II} - X_{\perp}}{X_{II}}$$

An absolute crystallinity value cannot be obtained due to contributions from crystalline content in the primary cell wall depending on how deeply the IR radiation penetrates the sample.

A crystallinity parameter was calculated for all of the samples studied except the sail cloth which was in a very encrusted state making it difficult to extract a single fibre for the

polarised-ATR-FTIR method. The overall results of the polarised-ATR-FTIR experiments are presented in Table 10.

Table 10 Table of results obtained from polarised ATR-FTIR spectra

Sample	Crystallinity Parameter	$X_{82.5}-X_{97.5}$
Modern Linen	0.60	0.038875
Flax 1851	0.59	0.010325
Soiled Linen 1800s	0.72	0.01476
Hemp 1910	0.73	0.03945
Anchor cable	0.63	-0.00476
Modern Viscose	0.36	0.00278

An increase in crystallinity is often observed first in textiles, even if it is degrading, before a drastic decrease in crystallinity as the amorphous regions holding together the crystalline fragments break. An increase in crystallinity is initially observed as amorphous regions are more vulnerable to attack so there seems to be more order, more alignment with the fibre axis because the disordered regions are removed. However, when degradation reaches a point where the amorphous regions are no longer holding the crystalline regions together, more disorder is observed, and degradation of crystalline regions is more likely to occur.

4.3 Concluding remarks

This chapter has explored a range of techniques to gain information primarily on two cellulose-based *Mary Rose* artefacts of sail cloth and anchor rope. This is the first reported FTIR and polarised-ATR-FTIR study of *Mary Rose* fibres. Optical microscopy has shown the samples to have cross-markings and nodes indicative of bast fibres but the difficulties in observing archaeological fibres through optical microscopy and identifying them are displayed clearly. Optical microscopy was also useful for showing the deterioration of the fibre surfaces and how dirt and other mineral inclusions are present in the sail cloth sample. SEM images further informed on surface degradation present in the anchor rope sample. This is in contrast to the lower levels of degradation observed in the historic samples of Flax1851 and Hemp1910.

ATR-FTIR spectroscopy was utilised to provide both qualitative and quantitative information on the bonding present in the samples for the first time. Peak positions and intensities were studied, indicating the dominance of crystalline or amorphous cellulose or lignin on the

spectra. This in turn gives an indication of the state of degradation of the artefact. Peak ratios have been used to compare the degradation in the fibres and to further identify the fibres. The total crystallinity index has shown sail cloth to be the most degraded of the samples studied. The anchor cable does not seem so badly degraded in comparison with the sail cloth based on the TCI and this could be attributed to the use of tar at the time to preserve the ropes for use at sea.

To extend this work in the future, other techniques to further answer some of the questions posed in the introduction to this chapter include: energy dispersive X-ray spectroscopy (EDX), XRD, and FTIR microscopy. Spatial information is particularly important with artefacts and natural fibres due to their variability and uniqueness. With this knowledge, a technique such as FTIR microscopy, where IR spectra can be correlated with pixels in an optical microscope image, would be very useful to correlate visual areas of degradation with IR data. EDX would be valuable for identifying elements comprising the debris on the surface of the fibres and to possibly determine if the organic fibre had been partially mineralised. Moreover, analysing the pair distribution function (PDF) from X-ray, neutron or total scattering data would be informative for these samples as this technique could identify and quantify amorphous and crystalline phases present in the samples.[17] This is particularly useful for fibres because they are complex structures with amorphous and crystalline regions and this information would be useful in determining the extent of their degradation.

Radiocarbon dating was unnecessary for these samples due to the advantage of having a record of the history of the *Mary Rose*. It is likely that these samples date from the early 16th century. Strontium isotope tracing generally can be used for gaining information on the provenance of textile artefacts, possibly illuminating where the raw materials originally came from before use on the ship, if further information like this was required.[18] This could lead to information on whether the sail cloth and rope were manufactured locally or otherwise.

References

1   M. Jones, *For Future Generations: Conservation of a Tudor Maritime Collection*, The Mary Rose Trust, 2003.

2   E. Haugan and B. Holst, Flax look-alikes: Pitfalls of ancient plant fibre identification, *Archaeometry*, 2014, **56**, 951–960.

3   E. Haugan and B. Holst, Determining the fibrillar orientation of bast fibres with polarized light microscopy: The modified Herzog test (red plate test) explained, *J. Microsc.*, 2013, **252**, 159–168.

4   J. A. Suomela, K. Vajanto and R. Räisänen, Seeking Nettle Textiles – Utilizing a Combination of Microscopic Methods for Fibre Identification, *Stud. Conserv.*, 2018, **63**, 412–422.

5   G. Skoglund, M. Nockert and B. Holst, Viking and early middle ages northern scandinavian textiles proven to be made with hemp, *Sci. Rep.*, 2013, **3**, 1–6.

6   M. Dunbar and T. M. Murphy, DNA analysis of natural fiber rope, *J. Forensic Sci.*, 2009, **54**, 108–113.

7   M. Gleba and D. Griffiths, Textile Remains From a Middle Bronze Age Burial in Sidon, *Archaeol. Hist. Lebanon Issue*, 2011, **34–35**, 285–296.

8   P. Garside and P. Wyeth, Identification of Cellulosic Fibres by FTIR Spectroscopy, *Stud. Conserv.*, 2003, **48**, 269–275.

9   S. Alix, E. Philippe, A. Bessadok, L. Lebrun, C. Morvan and S. Marais, Effect of chemical treatments on water sorption and mechanical properties of flax fibres, *Bioresour. Technol.*, 2009, **100**, 4742–4749.

10   I. L. A. da Silva, A. B. Bevitori, L. Araujo Rohen, F. Muylaert Margem, F. de Oliveira Braga and S. Neves Monteiro, Characterization by Fourier transform infrared (FTIR) analysis for natural jute fiber, *Mater. Sci. Forum*, 2016, **869**, 283–287.

11   K. Kavkler, N. Gunde-Cimerman, P. Zalar and A. Demšar, FTIR spectroscopy of biodegraded historical textiles, *Polym. Degrad. Stab.*, 2011, **96**, 574–580.

12   K. Kavkler, Z. Smit, D. Jezersek, D. Eichert and A. Demsar, Investigation of biodeteriorated historical textiles by conventional and synchrotron radiation FTIR

spectroscopy, *Polym. Degrad. Stab.*, 2011, **96**, 1081–1086.

13   P. Garside, University of Southampton, 2002.

14   Y. P. Yang, Y. Zhang, Y. X. Lang and M. H. Yu, Structural ATR-IR analysis of cellulose fibers prepared from a NaOH complex aqueous solution, *IOP Conf. Ser. Mater. Sci. Eng.*, , DOI:10.1088/1757-899X/213/1/012039.

15   Investigating Polymer Orientation with FTIR-ATR - ProQuest, https://search-proquest-com.sheffield.idm.oclc.org/docview/1505018918?rfr_id=info%3Axri%2Fsid%3Aprimo, (accessed 9 March 2020).

16   P. Garside and P. Wyeth, Identification of Cellulosic Fibres by FTIR Spectroscopy: Differentiation of Flax and Hemp by Polarized ATR FTIR, 2006, **51**, 205–211.

17   P. Bordet, Comptes Rendus Physique Application of the pair distribution function analysis for the study of cultural heritage materials, *Comptes Rendus Phys.*, 2018, **19**, 561–574.

18   L. Bender Jørgensen and K. Grömer, The Archaeology of Textiles – Recent advances and new methods, *Portal, Godišnjak Hrvat. Restaur. zavoda*, 2012, 45–68.

Chapter 5: Characterisation of proteinaceous artefacts retrieved from the *Mary Rose*

This chapter explores routes to characterising proteinaceous artefacts, specifically wool and leather samples retrieved from the *Mary Rose,* to investigate their nature and provenance. A series of investigations using optical microscopy and spectroscopic methods were applied.

5.1 Characterisation of wool fibres

For comparative analysis, reference wool samples from modern sources have also been subjected to the same characterisation techniques. The *Mary Rose* wool sample (given the artefact code MR81 A4124) was found attached to a heavily concreted piece of sail cloth. The artefact card description notes that this was padding and associated with leather (artefact A1194), which was a personal metal and organic accessory. This suggests the wool is not only interesting to look at purely from a material properties viewpoint but also from a historical point of view. The fibres from the *Mary Rose* wool sample have been examined visually and with optical and scanning electron microscopy. The FTIR spectra of the *Mary Rose* wool fibres have then been compared with those of modern reference wool samples to investigate the extent of degradation in these historic artefacts. The modern reference samples include a set of different wool fibre types: Cochno, Jacobs, and Shetland. Cochno wool is a reference fibre obtained from the University of Glasgow's Cochno farm where Scotch Mule sheep are bred. It is an undyed, double-knit, and worsted-spun wool that had been subjected to cleaning, carding, and spinning processes. The reference Jacobs sample came from black Jacobs tops that were purchased from wildfibers.co.uk. Wool tops are fibres normally used for spinning, felting, and dyeing so have not yet been spun into yarn. The Jacobs tops were naturally black and undyed fibres, which had been carded and combed before purchase. Carding and combing processes allow for separation of short and long fibres, disentanglement, fibre separation and removal of any foreign species. The Shetland sample was also obtained from wildfibres.co.uk and came from black Shetland tops which have also been carded and combed.

5.1.1 Microscopic analysis of *Mary Rose* wool fibres

Figure 48 displays a photograph and digital microscope image of the *Mary Rose* wool sample. It is clear that this sample comprises roughly spun wool fibres, which appear to be assembled

in thin, bent, and twisted strands. This bending may be a result of how this artefact was found in storage. A closer look at a bend in a wool fragment in Figure 48(b) shows some other small contaminating fibres, lighter in colour. These are most likely to have come from the sail cloth found associated with the wool. In the bottom left corner of Figure 48(b) there is also some evidence of salt or sand deposits on some areas of the fibres. Although the wool fibres from this sample are roughly spun together and shedding of fibres can be observed, the fibres appear to be well-preserved when viewed by eye or with a digital microscope. It should be noted that it is often the case that archaeological fibres, particularly woollen fibres, appear by eye to be well-preserved. However, the extent of degradation is more evident upon closer detailed study.[1] In the case of marine archaeological wool fibres, there exist multiple degradation paths which may affect the artefact, including a combination of slow hydrolysis, anaerobic bacterial degradation, and mechanical erosion over time. It is possible that some degradation processes may still be occurring during storage.
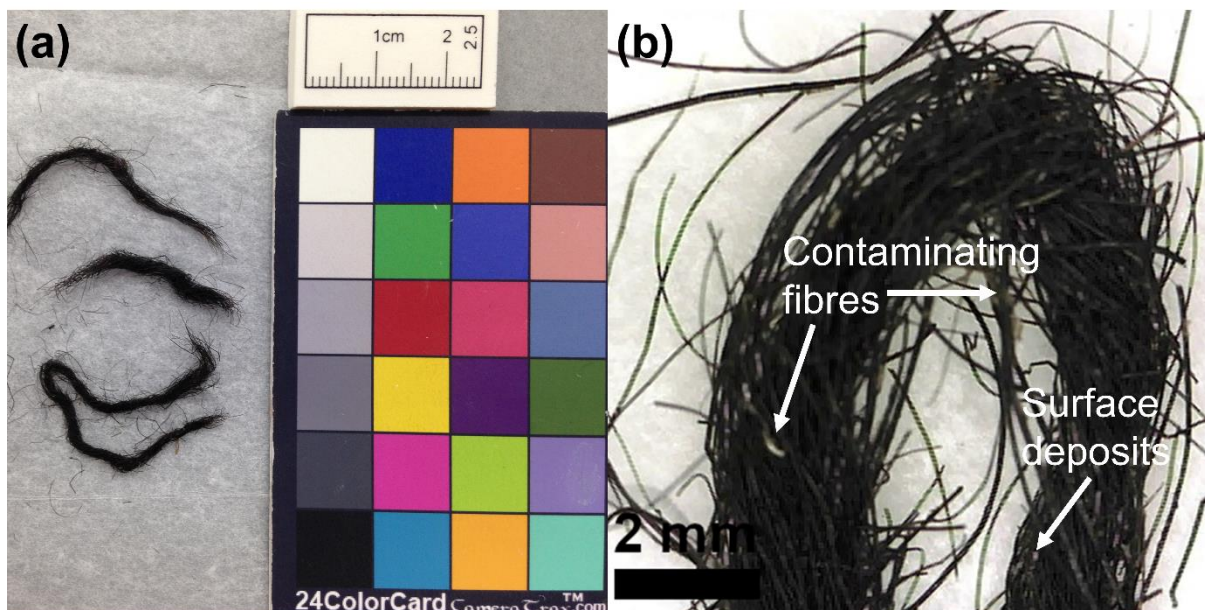
Figure 48 The *Mary Rose* wool sample **(a)** from a macroscopic level compared with a colour card and **(b)** viewed with a digital microscope with annotations displaying contaminating fibres and surface deposits.

It is clear from optical microscopy observations that the *Mary Rose* wool fibres have undergone some damage. A series of optical microscope images are given in Figure 49 of *Mary Rose* wool fibres which clearly show regions with breakages and splitting of the fibre. Usually, the cell walls and intercellular materials between the cuticle and the cortex prevent water

and other potentially harmful compounds from penetrating the fibre.[2] However, the split in the fibre apparent in Figure 49(a) penetrates into the middle of the wool fibre and could act as a facile route for water ingress as well as for other harmful compounds to reach and degrade the interior of the fibre. Longitudinal splitting such as this has previously been attributed to mechanical erosion or bacterial degradation processes.[3] Although there is noticeable damage and evidence of dirt on the surface, the fibres are still distinguishable as animal hair fibres under the optical microscope. Polarised light was used when taking both images in Figure 49 to highlight the features of the fibre. The advantage of polarised light is owing to the black colour of the fibre which prevents any details being observed when viewed with ordinary light.
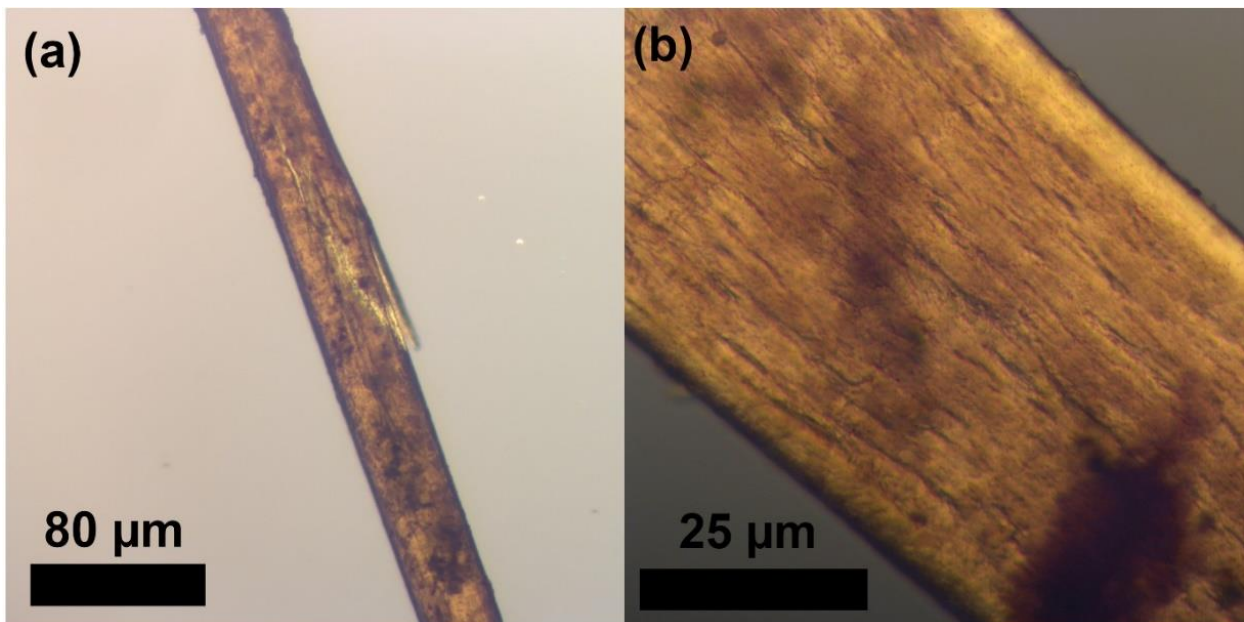
Figure 49 Optical microscope (Zeiss Axiolab polarised light microscope PM2) images of *Mary Rose* wool fibres at magnifications of **(a)** 10x and **(b)** 40x.

Optical microscopy can also provide information on the interior structure of the fibres. This is in contrast to SEM, which primarily interrogates the surface morphology. In Figure 49(b), a difference between the edge of the fibre (the cuticle) and the interior cortex can be observed. The cortex is composed of crystalline proteins in an amorphous protein matrix.[1] In some animal fibres, the cortex surrounds a medulla in the centre of the fibre. This can usually be observed by optical microscopy and can be intermittent, continuous, or even absent.[4] In the case of these *Mary Rose* fibres, the presence of a medulla was not observed. This could be due to the difficulties in observing details of the opaque fibres or simply that the medulla is

absent as is the case for some animal fibres.[4] It is usually the case, however, that coarse sheep wool fibres have a continuous, hollow medulla so it is unusual to not have observed this.[2]

SEM images, presented in Figure 50, provide further detail of the surface morphology of the *Mary Rose* wool fibres. From the SEM images below, it is possible to observe the cuticular scales of the wool. It can be clearly observed in these images that, in many areas, these scales are covered in dirt which could be due to debris on the surface or due to partial mineralisation of the fibre where the structure has become more amorphous over time. This debris could be soil, dust, sand, or derived from biological substances. Although these fibres have undergone a cleaning process, these SEM images show that contaminants continue to persist. Microbial degradation is also known to cause the loss of scale structure in wool fibres and lead to fracturing and this is highly likely in the environmental conditions experienced by the *Mary Rose* artefacts.[5]
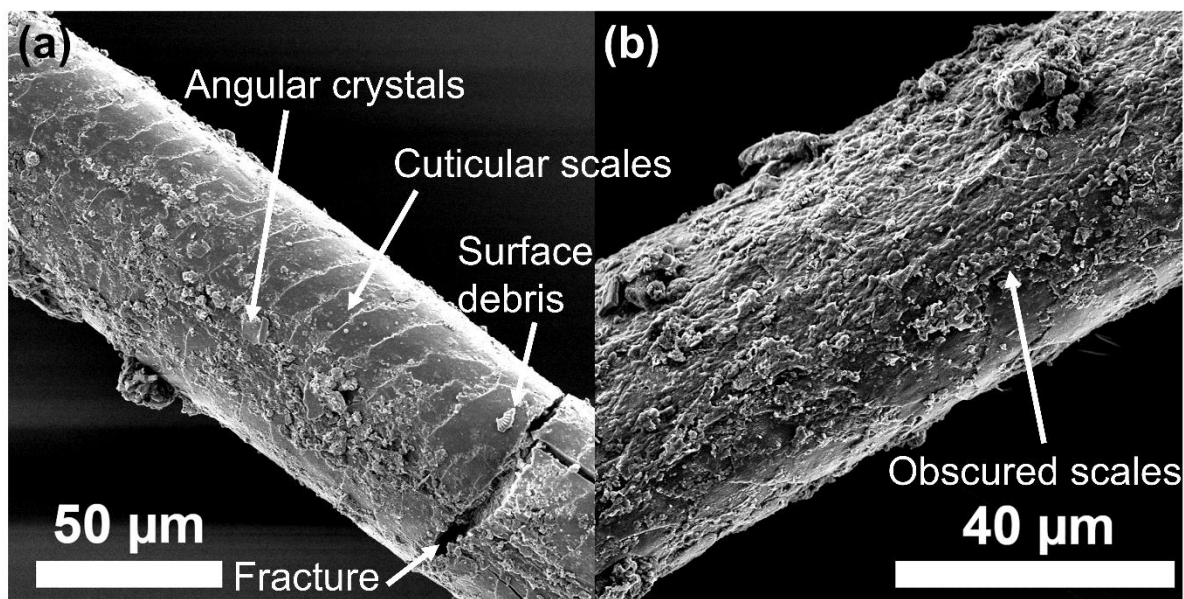
Figure 50 Annotated SEM images of the *Mary Rose* wool fibres at **(a)** 1600x magnification and **(b)** 3000x magnification.

The cuticular scales identify the fibre definitively as animal hair and the scale pattern can be used to determine the animal from which the hair came.[6] The scales in this sample are quite regularly spaced and close together, indicating the wool is quite fine and not as coarse as presumed from a macroscopic view of the artefact. However, these fibres are reasonably wide compared to modern wool fibres, especially merino wool fibres, which tend to be

between 10 μm and 25 μm.[7] Fibre width is often an important indication of wool quality because thicker fibres (usually over 30 μm) tend to make the final product feel coarser next to the skin.[7] A system of classifying wool based on fibre diameter developed by Ryder considers fine wool fibres are to have a mean and modal width of 20 μm with an upper width of 35 μm, and medium wool is often between 30-40 μm with an upper width of 60 μm.[8,9] This is an indication that the *Mary Rose* wool fibres studied are a medium wool but a greater amount of fibres from the sample would need to be measured to investigate their width distribution to better classify these fibres. The *Mary Rose* fibres studied here are approximately 50 μm in diameter, showing that they are quite coarse fibres. As fibre diameter is related to the roughness of the wool fibres, the width of these fibres may also provide some clue as to their function: the roughness and quality of the fibres may not have mattered if the function of these wool pieces were for padding in ship materials rather than as clothing.

Visual levels of preservation are extremely variable between fibres and even on the same fibre. Some areas of the wool fibres appear well preserved with intact scales, whereas other regions show deep splits or scales completely obscured by dirt. Furthermore, in Figure 50(a) there is a piece of debris near the split in the fibre (labelled as surface debris in the figure) that looks like a piece of shell which could be evidence of bacterial deterioration, SEM-EDS could be used in the future to investigate the composition of this surface debris. The angular crystal structures on the surfaces are likely to be salt deposits. It is a good sign that cuticular scales are still present in these archaeological fibres, indicating structural integrity, as this is not observed for some wool artefacts.[3] However, the fractures and obscuration of the scales show this artefact has degradation issues not easily observed by visual examination and require more in-depth spectroscopic investigations.

5.1.2 FTIR Spectroscopic Analysis of Wool Fibres

The FTIR spectra of proteinaceous fibres are dominated by amide bands. This is indeed the case for the FTIR spectra displayed in Figure 51 of the *Mary Rose* wool fibre and the modern Cochno wool fibre samples. The high intensity and position of the amide I and II vibrational modes at 1630 cm^{-1} and 1520 cm^{-1}, respectively, further confirm this *Mary Rose* sample as a wool fibre.[10] The amide I vibration corresponds to α-helical conformation of keratin, primarily associated with the C=O stretching vibration of the peptide backbone, while the amide II vibration results from N-H bending and C-N stretching vibrations.[11,12]

There is a remarkable similarity between the FTIR spectra collected of the *Mary Rose* fibre and the reference wool fibre. This is particularly notable when one considers the variation observed between modern and historic cellulosic fibres, explored in previous chapters of this thesis. This suggests that the wool may not be as deteriorated as might have been expected considering its age (~500 years old) and the long duration this sample has spent in a marine environment. It has been acknowledged that proteinaceous fibres such as wool are less prone to degradation than cellulosic fibres, particularly through biological means, and can be slightly better preserved by a slightly acidic environment.[6] Proteinaceous fibres in waterlogged, anaerobic environments are more likely to survive than in aerobic environments, although anaerobic bacteria can still degrade the fibres.
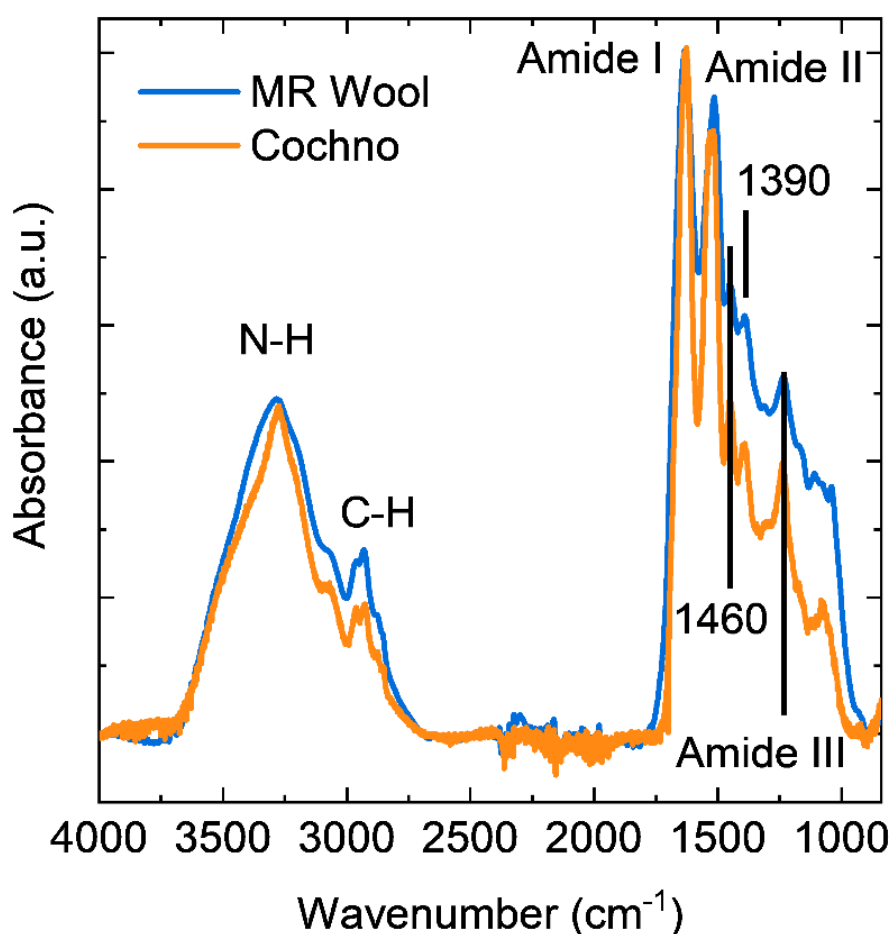

Figure 51 Annotated FTIR spectra comparison of *Mary Rose* wool (MR wool, blue line) and modern Cochno wool (Cochno, orange line) which have both been baseline corrected and normalised to the amide I band at 1630 cm^{-1}.

One should remain cautious in reaching definitive conclusions about the degradation of the whole artefact from spectra collected from small areas of different fibres. As noted in the optical and scanning electron microscope images in Figure 49 and Figure 50, some regions of the wool fibres are more contaminated and damaged than others. Taking FTIR spectra from different fibres and various areas on those fibres may give a representative picture of the structure of the fibres but may not necessarily be measuring severely degraded regions. To be able to correlate visually degraded areas with FTIR spectra to map changes in peak intensities, FTIR microscopy would be very helpful in the future. FTIR microscopy is a combination of an optical microscope and a FTIR spectrometer. The optical microscope allows a region of interest to be selected and the FTIR spectrometer collects spectra at points of interest. FTIR imaging allows spatial distribution of chemical components in the sample to be obtained by monitoring characteristic bands of chemical species of interest across the image with each pixel of the image representing an IR spectrum.[13] This makes it ideally suited to analysing heterogeneous materials like archaeological artefacts.

The two wool samples as well as differing in age, differ in colour. The pigment melanin is responsible for providing wool with a black or a brown colour. Due to the similarity of the FTIR spectra, it is likely that the pigment is not detected by this method, but melanin bands such as CH, CH_2, N-H are also present in keratin and therefore an overlap of bands is to be expected. A band from melanin that is not likely to be present in keratin would be the C-C aromatic stretch usually found in the 1400-1600 cm^{-1} region; however, this would also coincide with the strong amide I and II vibrations. It is possible that the wool fibres were dyed black with $FeSO_4$.The strongest sulfate band that would occur in the FTIR spectrum if $FeSO_4$ was present is the asymmetric stretch between 1210 and 1040 cm^{-1} and the difficulty here is that this band overlaps with bands arising from the degradation products of wool.[14] using an oak gall mordant, but further investigation of this possibility would be required to check for any further implications this may have for the degradation of this artefact.[12] It is more likely that the *Mary Rose* wool fibres are naturally black due to the difficulty of achieving this colour with dyes. If such dyes were present, further techniques such as XRD, HPLC, and Raman spectroscopy would be required. Raman spectroscopy would also be useful for detecting the disulfide bridging bonds which stabilise the keratin polymers and can be a key indicator of

degradation. The disulfide bond in cystine is homonuclear so unfortunately IR inactive but would be possible to detect with Raman spectroscopy.[15]

The C-H stretching region is arising due to contributions from the amino acids in the wool and could also represent waxy and greasy substances commonly found in wool such as lanolin and suint. Lanolin is an oil naturally present in wool fibres from sheep and acts in a waterproofing capacity.[2] Waxes and fatty acids can be found in the epicuticle of wool fibres.[2] Certain amino acids have specific bands originating from CH_2 and CH_3 side groups.[15] The peak at 1390 cm^{-1} also corresponds to a CH_3 symmetrical deformation.

Fibre embrittlement is associated with the presence of cystine breakdown products. These breakdown products are indicated by the presence of SO and SO_2 peaks in FTIR spectra.[16] Other breakdown products of cystine include: disulfides, thiols, sulfur-carbon, and sulfonate groups. Cystine monoxide, cystine dioxide, and cysteic acid are also breakdown products of cystine associated with fibre embrittlement.[16] In comparing the FTIR spectra of *Mary Rose* wool and modern Cochno wool (Figure 51), interesting differences in band positions and intensities are observed. For example, in the spectrum of the *Mary Rose* wool, the band at 1040 cm^{-1} is greater in intensity than in the modern sample. This peak corresponds to the $-SO_3^-$ vibrational mode present in cysteic acid, a degradation product of cystine.[16] This band is not dominant in the Cochno sample but this modern sample does have a peak at approximately 1070 cm^{-1} indicating the modern wool sample is more likely to contain cystine monoxide (-SO-S-), another degradation product of cystine. The asymmetrical C-O-C stretch and the C-N stretching vibrations also appear in this region at 1055 cm^{-1} which complicates drawing a conclusion on the levels of degradation in the *Mary Rose* wool fibre based on this region of its FTIR spectrum.[10]

The Cochno, Jacobs, and Shetland wool used as modern references are compared with the *Mary Rose* wool in Figure 52. The FTIR spectrum from the *Mary Rose* wool was collected from a different fibre to the spectra collected in Figure 51 (the spectra in Figure 52 were also collected on a different spectrometer). The spectra in Figure 52 were all baseline corrected at 3986, 3712, 2693, 2385, 2117, 1778 and 830 cm^{-1} and normalised to the 1630 cm^{-1} amide I band for comparison purposes. The band displayed as a shoulder at 3070 cm^{-1} can be attributed to the amide B band which is an overtone of the amide II band. The broad band

around 3300 cm^{-1} correlates with the N-H stretch of the amino acids as well as the O-H stretch due to water associated with the fibres. Given that wool is hygroscopic in nature, IR stretches associated with water are to be expected.
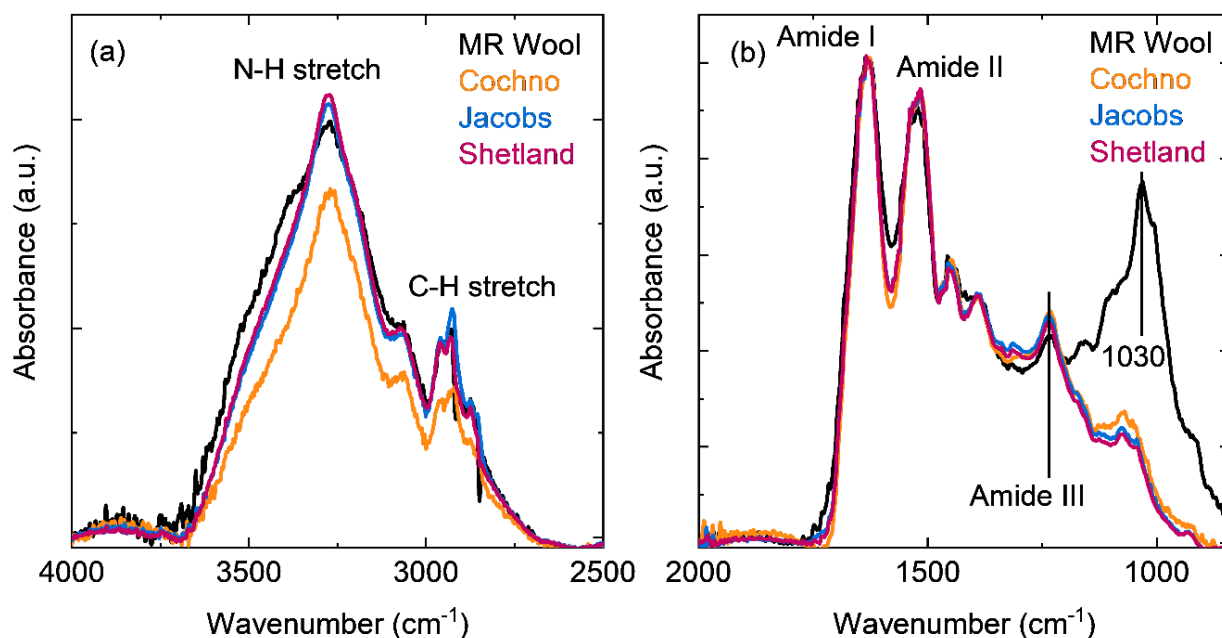

Figure 52 Comparison of the FTIR spectra of *Mary Rose* wool (MR wool, black line) fibres to modern wool reference fibres (Cochno, orange line; Jacobs, blue line; and Shetland, pink line) showing the **(a)** 4000-2500 cm^{-1} and the **(b)** 2000-840 cm^{-1} wavenumber ranges. All spectra were baseline corrected and normalised to the amide I band at 1630 cm^{-1}.

The positions of the amide I, II, and III vibrational modes are very similar for all the samples studied. This suggests that the *Mary Rose* fibres are not significantly degraded, as peak shifts to higher wavenumbers and broadening of the peaks would likely be observed if this were the case.[12] The uncoiling of α-helices to random coil or β-sheet conformations due to degradation would also be observed in the spectra of archaeological wool fibres by a shift of this amide I mode.[15] The intensity of the amide III band is slightly lower in this *Mary Rose* spectrum which is an indicator of degradation, as this band is influenced by hydrogen bond changes possibly caused by keratin denaturation.[12] The band at 1160 cm^{-1} is also of a higher intensity in the *Mary Rose* sample compared with the modern references which could be an indication of ester bond formations in amino acids, another indication of degradation.[12]

The large peak at 1030 cm^{-1} in the *Mary Rose* wool sample has been detected in other archaeological wool FTIR spectra and can be correlated to silica (silicon dioxide) or sand which

is expected given the artefacts were raised from the sea floor.[3,6] Even though the wool fibres have been through a cleaning process, it is likely some sand would remain. This could explain the debris observed in the SEM images in Figure 50. This peak is not as prominent in the *Mary Rose* wool FTIR spectrum from Figure 51, which is a spectrum of a different fibre from the same artefact and demonstrates the variation observed between fibres. This peak can also influence the cysteic acid peak at 1040 cm^{-1} and the large difference between the *Mary Rose* wool spectrum in Figure 52 and the modern references in this region could be a key indicator of the degradation of the cystine residues in the archaeological sample. The ATR method employed here means the cuticle layer of the fibres are more readily analysed, meaning the presence of sand on the surface is likely to influence the cysteic acid band, which would more likely be found in the interior of the fibre.[3]

5.2 Characterisation of *Mary Rose* Leather

Two leather samples from the *Mary Rose* collection have also been analysed with optical microscopy, SEM, and FTIR spectroscopy. These samples were leather fragments (no artefact number was recorded) and a leather shoe sample (MR83 A486) which is a fragment of a leather sole. The artefact card notes that the shoe has been cleaned with distilled water and consolidated with 10% Bavon 520S. Bavon 520S was regularly used in the conservation of the *Mary Rose* leather artefacts and acts as a lubricant; it is an emulsified alkylated succinic acid derivative.[17]

5.2.1 Visual Assessment of *Mary Rose* Leather

In Figure 53(a) and (b), the front and back of the *Mary Rose* leather fragments sample is presented with a colour card and scale bar. This sample is very dark in colour with orange spots of corrosion clearly visible. This sample appears thinner than the leather shoe sample, with rougher edges. Images of the *Mary Rose* leather shoe sample (Figure 53(c) and (d)) show that this piece of leather is clearly very heavily iron stained and concreted with salts apparent on its surface. This thick leather sample has hard creases, stiff folds, and very orange areas of layered heavy corrosion. The degraded state of these artefacts and surface contamination makes the analysis of the grain pattern very difficult for identifying the animal from which the leather originated.[18] Zooarchaeology by mass spectrometry (ZooMS) (discussed in section 1.9.3) would be required for a more objective and accurate animal species determination in this instance, although visual assessment is still useful for complementary information.[19]
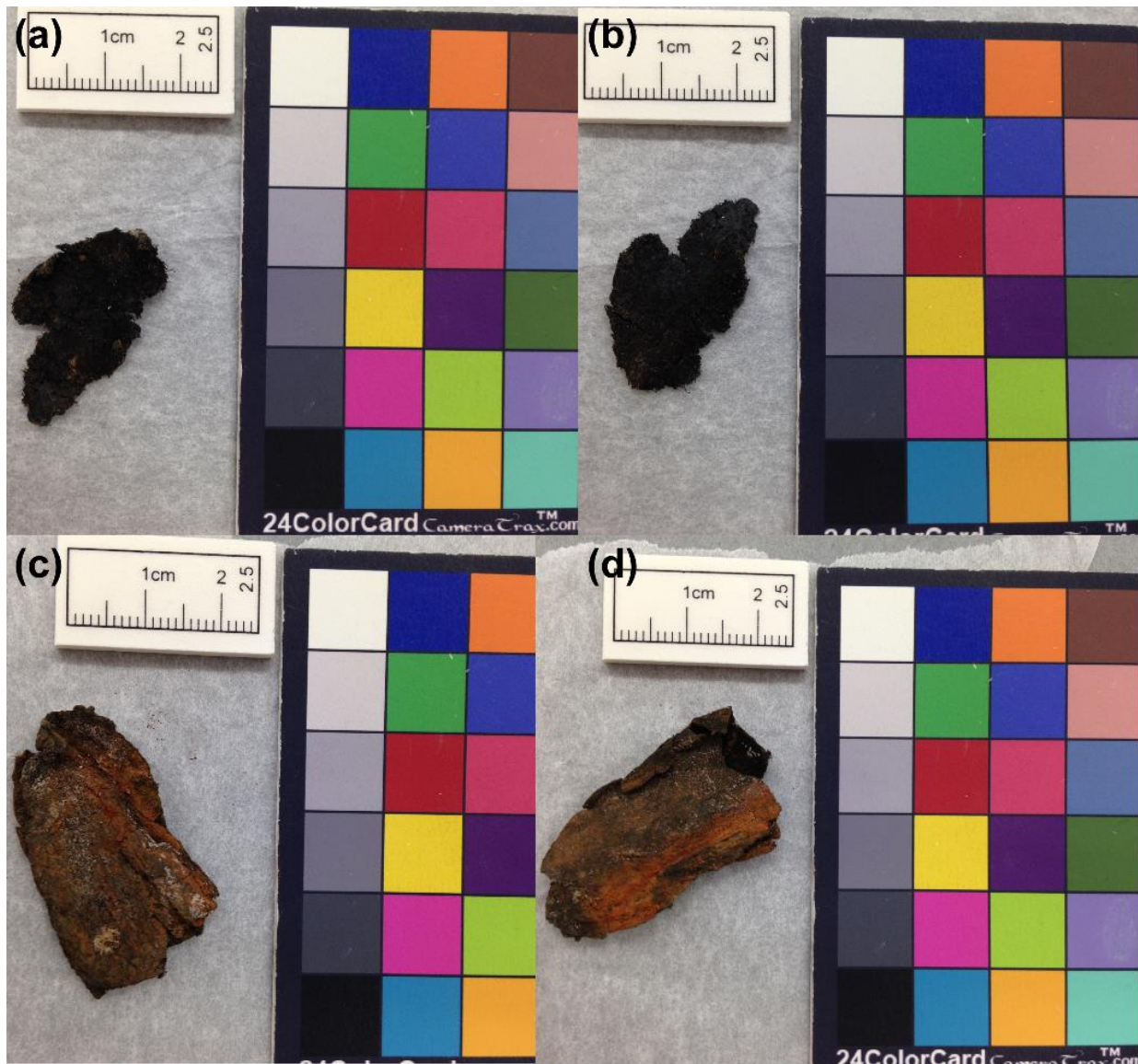
Figure 53 Photographs of the *Mary Rose* leather **(a)** front side of 'leather fragments' and **(b)** the back of the same sample **(c)** front side of the 'leather shoe' sample and **(d)** the back of this sample.

Digital microscope images in Figure 54 show a closer look at the surfaces of the leather artefacts. The leather fragments sample in Figure 54(a) and (b) exemplifies the structure of leather materials as a fibrous interwoven structure embedded amongst a gelatinous substance. Small, thin fibres are noted both on the surface and within the sample. At this higher magnification, small white dots, presumably attributed to salts, can be seen, along with patches of iron corrosion. Fibres within and on the surface can also be observed in the leather shoe sample (Figure 54(c) and (d)). This sample appears drier and more fibrous with less tar-like gelatinous material than the leather fragments sample. It could be thicker because its original use was as a sole of a shoe where harder-wearing leather would be more applicable,

whereas the leather fragments appear more flexible. On the other hand, this could be evidence that the leather shoe sample is more severely corroded and degraded than the leather fragments. In both samples, many cracks in the grain layer can be observed and both appear to be in an extremely degraded state.
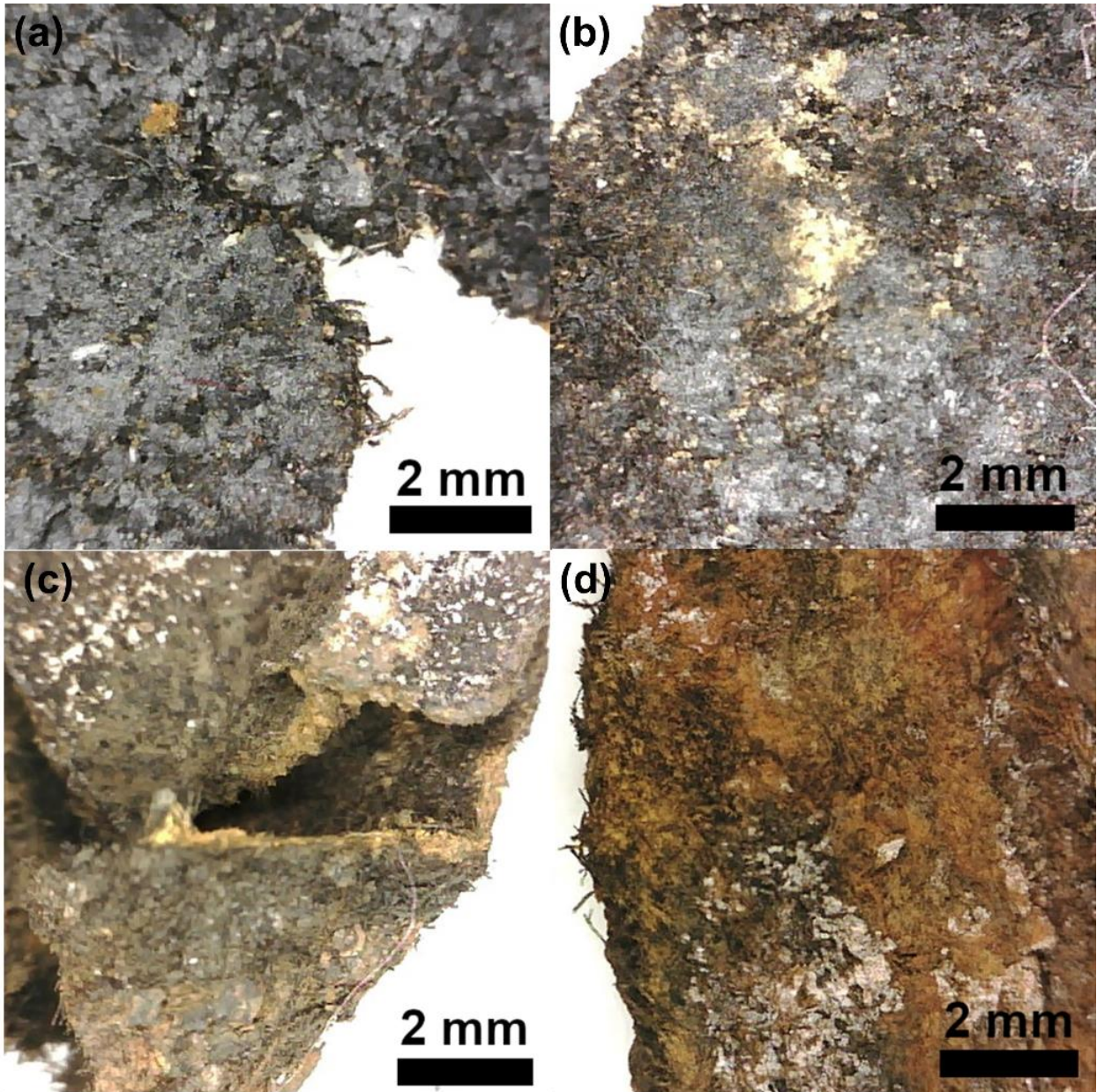
Figure 54 Digital microscope images of *Mary Rose* leather samples **(a)** and **(b)** taken from different areas of the leather fragments sample and **(c)** and **(d)** are taken from different areas of the leather shoe sample.

The leather fragments sample has been studied further with SEM, the results of which are displayed in Figure 55. These images show fibres of approximately 50 μm with gelatinous material surrounding the fibres. The corium fibres are twisted, flattened in some areas and

appear separated, not bundled together as is the case in more preserved leather. Corium fibres are interwoven bundles of collagen found in the layer below the grain layer (the layers in typical animal skin are shown in Figure 11 section 1.9.1). The leather material in Figure 55 is not homogeneous, displaying large gaps in the structure, indicating severe levels of degradation. Evidence of biodegradation was not observed in these SEM images of the leather fragments which is consistent with knowledge that tanned leather is very resistant to microbial attack, even underwater.[20] Although tanned animal hides are quite resistant to bacterial attack, they can be attacked by fungi. Presence of fungal spores (thin web-like hyphae or disc-shaped structures) would be observed in an SEM image of heavily biodegraded leather.[21] This does not necessarily mean biological degradation has not taken place, as this was only a small area of the sample and evidence may have been removed during cleaning processes but it may be more likely that this sample has been degraded by chemical or mechanical means.
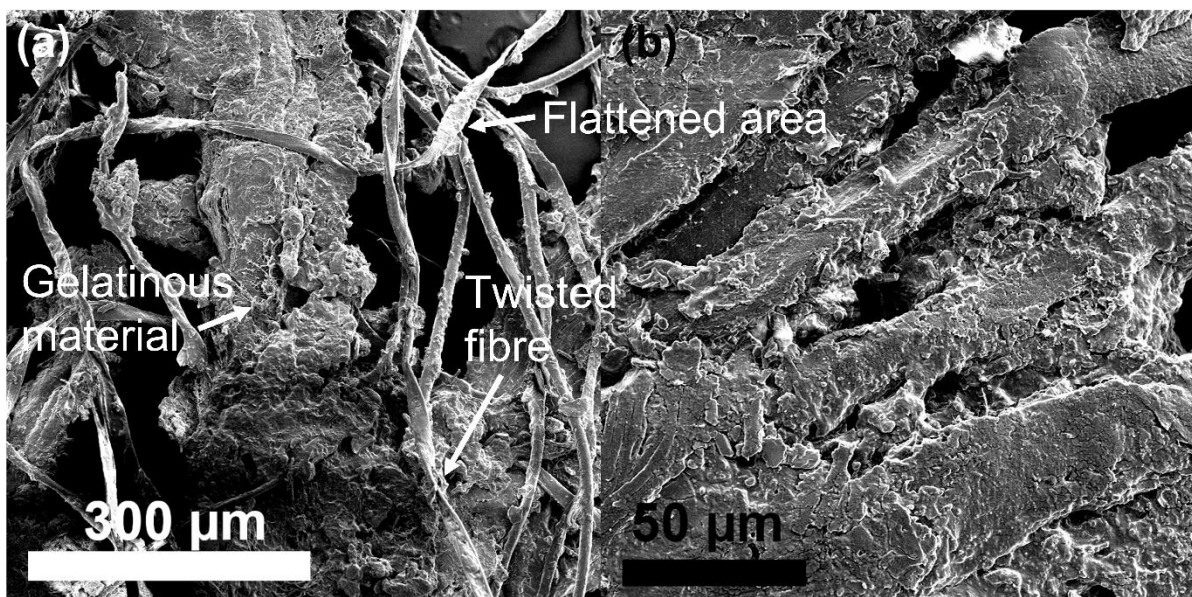
Figure 55 SEM micrographs of different areas from *Mary Rose* leather fragments **(a)** at 400x and **(b)** 1600x.

5.2.1 FTIR spectroscopic analysis of *Mary Rose* Leather

FTIR spectroscopy can be used to study the structure and degradation of leather artefacts. presents the FTIR spectra of the *Mary Rose* leather shoe and leather fragments samples together for ease of comparison and highlights key areas where significant differences are observed in Figure 56. Spectra were collected from different areas on each sample which

demonstrate that there are variations within the sample itself and these results are included in the appendix (Figures 69-71).

Acid hydrolysis can lead to the breakdown of collagen to gelatin and this breakdown can be observed in the FTIR spectra of the leather samples.[22] The lack of a prominent amide I band in the leather shoe sample signifies significant deterioration of the collagen fibres. Focusing on the amide I band, Vichi *et. al.*, when studying historical leather book covers, assigned the amide I band in preserved collagen to the 1645-1638 cm^{-1} region.[23] With some unfolding of the protein helices, the amide I band occurred between 1630 and 1637 cm^{-1} and when gelatin was present, the band occurred below 1630 cm^{-1}.[23] A shoulder at 1655 cm^{-1} was observed when gelatin was present which was attributed to remaining α-helical chains.[23] This band has also been noted to occur at 1650 cm^{-1} for gelatin.[24] A shoulder at 1633 cm^{-1} is observed in the leather shoe sample which suggests some unfolding of the α-helical chains has occurred. The amide I band is clearly observed in the leather fragments spectrum on the other hand, evidencing degradation in the sample with unfolding of the chains, some preserved collagen, and gelatin.
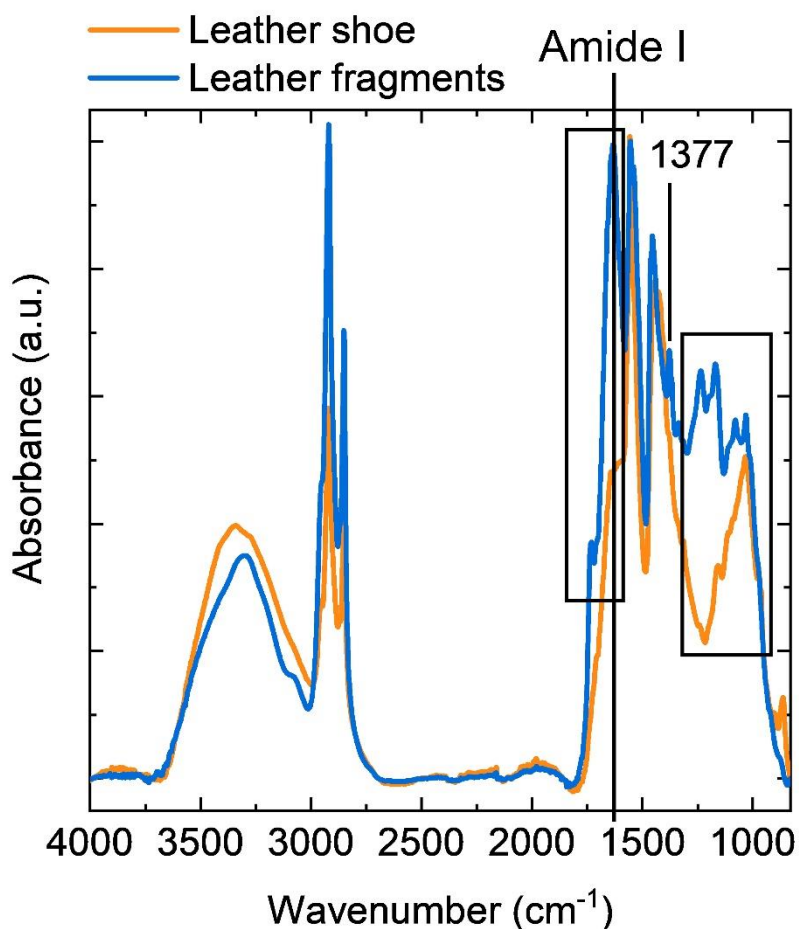
Figure 56 Comparison of leather shoe (orange line) and leather fragments (blue line) FTIR spectra with prominent differences highlighted including the amide I band. These spectra were baseline corrected and normalised at the 1553 cm^{-1} amide II band.

The *Mary Rose* leather shoe and leather fragments FTIR spectra have been presented in closer detail and with annotation in Figure 57(a) and (b). These results were baseline corrected and not normalised. Upon initial inspection of Figure 57(a) and (b), it is apparent that the leather shoe spectrum is generally less intense than that of the leather fragments which is typical for more degraded artefacts. In this case, the force of the ATR tip pressing the sample against the ATR crystal was kept approximately the same throughout the collection of each spectrum. Although this was considered, it is also likely that poorer contact between the leather shoe surface and the crystal occurred, where better contact may have been achieved with the leather fragments sample due to its relatively flat surface. This makes analysis of the levels of

degradation in the artefacts more complicated as decreases in peak intensities are associated with a greater extent of degradation.

The band at approximately 3300 cm^{-1} is representative of the asymmetrical N-H stretching vibration and the symmetrical N-H stretch at 3200 cm^{-1}, which both overlap with the O-H stretch.[19,25] 2920 cm^{-1} and 2850 cm^{-1} bands correspond to CH_2 asymmetric and symmetric stretching vibrations.[23]
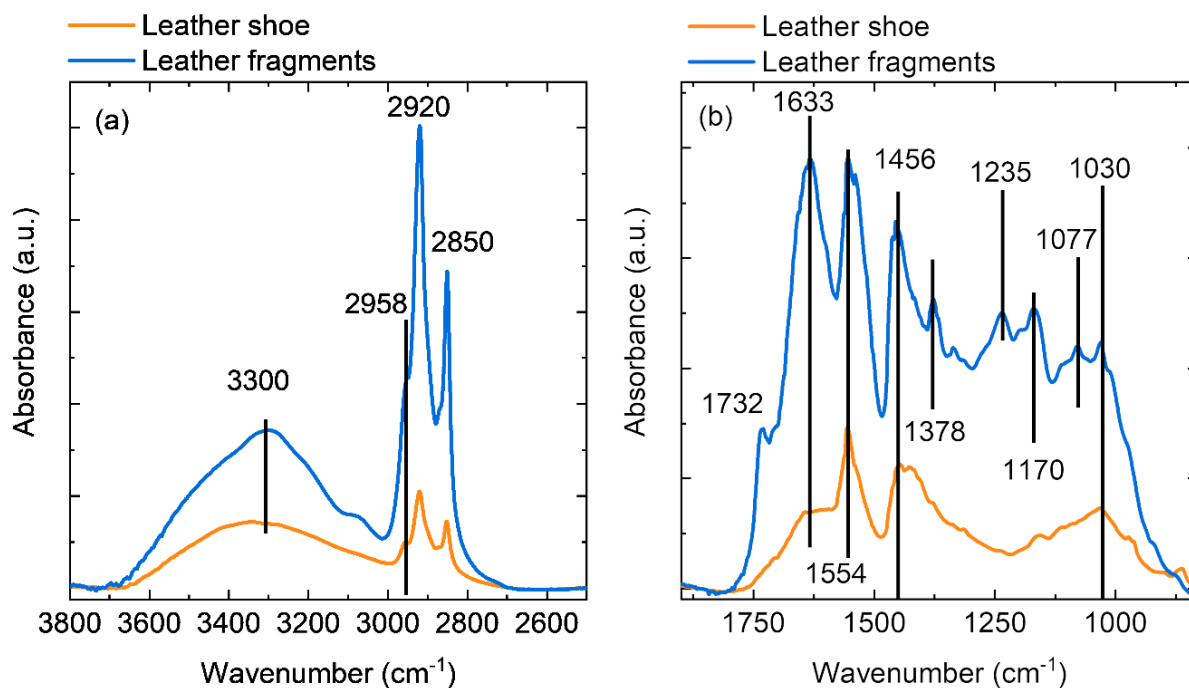

Figure 57 Annotated FTIR spectra comparing the leather shoe spectrum (orange line) with that of the leather fragments sample (blue line) in the **(a)** 3800-2550 cm^{-1} and **(b)** 1800-800 cm^{-1} regions. The spectra were baseline corrected.

The band at 1732 cm^{-1} is present in the leather fragments spectrum but not prominent in the leather shoe spectrum. This peak corresponds to the asymmetric C=O stretching vibration, often a good indicator of degradation. This carbonyl stretch is found in the amino acids that form collagen and is often present in degradation products of proteins as the carboxylic acid group is usually formed, especially through hydrolytic processes.[20] However, this band could also be attributed to contributions from lipids or tannins which also contain carbonyl groups.[23]

The amide II band is reported as appearing at 1539 cm^{-1} for collagen and around 1547 cm^{-1} for gelatin.[23] In both the leather fragments and leather shoe sample there is a main peak at

168

1554 cm^{-1} with a shoulder at 1538 cm^{-1}. This could be illustrating that collagen is still present but that there is a large contribution from gelatin. This peak is at a slightly higher wavenumber than the reported value for the amide II band of gelatin, which could be due to differing levels of hydration.

Characteristic bands of vegetable tannins occur in the leather fragments spectrum. The C=C aromatic stretching vibrational mode is characteristic of tannins and can be attributed to the peak at 1456 cm^{-1} (this could also correspond to CH vibrations in lipids).[26] The peak at approximately 1378 cm^{-1} is observed in the leather fragments spectrum but not the leather shoe sample and could correspond with the C-O phenolic stretch and OH deformation common in tannins.[26] The peaks observed at approximately 1240 cm^{-1} and 1170 cm^{-1} can be attributed to the asymmetric and symmetric C-O-C stretches.[23] The band at 1240 cm^{-1} could also be assigned as the amide III peak and it is interesting to note that this is present in the spectrum of the leather fragments sample, but not in the leather shoe spectrum.[26] As well as indicating the presence of silicate materials which would be common surface contaminant of marine archaeological artefacts, the 1030 cm^{-1} band could overlap with the in-plane C-H deformation observed in vegetable tannins.[26] These bands are all more prominent in the leather fragments spectrum and can be associated with the presence of vegetable tannins.[26] The band positions in the leather fragments spectrum indicate the tannins in these samples are probably hydrolysable tannins due to the presence of the 1732 cm^{-1} and 1334 cm^{-1} peaks.[26]

The 863 cm^{-1} peak in the leather shoe sample (not present in leather fragments) could possibly be a carbonate in-plane bend originating from calcium carbonate due to calcium hydroxide in the liming baths reacting with CO_2 in the atmosphere or present due to the marine environment.[23] SEM-EDS would be useful to detect the presence of calcium compounds and possibly correlate with the FTIR spectra of these leather samples.

5.3 Conclusions

Characterisation of the *Mary Rose* wool sample by optical microscopy, SEM, and FTIR spectroscopy has provided key insights into the nature and provenance of these fibres. On the surface, the fibres do not seem degraded, although they are roughly spun and shedding. Upon inspection with optical microscopy and SEM, the fibres can be identified positively as

animal hair and breakages and splitting in the fibres are observed. The FTIR spectrum of the *Mary Rose* wool is very similar to those of the modern wool references indicating that the conformational structure is quite well preserved for its age. The major difference in the spectrum of an area of the *Mary Rose* wool is the peak at 1030 cm^{-1} which can be due to cysteic acid, a degradation product, or the presence of silicate materials on the surface of the fibres. In the future, amino acid analysis would be very useful to analyse the degradation products of keratin. Amino acid markers for oxidative degradation of keratin can be used to examine whether the artefact has suffered from this form of degradation.[27]

Characterisation of the *Mary Rose* leather fragments and leather shoe samples has been undertaken with microscopy, SEM, and FTIR spectroscopy. Visually, the leather samples appeared heavily degraded with surface corrosion and salts. SEM further confirmed the fragmented state of the leather fragments, showing corium fibres exposed from the material and not bundled together as would be the case for preserved leather. FTIR spectroscopy revealed that these samples were tanned with tannins of vegetable origin and that degradation of the collagen has occurred. To obtain a scale of degradation levels through FTIR and SEM, comparable modern leather and historic (not-waterlogged) leather samples would be required. This would be useful, especially when developing novel treatments, but ultimately the leather is in a variable condition even within the same sample, so it is important to consider the artefacts on a case-by-case basis.

Future work could include amino acid analysis to determine the mechanism of degradation. For example, to establish whether the leather degradation was due to acid hydrolysis or oxidative degradation by studying polar amino acid residues.[19] It might also be interesting to explore the surface contaminants by XRF, Raman, and EDX spectroscopy. HPLC could be used to gain further understanding of the tanning agents in these leather samples.[28]

References

1 J. M. Cronyn, *The Elements of Archaeological Conservation*, Routeledge, London, 1990.

2 P. Garside and P. Wyeth, in *Conservation Science: Heritage Materials*, eds. E. May and M. Jones, RSC Publishing, Cambridge, UK, 2006, pp. 56–91.

3 A. Jabur, University of Manchester, 2014.

4 K. Steingart, Hair & Fiber, 2007, **7**, 37–48.

5 U. Kkber-Grohne, *Microscopic Methods for Identification of Plant Fibres and Animal Hairs from the Prince's Tomb of Hochdorf, Southwest Germany*, 1988, vol. 15.

6 W. F. Rowe, Forensic Hair and Fiber Examinations in Archaeology: Analysis of Materials from Gravesites at the Home of Samuel Washington, *Tech. Briefs Hist. Archaeol.*, 2010, **5**, 43–51.

7 L. K. Hillbrick, Deakin University, 2012.

8 M. L. Ryder, Issues in Conserving Archaeological Textiles, *Archaeol. Text. Newsl.*, 2000, **31**, 2–7.

9 M. Gleba, From textiles to sheep: Investigating wool fibre development in pre-Roman Italy using scanning electron microscopy (SEM), *J. Archaeol. Sci.*, 2012, **39**, 3643–3661.

10 V. Raditoiu, I. E. Chican, A. Raditoiu, I. Fierascu, R. C. Fierascu and P. Fotea, in *VR Technologies in Cultural Heritage*, eds. D. M., C. M., G. M. and T. I., Springer, Cham, 2019, pp. 3–9.

11 B. A. Mcgregor, X. Liu and X. G. Wang, Comparisons of the Fourier Transform Infrared Spectra of cashmere, guard hair, wool and other animal fibres, *J. Text. Inst.*, 2018, **109**, 813–822.

12 M. Odlyha, C. Theodorakopoulos and R. Campana, Studies on Woollen Threads from Historical Tapestries, *AUTEX Res. J.*, 2007, **7**, 9–18.

13 N. Labbé, T. G. Rials and S. S. Kelley, in *Characterization of the Cellulosic Cell Wall*, eds. D. D. Stokke and L. H. Groom, John Wiley & Sons, 2006, pp. 110–122.

14   J. G. Dunn, W. Gong and D. Shi, A Fourier transform infrared study of the oxidation of pyrite, *Thermochim. Acta*, 1992, **208**, 293–303.

15   H. G. M. Edwards and P. Wyeth, in *Raman Spectroscopy in Art and Archaeology*, eds. H. G. M. Edwards and J. M. Chalmers, Royal Society of Chemistry, Cambridge, UK, 2005, pp. 304–324.

16   N. Kissi, K. Curran, C. Vlachou-Mogire, T. Fearn and L. Mccullough, Developing a non-invasive tool to assess the impact of oxidation on the structural integrity of historic wool in Tudor tapestries, *Herit Sci*, 2017, **5**, 49.

17   M. Jones, *For Future Generations: Conservation of a Tudor Maritime Collection*, The Mary Rose Trust, 2003.

18   J. A. Ebsen, K. Haase, R. Larsen, D. V. P. Sommer and L. Ø. Brandt, Identifying archaeological leather – discussing the potential of grain pattern analysis and zooarchaeology by mass spectrometry (ZooMS) through a case study involving medieval shoe parts from Denmark, *J. Cult. Herit.*, 2019, **39**, 21–31.

19   R. Rabee, A. Hassan, M. F. Ali and A.-G. A. Fahmy, Use of SEM, FTIR, and amino acid analysais methods to assess the damage of some historical leather bindings from the XIXth century, stored in National Archive, Cairo, *Int. J. Conserv. Sci.*, 2018, **9**, 127–136.

20   R. Thomson, in *Conservation Science: Heritage Materials*, eds. E. May and M. Jones, RSC Publishing, Cambridge, UK, 2006, pp. 92–120.

21   A. B. Strzelczyk, J. Kuroczkin and W. E. Krumbein, Studies on the microbial degradation of ancient leather bookbindings: Part I, *Int. Biodeterior.*, 1987, **23**, 3–27.

22   M. Baglioni, A. Bartoletti, L. Bozec, D. Chelazzi, R. Giorgi, M. Odlyha, D. Pianorsi, G. Poggi and P. Baglioni, Nanomaterials for the cleaning and pH adjustment of vegetable-tanned leather, *Appl. Phys. A Mater. Sci. Process.*, 2016, **122**, 1–11.

23   A. Vichi, G. Eliazyan and S. G. Kazarian, Study of the Degradation and Conservation of Historical Leather Book Covers with Macro Attenuated Total Reflection-Fourier Transform Infrared Spectroscopic Imaging, *ACS Omega*, 2018, **3**, 7150–7157.

24   A. Kupczak, Ł. Bratasz, J. Kryściak-Czerwenka and R. Kozłowski, Moisture sorption and diffusion in historical cellulose-based materials, *Cellulose*, 2018, **25**, 2873–2884.

25   M. Mansour, R. Hassan and & Salem, Characterisation of historical bookbinding leather by FTIR, SEM-EDX and investigation of fungal species isolated from the leather, *Egypt. J. Archaeol. Restor. Stud. 'EJARS'*, 2017, **7**, 1–10.

26   L. Falcão and M. E. M. Araújo, Application of ATR-FTIR spectroscopy to the analysis of tannins in historic leathers: The case study of the upholstery from the 19th century Portuguese Royal Train, *Vib. Spectrosc.*, 2014, **74**, 98–103.

27   I. Vanden Berghe, Towards an early warning system for oxidative degradation of protein fibres in historical tapestries by means of calibrated amino acid analysis, *J. Archaeol. Sci.*, 2012, **39**, 1349–1359.

28   A. Elnaggar, M. Leona, A. Nevin and A. Heywood, The Characterization of Vegetable Tannins and Colouring Agents in Ancient Egyptian Leather from the Collection of the Metropolitan Museum of Art, *Archaeometry*, 2017, **59**, 133–147.

Chapter 6: Conclusions and Future Work

6.1 Conclusions

This thesis has investigated a $SrCO_3$-cellulose based nanoparticle treatment for the conservation of marine archaeological wood and has explored various methods of synthesising $SrCO_3$ nanoparticles for future use in conservation treatments. Organic-based *Mary Rose* artefacts of sail cloth, anchor rope, wool, leather fragments, and a leather shoe were examined microscopically and spectroscopically. This has ultimately led to a deeper understanding of these artefacts in terms of identification and their state of degradation.

$SrCO_3$-cellulose patches were investigated as spot treatments that could be applied to specific regions of artefacts exhibiting common problems associated with iron and sulfur compounds. Analysis of XANES from test wood and $SrCO_3$-cellulose patches has revealed this to be a promising future treatment for marine archaeological wood. Iron and sulfur compounds were present in the patch post-treatment, shown by XANES, EXAFS, FTIR, Raman, and XRF analysis. LCF of the XANES data was undertaken on these samples for the first time and the S K-edge results showed the sulfur in the Fe-Oak-treated and patch sample spectra was largely in an environment similar to that of the $SrSO_4$ standard. The Fe K-edge LCF results suggested that iron in these same samples were in an environment like that of $Fe_2(SO_4)_3$ and $FeCO_3$. Analysis and fitting of the EXAFS region of the Fe K-edge data provided further information to the XANES LCF results. The fits showed that the Fe-Oak and Fe-Oak-treated data were consistent with the first single scattering path calculated from the $Fe_2(SO_4)_3$ CIF. FTIR and Raman spectroscopy provided evidence for sulfate bands in the patches but also carbonate bands from unreacted $SrCO_3$.

Synthesis methods and subsequent characterisation of $SrCO_3$ nanoparticles were investigated with the aim of incorporating them into a future conservation treatment. Microwave, sonication, and controlled-precipitation methods were explored in EG, 1:1 EG:water, and water solvent systems. The products were characterised by powder XRD, FTIR, and SEM. Rietveld refinements, FTIR, and Raman spectroscopy were used to confirm $SrCO_3$ as the product and SEM studied the morphology of the nanoparticles. It was apparent that the

solvent system had a greater effect on the $SrCO_3$ nanoparticles than the method of synthesis and that using EG as a solvent seemed to provide the best route for $SrCO_3$ nanoparticle synthesis, which could be due to the precursors not dissolving as readily in EG so reacting in a more controlled way. The nanoparticles synthesised by sonochemical and microwave-assisted methods in EG would be preferred for future incorporation into the cellulose patch treatment.

Textile fibres such as wool and linen are not commonly found in archaeological contexts. They are often only preserved in certain environments, such as waterlogged, or extremely dry environments, or alongside metal artefacts which prohibit bacterial activity. Due to their scarcity, it is extremely important to preserve these fragile artefacts and to learn as much as possible from them because they provide a wealth of information on how people lived and traded.

The *Mary Rose* anchor rope and sail cloth samples were identified through optical microscopy and FTIR spectroscopy as bast fibres. It is a challenge to distinguish between bast fibres due to their similarities. Polarised-ATR-FTIR was employed as a method for distinguishing them objectively. Identification proved difficult possibly due to challenges posed by archaeological samples. This method was further used to determine a scale of degradation through the crystallinity parameter. The results are difficult to interpret because the crystalline content of fibres will vary depending on the type of fibre (e.g. flax or hemp) as well as the levels of degradation. The marine artefacts have also clearly been subject to different sources of degradation than the historical samples.

This is the first time a FTIR study has been conducted on organic-based textile artefacts of the *Mary Rose* to the author's knowledge. Peak ratios from the FTIR spectra of the *Mary Rose* and the modern references were used to examine and compare degradation in the fibres. The *Mary Rose* sail cloth was the most degraded of the samples studied based on the total crystallinity index and this is supported by the optical microscope images. Optical microscopy and SEM indicated the presence of surface concretions and greater levels of degradation in both *Mary Rose* artefacts in comparison to modern and historic samples. The anchor cable seems to have fared slightly better than the sail cloth, which could be due to tar being used to preserve the rope for use at sea. Degradation levels derived from peak ratios can be

influenced by the areas of the fibres analysed. From SEM images of the Mary Rose anchor rope, it is clear some areas of the fibres were more degraded than others and it is not possible to ensure which areas of the fibres are measured with FTIR spectroscopy. The spectra could come from better preserved areas or very degraded regions. This is where FTIR microscopy would be very beneficial for mapping visually degraded areas with their FTIR spectra.

A *Mary Rose* wool sample which was found attached to concreted sail cloth was characterised by optical microscopy, SEM, and FTIR spectroscopy. These methods confirmed the sample was animal hair and allowed observation of split, soiled, and degraded regions on the surface the fibres. The FTIR spectra of the modern wool references and the *Mary Rose* wool sample are very similar, revealing good preservation of the keratin structure. Again, this can change depending on area of the fibre studied as evidenced by a spectrum from a different Mary Rose wool fibre showing a strong peak at 1030 cm^{-1} which can be attributed to cysteic acid, a degradation product of cystine, the main component of wool, or the presence of silicate materials on the surface of the fibres. This has been explored in archaeological wool samples previously, but this thesis examines this for the first time in a *Mary Rose* wool sample.

Leather was an important material for shoes and clothing and so its preservation is of interest for museums and collections with many leather artefacts. Although it is quite chemically resistant, archaeological leather can easily become very brittle and disintegrate if it is allowed to dry uncontrollably once removed from a waterlogged environment. Understanding this complex material is therefore very valuable for preventing its degradation. Understanding which tannins were used in the manufacture of the leather samples is valuable for understanding its subsequent degradation. For example, condensed tannins cross-link to form insoluble polymers, whereas hydrolysable tannins of vegetable origin are degraded via hydrolysis. For the *Mary Rose* leather fragments studied, FTIR spectroscopy demonstrated that it was likely tanned with hydrolysable tannins. Both *Mary Rose* leather samples were visually degraded with observable corrosion and salts on their surfaces and degradation of the collagen is also evidenced in their FTIR spectra. It is not surprising that degradation was observed in the *Mary Rose* leather samples because these were sampled from highly fragmented artefacts. Artefacts in observably better preservation states are usually used for display purposes in the museum.

6.2 Future work

There is huge scope for further work to be developed from the results of this thesis. This is a fascinating, interdisciplinary, vast area of research. Results can be used to develop future conservation treatments for rope, sail cloth, wool, leather which should all be treated individually on a case-by-case basis. Moreover, the results have implications for the development of identification methods to distinguish between fibres objectively and the development of characterisation methods in order to understand these artefacts and effects of possible treatments.

For the $SrCO_3$-cellulose patch treatment, the effect of the treatment duration could be investigated further as well as studying the depth the treatment reaches and if there are any dimensional changes in the wood surface due to water absorption. These should be considered before the treatment is applied to artefacts themselves. Knowledge of the amount of iron sulfate removed would be valuable too. The $SrCO_3$ microwave synthesised nanoparticles in EG could be incorporated into the patch for future treatment of wooden artefacts with iron and sulfur problems.

Through characterising the cellulosic fibres studied here it became apparent that spatial information is vitally important when studying degradation of artefacts. Characterisation methods including EDX, XRD, FTIR microscopy, and Raman spectroscopy would be very useful for correlating visual areas of degradation with chemical knowledge of the sample. Raman or FTIR spectra of different areas on the same cellulosic fibre could be used to determine which functional groups were responsible for the observed degradation. XRD could be used to study the crystallinity of cellulose present in the fibre, which is closely linked to its degradation. Furthermore, EDX would be useful for investigating the surface debris on the fibres shown in the SEM images to determine whether, for example, iron, silicon, or magnesium were likely present.

Amino acid analysis of the leather and wool *Mary Rose* artefacts would be extremely useful to analyse the degradation products of collagen and keratin. This would allow determination of the type of degradation pathways in these artefacts, for example, acid hydrolysis or oxidative degradation. Chromatographic techniques could also be used to determine the

extent of degradation in the samples. HPLC could potentially be used to develop a greater understanding of the tannins used in the leather samples. Furthermore, it would be useful to obtain results from EDX and XRF spectroscopy for the wool and leather samples to ascertain which elements comprise the dirt, salts, or concretions on their surfaces and whether the samples were mineralised. EDX would be more useful here as the elements can be mapped to areas of severe degradation that have been observed. Raman spectroscopy would be of use in complementing the FTIR results when studying degradation and for identifying pigments if present. FTIR spectroscopy and SEM of modern leather and historic (not previously waterlogged or from a marine environment) leather for comparison to the *Mary Rose* samples would be of immense use for study of degradation and for potential development of future novel treatments.

The overarching aim of this research was to develop a treatment applicable to organic-based marine archaeological materials. A possible treatment was assessed on model wood and was found to be effective for removal of harmful iron and sulfur compounds. This is successful in that the treatment worked but also because it is often complicated to assess conservation treatments and, utilising methods like XAS, FTIR and Raman, it was possible to gain more in-depth knowledge of the treatment. These methods would also be useful for characterising materials before and after treatments, for example, for study of a hemp fibre before application of treatment, then study of the same sample after treatment by SEM-EDS, FTIR spectroscopy and potentially XAS.

Analysis of the fibres is important because each artefact has its unique considerations and it is useful to know more about these problems before developing a treatment and even to assess whether treatment would be necessary. By knowing more about how these artefacts react and behave, a clearer picture of how to deal with them can be obtained. Much research has been carried out on the characterisation and treatment of artefacts and this thesis contributes to this area. Characterisation of fibres is also important for investigating the effectiveness of future treatments. Conservation aims for minimal intervention and reversibility of treatment; it is about balance and consideration of many factors. This is where having a bounty of knowledge about how materials interact, and details of artefacts and how they degrade can be of great utility.

Future directions of this research could include application of the $SrCO_3$ treatment onto test modern textiles. With characterisation of the effectiveness of the treatment investigated by XAS, FTIR spectroscopy, and SEM-EDS. Alternatively, different conservation treatments could be researched and considered. Overall, characterisation of these artefacts and comparison to their modern counterparts has led to further understanding of these less-studied organic *Mary Rose* artefacts, making it easier to investigate and develop feasible treatments in the future.

Appendix

Chapter3 SrCO$_3$ Nanoparticle Treatments for *Mary Rose* Timbers

3.1 SrCO$_3$ Cellulose Patch Treatment
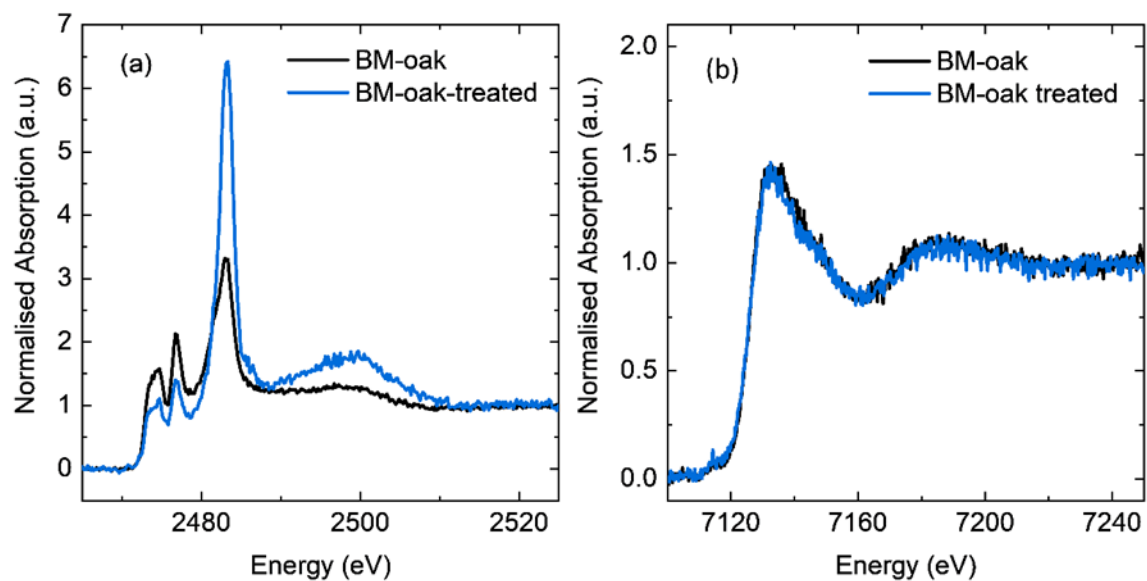
Figure 58(a) S K-edge XANES spectra for benchmark oak before and after treatment with the SrCO$_3$ cellulose patch **(b)** Fe K-edge XANES spectra of BM-oak samples before and after treatment.
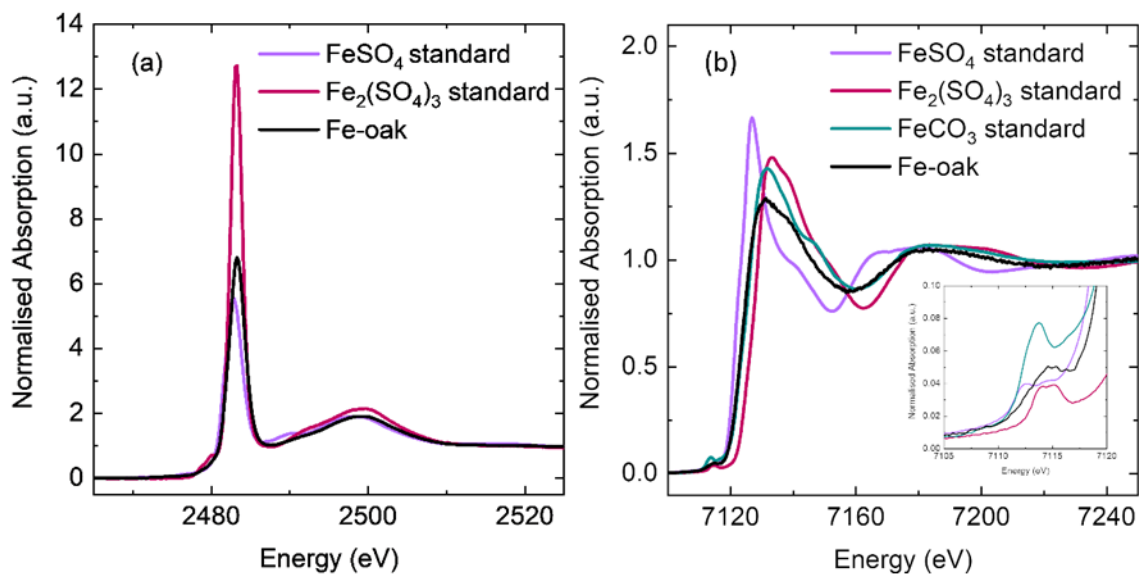
Figure 59 (a) S K-edge XANES of Fe(III) sulfate soaked oak sample (before treatment with the SrCO$_3$ patch) compared with iron (II) and (III) sulfate standards **(b)** Fe K-edge XANES of Fe(III)-oak sample compared with FeSO$_4$, Fe$_2$(SO$_4$)$_3$ and FeCO$_3$ standards.
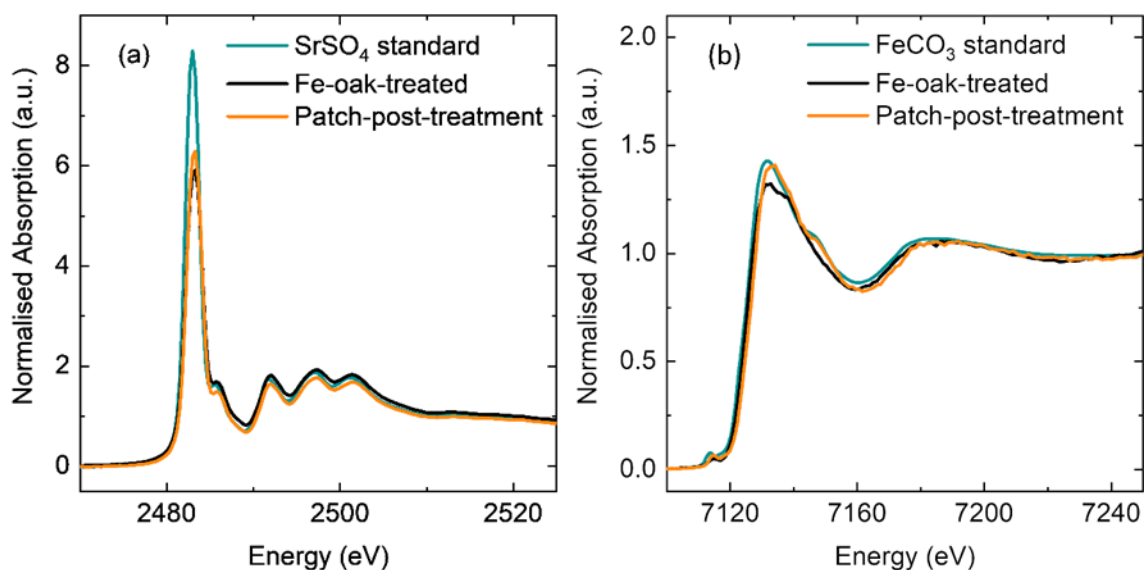
Figure 60 (a) S K-edge XANES spectra of Fe(III) soaked wood after treatment and the SrCO$_3$ cellulose patch after treatment compared with the SrSO$_4$ standard spectrum **(b)** Fe K-edge XANES spectra of Fe-oak-treated and patch-post-treatment samples compared with the siderite (FeCO$_3$) standard.

Linear Combination Fitting (LCF)
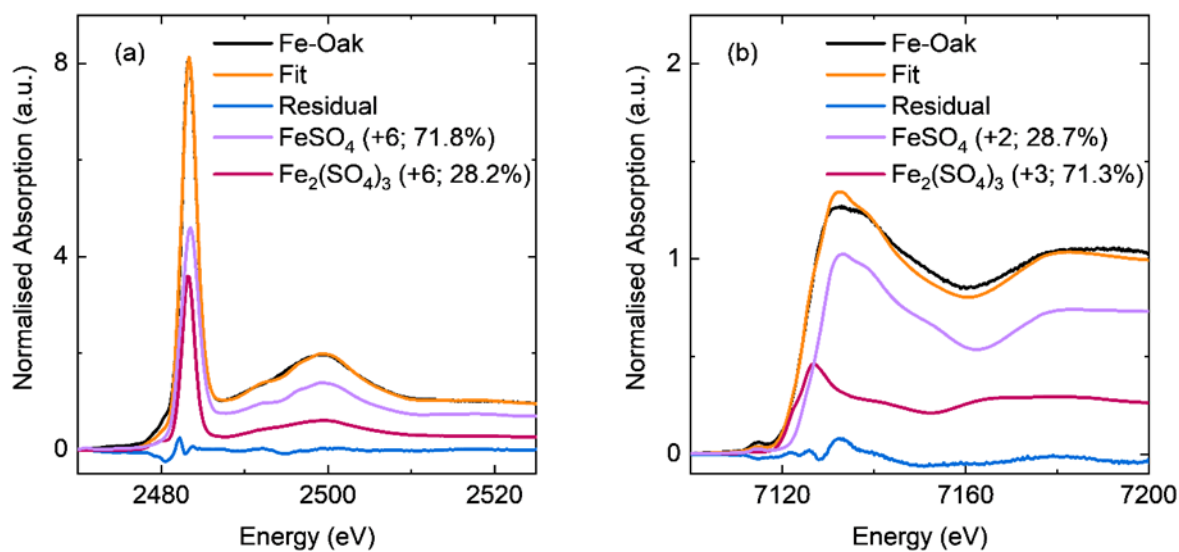
Figure 61 (a) showing the linear combination fit of FeSO₄ soaked wood before treatment including the oxidation state of the sulfur in the standards and their relative percentages obtained from the fit **(b)** LCF analysis of the FeSO₄ soaked wood showing the iron oxidation states and the relative percentages of the standards obtained from the fit.
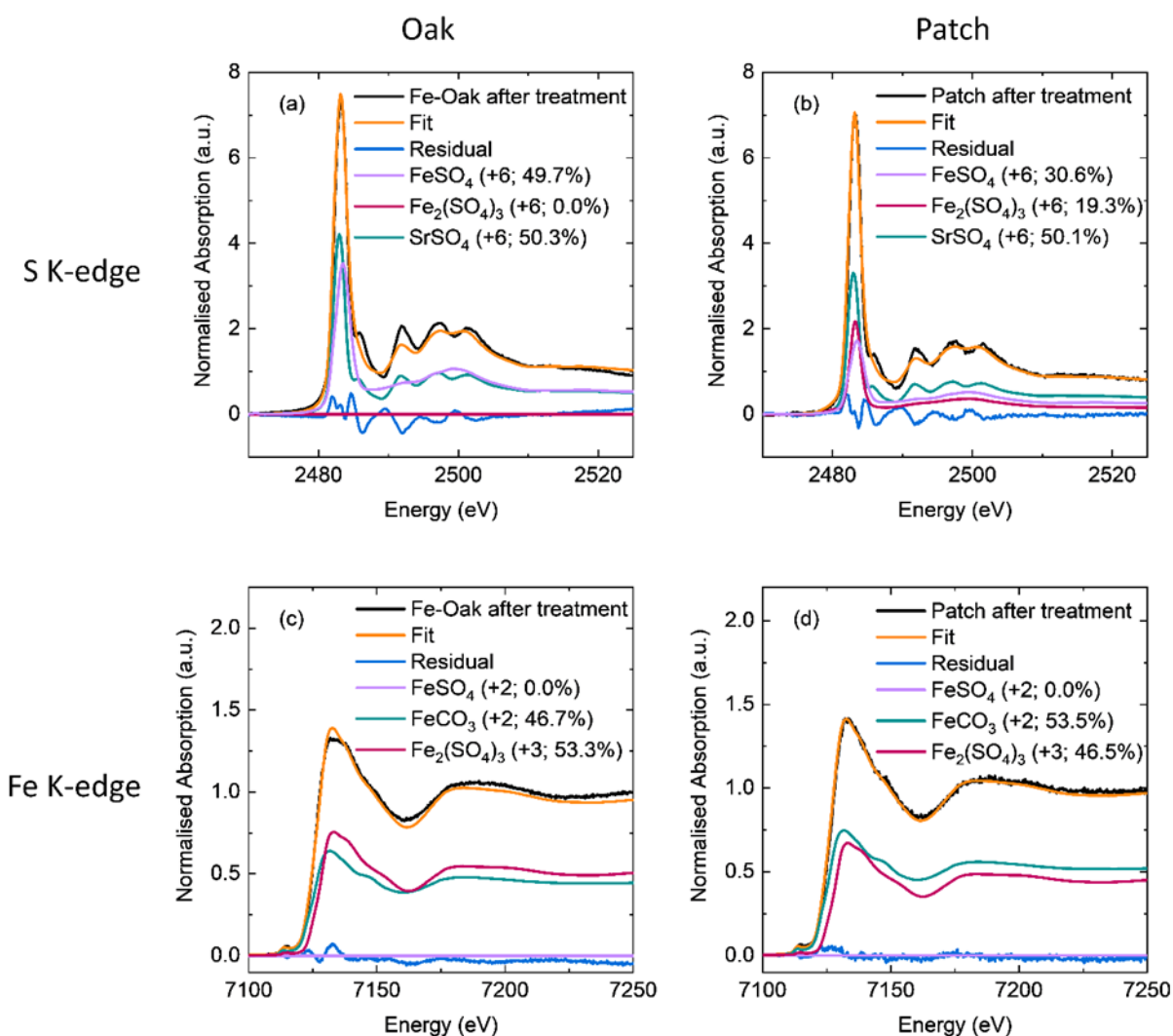
Figure 62 (a) LCF of S K-edge XANES spectrum of iron (II) sulfate soaked wood after treatment with the SrCO₃ cellulose patch **(b)** LCF of XANES spectrum of the SrCO₃ cellulose patch after treatment **(c)** The LCF analysis of Fe K-edge XANES data of FeSO₄ soaked wood after it had been treated with a SrCO₃ cellulose patch **(d)** showing the LCF analysis of the SrCO₃ cellulose patch sample spectrum after it had been removed from the soaked wood.

Table 11 Table displaying the raw data from LCF analysis of the S K-edge XANES spectra of BM-Oak and BM-Oak-treated samples.

Standard	BM-Oak Weight	Error	BM-Oak-treated Weight	Error
R-SH	0.387	0.028	0.215	0.039
R-S-S-R	0.153	0.029	0.182	0.040
R-SO-R	0.265	0.010	0.187	0.014
$R-SO_3^-$	0.133	0.010	0.059	0.013
SO_4^{2-}	0.182	0.006	0.569	0.008

Table 12 Summary of the raw data from LCF analysis of XANES spectra for both Fe(II) and Fe(III) sulfate soaked samples.

|		Fe(II) samples		Fe(III) samples			Fe(II) samples		Fe(III) samples	
	S Standards	S K-edge weight	Error	S K-edge weight	Error	Fe Standards	Fe K-edge weight	Error	Fe K-edge weight	Error
Fe-Oak	$FeSO_4$	0.729	0.007	0.668	0.006	$FeSO_4$	0.279	0.007	0.457	0.004
	$Fe_2(SO_4)_3$	0.285	0.005	0.165	0.003	$Fe_2(SO_4)_3$	0.693	0.007	0.534	0.004
Fe-Oak treated	$FeSO_4$	0.559	0.020	0.513	0.0025	$FeSO_4$	0.000	0.022	0.203	0.014
	$Fe_2(SO_4)_3$	0.000	0.016	0.000	0.015	$Fe_2(SO_4)_3$	0.511	0.037	0.550	0.025
	$SrSO_4$	0.569	0.023	0.392	0.036	$FeCO_3$	0.448	0.056	0.227	0.037
Patch	$FeSO_4$	0.272	0.015	0.336	0.017	$FeSO_4$	0.000	0.020	0.000	0.013
	$Fe_2(SO_4)_3$	0.173	0.012	0.000	0.010	$Fe_2(SO_4)_3$	0.454	0.034	0.513	0.021
	$SrSO_4$	0.445	0.017	0.626	0.024	$FeCO_3$	0.523	0.051	0.467	0.032

3.3 Synthesis of SrCO₃ Nanoparticles
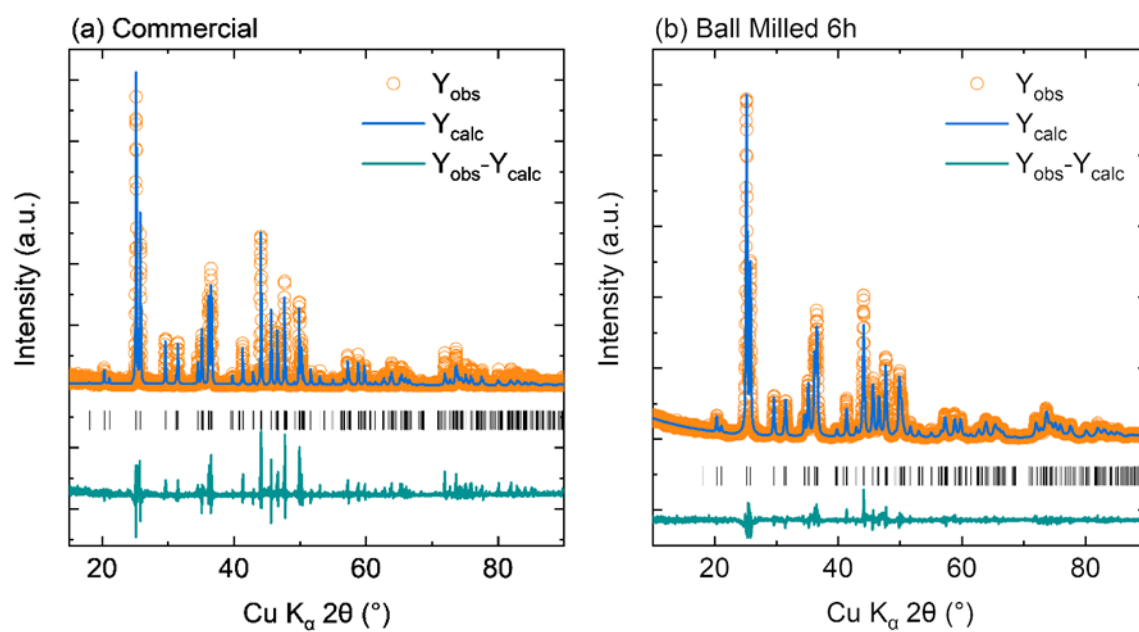
Figure 63 Rietveld refinements of **(a)** commercial SrCO₃ and **(b)** the ball milled for 6 hours SrCO₃ sample
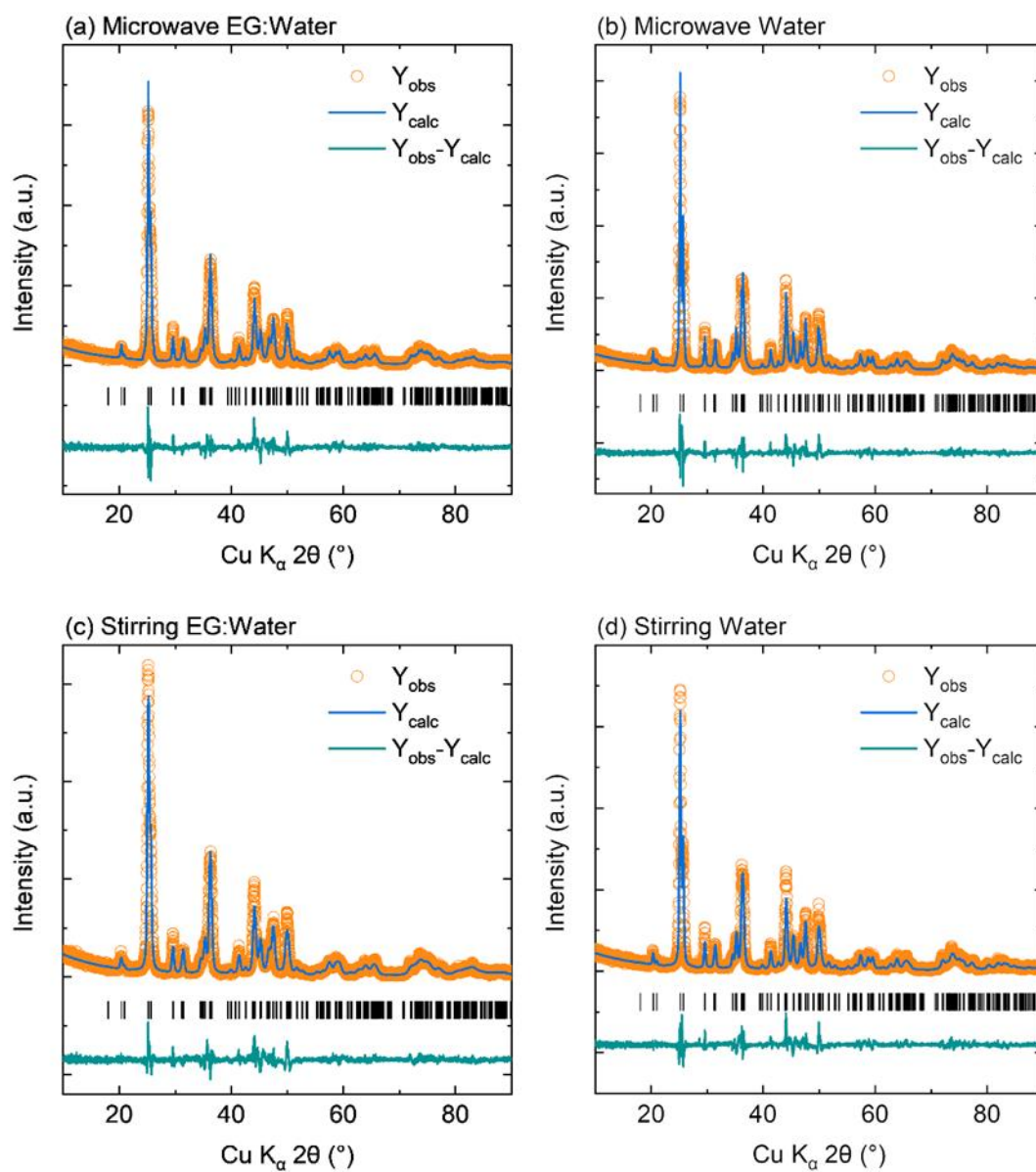
Figure 64 Rietveld refinements of **(a)** microwave synthesised sample in EG:Water **(b)** microwave synthesised sample in water **(c)** controlled precipitation synthesis of SrCO₃ in EG:water and **(d)** stirred in water.
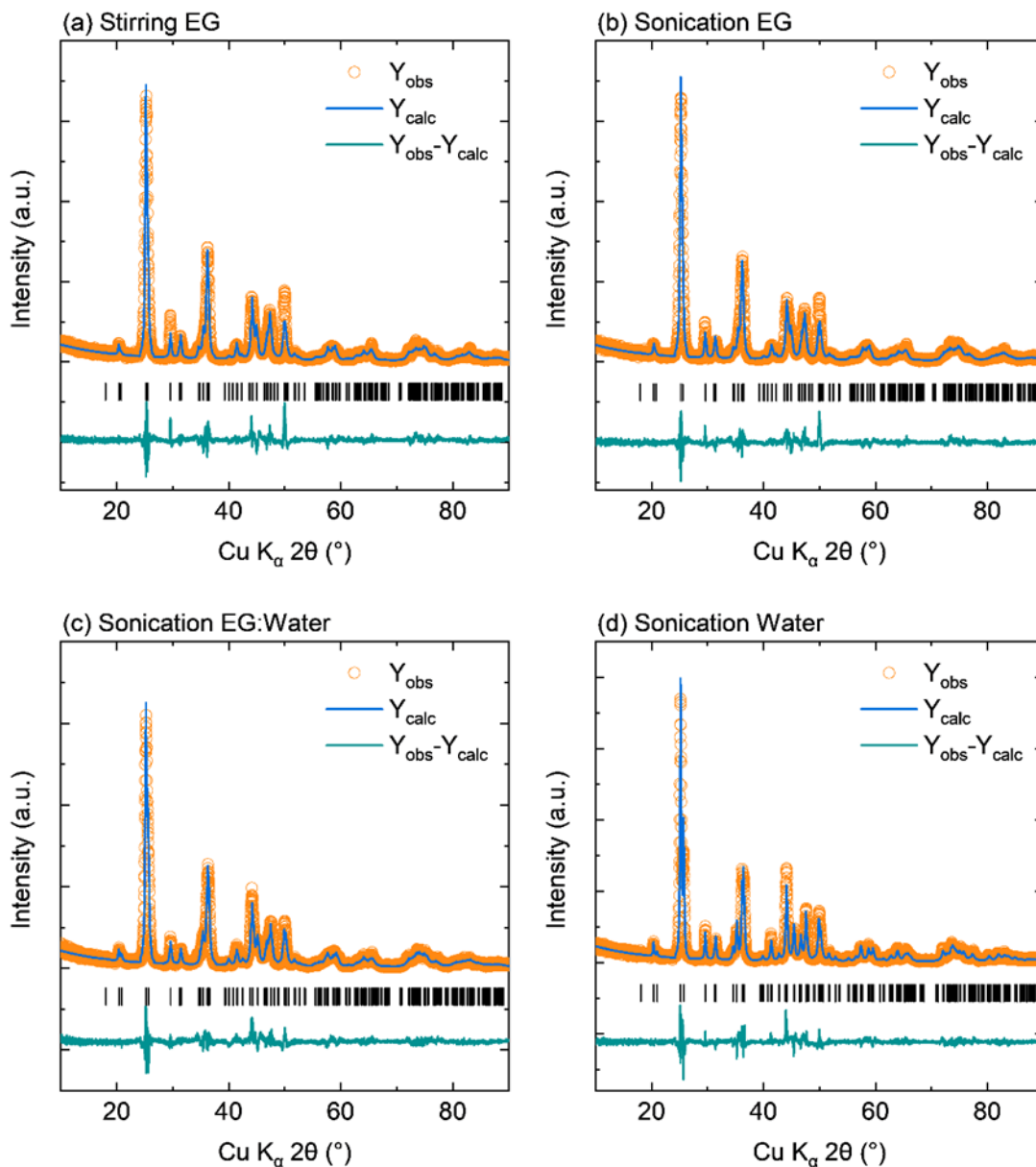
Figure 65 Rietveld refinements of **(a)** controlled precipitation synthesised $SrCO_3$ in EG **(b)** Sonochemical synthesis in EG **(c)** sonochemical synthesis in EG:water and **(d)** sonochemical synthesis in water.
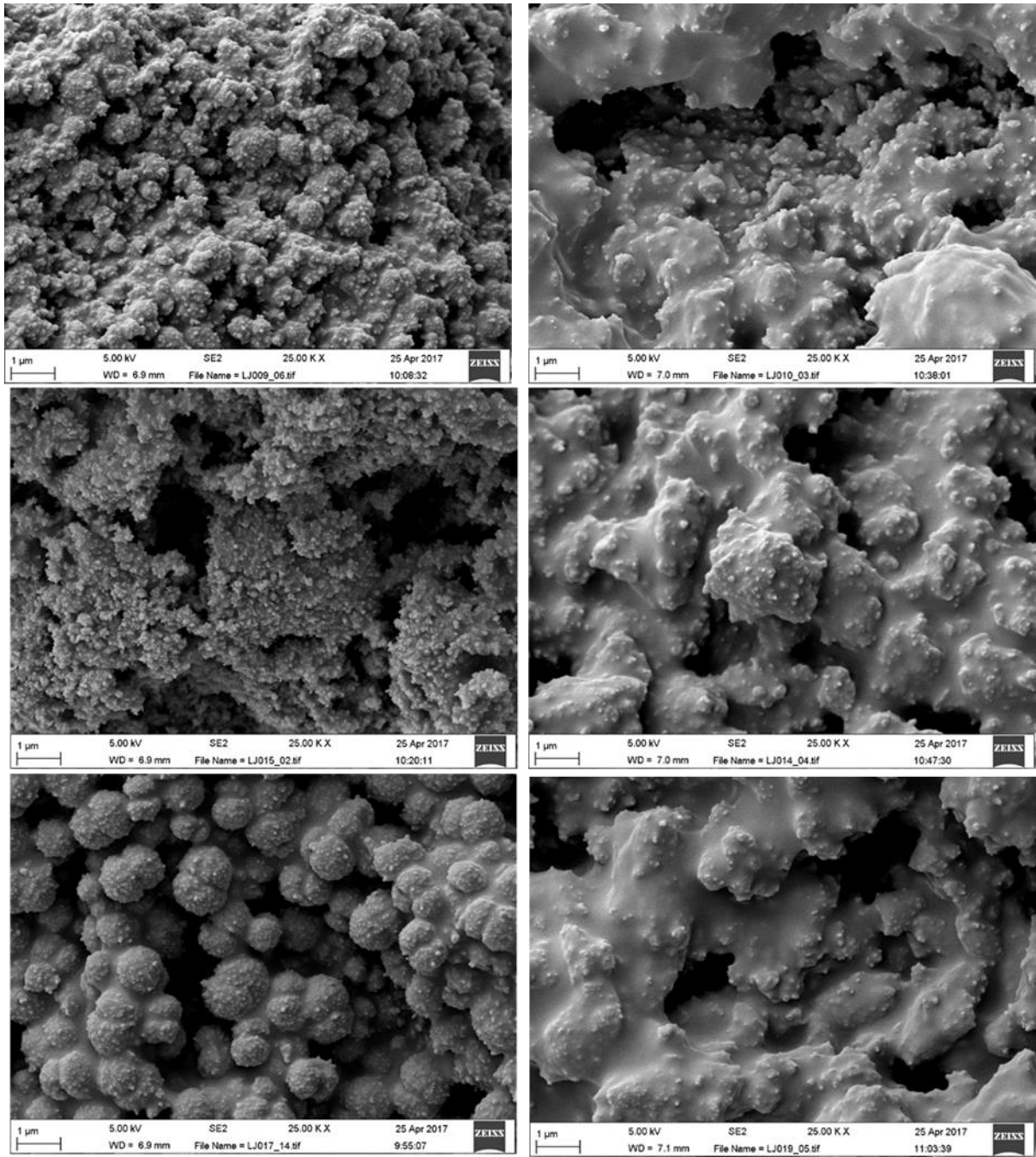
Figure 66 SEM images of synthesised $SrCO_3$ (from top to bottom) microwave, controlled precipitation, sonication methods with those synthesised in EG on the left and in EG:water on the right.

# 5 Characterisation of Proteinaceous Materials

5.1 Characterisation of Wool Fibres
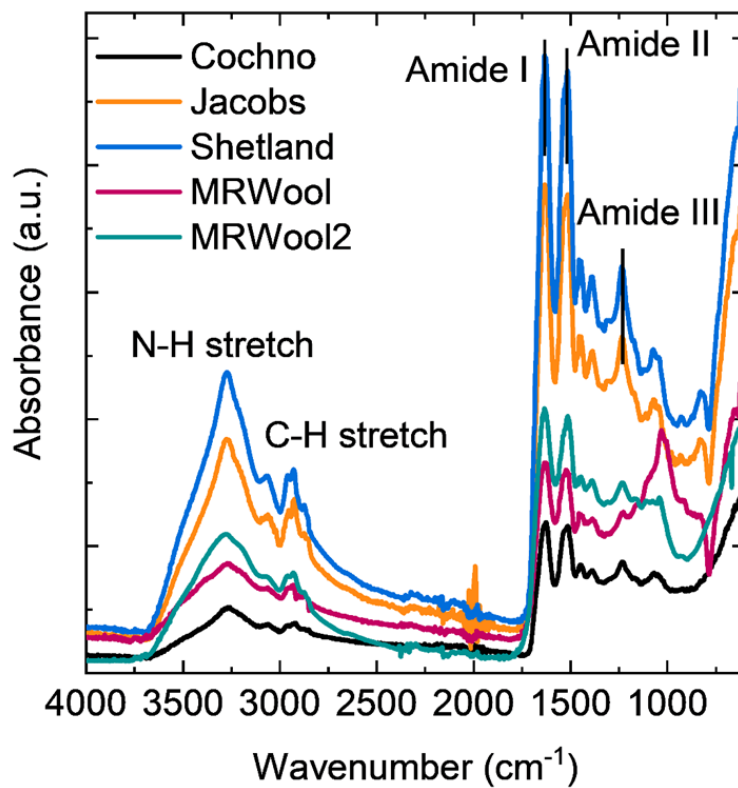
Figure 67 FTIR spectra of *Mary Rose* wool and modern wool fibre samples without baseline correction or normalisation.
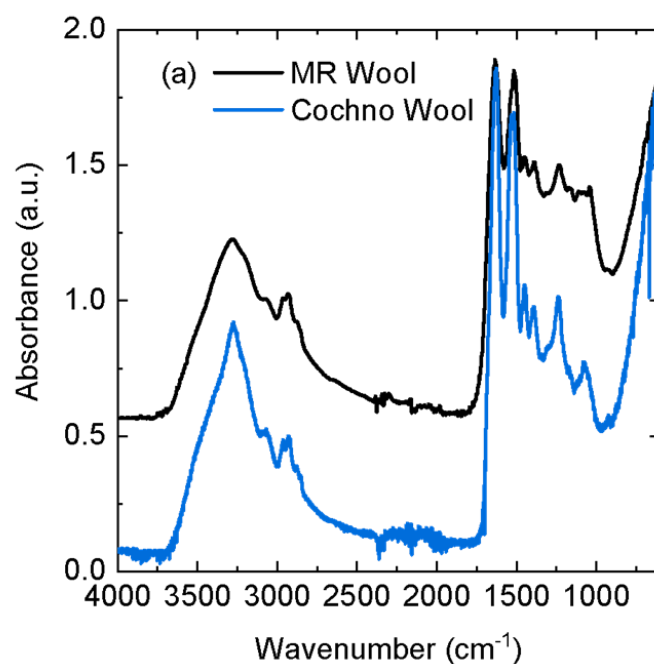
Figure 68 normalised to amide III band at 1232 cm^{-1}.

5.2 Characterisation of *Mary Rose* Leather
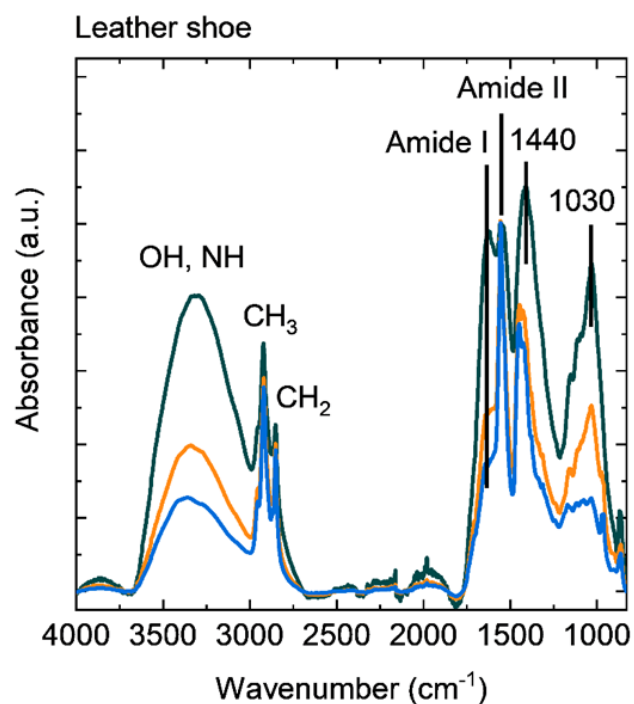
Figure 69 FTIR spectra of the *Mary Rose* leather shoe sample with spectra taken from different areas on the sample indicated by the differently coloured spectra. All spectra were baseline corrected and normalised to the amide II band (1553 cm^{-1}).
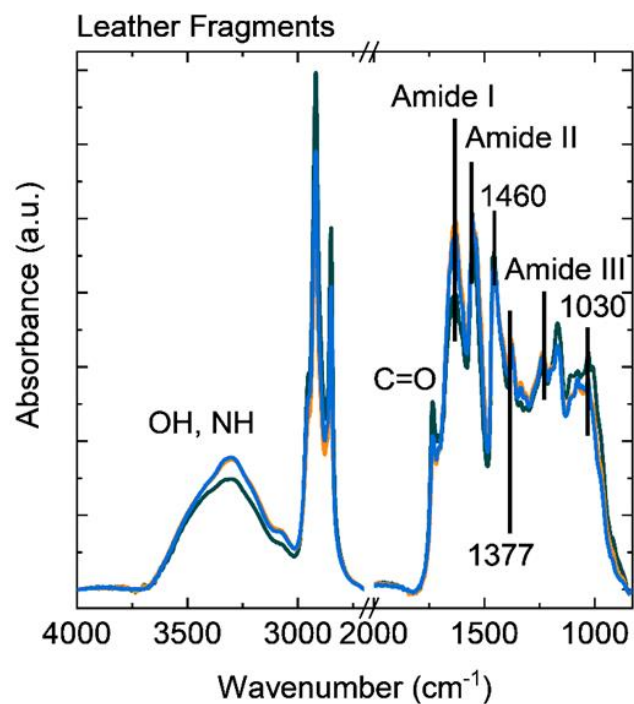
Figure 70 Annotated FTIR spectra of different areas on the leather fragments sample. All spectra were baseline corrected and normalised to the amide II band at 1553 cm^{-1}.
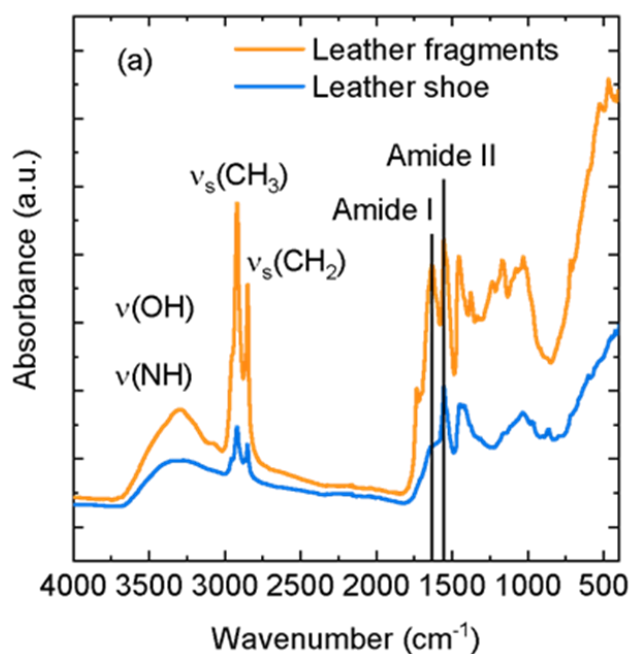

Figure 71 Annotated FTIR spectra of *Mary Rose* leather fragments (orange line) and shoe (blue line) samples without baseline correction or normalisation.